THÈSE DE DOCTORAT DE L'UNIVERSITE PIERRE ET MARIE CURIE

Spécialité : **Génie des procédés et Technologies Avancées**

EN COTUTELLE AVEC L'UNIVERSITE DE TRENTO

Présenté par

RAJESH PANDIYAN

Pour obtenir le grade

DOCTEUR DE L'UNIVERSITÉ PIERRE ET MARIE CURIE DE PARIS ET DE L'UNIVERSITÉ DE TRENTO

Sujet de la thèse:

GROWTH BY RADIO FREQUENCY SPUTTERING AND

CHARACTERISATION OF RARE EARTH DOPED

WIDE BANDGAP OXIDES

Soutenue le 9/9/2013 devant le jury composé de:

Encadrement:

Mme. NADHIRA BENSAADA LAIDANI Head, PAM-SE, Fondazione Bruno Kessler, Italy

Mme. FARZANEH AREFI-KHONSARI Professor, LGPPTS, UPMC-Sorbonne Univ, France

Rapporteurs:

M. GABORIAUD ROLLY   **Emeritus Professor, Univ. Poitiers, France**

M. LORENZO PAVESI   **Professor, Dept. of Physics, Univ. of Trento, Italy**

Examinateur:

Mme. LEBORGNE CHANTAL   **Professor, GREMI, Polytech Orleans, Ecole polytechnique de l'université, France**

M. STEFANO GIORGINI   **Professor, Head of the PhD doctoral school, Dept. of Physics, Univ. of Trento, Italy**

Acknowledgements

First and the foremost, I thank the *"Almighty God"* for giving me the strength and faith in successful completion of my thesis. I would also like to thank him for blessing me with wonderful tutors, colleagues and friends around me in these periods.

I express my most sincere and heartfelt gratitude to my thesis director Mme. Dr. Nadhira Bensaada Laidani for her inspiring guidance, valuable discussions, continuous encouragements, moral support and constructive comments and also her hard work and immense knowledge in the research field which helped me in the successful completion of this thesis. The care she took and her motherly approach is sincerely appreciable and am really fortunate to have her as my thesis supervisor and it is indeed a rare privilege to work under her guidance.

Equally, I am extremely thankful to my thesis advisor, Mme. Prof. Farzaneh Arefi-Khonsari for giving me this wonderful opportunity to work under her guidance and for the valuable suggestions and constant motivation throughout my research work. Still I remember on the first day of my arrival to UPMC, the care she took and the immense guidance is really invaluable.

It is a great pleasure for me to thank my wonderful colleagues at this moment, especially Victor Micheli, Gloria Gottardi and Ruben Bartali for their immense help, kindness, motivation, moral support and encouragement and moreover for treating me as their family friend. In these three years, the most time I spend with them inside and outside the laboratory is invaluable and enjoyable.

I would also like to thank my other colleagues in my group Gianni Coser, Giorgio Speranza, Ioana Luciu and Mian Kashif for their immense help and support during this period.

I express my sincere thanks to Dr. Davor Ristic and Prof. Maurizio Ferrari for their timely help, invaluable discussions and for allowing me to use the Photoluminescence experimental facilities in their laboratory.

CONTENTS

Chapter – 2: SYNTHESIS, METHODS AND MATERIALS

Abstract

The thesis reports the results of an experimental research on rare earth ion-doping effects on the structural, chemical, optical and near-infra-red photoluminescence properties of wide band gap oxide films. The aim of the work was to develop materials with good photoluminescence properties, which can be applied to increase the photovoltaic conversion efficiency of crystalline Si-based solar cells, through the increase of the most efficient and useful fraction of the solar spectrum which hits the cells, thanks to a photon frequency down-shifting process.

Neodymium trivalent ion (Nd^{3+}) was used as dopant of TiO_2 and ZnO thin films. The films, with different Nd concentrations were grown onto quartz by RF plasma co-sputtering and annealed at different temperatures (400°-800°). Different film architectures were investigated for their photoluminescence properties. Structural changes such as phase transformation from anatase to rutile, internal strain building and lattice distortion due to Nd^{3+} incorporation in titania, correlated with optical changes, were evidenced. Exciting titania and zinc oxide matrices with optimal Nd concentrations, with ultra-violet (UV) light energies equal to or above their gap values resulted in an efficient frequency down-shifting from UV to near-infra-red emission. The joint study of the vibrational, chemical and structural properties of the doped films allows the understanding of the excitation energy transfer process between the matrix to the ion, where self-trapped excitons can be involved. To conclude this study, the doped films were tested as down-shifter layers onto a Si-solar cell where they gave promising results. They were also tested for their photoactivity with methylene blue, showing their inhibitor effect on the photo-degradation of this organic dye molecule.

Keywords: Co-Sputtering, rare earth doping, Neodymium, Titanium dioxide, Zinc oxide thin films, Photoluminescence

Le travail de thèse a porté sur l' étude des effets de dopage de couches minces d'oxydes à large bande interdite par des ions de terre rare sur leur propriétés chimiques, structurelles, morphologiques, optiques et de photoluminescence dans le proche infra-rouge. Les couches dopées ont été produites par co-sputtering en radio-fréquence. Le travail a eu pour but de déveloper un matériau fonctionnel "photon downshifter", susceptible d'être appliqué dans le domaine de conversion photovoltaique sur des cellules solaires à base de silicium, pour en augmenter le rendement. Par ses proprietés de photoluminescence et de downshifting, ce materiau intervient dans ce processus en augmentant la fraction utile du spectre solaire incident sur la cellule.

L'ion trivalent du neodyme (Nd^{3+}) a été utilisé comme dopant de couches minces de TiO_2 et de ZnO, deposées avec différentes concentrations de Nd sur des substrats de quartz et recuits à différentes temperatures, entre 400°C et 800°C.

L'étude a mis en evidence des modifications structurelles, des transformation de phase, la creation de tensions mécaniques internes resultant en des distortions importantes du réseau crystallin et corrélées avec des modifications des propriétés optiques et de photoluminescence. L'excitation des matrices de TiO_2 et de ZnO dopées avec des concentrations de Nd optimales, avec la radiation UV correspondant à la valeur de la bande interdite, a donné lieu à d'intenses emissions dans le proche infra-rouge, grâce à un processus de transfert d'energie entre la matrice et l'ion Nd^{3+}. L'accés à de nombreuses techniques d'analyse a permis d' accéder à la compréhension du processus de transfert d'énergie entre la matrice et l'ion, dans lequel des excitons auto-piégés peuvent avoir un rôle. Pour conclure cette étude, les couches de TiO_2 dopées ont été testées pour leur function de downshifter sur des cellules solaires à base de silicium, donnant des résultats prometteurs. En testant leur photo-activité en presence de methylène bleu, ces couches ont montré leur caractère inhibiteur de dégradation de cette molecule organique.

Keywords: Co-Sputtering, dopage aux terres rares, néodyme, TiO_2, ZnO, photoluminescence.

Introduction

Crystalline and wide bandgap oxides thin films (3–5eV) are finding applications in a wide range of energy technologies, such as photovoltaics, ion conductors, thermoelectric, dielectrics and capacitors, bio-medical engineering (bio-electrodes) and environmental cleaning (photo-catalysis). Each of these energy technologies requires a thorough understanding of the materials chemistry of the oxide film and its interactions with the environment, substrate etc. Their application in photovoltaics in improving the solar cell efficiency has been of intense interest in recent years being investigated with a variety of experimental and theoretical approaches. Different processes have been proposed to overcome the efficiency loss, and all of these methods concentrate on a better exploitation of the solar spectrum like quantum dot concentrators, multijunction solar cells, interband transitions, photon frequency down converters and up-converters. Specifically, photon frequency conversion is an appreciable approach which allows to modify the solar spectrum by shifting or converting a spectral range to a region where the solar cell has a better response, as the mismatch between incident solar spectrum and the spectral response is one of the main reason for the efficiency loss in solar cells. It is noteworthy that with these nanostructured materials one can address a problem that affects conventional Si solar cells efficiency, i.e. the inefficient use of high energy photons.

The main objective of present work is to develop materials to increase the photovoltaic conversion efficiency of crystalline Si-based solar cells, through the increase of the most efficient and useful fraction of the solar spectrum which hits the cells, thanks to photon frequency down-shifting processes. In that sense, the

development of oxides doped with rare earths offers new opportunities to realize active materials for the efficient absorption and conversion of the solar radiation in a silicon solar cell.

This thesis reports an research results concerning the rare earth doping effects on the structural, chemical, optical and photoluminescence properties of wide bandgap oxide based materials for the applications of photon frequency downshifting processes. The work undertaken in this thesis is a study of the rare earth doping processes of thin films of wide bandgap oxide semiconductors such as titanium dioxide (TiO_2), Zinc Oxide (ZnO) amongst the favorite hosts; two cheap, chemically stable, biocompatible and non-toxic materials. Lanthanides are usually famous for their unique optical and luminescence properties when incorporated in a glass or semiconductors. The motivation of using rare earth ions is that it can absorb and emit over a wide range of wavelengths from near infra-red (NIR) through the visible to UV. Most recent research has been focused in the near infra-red region, where Nd^{3+} ions emits at three NIR luminescence emission peak at 880 nm, 1060 nm and 1330 nm corresponds to $^4F_{3/2}$ to $^4I_{9/2}$, $^4F_{3/2}$ to $^4I_{11/2}$ and $^4F_{3/2}$ to $^4I_{13/2}$. As of prime interest, trivalent Neodymium (Nd) is considered to be an excellent candidate due to its sharp and intense luminescence in the near infra-red which falls within the range of intrinsic spectral absorption of silicon solar cells. Neodymium (Nd^{3+}) was selected for the extrinsic doping of the TiO_2 and ZnO matrices.

AIM OF THE WORK

With the scenario described above, our objectives of this dissertation were focused on to these disciplines:

❑ To study the growth mechanisms (both growth process & doping conditions optimization) of rare earth (RE) doped oxide films by plasma processes,

aiming primarily to develop highly luminescent materials and to study their physico-chemical properties.

❑ Characterisation of the deposited thin films by using different techniques in order to find the suitable parameters to achieve efficient energy transfer process of the excitation energy of the matrix to the Nd^{3+} ions..

❑ To understand the factors dominating the doping process as well as those limiting it (understanding of the relationship between luminescence properties, the matrix excitation energy transfer characteristics)

❑ To demonstrate the practical possibility to use the developed materials in solar energy applications as efficient photon down-shifter layers that can be applied to the existing silicon based solar cells and to explore other potential functionality photoactivity.

Results suggest that the approach is in the right direction. Here, a note should be made that no attempt have been made in these host matrices concerning the experimental investigation on the influence of doping limit, for such a wide series of concentrations beyond which no photon down-shifting effect occurs.

PLAN OF THE THESIS

The thesis is composed of seven chapters, organized as follows. Starting with the general introduction, the chapter 1 will give an overview of the Synthesis, fundamentals of the wide bandgap oxides, the choice of rare earth ions used and their radiative properties. This chapter also gives the state-of-the art from the current research status on rare earth doping effects in wide bandgap oxide materials and also highlights the visible outcome of the research carried out, which serves as a good platform for future perspectives.

The second chapter describes the experimental details used for the growth of thin films by RF sputtering and a brief explanation on the principles of the characterisation technique used will be done.

Chapter 3 focuses on the results of the investigation of the neodymium effects on the structural, morphological, optical and photoluminescence properties of titania thin films. Only doping with low concentrations is generally pursued in order to avoid luminescence quenching.

Chapter 4 describes the investigation on the neodymium effects on the structural, chemical, optical, morphological and photoluminescence of Zinc oxide thin films. In this chapter, the first section will describe the doping effects of neodymium for such a wide concentrations, later part will describe the doping with very low concentrations of neodymium in the zinc oxide matrix, in order to achieve intense photoluminescence.

Chapter 5 elaborates in detail the investigations of the activation process of luminescent Nd^{3+} ions by the electronic structure of titania and zinc oxide matrices. Understanding the mechanism of near infra-red photoluminescence emission when the matrix is excited by UV photons is of great importance for controlling and also enhancing the optical properties of the novel materials.

Chapter 6 will describe the possible application of the above materials in photovoltaics as photon downshifter layers. The results of photoactivity tests in presence of organic dye molecules will be described.

Chapter 1

Chapter 1

Background and Literature Survey

"What you are is what you have been and what you will be is what you do now"
-Gautam Buddha

1.1   INTRODUCTION

1.1.1 TECHNOLOGICAL INTEREST IN LUMINESCENT MATERIALS

Wide-band-gap semiconductor nanostructures have been attracting intensive attention because of their unique properties resulting from the low dimensionality and the advantages provided by the wide-band-gap semiconductor materials. Recently, advanced technologies heavily rely on the exciting magnetic and spectroscopic properties of lanthanide ions. In particular, their ability to generate well-characterized and intense near-infrared (NIR) luminescence is exploited in any modern fiber-optic telecommunication network [1]. Rare earths luminescent material plays a vital role to a wealth of advanced optical materials and technologies and those involving near-infrared (NIR) luminescence have stirred particular interest in view of exciting applications in Telecommunications [2] and associated lasers and LED/OLED devices [3–5], as well as in bio-sciences [2, 4–12], and solar energy conversion [13–17]. Crystalline and wide gap oxides doped with trivalent lanthanide ions are increasingly gaining importance in the last few years for their useful applications in optoelectronics and lighting devices, in photo-catalysis, optical imaging and also in photon frequency down- and up- conversion. For the latter, the optical frequency conversion through photoluminescence has been suggested in the 70's in solar cells

coupled with luminescent concentrators [18]. Different processes have been proposed to overcome the efficiency loss, and all of these methods concentrate on a better exploitation of the solar spectrum like quantum dot concentrators, multijunction solar cells, interband transitions, photon frequency down conversion [19, 20] (one high energy photon can be splitted into two or more lower energy photons that can be absorbed) and up-conversion [21] (two lower energy photons can be added together to obtain one high energy photons) etc. Specifically, photon frequency conversion [22, 23, 24] is an appreciable approach which allows to modify the solar spectrum by shifting or converting a spectral range to a region where the solar cell has a better response, as the mismatch between incident solar spectrum and the spectral response is one of the main reason for the efficiency loss in solar cells. Since the pioneering studies [1], this frequency conversion approach was coupled with luminescent concentrators employing organic dye molecules. In contrast, due to the low quantum efficiency and stability of these organic materials, efforts have been focussed primarily on finding new nanostructured materials (particularly quantum dots, doped wide bandgap oxide semiconductors) have increased the interest in this topic and many literatures have been devoted to study these materials. The process of photon absorption in oxide semiconductors followed by an energy transfer toward some levels of the ions of rare earth is particularly effective [25]. In the literature, many works reported on doping of oxide semiconductors by numerous lanthanide ions, investigating the effect on the luminescence and structural properties [26-32]. It has been demonstrated that the properties of oxides can be tuned through the addition of variety of dopant ions and also the processing conditions [33, 34, 35]. From the viewpoint of luminescence applications in UV, Visible and NIR emissions, wide

bandgap oxides is an attractive host matrix for intentionally doping impurities for the effective optical activation for many technological applications.

Titania was synthesized either as nanoparticles or thin films. Sol-gel dip-coating was the most used method to prepare titania and doping with lanthanide ions like Sm^{3+}, Eu^{3+}, Yb^{3+}, Er^{3+}, Pr^{3+} and Nd^{3+}. Doping with these ions and the related luminescence and structural effects have been investigated in many semi-conductor matrices such as GaN [36, 37], AlN [38], Si-ZrO$_2$ [39] and (Y, Gd)BO$_3$ phosphors [40]. Several authors were also investigated this Nd^{3+} ion for doping other semiconductor and glass matrices such as Gallium Nitride (GaN) [41], Silicon-rich silicon oxide (SRSO) [42], Telluride glass series (TeO$_2$-WO$_3$-LiO$_2$) [43] etc. Near-infrared luminescence induced by Nd^{3+} in lower gap semi-conductors incorporation in silicon - rich silicon oxide (SRSO) and amorphous hydrogenated silicon sub-nitrides was also explored [44, 45]. It is noteworthy that with these nanostructured materials one can address a problem that affects conventional Si solar cells efficiency, i.e. the inefficient use of high energy photons.

In this chapter an overview of the Synthesis, physico-chemical properties, modifications and finally energy applications of the rare earth ion doped titanium dioxide and zinc oxide nanomaterials will be discussed. The introduction surveys their different approaches of synthesis methods, and the influence of doping effects in the wide bandgap oxide host matrix on their structural, morphological, optical and photoluminescence properties and finally their applications onto photovoltaics (as a photon converter) and as a photocatalyts will be discussed.

1.2 FUNDAMENTALS OF DOPING

One of the most efficient ways in altering the properties of semiconductor is doping. Doping can be also called as "controlled impurity" added to the material in a

homogeneous way. When large amounts of dopants are added to the material, either a mixed oxide phase or a second phase could form which depends on the solubility limit of the two components. Doping levels/limit and doping efficiency depends mainly on the ionic size and the electronegativity moreover on growth process too. Doping is used as a modification method for altering phase structure, electronic structure, and surface structure [46]. Dopants can be stay either as a substitutional or interstitial. Dopants are introduced in a semiconductor either by defects or impurities. Defects may also acts as a donors or acceptors. Some of the common defects found include vacancies, interstitials, dislocations and anitisites. The generation of free carriers requires not only the presence of impurities, but also that the impurities give off electrons to the conduction band in which case they are called *donors* or that they give off holes to the valence band in which case they are called *acceptors.*
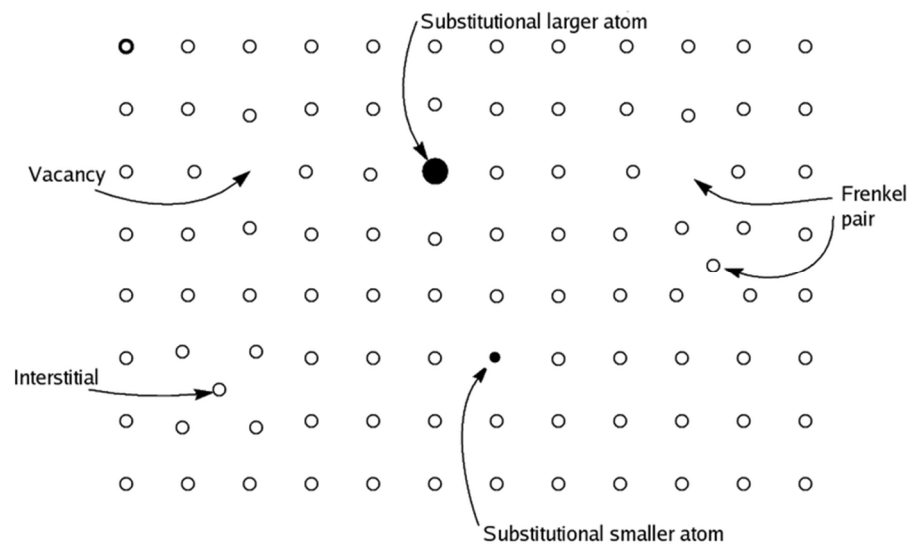
Figure 1.1: *Schematic representation of possibilities of dopants in lattice sites [47]*

Intrinsic doping

Intrinsic doping is present due to defects in the crystal lattice, away from stoichiometry. This leads to the oxygen deficiency and thus to oxygen vacancies in those materials. These oxygen vacancies give rise to shallow donor states just below

the conduction band and act as an n-type impurity band [48].

Extrinsic doping

The incorporation of extrinsic defects (cations or anions doping) into the TiO_2 lattice leads to the formation of donors and acceptors when their valency is higher and lower than that of host lattice ions. Several approaches for TiO_2 modification have been proposed: metal-ion implanted TiO_2 (using transition metals: Cu, Co, Ni, Cr, Mn, Mo, Nb, V, Fe, Ru, Au, Ag, Pt), reduced TiOx photocatalysts, non-metal doped- TiO_2 (N, S, C, B, P, I, F), composites of TiO_2 with semiconductor having lower band gap energy (e.g. Cd-S particles, sensitizing of TiO_2 with dyes (e.g. thionine) and TiO_2 doped with upconversion luminescence agent [48, 49].

1.2.1 DOPING MECHANISM

Nowotny et al. [50] reported a work based on the concepts of defect chemistry and photo electrochemistry in order to consider TiO_2 as a photocatalysts with aliovalent ions forming donors and acceptors. The effects of doping with aliovalent ions include both cations and anions were discussed. Interestingly, different kinds of doping mechanism have been proposed and these mechanism leads to different distributions of dopants and result in entirely different effects on properties.

Figure (1.2) shows below the possible mechanism of polycrystalline TiO_2 involving different distributions of dopants.
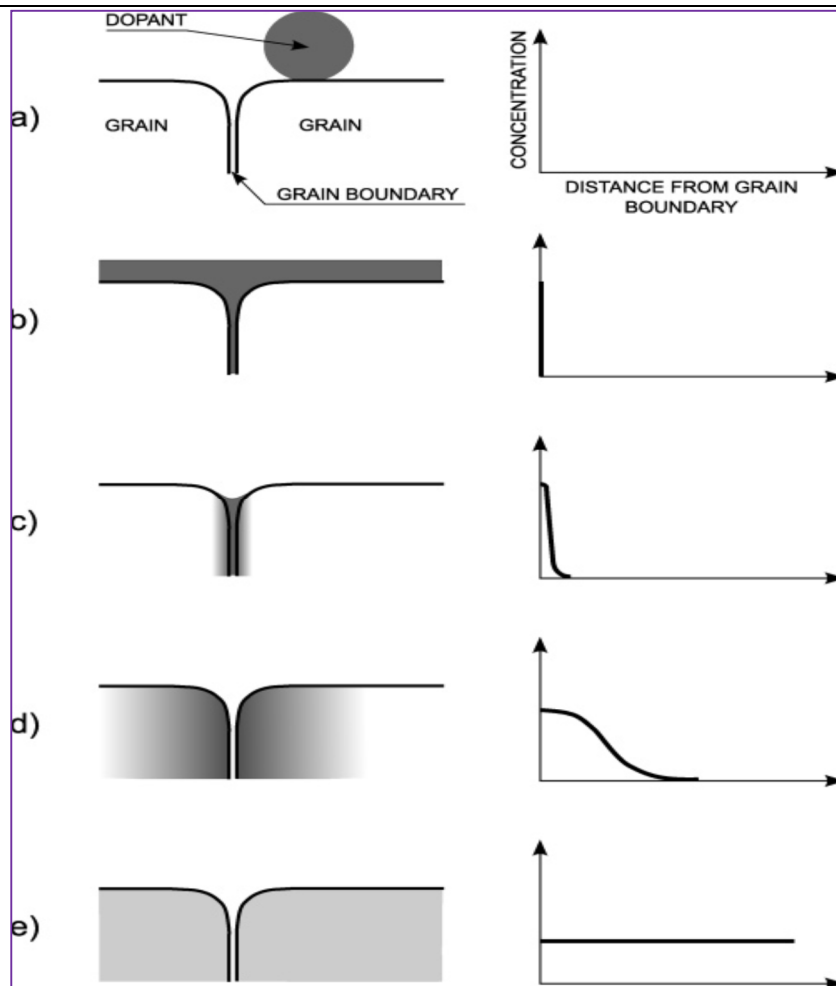
Figure 1.2: *Possible doping mechanisms of polycrystalline TiO$_2$, involving (a) deposition of isolated islets on the surface, (b) spread of the dopants on the surface and within grain boundaries, (c) filling of grain boundaries leading to limited diffusion profile, (d) limited bulk transport leading to the formation of a concentration gradient, and (e) homogeneous distribution of the dopant within the specimen. [Figure & concepts adapted from Reference 50]*

- The first mechanism represents surface coverage with small islets (Figure 1.2a). The effect of this kind of doping on properties depends on the surface coverage, the size of particles, and the nature of the interface formed between these particles.

- The second mechanism (Figure 1.2b) represents the dopant spread over the surface and along the grain boundaries, thus forming a thin oxide layer. This

kind of doping may lead to the blockage of the entire surface of TiO_2 with the dopant [50].

- The third mechanism (Figure 1.2c) involves the grain boundary penetration of the dopant by grain boundary diffusion (that is faster than bulk diffusion). This doping, which may occur at elevated temperatures [50]

- Figure 1.2d represents the limited diffusion penetration of the dopants into the grains, resulting in the formation of a solid solution and a compositional gradient. Although this kind of doping leads to changes of semiconducting properties, these changes are not well-defined because of the unknown effect of dopant concentration gradients [50].

- However, when the system is brought into the gas/solid equilibrium, then the dopant is distributed homogeneously within the grains (Figure 1.2e). This system is well-defined and may be assessed in terms of defect chemistry [50].

The choice of host materials is of great importance in designing a rare earth ion based luminescence for efficient energy applications. Generally luminescent materials require a host matrix with high crystalline structure. The characteristic luminescence properties can be achieved by doping the host matrix with a relatively small loading of rare earth ions.

1.3 SEARCH FOR A HOST MATERIAL FOR LUMINESCENT CENTRE

1.3.1 TITANIUM DIOXIDE (TiO$_2$)

1.3.1.1 FUNDAMENTAL PROPERTIES OF TITANIUM DIOXIDE

Titanium dioxide (TiO_2) is one of the very interesting metal oxide nanomaterial used for wide range applications because of its unique optical and physical properties. It is non-toxic, chemically stable, cheaper (low cost), bio compatible material. Titanium is

one of the more abundant metals on earth (exceeded only by aluminium, iron and magnesium); it constitutes about 0.63% of the earth's crust.

A glimpse on the applications of TiO_2 is as follows:

- Photovoltaics: as an antireflection coating layer, surface passivation, metallisation mask, ohmic contacts etc.

- Pigments: TiO_2 is used as a white pigment to provide whiteness and opacity in the products such as paints, coatings, plastics etc.

- Photocatalyst: TiO_2 is used as an effective photocatalyst material in heterogeneous catalysis and also in the photolysis of water.

- Cosmetics: In cosmetic products, titanium dioxide is used as a sunscreen because of its high refractive index.

Other applications include TiO_2 electrodes are used in electrochromic devices [51] and dye sensitized solar cells [52]. TiO_2 is extensively used in thin film optical interference coatings [53]. Some of the physical and chemical properties of TiO_2 include:

- Optical properties: higher refractive index (2.6) and high transmittance in the visible region.

- Electrical properties: Because of high dielectric constant, TiO_2 is used as a dielectric material in electronic applications

- Mechanical properties: High hardness and high durability

- Chemical properties includes: high chemical stability, and good chemical resistance.

Various fabrication techniques, such as sol-gel, sol, hydrothermal/ solvothermal, physical/chemical vapour deposition, electrodeposition, etc., have been successfully used in making TiO_2 thin films.

This section gives brief discussions based on the material structure and some of its properties reported in the literatures on TiO_2 thin films. Finally, the extensive survey on the influence of rare earth ion doping in TiO_2 is discussed in the last part.

1.3.1.2 CRYSTAL STRUCTURE OF TiO₂

Titanium dioxide crystallizes in three major different polymorphs in nature. They are anatase [A], rutile [R] and brookite [B] which exhibits different physical and chemical properties. However, only anatase and rutile play a major role in the applications of TiO_2. The most common and studied structure is rutile, the thermodynamically stable phase of titania; at higher temperatures (more than 700°C) anatase phase will be transformed in rutile phase. The brookite structure evolves only when stabilised by certain impurities. It is also well known that anatase is suitable for catalyst and support while the rutile is stable and suitable for optical and electronic applications because of its high refractive index and high dielectric constant. Deposition of TiO_2 films in room temperature results in the formation of amorphous TiO_2. The resulting phase (anatase and rutile) plays a major role in determining the structural, morphological, optical properties of the thin films. In the present work, we are interested only in the technologically important anatase and rutile phases, which were also intensively studied by different research groups.

Table below summarizes the physical properties of anatase and rutile titanium dioxide.

	Anatase	**Rutile**
Crystal structure	Tetragonal	Tetragonal
Space group	$I4_1/amd$	$P4_2/mnm$
Atoms per unit cell	4	2
Lattice parameters	a=0.3785 nm c=0.9514 nm c/a=0.2514	a=0.4594 nm c=0.2958 nm c/a=0.6441
Unit cell volume (nm^3)	0.1363	0.0624
Most stable surface	[101]	[110]
Density (Kg/m^3)	3894	4250
Refractive index	2.49 - 2.54	2.79 - 2.90
Bandgap (eV)	Direct = 3.42 Indirect= 3.46	Direct= 3.04 Indirect = 3.05
Hardness (Mohs)	5.5-6	6-6.5
Electron effective mass	$1m_e$	$9\text{-}13m_e$ $10\text{-}30m_e$

Table 1.1: *Physical Properties of anatase and rutile phase of titania [56].*

The structure and the unit cells of anatase and rutile structure of TiO_2 are shown in figure below.

Both rutile and anatase, with their tetragonal symmetry, can be described as a network of TiO_6 octahedra, where each Ti^{4+} ions is surrounded by an octahedron of six O^{2-} ions. In both the structures, a slightly distorted octahedral is considered to be the basic building block units. The two structures differ in the distortion of each octahedron and linkage of the octahedra. In the anatase structure, each octahedron is in contact with the eight neighbours (i.e, four sharing the edge and four sharing the corner). In the

case of rutile phase, each octahedron is in contact with the 10 neighbour octahedron (i.e), two sharing edge oxygen pairs and eight sharing corner oxygen atoms.
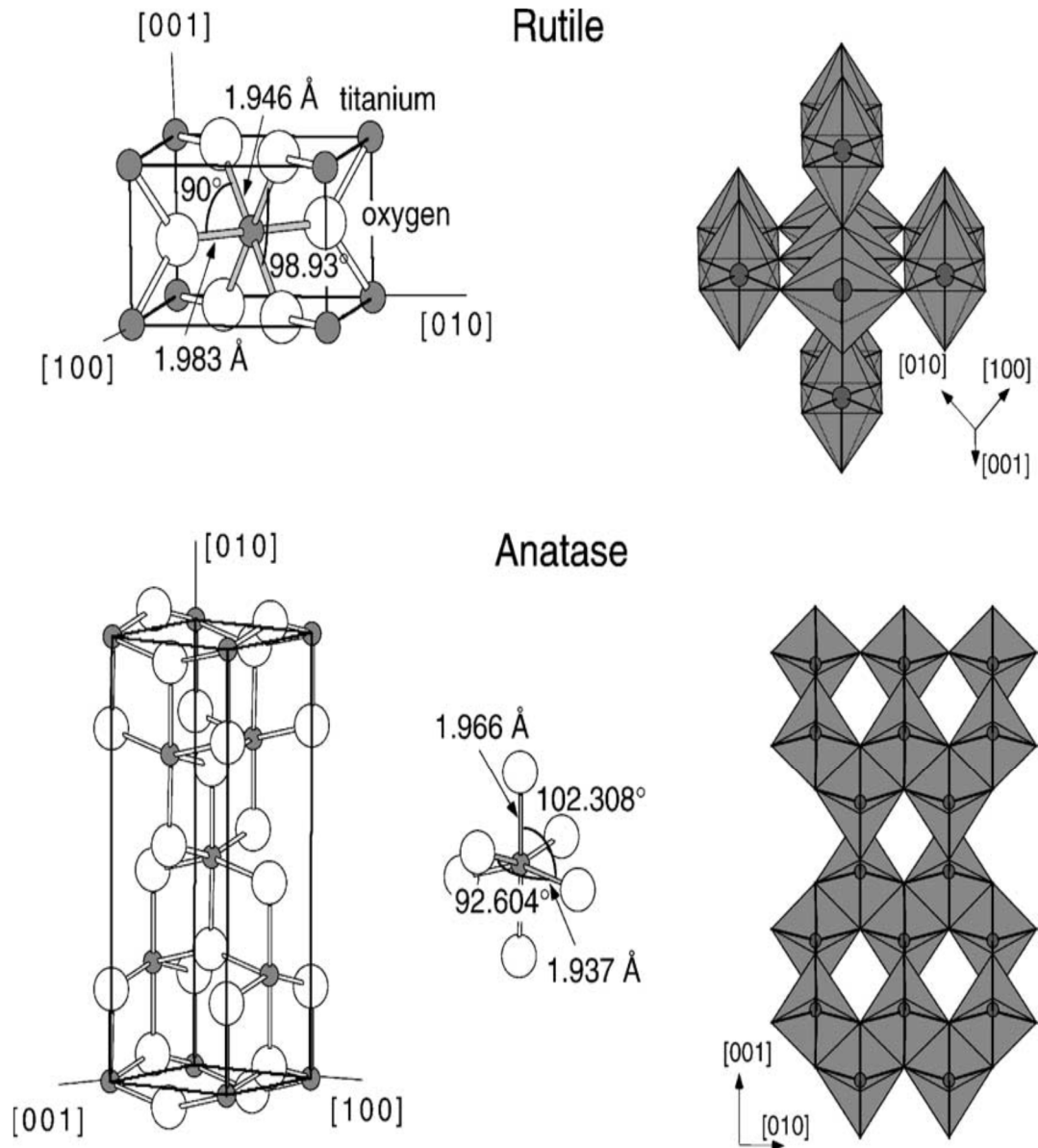
Figure 1.3: *Crystal structures of Rutile and Anatase of titanium dioxide with bond lengths and bond angles between them. Figure is reproduced from Ref [54].*

In rutile structure, the unit cell contains two Ti atoms situated at (0, 0, 0) and $(\frac{1}{2}a, \frac{1}{2}a, \frac{1}{2}c)$ and four oxygen atoms. The bond distance between the two Ti-Ti is

larger in anatase compared to rutile phase, but the bond distance between Ti-O is larger in rutile than those of anatase.

1.3.1.3 PHASE DIAGRAM AND PHASE TRANSFORMATION

Considering the thermodynamic stability of TiO_2, at all temperatures rutile is more stable than anatase. It is also evident from the thermodynamic theoretical calculations. Annealing Titania at various temperatures leads to the following phase transformations: Anatase to brookite to rutile, anatase to rutile, brookite to anatase to rutile.
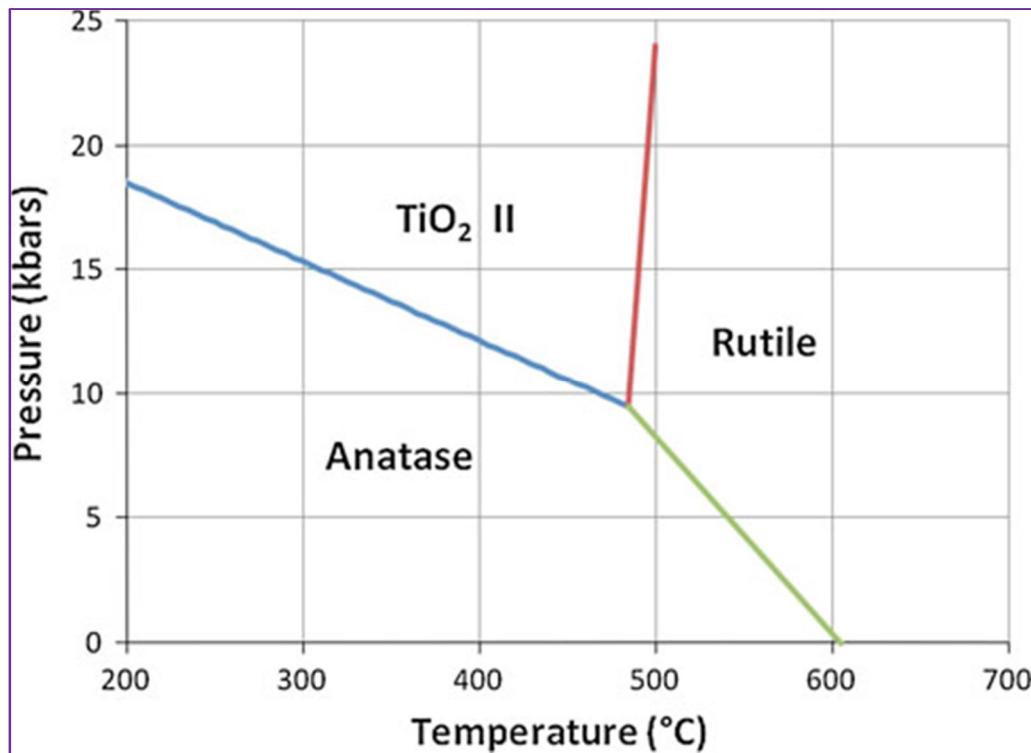
Figure 1.4: *Phase transformations in TiO$_2$ as a function of annealing temperature [55]*

These phase transformations is depends on the preparation methods, particle size, doping also. The transition from amorphous titania to anatase phase occurs around 300°C. Rutile phase transformation occurs when the annealing temperature exceeds 700°C and also the transformation of rutile is irreversible process (i.e.,) which cannot be transformed to anatase. Hanaor et al [56] described the transformation of anatase to

rutile by varying the transition temperature with respect to the deposition pressure. Figure (1.5) shows the phase transitions in TiO_2 with respect to annealing temperature and working pressure. As it is reported, the anatase to rutile phase transformation occurs around 605°C at 1 atm pressure.
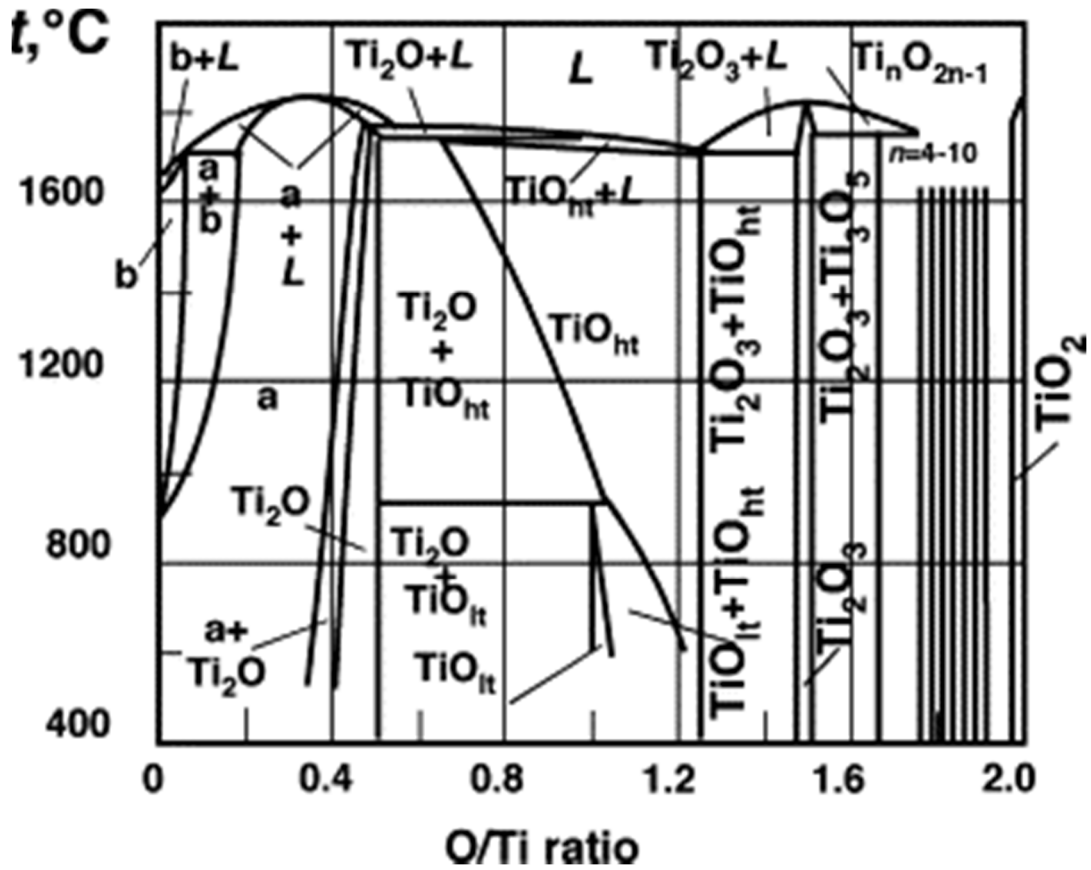
Figure 1.5: *Phase Diagram of Titanium dioxide [adapted from ref 57]*

Another factor affecting the phase transformation is the presence of defects on the oxygen sublattice (increase in the oxygen vacancies – TiO_{2-x}). Oxygen vacancies are also known to be created in hydrogen atmosphere, thereby favouring the transformation to rutile. When both rutile phase and anatase phase possess a tetragonal structure, rutile is more densely packed and thus possesses a greater density (4.26 g/cm^3) than anatase (3.89g/cm^3). Amorphous TiO_2 films possess a wide range of densities, from 2.4g/cm^3 for porous films [58] to 3.2 – 3.65 g/cm^3 [59]. TiO_2 films with lower density favours impurity diffusion, so in the case doping with impurities

[60], anatase phase is preferred. Let's have a look on the figure which shows the Ti-O phase equilibria of titanium dioxide with respect to the oxygen to titanium ratio (O/Ti) and the temperature. Figure reveals that TiO_2 is an oxygen deficient oxide TiO_{2-x}. In the phase diagram as we see there are large number of compounds varies with respect to the stoichiometry. At low stoichiometric ratio, the evolution of Ti, Ti_2O, TiO, Ti_2O_3, Ti_3O_5 can be found. At higher stoichiometric ratio between Ti_3O_5 and TiO_2, there is an evolution of homologous series Ti_nO_{2n-1}, termed as Magneli phases or crystallographic phase (n>=4) [57].

Extensive study was adopted in the literatures based on the effect of impurities and dopants on the anatase to rutile phase transformation. It has been reported that inclusion of certain amount of impurities or addition of dopants remarkably changes the phase transformation. It has been reported that these dopants can also acts as an inhibitors or promoter of the phase transformation based on the size, valence etc.

1.3.2 ZINC OXIDE (ZnO)

1.3.2.1 FUNDAMENTAL PROPERTIES OF ZINC OXIDE (ZnO)

Zinc oxide is a wide bandgap semiconductor (3.4 eV) having a large exciton binding energy of 60 meV at room temperature, considered as the most promising semiconductor for many technological applications [61-64]. Many particular features of ZnO are determined by the fact that, among the elements of the sixth group, the ionization energy of oxygen is the highest, which leads to a strongest interaction between the Zn*3d* and O*2p*- orbitals [65]. Zinc oxide is a versatile material that have been used in variety of applications such as UV absorption, sunscreen lotions, antibacterial treatments[66], catalysts [67], photocatalysis [68], and as an additive in many industrial applications. ZnO nanostructures are also attractive for solar cells [69], liquid crystal displays. The lack of a centre of symmetry in wurtzite structure

combined with large electromechanical coupling results in piezoelectric and pyroelectric properties which can be used in mechanical actuators and piezoelectric sensors [70-74].

1.3.2.2 CRYSTAL STRUCTURE OF ZnO

Zinc Oxide crystallizes in the hexagonal wurtzite structure. The other structural form of ZnO are cubic blende, cubic rocksalt. At ambient pressure and temperature conditions, ZnO exhibits the thermodynamically stable wurtzite structure as shown in figure. At high pressures, a cubic structure is formed (NaCl lattice); cubic ZnO is an indirect gap semiconductor with a band gap width of Eg = 2.7 eV [65]. As ZnO belongs to hexagonal lattice, it belongs to the space group of P63mc or c_{6v}^4 with two lattice constants "a: 0.32539 nm" and "c: 0.52098 nm" in the ratio of $\frac{c}{a} = \sqrt{\frac{8}{3}} = 1.6333$.

A schematic representation of wurtzite structure is shown in the figure below.
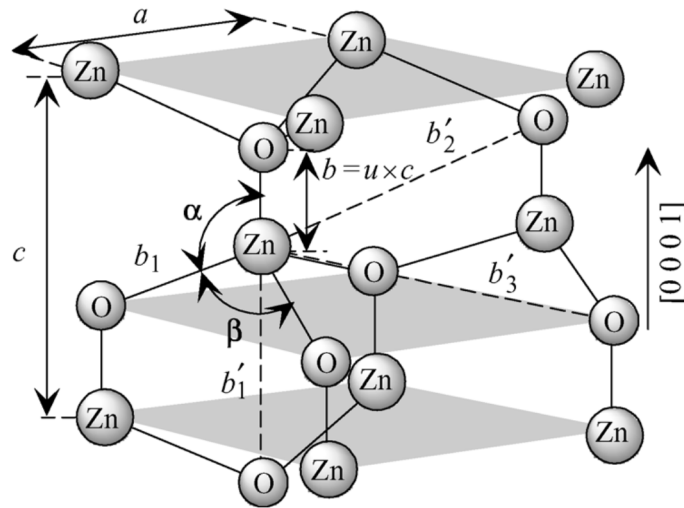
Figure 1.6: *Schematic representation of a wurtzitic ZnO structure having lattice constants "a" in the basal plane and "c" in the basal direction, u parameter, which is expressed as the bond length or the nearest-neighbor distance b divided by c (0.375 in ideal crystal), a and b (109.47° in ideal crystal) bond angles [Figure adapted from Ref 75]*

As ZnO crystallizes in hexagonal structure, each anion (O^{2-}) is surrounded by four cations (Zn^{2+}) at the four corners of tetrahedron. The structure is composed of two interconnecting hexagonal closepacked (hcp) sublattices of Zn^{2+} and O^{2-}, each of which consists of one type of atom displaced with respect to each other along the threefold c-axis. Another important characteristic of ZnO is polar surface and the most common polar surface is basal plane. Besides the stable polar plane [0001], two non-polar surfaces [10$\bar{1}$0],[11$\bar{2}$0] and one polar [000$\bar{1}$] facets exist in the structure [76].

Physical Parameters	Values
Stable phase at 300K	Wurtzite
Lattice Parameters	a= 0.32495 nm, c= 0.52069 nm, u= 0.345, c/a = 1.602
Density	5.606 g/cm3
Melting point	1975°C
Refractive index	2.008
Energy gap	3.4eV, direct
Exciton binding energy	60meV
Electron effective mass	0.24

Table 1.2: *The summary of the basic physical parameters of ZnO.*

1.3.2.3 LUMINESCENCE PROPERTIES OF ZnO

At room temperature, photoluminescence spectrum of ZnO typically exhibits two luminescence bands, a short wavelength band which is located near the absorption edge of the material (i.e.,) near band edge luminescence. A broad wavelength band also could be observed which is usually in the green spectral range. The broad emission band ranges from 420 nm to 700 nm which is attributed to the deep level emission band (DLE). This deep level emission band arises due to the native defects

in ZnO material such as Zinc interstitial (Zn$_i$) [77], Oxygen vacancies (V$_o$) [78-81], Zinc vacancies (V$_{zn}$) [82, 83] and Oxygen antisites (Zn$_o$) [84].

1.4 CHOICE OF LUMINESCENT DOPANTS

1.4.1 RARE EARTH IONS AS ACTIVE LUMINESCENT CENTRES

Rare earth ions – jewels for functional materials of the future [85] are intensively investigated concerning their optical and unique spectroscopic properties due to their electronic configurations.
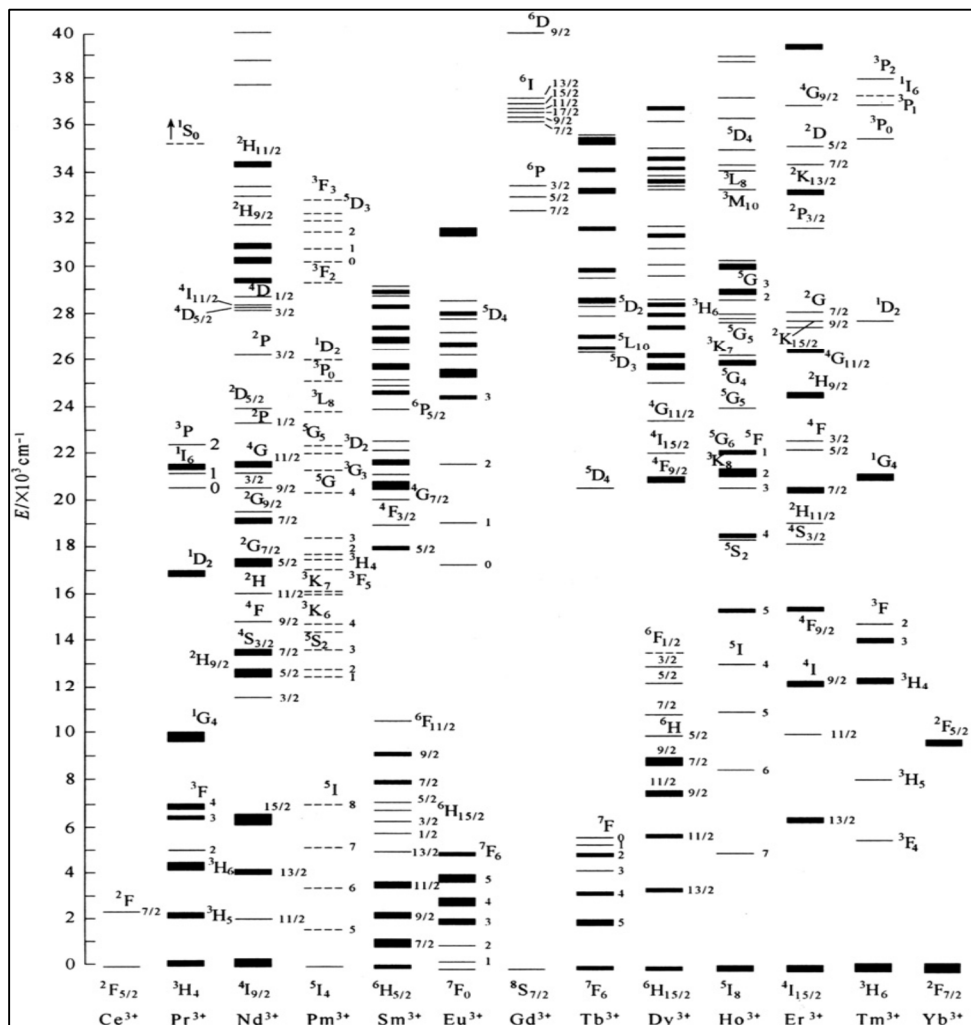
Figure 1.7: *Energy level structure (Dieke Diagram) of rare earth ions[86]*

They are used in wide range of applications such as lighting, displays, lasers and fibre amplifiers and (bio) medical applications including imaging and labelling [87-89].The lanthanide ions are a group of elements that is listed at the bottom of the periodic table

after lanthanum. They are isotopically stable and the outer electronic configurations of trivalent ions with dominant oxidation state of RE^{3+} having a general form of [Xe] $5s^2 5p^6 4f^n$ with n refers to the number of 4f electrons. The partially filled $4f$ electrons are responsible for the characteristic optical transitions properties for Ln^{3+}. The group of elements from cerium (58) to ytterbium (70) are often denoted as rare earth ions. The partially filled 4f orbitals have different energies exhibiting rich energy level structure, wavelength covering from ultraviolet, visible to infra-red part of the spectrum. The rich energy level structure makes that lanthanide ion as a perfect "photon managers" that can be used to efficiently convert the radiation into photons of any desired wavelength [90, 91]. The vast difference between the transition metal ion and the lanthanide ions lies in the nature of $4f$ orbitals. The characteristic energy level structure of rare earth ions is illustrated in the figure, which is also called as Dieke Diagram [86]. Since the $4f$ electrons are shielded by the completely filled outer $5s^2$ and $5p^6$ electrons, they are only weakly affected from the ions in the surrounding medium in the host matrix. Due to this shielding, all the trivalent ions result in very narrow sharp optical absorption and emission bands which are relatively independent of the host matrix. The transition between the parity forbidden $4f$-$4f$ states (no change in the dipole moment) and the shielding by outer electrons, minimizing the interactions between the doped ions and the host matrix , the excited states have relatively longer lifetimes; up to milliseconds.
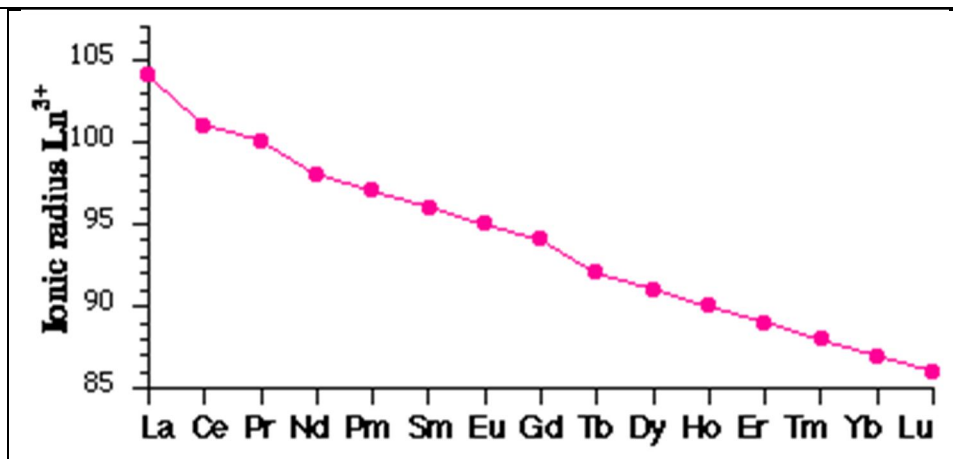
Figure 1.8: *Ionic Radii of the trivalent lanthanide ions*

The poor shielding of the 4*f* electrons provides a progressive increment of the effective nuclear charge resulting in a smaller atomic radius. This trend is then so called lanthanide contraction [92]. The ionic radii of the lanthanides decrease from 103 pm (La^{3+}) to 86 pm (Lu^{3+}) in the lanthanide series [93].
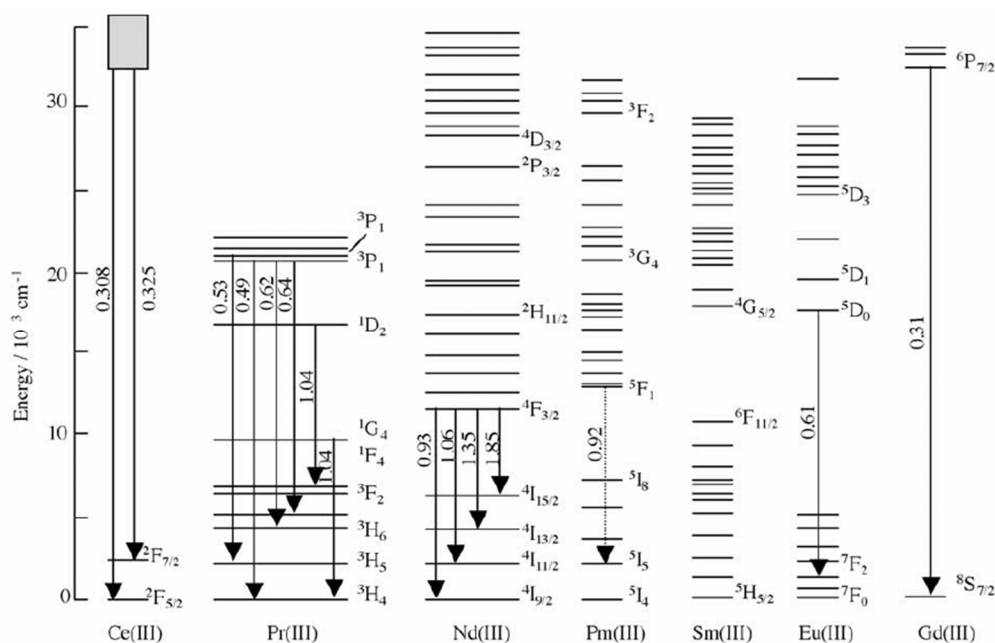
Figure 1.9: *Electronic states (Dieke diagram) for a selective of Ln(III) ions (Cerium, Praseodymium, Neodymium promethium, Samarium, Europium, Gadolinium). Solid black arrows indicate radiative transitions [Figure adapted from 231]*

From the classical approximation, the Russel-Saunders (RS) coupling allows the representation of the electronic states (Dieke diagram) denoted as $^{2s+1}L_j$ where (L) the orbital angular momentum, (s) the spin angular momentum and (j) total angular quantum momentum, respectively. S and j are represented with numbers 0, ½, 1, 3/2 etc. L represents orbitals S, P, D, F… when L is equal to 0, 1, 2, 3, 4… respectively [94, 231].

1.4.2 NEODYMIUM (Nd³⁺) CHARACTERISTICS

Neodymium is one of the rare-earth element in the group of Lanthanides have been the focus of numerous investigations because of their unique optical properties [95, 96] and promising applications in optoelectronic [97, 98] and magnetic devices. Neodymium ion presents an interesting emission in the near infrared region which is widely used for laser operation [99]. These elements have a partially filled 4f electron band. Five major absorption bands Nd^{3+} in the visible and NIR range can be observed at 520nm, 580nm, 745nm, 800nm, 880nm. In neodymium, the ground state, $^4I_{9/2}$, is stable and the $^4F_{3/2}$ state is meta-stable. The three NIR luminescence emission peak at 880 nm, 1060 nm (strong photoluminescence emission, long PL lifetime) and 1330 nm corresponds to $^4F_{3/2} \rightarrow ^4I_{9/2}$, $^4F_{3/2} \rightarrow ^4I_{11/2}$ and $^4F_{3/2} \rightarrow ^4I_{13/2}$. The Nd^{3+} transition around 1330 nm is interesting for the amplification of optical signal in intergrated systems and devices [100]

1.5 STATE OF ART ON THE RECENT PROGRESS ON DOPING ON RARE EARTH IONS IN THE OXIDE NANOMATERIALS

Doping luminescent lanthanide ions into semiconductor nanocrystals is an ideal approach for developing novel nanomaterials and nanodevices for many technological applications. Luminescent nanomaterials are, in principle, relevant to all the well-known applications of classical bulk-phosphors (i.e., fluorescent lamps, light-emitting

diodes, emissive displays, tomographs, X-ray detectors) [101]. The luminescent nanomaterials can be broadly classified into two categories. In the first category of nanomaterials luminescence is arising due to the inherent nature of the material or the type of structural units present in the material, whereas in the second category, luminescence is attributed to the dopant ion present in the non-luminescent host having nano size dimensions. Oxides like ZrO_2, Ga_2O_3, SnO_2, ZnO, Sb_2O_3 etc. are examples of the first category of materials. Systems like Y_2O_3:Ln, YPO_4:Ln, $CePO_4$:Ln, LaF_3:Ln, GdF_3:Ln, etc. (where Ln stands for the lanthanide ion) are few examples of second category of materials. Some of the transition metal ions also act as luminescent centres in different inorganic hosts.

Compared with III-IV and II-VI semiconductor nanocrystals, much less work has been done on lanthanide-doped III-VI (such as In_2S_3) or IV-VI (such as TiO_2, SnO_2 etc) semiconducting oxides. Rare earth ions modified wide bandgap oxides have been explored for the applications of photovoltaics (photon frequency conversion, photoluminescence) and also in photocatalysis. In case of application in PV devices, the optical absorption cross sections of rare earth ions are usually rather small due to their intrinsic 4f–4f forbidden transitions and their absorption is limited to narrow lines, which prevent the efficient absorption of the incoming photons. To solve this problem, one of the effective routes is to utilize the broadband absorption sensitizers. For example, semiconductors such as CdS, ZnO, TiO_2, SnO_2 and In_2O_3 are able to efficiently absorb the incident energy and then transfer it to rare earth ion, inducing the enhancement of rare earth DS emissions. This section provides a deeper insight analysis of rare earth ion doping with wide bandgap oxides (TiO_2 and ZnO) and their photoluminescence properties and mechanism are introduced, together with their attributes and affecting factors are discussed.

1.5.1 REVIEW OF STUDY OF RARE EARTH (RE) IONS DOPED TiO₂ NANOMATERIAL

Different rare earth ions have been doped into TiO₂ nanomaterials [102-123]. The preparation method of these materials differs widely such as wet chemistry, PVD processes, ion implantation etc. Jia et al. prepared Eu^{3+} doped TiO₂ films by sol gel method to study the visible and near infra-red luminescence properties of Eu ions by annealing at different temperatures [124]. Kiisk et al prepared Sm^{3+} doped TiO₂ powders by sol gel route to study the luminescence characteristics exposing significant quantum yield at room temperature [125]. Similarly, Eu^{3+} doped TiO₂ nanorods, successfully synthesized by a hydrothermal method, were used to assemble a DSSC with a Eu^{3+} doped TiO₂ nanorod/TiO₂ nanoparticle (Eu-NR/NP) bilayer electrode [126]. Y. Zhang et al. prepared various amounts of neodymium doped mesoporous TiO₂ thin films synthesized by copolymer templating. It was observed that the titania mesostructure was preserved for dopant additions upto 30 mol.% of Nd/Ti [127].

Jeon and Braun developed a new route to synthesize luminescent Er^{3+}-doped TiO₂, anatase phase nanoparticles having the particle size of 50nm through a simple hydrothermal method starting from sol - gel precursors [128]. They observed a remarkably enhanced luminescence from thin films of the nanoparticles by annealing at 500°C to remove surface hydroxyl groups, whereas the as-deposited films have weaker luminescence. Wang Yue et al [129] prepared Nd-doped TiO₂ nanoparticles by sol-gel method with various annealing temperatures in the range 70–1100°C. They reported a significant lattice distortion in Nd-doped TiO₂ nanoparticles annealed below 900°C. Extensive study were made by Li et al [130] on the dopant location identification and also the lattice distortion in Nd^{3+} doped TiO₂ nanoparticles

synthesized by MOCVD method. Yanqin Wang et al [131] studied the photoelectrochemistry of Nd^{3+} doped TiO_2 nanocrystalline electrodes prepared by hydrothermal process for the applications on dye sensitized photochemical solar cell systems. Atomic layer deposition is one of the methods that are viable for preparation of metal-oxide films with a controllable thickness, structure and optical parameters. S.Lange et al [132] studied the energy transfer photoexcitaion of Sm^{3+} implanted TiO_2 thin films by ALD deposition and they demonstrated the energy transfer from the host matrix to the Sm^{3+} ions and they discussed on the participation of bound excitonic states in the energy transfer. Nassoko et al [133] studied Nd doped TiO_2 with anatase and brookite two phases synthesized by sol gel route and they discussed the mechanism for Photocatalytic activity enhancement under visible light for the degradation of Rhodamine B. It was found that hydroxide radicals produced by Nd-doped TiO_2 under visible light are one of reactive species for Rh-B degradation and photogenerated electrons are mainly responsible for the formation of the reactive species.

Recent studies made by A. Ali et al [134] showed that incorporation of Nd in TiO_2 lattice causes texturing and it has been demonstrated that enhanced texturing along a certain plane direction (004) could be achieved with the control of Nd concentration and growth conditions by sputter deposition. Soft-chemistry routes to design inorganic or hybrid nanomaterials open a land of opportunities for the development of new materials for optics. Celine Marie Leroy et al. [135] prepared mesoporous anatase-type titanium dioxide thin films (300 nm thick) with uniform pore diameters were prepared by dip-coating on silicon and quartz substrates, following the Evaporation-Induced Self Assembly (EISA) procedure. They reported about the rare earth locations and the emission fluctuations under illumination. These fluctuations

are attributed to charge trapping and appear to be strongly dependent on the amount of europium and the level of crystallinity. Domaradzki et al [136] studied the influence of annealing on the structure and stoichiometry of europium-doped titanium dioxide thin films fabricated by magnetron sputtering from a metallic Ti – Eu target in oxygen atmosphere and the films were additionally annealed in air up to 1070 K. It has been shown that Eu dopant enhances absorption of OH⁻ groups at the surface of the Eu/TiO$_2$ as compared to the pure titania. Eu dopant at the concentration of 0.1at%, introduced into TiO$_2$ thin films, restrains structural anatase to rutile transformation even after an additional annealing up to 1070 K. Stengl et al. [137] recently patented a new methodology in preparation of rare earth doped TiO$_2$ nanoparticles where a one-step, a one-pot, no post synthesis calcination and no sol gel synthesis was used for the preparation. These samples were prepared in aqueous solution by homogenous hydrolysis from TiOSO$_4$. The overall PC activity for Orange II dye degradation under UV or visible light irradiation was significantly enhanced by doping with rare earth ions and also they reported that using homogeneous hydrolysis have a considerable effect on optical properties of as-prepared samples (without any additional annealing) and leads to lowers band-gap energy comparing with another methods. Borkowska et al.[138] studied the photoluminescence properties in TiO$_2$ matrix doped with Eu and Nd ions prepared by High Energy reactive Magnetron Sputtering (HE RMS) technique using metallic Ti-Eu and Ti-Nd mosaic targets for the film deposition.

Burns et al. [139] studied the pure and neodymium ion dopant effects on the on the anatase to rutile structural transformation phase transformation in sol–gel derived titania nanostructures. They proposed that Nd^{3+} ions occupies lattice positions at lower concentration of doping and at higher doping concentrations (>0.1 mol.%) it occupies the interstitial position. Shannon and Pask [140] observed that anatase to

rutile phase transformation was enhanced by oxygen vacancies and proposed that oxygen vacancies acts as a nucleation centres for the transformation. Chao et al. [141] synthesized Nd doped TiO_2 hollow spheres were prepared using carbon spheres as template and Nd-doped titania nanoparticles as a building blocks. They showed that modification of titania with Nd significantly affects the light absorption property of the photocatalysts. The red shift in absorption band edge of the doped samples attributed to the charge transfer between the titania valence or conduction band and the Nd ions 4f level. Li et al [142] reported an interesting result on the bandgap tailoring of Nd^{3+} doped TiO_2 nanoparticles. Pure and Nd doped TiO_2 were synthesized by chemical vapour deposition (CVD) technique in order to tailor the band gap of TiO_2. The band gap was measured by ultraviolet-visible light absorption experiments and by near-edge x-ray absorption fine structure and some DFT calculations were used to interpret the band gap narrowing. They interpreted that the band gap narrowing was attributed to the substitutional Nd^{3+} ions which introduced electron states into the band gap of TiO_2 to form the new lowest unoccupied molecular orbital. Li et al [143] used a novel technique in preparing rare earth (Eu and Sm) doped nanocrystalline microspheres emitting photoluminescence via energy transfer. The technique adopted is ultrasonic spray pyrolysis (USP) combined with solvent evaporation induced self-assembly. Intense broad PL emission spectra achieved by exciting at 330 nm (UV – bandgap absorption of titania) via energy transfer from the host to rare earth ions mediated by titania defect states. Ghigna et al [144] published an interesting article based on the unusual Ln^{3+} substitutional defects studies: to study the local structural environment of two rare earth ions (Pr^{3+} and Nd^{3+}) doped TiO_2 by EXAFS studies. It has been demonstrated that the Ln^{3+} cations enter the anatase structure as substitutional defects with respect to Ti. They also clearly

explained that in the TiO$_2$ the local structure at the Ln^{3+} cations is affected by strong disorder that broadens the emission features. Yang et al [145] studied the Raman spectral analysis of TiO$_2$ thin films doped with rare earth ion (Sm) prepared by sol gel technique. They reported that, Sm doping can inhibit the phase transition of anatase to rutile by refining grains of TiO$_2$ thin films and increasing the internal stress, thereby reducing the Raman intensity. Kaczmarek et al. [146] showed that doping of neodymium ion in TiO$_2$ prepared by high energy magnetron sputtering caused high densification of the structure. The structural densification by Nd doping allows obtain a highly nanocrystalline anatase phase. Podhorodecki et al. [147] studied the excitation mechanism of Eu ions embedded into nanocrystalline TiO$_2$ matrix by low pressure hot target reactive sputtering. The strong emission related to europium ions in the visible range has been observed at a indirect excitation wavelength suggesting an efficient excitation transfer from the host matrix to the ions. Luo et al. [148] reported host sensitized luminescence of Nd^{3+} and Sm^{3+} ions incorporated in anatase titania nanocrystals prepared by sol gel technique. They reported that Ln^{3+} ions were effectively incorporated into TiO$_2$ lattice exhibiting sharp and well resolved CF transitions of Ln^{3+}. The host sensitization may occur via phonon-assisted ET processes. The sensitized emissions of Nd^{3+} and Sm^{3+} found to be much more efficient than a direct excitation of lanthanide ions (Ln^{3+}). Tachikawa et al. [149] studied the defect mediated photoluminescence dynamics of Eu doped TiO$_2$ nanocrystals at the single particle or single aggregate level prepared by RF Ar/O$_2$ thermal plasma oxidation of mists of liquid precursors. They showed an interesting fact that photoactivation is accompanied by numerous "photon bursts" until saturation of the PL intensity occurred. They suggested that the PL band originating from defects at the TiO$_2$ surface appears in the visible region with numerous photon bursts

on photoirradiation. Some of the recent articles on the photoluminescence of lanthanides ions doped TiO_2 matrix [150-156]. Zeng et al. [157] studied the temperature dependence of the fluorescence emission of Eu doped TiO_2 and they suggested that phonon assisted absorption and temperature quenching effect is the two key factors for the quenching effect when the temperature varied from room temperature to 573 K for different doping concentrations of Europium.

1.5.2 REVIEW OF THE STUDY OF RE IONS IN ZnO NANOMATERIAL

Rare earth ions doped ZnO matrix have been attracted much interest in may technological applications in optoelectronic devices such as LEDs, high power lasers, phosphor displays etc [158-163]. Due to its wide bandgap of 3.37 eV and an exciton binding energy of 60 meV, ZnO is also a suitable host material for the doping of rare earth ions [164, 165]. Doping methods have been extensively utilized for modifying the electronic structures of ZnO material to achieve new or improved physico-chemical, electronic, optical and magnetic properties. The optical properties of rare earth ion doped ZnO depends on many factors like dopant concentration, host structure and also on the preparation parameters. Dopants can segregate as a separate phase on the surface structure of ZnO or they can either be substitutional or interstitial or both [166]. Since the pioneering studies by Destriau et al [167] on the properties of ZnO and ZnS type phosphors, knowledge concerning the luminescence of II-IV materials has been enlarged. Up to date, ZnO doped with Ce [168], Pr [169], Nd [170], Eu [171], Gd [172], Tb [173], Dy [174], Er [175-177], Tm [178] and Yb [179] have been intensively studied. ZnO with unique optical, electrical, ferromagnetic, and morphological properties were prepared by the doping of rare earth elements. A large variety of ZnO-based nanostructures has been prepared by several methodologies,

including vapour solid synthesis [180, 181], thermal evaporation [182- 187], chemical vapor deposition [188], sol-gel methods [189] and solution phase procedures [190]. Presented here is a review on the literatures covering the recent developments in rare earth doped ZnO, which highlights the crucial points involved in the synthesis and also the effect of doping along with the photo physical properties.

Lidia et al. [189] reported an interesting correlation between the structure and the luminescence properties in Eu doped ZnO nanopowders prepared by sol-gel method. Significant result has been reported that simultaneous green and red luminescence has been achieved upon excitation at 394 nm. In this fashion, the low-energy transfer efficiency from the ZnO host to the Eu^{3+} centres can be synergistically exploited for single or multi-coloured emission through the proper choice of excitation wavelength. Subramanian et al [191] made a detail study on the doping effects on the structural, optical and electronic properties of Nd doped ZnO films prepared by spray pyrolysis technique. The electronic structure was studied by using NEXAFS experiments which shows strong evidence for hybridization of Nd ions with O ions in the ZnO lattice. Recently, Ungureanu *et al* [192] studied the electrical and magnetic properties of Nd doped ZnO thin films and showed that the resistivity of Nd doped ZnO reduces by increasing the thickness of the film. Shahmoradi et al. [166] fabricated neodymium doped ZnO hybrid nanoparticles under mild hydrothermal conditions with temperatures of 150°C using two surface modifiers. They showed that these surface modifiers changed the morphology and size of the nanoparticles and it also changed the surface charges and increased the stability of the nanoparticles. They reported that Nd^{3+} reduce the bandgap energy and enhanced the feasibility of photodegradation in the visible light. Xian et al. [193] studied the effect of Nd doping level on optical and structural properties of films synthesized by sol gel route. They proposed that the

intensity of ultraviolet emission is greatly enhanced when Nd doping concentration is 1% and the green emission intensity is gradually increased with increase in the Nd doping concentration. Interestingly, Yao Zhu et al. [194] proposed that zinc oxide nanoparticles can be used as a luminescent down-shifting layer for solar cells and the nanoparticles were prepared by low energy cluster beam deposition (LECBD). Achamma et al [195] studied the luminescence properties in Ce doped ZnO nanocrystals prepared by simple refluxing technique, the emission intensity decreases and is anticipated to be due to formation of additional surface defects (surface bound states) leading to non-radiative relaxation. Magnetic property analysis of Nd-doped ZnO films were studied by Subramanian et al [196] and they reported that these films exhibit room temperature ferromagnetism. Recently, it has been reported that Gd doped ZnO shows magnetic anisotropy as well as the intrinsic ferromagnetic property [197]. Zhang et al. [198] studied the PL properties in Eu doped ZnO nanospheres by wet chemical method. They proposed energy transfer mechanism by presuming that most of electrons are captured by traps of substituted Eu ions and Zn related effects and then transfer one of the levels of Eu ions thereby Eu emission takes place. Visible upconversion properties of Er doped ZnO nanocrystals were studied by Wang et al [199]. Some of the recent reported works based on the upconversion luminescence based on ZnO host matrix [200-203]. Liu et al [204] reported near infra-red luminescence of Nd^{3+} and Tm^{3+} ions doped ZnO fabricated by sol gel process. They reported the existence of multiple luminescence site structure of Nd^{3+} ions in the lattice sites of ZnO that possess various crystal field surroundings with various PL lifetimes. Park et al [205] reported that extrinsic defects like chlorine impurities can assist the red emission in Eu^{3+} doped ZnO. Most recent work by Zeng et al. [206] reported that Eu^{2+} ions can acts as a trapping centres and transfer energy to the Eu^{3+}

ions, leading to the red emission in Eu doped ZnO nanosheet based microspheres. Chao et al [207] studied the annealing effects on the properties of Nd containing ZnO prepared by sol gel route. They reported that Nd^{3+} emission at 899 nm reaches a maximum after annealing at 600°C. Higher annealing temperature (1000°C) causes a separate phase segregation of Nd_2O_3.

1.6 APPLICATIONS OF NANOSTRUCTURED MATERIAL (TiO₂)

1.6.1 DOWNSHIFTING OF THE INCIDENT LIGHT FOR PHOTOVOLTAIC APPLICATIONS

1.6.1.1 ENERGY LOSSES IN SOLAR CELLS

The theoretical Shockley-Queisser limit [208] for single junction crystalline silicon semiconducting solar cell of 31% is possible for a material with a band-gap of 1.1 eV. Fundamental spectral losses limits the theoretical efficiency to $\eta=25\%$, observed experimentally with respect to AM 1.5G spectra [209].
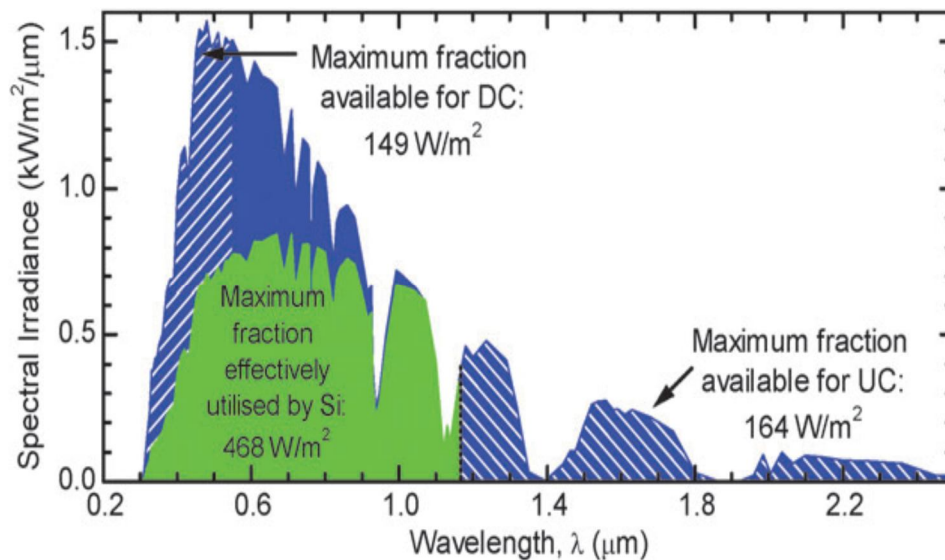
Figure 1.10: *Representation of Air mass 1.5G spectra [adapted from 210, 211]*

However, with a single-junction solar cell not all of the solar energy is utilized: some of the energy is lost to lower energy photons that are transparent to the semiconductor

and higher energy photons is lost due to thermalization. Figure shows the loss mechanism in a single junction solar cell.
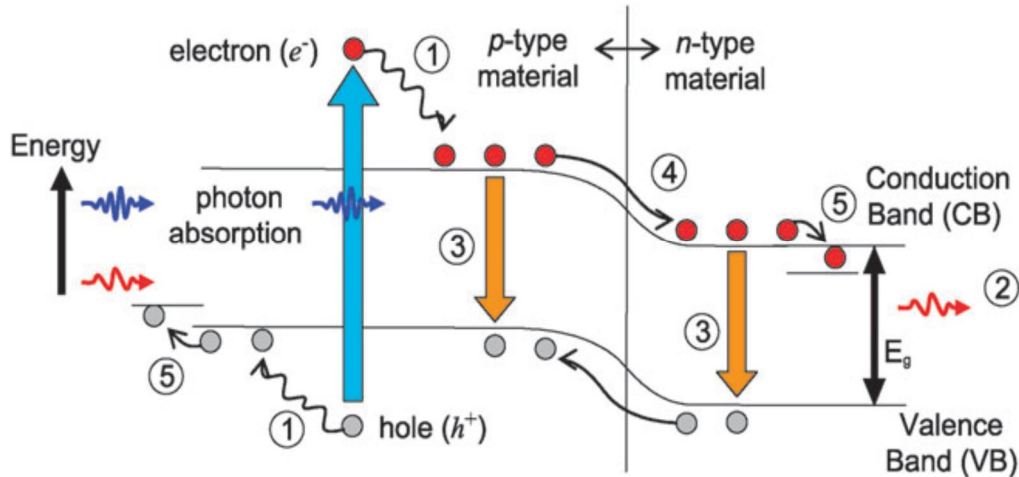
Figure 1.11: *Loss Mechanism in a single junction solar cell [adapted from 210, 211]*

The two main loss mechanisms in the solar cells are due to the absorption high energy photons or shorter wavelength (i.e,) photons having energy higher than the bandgap E_g (process (1)) induce the thermalisation loss. In this case photons are lost via non radiative relaxation of the excited electrons towards the conduction band in the form of heat. The second major loss is the transmission loss, in which the photons having energy lower than the bandgap E_g are not absorbed (process 2). Other loss corresponds to process 3, the recombination loss while 4 and 5 corresponds to junction and contact voltage loss. Losses 1 and 2 (upto 70%) refers to the spectral mismatch loss. To overcome these fundamental losses and conversely increase the efficiency of the solar cells, novel concepts have been investigated. Modifying the incoming spectrum can be realized by incorporating passive luminescence layers optically coupled above (for down-conversion and photoluminescence/downshifting) or below (for up-conversion) without alterating the existing solar cells for better utilization.

1.6.1.2 CONCEPTS OF LUMINESCENT DOWNSHIFTING

In 1970's Hovel et al [212] first reported the concept of luminescent downshifting in the area of luminescent solar concentrators [213]. With the aim of utilizing the short wavelength region of solar spectrum to improve the efficiency of the solar cell performance by developing active layers which can modify the high energy incoming photons. The downshifting material absorb the short wavelength incident light (300 to 500 nm), and reemit it at more favourable longer wavelength where the external quantum efficiency of the photovoltaic is high. A schematic representation of photovoltaic downshifting based device is shown below:

It consists of four different layers in which the luminescent downshifter layer placed on top surface of the solar cell. The luminescence converter is electronically isolated from the solar cell, i.e., the coupling between the converter and the solar cell is purely radiative. A large number of ideal materials are available for luminescent downshifter layer for all existing solar cells, but they should possess the following characteristics [214,215]:

1. A wide band absorption (UV- blue region), particularly to cover the region where the spectral response (IQE) is low

2. High absorption coefficient

3. High transmittance and narrow band emission where the IQE is high

4. Large stokes shift, the energy difference between the absorption and emission should be large enough to avoid reabsorption phenomena.
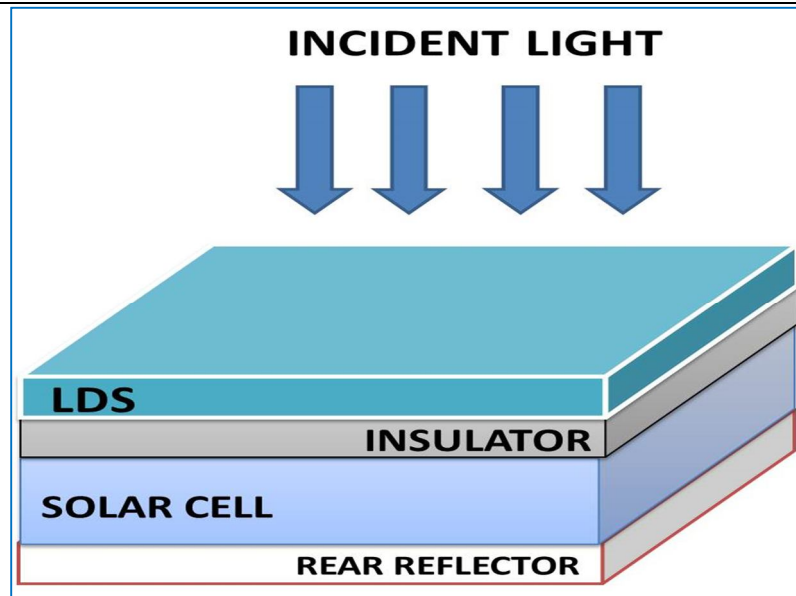
Figure 1.12: *Schematic representation of a solar cell device with a luminescent down-shifting layer placed onto the top of the solar cell [216]*
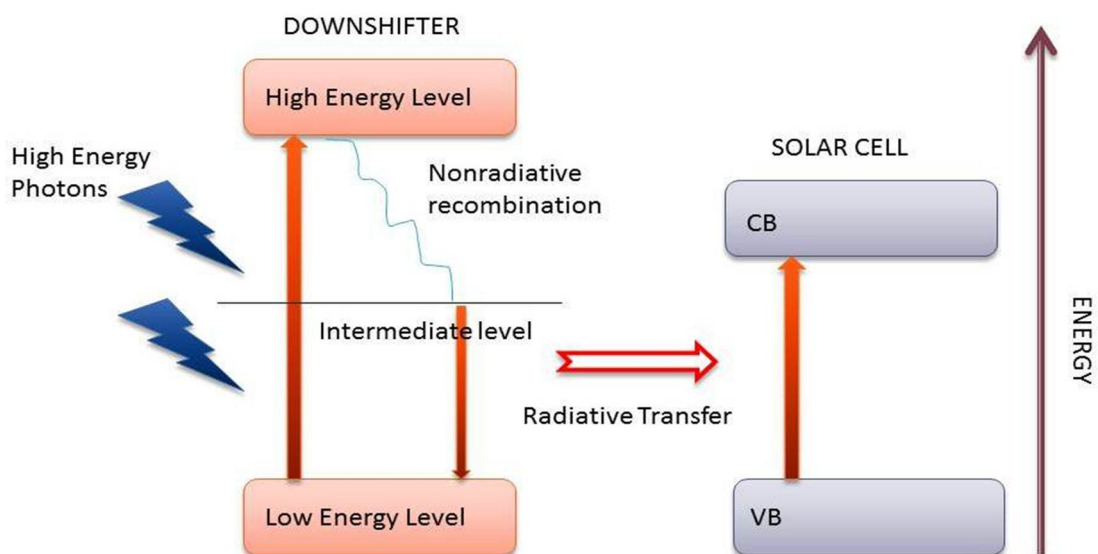
Figure 1.13: *Schematic Energy diagram of a solar cell in combination with active luminescence downshifter layer [217]*

The absorption of higher energy photon leads to the transition of electrons from the ground state to the excited state level. The non radiative recombination takes places between the excited levels to the intermediate level; the emission of one lower energy photon is accompanied by the radiative recombination of electron from the

intermediate level to the lowest ground state. As a result of luminescent process, a part of incident photons is shifted towards the longer wavelength before reaching the active photovoltaic material of the device, this result in an increase in the electron hole generation which inturn improves the EQE (external quantum efficiency) and the short circuit of the device.

1.6.2 PHOTOCATALYSIS

There are several books and review articles based on photocatalysis. Below is a brief introduction on photocatalysis concept relevant to the work. TiO_2 is regarded as an environmentally benign photocatalysts and it has been widely used in photodegradation of organic pollutants.
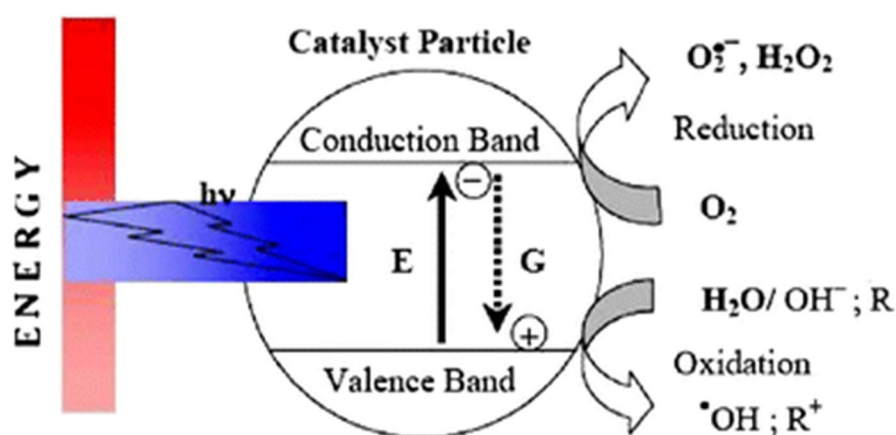
Figure 1.14: *Schematic representation of photocatalytic process [figure adapted from 230]*

When a photon of energy ($\lambda \geq E_g$) is incident on the semiconductor material, the electron-hole pairs are produced (i.e.,) the electrons in the valence band move towards the conduction band leaving behind the positively charged hole. The photogenerated electron-hole pair is mobile and it can move onto the surface of the semiconductor material (catalyst) and participate in the redox reactions with the liquid interface and generate highly reactive oxidizing species hydroxyl radical (OH*) which initiate

further chemical reactions. For example, water molecules are reduced by electrons to form H^+ and the OH radicals are oxidized by the holes to form O_2.

Some of the literature review with focus on rare earth doping with titania based photocatalysts. Neodymium modified TiO_2 photocatalysts has been studied by some research groups [218]. A series of doped titania nanoparticles were prepared by MOCVD and among the dopants Nd – TiO_2 exhibited higher activity in degradation of 2 chlorophenol by UV light [219, 220]. The doping level of Nd was kept constant at 1 at. %. The photodegradation about 90% were achieved for the illumination time of 25 minutes from 60 min in the case of undoped TiO_2. Visible light activity was also studied with Nd doped TiO_2 sol in the degradation of phenol [221]. The photocatalytic degradation of several dyes was examined over Nd- TiO_2 materials. Luan et al [222] studied the photocatalytic degradation of methylene blue dye using Nd-TiO_2 as a catalyst prepared via sol gel method, a combined route involving first doping of Nd ions followed by acidification of doped TiO_2 particles. The dopant concentration of Nd in TiO_2 was kept as 1.5 and 3.0wt.% and nearly 80% of MB degradation was observed for the sample having 3.0wt.% of Nd doping. The photocatalytic degradation of methyl orange (MO) [223, 224], azo dye (X-3B) [225,226], Remazolblack B [227] were also studied using Nd-TiO_2 as a photocatalyst. Zhang et al. [228] observed that Eu- TiO_2 catalysts prepared by sol-gel technique were more active than by impregnation method. This result suggests that the preparation method strongly influences the dispersion of the Eu^{3+} ions and thus the resulting photoactivity is greatly affected. Rare earth ions such as Gd, Yb, Er, Pr, Ho, Sm and Tb have also been used to modify titania and their photocatalytic activity were explored [229].

REFERENCES

[1] Jean-Claude G. Bünzli, Svetlana V. Eliseeva, J. of Rare Earths, 28, (2010) 824.

[2] Bünzli J C G, Comby S, Chauvin A S, Vandevyver C D B, J. Rare Earths, 25, (2007) 257

[3] Suzuki H. J. Photochem. Photobiol., A 166 (2004) 155.

[4] Chen Z Q, Bian Z Q, Huang C H. Adv. Mater., 22 (2010) 1534.

[5] Eliseeva S V, Bünzli J C G Chem. Soc. Rev., 39 (2010) 189

[6] Bünzli J C G. Chem. Rev., 110 (2010) 2729.

[7] Wang F, Banerjee D, Liu Y S, Chen X Y, Liu X G. Analyst, 135 (2010) 1839.

[8] Uh H, Petoud S. Comptes Rendus Chimie, 13 (2010) 668.

[9] Bünzli J C G, Chauvin A S, Vandevyver C D B, Song B, Comby S. Ann. N. Y. Acad. Sci., 1130 (2008) 97.

[10] Amiot C L, Xu S P, Liang S, Pan L Y, Zhao J X J. Sensors, 8 (2008) 3082.

[11] Cooper D E, D'Andrea A, Faris G W, MacQueen B, Wright W Up-converting phosphors for detection and identification using antibodies. Van Emon J M, Ed. Immunoassay and Other Bioanalytical Techniques. Boca Raton: CRC Press, Taylor & Francis group (2007) Ch. 9, 217-47.

[12] Comby S, Bünzli J C G. Lanthanide near-infrared luminescence in molecular probes and devices, Gschneidner K A Jr, Bünzli J -C G, Pecharsky V K, Eds. Handbook on the Physics and Chemistry of Rare Earths. Amsterdam: Elsevier Science B.V. (2007) 37, Ch. 235.

[13] Zhang Q Y, Huang X Y. Prog. Mater. Sci., 55 (2010) 353.

[14] Van der Ende B M, Aarts L, Meijerink A. Phys. Chem. Chem. Phys., 11 (2009) 11081.

[15] Andrews D L. J. Nanophoton., 2 (2008) 022502.

[16] Strümpel C, McCann M, Beaucarne G, Arkhipov V, Slaoui A, Svrcek V, del Canizo C, Tobias I. Solar En. Mat. Sol. Cells, 91 (2007) 238.

[17] Shalav A, Richards B S, Green M A. Solar Energy Mat. Sol. Cells, 91 (2007), 829.

[18] A. Goetzberger and W. Greube, App. Phys., 14 (1977) 123

[19] B.S. Richards, Sol. Energy. Mater. Sol. Cells 90 (2006) 1189–1207.

[20] C. Strümpel, M. McCanna, G. Beaucarneb, V. Arkhipovb, A. Slaoui, V. Švrˇcek, C. del Cañizod, and I. Tobias, Sol. Energy. Mater. Sol. Cells 91 (2007) 238-249.

[21] J. de. Wild, A. Meijerink, J. K. Rath, W. G. J. H. M. van Sark and R. E. I. Schropp, Energy Environ. Sci. 4 (2011) 4835-4848.

[22] E. Klampaftis, D. Ross, K. R.McIntosh, B. S. Richards, Sol. Energy. Mater. Sol. Cells 93 (2009) 1182-1194.

[23] B.S. Richards, Sol. Energy. Mater. Sol. Cells 90 (2006) 2329–2337.

[24] C. P. Thomas, A. B. Wedding, S. O. Martin, Sol. Energy. Mater. Sol. Cells 98 (2012) 455–464.

[25] V. Svrcek, A. Slaoui and J. C. Muller, Thin Solid Films, 451 (2004) 384.

[26] Y. Wang, D. -J. Wu, Y.-T. Yang and X.-J. Liu, Chinese Phys. Lett., 28 (2011) 027804.

[27] W. Luo, R. Li and X. Chen, J. Phys. Chem. C, 113 (2009) 8772.

[28] C. M. Leroy, T. Cardinal, V. Jubera, M. Treguer-Delapierre, J. Majimel, J. P. Manaud, R. Backov, C. Boissière, D. Grosso, C. Sanchez, B. Viana and F. Pellé, ChemPhysChem., 9 (2008) 2077.

[29] P. Ghigna, A. Speghini and M. Bettinelli, J. Solid State Chem., 180 (2007) 3296.

[30] W. Li, A. I. Frenkel, J. C. Woicik, C. Ni and S. Ismat Shah, Phys. Rev. B, 72 (2005) 155315.

[31] K. L. Frindell, M. H. Bartl, M. R. Robinson, G. C. Bazan, A. Popitsch and G. D. Stucky, J. Solid State Chem., 172 (2003) 81.

[32] A. Burns, G. Hayes, W. Li, J. Hirvonen, J. D. Demaree and S. Ismat Shah, Mater. Sci. Eng. B, 111 (2004) 150

[33] Mi-Hyae Park, Juo-Hao Li, Ankit Kumar, Gang Li, Yang Yang, Adv. Functional Materials 19 (2009) 1241

[34] Jimmy C. Yu, Jiaguo Yu, Wingkei Ho, Zitao Jiang, and Lizhi Zhang Chem. Mater. 14 (2002) 3808

[35] Clemens Burda, Yongbing Lou,Xiaobo Chen, Anna C. S. Samia, John Stout, and James L. Gole Nano letters 3 (2003) 1049

[36] G. D. Metcalfe, E. D. Readinger, H. Shen, N. T. Woodward, V. Dierolf and M. Wraback, Phys. Status Solidi C, 6 (2009) S671.

[37] G. D. Metcalfe, E. D. Readinger, H. Shen, N. T. Woodward, V. Dierolf and M. Wraback, J. Appl. Phys., 105 (2009) 053101.

[38] G. D. Metcalfe, E. D. Readinger, R. Enck, H. Shen, M. Wraback, N. T. Woodward, J. Poplawsky and V. Dierolf, Opt. Mater. Express, 1 (2011) 78.

[39]   Rozo and L. F. Fonseca, J. Phys.: Condens. Matter, 20 (2008) 315003.

[40]   S. S. Yi, J.-C. Kim, D. W. Kim, R. Balakrishnaiah, S. H. Kim, K. Jang, H. S. Lee, B. K. Moon and J. H. Jeong, Thin Solid Films, 518 (2010) 6163.

[41]   S. Kim, S. J. Rhee, X. Li, J. J. Coleman and S. G. Bishop, Phys. Rev. B 57 (1998) 14588-14591.

[42]   D. Bréard, F. Gourbilleau, C. Dufour, R. Rizk, J.-L. Doualan, P. Camy, Mater. Sci. Eng. B 146 (2008) 179-182.

[43]   I. Z. Hager, R. El-Mallawany, A. Bulou, Physica B 406 (2011) 972-980.

[44]   S. -Y. Seo, M. -J. Kim and J. H. Shin, Appl. Phys. Lett., 83 (2003) 2778.

[45]   D. Biggemann and L. R. Tessler, Mater. Sci. Eng. B, 105 (2003) 188.

[46]   Sue-min Chang, Wei-szu Liu, Applied Catalysis B: Environmental, 101 (2011) 333-342

[47]   http://en.academic.ru/pictures/enwiki/68/Defecttypes.png

[48]   Ioana Luciu, "RF plasma synthesis and characterization of thin films for transparent conductors", PhD Thesis, March 2012

[49]   Adriana Zaleska, Recent Patents on Engineering 2 (2008) 157-164

[50]   M. K. Nowotny, L. R. Sheppard, T. Bak, and J. Nowotny, JPC C 112 (2008) 5275

[51]   F. Campus, P. Bonhôte, M. Grätzel, S. Heinen, L. Walder Sol. Energy Mater. Sol. Cells, 56 (1999) 281-297

[52]   S. Senthilarasu, T. A. Nirmal Peiris, Jorge García-Cañadas, and K. G. Upul Wijayantha J. Phys. Chem. C 116 (36) (2012) 19053-19061

[53]   H. Selhofer, Vacuum Thin Film (1999) 15

[54]   Ulrike Diebold, Surf. Sci. Rep. 48 (2003) 53

[55]   Dorian A. H. Hanaor, Charles C. Sorrell J Mater Sci 46 (2011) 855–874

[56]   D. Hanaor, C Sorrell, J. Mater. Sci., 46 (2011) 855–874

[57]   Phillip G. Wahlbeck, Paul W. Gilles J. Amer. Ceramic Society 49 (1966) 180

[58]   M. Yokozawa, H. Iwasa, and I. Teramoto, Jpn. J. Appl. Phys. 7 (1968) 96–97

[59]   P. Lobl, M. Huppertz, and D. Mergel, Thin Solid Films, 251 (1994) 72–79

[60]   H. Tang, H. Berger, P.E. Schmid, and F. L´evy, Solid State Commun., 92 (1994) 267–271

[61]   Ü. Özgür, Ya. I. Alivov, C. Liu, A. Teke, M. A. Reshchikov, S. Doğan, V. Avrutin, S.-J. Cho, and H. Morkoç J. Appl. Phys.98 (2005) 041301

[62] Klingshirn C. Chem Phys chem 8 (2007) 782

[63] C. Klingshirn, R. Hauschild, H. Priller, M. Decker, J. Zeller, H. Kalt Superlattices and microstruct. 38 (2005) 209

[64] R. Thangavel, Rakesh Singh Moirangthem, Wei-Shan Lee, Yia-Chung Chang, Pei-Kuen Wei, J. Kumar J. Raman Spec 41 (2010) 1594

[65] E.K. Ellmer, A. Klein and B. Rech, Transparent Conductive Zinc Oxide Springer, Berlin, (2008)

[66] L. Zhang, Y. Jiang, Y. Ding, M. Povey and D. York, J. Nanopart. Res., 9 (3) (2007) 479–489.

[67] J. Strunk, K. K€ahler, X. Xia and M. Muhler, Surf. Sci., 603 (10-12) (2009) 1776–1783.

[68] Shahmoradi B, Ibrahim IA, Sakamoto N, Ananda S, Row TN, Soga K, Byrappa K, Parsons S, Shimizu Y. Environ Technol. 31 (11) (2010) 1213-20

[69] Nuruddin A, Abelson JR, Thin Solid Films 394, 48, 2001

[70] Z. L. Wang and J. H. Song, Science, 14 (2006) 242-246

[71] P. G. Gao, J. H. Song, J. Liu and Z. L. Wang, Adv. Mater. 19 (2007) 67-7

[72] Z. L. Wang, Nanopiezotronics, Adv. Mater.19 (2007) 889-892.

[73] J. H. Song, X. D. Wang, J. Liu, H. B. Liu, Y. L. Li and Z. L. Wang, Nano Lett. 8 (2008) 203-207.

[74] M. P. Lu, J. H. Song, M. Y. Lu, M. T. Chen, Y. F. Gao, L. J. Chen, and Z. L. 9 (2009) 1223-1227

[75] Hadis Morko and Umit Ozgur, "Zinc Oxide: Fundamentals, Materials and Device Technology, Wiley-VCH; 1 edition (February 17, 2009)

[76] Ü. Özgür,Ya. I. Alivov, C. Liu, A. Teke, M. A. Reshchikov, S. Doğan, V. Avrutin, S.-J. Cho, and H. Morkoç, J. Appl. Phys. 98, (2005) 041301

[77] M. Liu, A. H. Kitai, and P. Mascher, J. Lumin. 54 (1992) 35

[78] B. Guo, Z. R. Qiu, and K. S. Wong, Appl. Phys. Lett. 82, (2003) 2290

[79] F. K. Shan, G. X. Liu, W. J. Lee, et al., Appl. Phys. Lett. 86 (2005) 221910

[80] F. H. Leiter, H. R. Alves, A. Hofstaetter, et al., Phys. Status Solidi 226 (1) (2001), R4

[81] F. H. Leiter, H. R. Alves, N. G. Romanov, et al., Physica B 201 (2003) 340

[82] A. F. Kohan, G. Ceder, D. Morgan, et al., Phys. Rev. 61 (2000) 15019

[83] B. Guo, Z. R. Qiu, and K. S. Wong, Appl. Phys. Lett. 82 (2003) 2290

[84]   D. C. Reynolds, D. C. Look, B. Jogai, et al., J. Appl. Phys. 88 (2000) 2152

[85]   Svetlana V. Eliseeva and Jean-Claude G. Bunzli New J. Chem., 35 (2011) 1165–1176

[86]   G. H. Dieke, Spectra and energy levels of rare earth ions in crystals, Interscience Publishers New york 1968

[87]   T. Justel, H. Nikol, C. Ronda, Angew. Chem. Int. Ed. 37 (1998) 3084-3103

[88]   K. W. Krämer, P. Dorenbos, H. U. Güdel and C. W. E. van Eijk J. mater chem 16 (2006) 2773

[89]   N. Sabbatini, M. Guardigli and J.-M. Lehn, Coord. Chem. Rev. 123 (1993) 201

[90]   Andries Meijerink, René Wegh, Peter Vergeer and Thijs Vlugt, Optical Materials 28 (2006) 575

[91]   G. Blasse and B. C. Grabmaier, Luminescent Material Springer Berlin Heidelberg 1994

[92]   A. Dossing Eur. J. Inorg. Chem.8 (2005) 1425-1434

[93]   K.S. Pitzer,Accounts of Chemical Research, 12 (1974) 271-276

[94]   D. Chen, Y. Wang, M. Hong, Nanoenergy 1 (2012) 73-90

[95]   X. Y. Zeng, J. L.Yuan, Z. Y. Wang, and L. D. Zhang, Adv. Mater. 19 (2007) 4510

[96]   A. Mehta, T. Thundat, M. D. Barnes, V. Chhabra, R. Bhargava, A. P. Bartko, and R. M. Dickson, Appl. Opt. 42 (2003) 2132

[97]   P. L. Chen, X. Y. Ma, and D. R. Yang, J. Alloys Compd. 431 (2007) 317

[98]   X. Wang, X. G. Kong, Y. Yu, Y. J. Sun, and H. Zhang, J. Phys. Chem. C 111 (2007) 15119

[99]   D. Bréard, F. Gourbilleau, A. Belarouci, C. Dufour, R. Rizk J. Lumin 121 (2006) 209

[100]   Jing Yang, Neodymium-doped Waveguide Amplifiers and Lasers for Integrated Optical Applications, PhD Thesis, 2010.

[101]   Claus Feldmann Nanoscale, 3 (2011) 1947-1948

[102]   P. Du, A. Bueno-Lopez, M. Verbaas, A. R. Almeida, M. Makkee, J. A. Moulijn and G. Mul, J. Catal.,260 (2008) 75–80

[103]   J. M. Xie, D. L. Jiang, M. Chen, D. Li, J. J. Zhu, X. M. Lu and C. H. Yan, Colloids Surf., A, 372 (2010) 107–114.

[104]   F. B. Li, X. Z. Li, M. F. Hou, K. W. Cheah and W. C. H. Choy, Appl. Catal., A, 285 (2005) 181–189.

[105]   K. T. Ranjit, H. Cohen, I. Willner, S. Bossmann and A. M. Braun, J. Mater. Sci., 34 (1999) 5273–5280

[106]   Y. Zhang, H. Zhang, Y. Xu and Y. Wang, J. Mater. Chem., 2003, 13, 2261–2265

[107]   S. Matsuo, N. Sakaguchi, K. Yamada, T. Matsuo and H. Wakita, Appl. Surf. Sci., 228 (2004) 233–244

[108]   W. Luo, R. Li, G. Liu, M. R. Antonio and X. Chen, J. Phys. Chem. C, 112 (2008) 10370–10377

[109]   W. Li, S. I. Shah, C. P. Huang, O. Jung and C. Ni, Mater. Sci. Eng., B, 96 (2002) 247–253.

[110]   O. J. Jung, S. H. Kim, K. H. Cheong, W. Li and S. I. Saha, Bull. Korean Chem. Soc., 24 (2003) 49–54.

[111]   Y. B. Xie and C. W. Yuan, Appl. Surf. Sci., 221 (2004) 17–24.

[112]   C. M. Whang, J. G. Kim, E. Y. Kim, Y. H. Kim and W. I. Lee Glass Phys. Chem., 31 (2005) 390–395

[113]   S. Rengaraj, S. Venkataraj, J. W. Yeon, Y. Kim, X. Z. Li and G. K. H. Pang, Appl. Catal., B, 77 (2007) 157–165

[114]   Y Y. Luan, P. F. Fu and X. G. Dai, Surf. Rev. Lett., 13 (2006) 429–438.

[115]   K. V. Baiju, P. Periyat, W. Wunderlich, P. K. Pillai, P. Mukundan and K. G. K. Warrier, J. Sol–Gel Sci. Technol., 43 (2007) 283–290.

[116]   M. F. Hou, F. B. Li, R. F. Li, H. F. Wan, G. Y. Zhou and K. C. Xie, J. Rare Earths, 22 (2004) 542–546.

[117]   Y. H. Xu, C. Chen, X. L. Yang, X. Li and B. F. Wang, Appl. Surf. Sci., 255 (2009) 8624–8628

[118]   X. L. Yang, L. Zhu, L. M. Yang, W. Y. Zhou and Y. H. Xu, Trans. Nonferrous Met. Soc. China, 21 (2011) 335–339

[119]   K. Byrappa, M. H. Sunitha, A. K. Subramani, S. Ananda, K. M. L. Rai, B. Basavalingu and M. Yoshimura, J. Mater. Sci., 41 (2006) 1369–1375.

[120]   A. Podhorodecki, G. Zatryb, J. Misiewicz, J. Domaradzki, D. Kaczmarek and A. Borkowska, J. Electrochem. Soc., 156 (2009) H214–H219

[121]   A. Podhorodecki, G. Zatryb, P. Sitarek, J. Misiewicz, D. Kaczmarek, J. Domaradzki, A. Borkowska and E. L. Prociow, Thin Solid Films, 517 (2009) 6331–6333

[122]   A. Nebatti, C. Pflitsch, C. Eckert and B. Atakan, Prog. Org. Coat., 68 (2010) 146–150

[123]   A. Nebatti, C. Pflitsch, C. Eckert and B. Atakan, Prog. Org. Coat., 67 (2010) 356–360

[124]   C. W. Jia, E. Q. Xie, J. G. Zhao, Z. W. Sun, and A. H. Peng J. Appl. Phys. 100 (2006) 023529

[125]   V Kiisk Optical Materials 31 (2009) 1376-1376

[126]   H. Hafez, J.H. Wu, Z. Lan, Q.H. Li, G.X. Xie, J.M. Lin, M.L. Huang, Y.F. Huang, M.S. Abdel-Mottaleb, Nanotechnology 21 (2010) 415201.

[127]   Synthesis and reactivity in inorganic: Metal-organic and nano –metal chemistry 38 (2008) 312

[128]   Jeon S, Braun P V. Hydrothermal synthesis of Er-doped luminescent TiO, nanoparticles Chem. Mater., 15 (2003) 1256

[129]   Wang Yue, Wu Da-Jian, Yang Yue-Tao, Liu Xiao-Jun Chin. Phys. Lett 28 (2011) 027804

[130]   W. Li, A. I. Frenkel , J. C. Woicik , C. Ni and S. Ismat Shah Phys. Rev. B 72 (2005) 155315

[131]   Y. Wang, H. Cheng, Y. Hao, J. Ma, B. Xu, W. Li, S. Cai, J. of Material Science Letters 18 (1999), 127-129

[132]   S. Lange, I. Sildos, and V. Kiisk: Mater. Sci. Eng. B 112 (2004) 87

[133]   D. Nassoko, Y.-F. Li, X. Li, Y. Yul, International J. of Photoenergy (2012) 716087, 1-10

[134]   A. Ali, E. Yassitepe, I. Ruzybayev, S. Ismat Shah and A. S. Bhatti J. Appl. Phys. 112 (2012) 113505

[135]   Celine Marie Leroy, Thierry Cardinal, Veronique Jubera, Mona Treguer-Delapierre, Jerome Majimel, Jean Pierre Manaud, Renal Backov, Cedric Boissire, David Grosso, Clement Sanchez, Bruno Viana, and Fabienne Pelle, Chem Phys Chem 9 (2008) 2077 – 2084

[136]   J. Domaradzki, D. Kaczmarek, A. Borkowska, D. Schmeisser, S. Mueller, R. Wasielewski, A. Ciszewski, D. Woijcieszaka, Vacuum 82, 10 (2008) 1007- 1012

[137]   Vaclav Stengl, Snejana Bakardjieva and Nataliya Murafa, Materials Chemistry and Physics 114 (2009) 217

[138]   Agnieszka Borkowska 2007 International students and Young scientists workshop on Photonics and microsystems

[139]   Fagner Ticiano, Gomes Vieiraa, Danniely Silva Melo, Severino Jackson Guedes de Lima, Elson Longo, Carlos Alberto Paskocimas, Wilson Silva Ju´nior, Antonio Gouveia de Souza, Ieˆda Maria Garcia dos Santos Mat sci and eng B 111 (2004) 150-155

[140]   R. D. Shannon and J. A. Pask, J. Am. Ceram. Soc. 48 (1965) 391

[141]   Chao Wang, Yanhui Ao, Peifang Wang, Jun Hou, Jin Qian Applied surface science 257 (2010) 227

[142]   W. Li, Y. Wang, H. Lin, S. Ismat Shah, C. P. Huang, D. J. Doren, Sergey A. Rykov, J. G. Chen, and M. A. Barteau Appl. Phys. Lett. 83 (2003) 4143

[143]   L. Li, C. K. Tsung, Z. Yang, G. D. Stucky, L. D. Sun, J. F. Wang, C. H. Yan Advanced Materials 20 (2008) 903-908

[144]   Ghigna Paolo, Speghini Adolfo and Bettinelli Marco, Solid State Chem 180 (2007) 3296

[145]   C. H Yang and Zhong-Quan Ma Applied Optics 51 (2012) 5438

[146]   D Kaczmarek, D Wojcieszak, J Domaradzki and E Prociow Journal of physics: conference series 146 (2009) 012019

[147]   Podhorodecki, G. Zatryb, P. Sitarek, J. Misiewicz, D. Kaczmarek, J. Domaradzki, A. Borkowska, E. Prociow, Thin Solid Films, 517 (2009) 6331

[148]   Wenqin Luo , Renfu Li and Xueyuan Chen J. Phys chem 113 (2009) 8772

[149]   Takashi Tachikawa, Takamasa Ishigaki, Ji-Guang Li Dr, Mamoru Fujitsuka, Tetsuro Majima, Angew. Chem 47 (2008) 5348

[150]   Christensen A E, Uhrenfeldt C, Julsgaard B, Balling P, Larsen A NM Energy Procedia 10 (2011) 111

[151]   V Kiisk, V Reedo, M Karbowiak, M G Brik[3] and I Sildos J. Phys D. Appl Physics 42 (2009) 125107

[152]   A. Conde-Gallardo, M. García-Rocha, I. Hernández-Calderón, and R. Palomino-Merino Appl. Phys. Lett. 78 (2001) 3436

[153]   Q.G. Zeng, Z.M. Zhang, Z.J. Ding, Y. Wang, Y.Q. Sheng Scripta Materialia 57 (2007) 897

[154]   Karen L. Frindell, Michael H. Bartl, Matthew R. Robinson, Guillermo C. Bazan, Alois Popitsch, Galen D. Stucky J. Solid State Chem. 172 (2003) 81

[155]   Yongsheng Liua, Wenqin Luoa, Haomiao Zhua and Xueyuan Chena J. of Lumin. 131 (2011) 415–422

[156]   Rajesh Pandiyan, Victor Micheli, Davor Ristic, Ruben Bartali, Giancarlo Pepponi, Mario Barozzi, Gloria Gottardi, Maurizio Ferrari and Nadhira Laidani J. Mater. Chem., 22 (2012) 22424-22432

[157]   Zeng Qing-Guang, Ding Z. J, Wang Yi and Sheng Ye-Qing Chin. Phys. Lett. 24, 2007, 1368

[158]   S. M. Liu, F. Q. Liu, and Z. G. Wang, Chem. Phys. Lett. 343 (2001) 489

[159] Shu-Man Liu, Feng-Qi Liu, Hai-Qing Guo, Zhi-Hua Zhang, Zhan-Guo Wang Phys lett A 271 (2000) 128

[160] Marco Kohls, Marc Bonanni, Lubomir Spanhel, Dangsheng Su, and Michael Giersig Appl. Phys. Lett. 81 (2002) 3858

[161] Z. B. Fang, Y. S. Tan, X. Q. Liu, Y. H. Yang, and Y. Y. Wang, Chin. Phys. 13 (2004) 1330

[162] L. Yang, Y. Li, Y. H. Xiao, C. H. Ye, and L. D. Zhang, Chem. Lett. 34 (2005) 828

[163] A. B. Djurišić, W. C. H. Choy, V. A. L. Roy, Y. H. Leung, C. Y. Kwong, K. W. Cheah, T. K. Gundu Rao, W. K. Chan, H. Fei Lui and C. Surya, Adv. Funct materials 14 (2004) 856

[164] L.C. Chao, P.C. Chiang, S.H. Yang, J.W. Huang, C.C. Liau, J.S. Chen, C.Y. Su, Appl. Phys. Lett. 88 (2006) 251111.

[165] L.C. Chao, P.C. Chiang, S.H. Yang, J.W. Huang, C.C. Liau, J.S. Chen, C.Y. Su, Jpn. J. Appl. Phys. 45 (2006) L938.

[166] Behzad Shahmoradi, K. Soga, S. Ananda, R. Somashekar and K. Byrappa Nanoscale 2 (2010) 1160

[167] G. Destriau, J. Chem. Phys. 33 (1936) 587

[168] B. Cheng, Y. Xiao, G. Wu, L. Zhang, Appl. Phys. Lett. 84 (2004) 416.

[169] Y. Sato, F. Oba, M. Yodogawa, T. Yamamoto, Y. Ikuhara, Appl. Phys. Lett. 95 (2004) 1258.

[170] W.M. Jadwisienczak, H.J. Lozykowski, A. Xu, B. Patel, J. Elect. Mater. 31 (2002) 776.

[171] P. Che, J. Meng, L. Guo, J. Lumin. 122 (2007) 168.

[172] K. Potzger, S. Zhou, F. Eichhorn, M. Helm, W. Skorupa, A. Mu¨cklich, J. Fassbender, T. Herrmannsdo¨rfer, A. Bianchi, J. Appl. Phys. 99 (2006) 063906.

[173] X.M. Teng, H.T. Fan, S.S. Pan, C. Ye, G.H. Li, J. Appl. Phys. 100 (2006) 053507.

[174] F. Gu, S.F. Wang, M.K. Lu¨, G.J. Zhou, D. Xu, D.R. Yuan, Langmuir 20 (2004) 3528.

[175] N. Mais, J.P. Reithmaier, A. Forchel, M. Kohs, L. Spanhel, G. Mu¨ller, Appl. Phys. Lett. 75 (1999) 2005.

[176] M. Ishii, S. Komuro, T. Morikawa, Y. Aoyagi, J. Appl. Phys. 89 (2001) 3679.

[177] J. Wang, M.J. Zhou, S.K. Hark, Q. Li, D. Tang, M.W. Chu, C.H. Chen, Appl. Phys. Lett. 89 (2006) 221917.

[178] T. Monteiro, A.J. Neves, M.J. Soares, M.C. Carmo, M. Peres, E. Alves, E. Rita, Appl. Phys. Lett. 87 (2005) 192108.

[179] U. Pal, R. Mele´ndrez, V. Chernov, M. Barboza-Flores, Appl. Phys. Lett. 89 (2006) 183118.

[180] Sun, X. H.; Lam, S.; Sham, T. K.; Heigl, F.; Ju¨rgensen, A.; Wong, N. B. J. Phys. Chem. B 109 (2005) 3120.

[181] Armelao, L.; Heigl, F.; Ju¨rgensen, A.; Blyth, R. I. R.; Regier, T.; Zhou, X.-T.; Sham, T. K. J. Phys. Chem. C 111 (2007), 10194.

[182] Huang, M. H.; Mao, S.; Feick, H.; Yan, H. Q.; Wu, Y. Y.; Kind, H.; Weber, E.; Russo, R.; Yang, P. D. Science (Washington, DC, U.S.) 292 (2001) 1897.

[183] Hu, J. Q.; Bando, Y. Appl. Phys. Lett. 82 (2003) 1401.

[184] Pan, Z. W.; Dai, Z. R.; Wang, Z. L. Science (Washington, DC, U.S.) 291 (2001) 1947.

[185] Yan, H. Q.; He, R. R.; Johnson, J.; Law, M.; Saykally, R. J.; Yang, P. D. J. Am. Chem. Soc. 125 (2003) 4728..

[186] Kong, X. Y.; Wang, Z. L. Nano Lett. 3 (2003) 1625

[187] Gao, P. X.; Wang, Z. L. Appl. Phys. Lett. 84 (2004) 2883

[188] Zhang, B. P.; Binh, N. T.; Wakatsuki, K.; Segawa, Y.; Yamada Y.; Usami, N.; Kawasaki, M.; Koinuma H. Appl. Phys. Lett. 84 (2004) 4098

[189] Lidia Armelao, Gregorio Bottaro, Michele Pascolini, Michele Sessolo, Eugenio Tondello, Marco Bettinelli, and Adolfo Speghini J. Phys. Chem. C, 112 (2008) 4049

[190] Greene, L. E.; Law, M.; Goldberger, J.; Kim, F.; Johnson, J. C.; Zhang, Y. F.; Saykally, R.; Yang, P. D. Angew. Chem., Int. Ed. 42 (2003) 3031

[191] B, J Chen; K, W Jang; H, S Lee; M, Jayasimhadri; E, J Cho; S, S Yi; J, H Jeong, J. Phys. D Applied Phys 42 (2009) 105401.

[192] Ungureanu M, Schmidt H, Xu Q, von Wenckstern H, Spemann D, Hochmuth H, Lorenz M and Grundmann M Superlatt. Microstruct. 42 (2007) 231

[193] Xian, Fenglin, Li, Xiangyin Optics & Laser Technology 45 (2013) 508–512

[194] SPIE newsroom 10.1117/2.1201212.004585

[195] Achamma George, Suchinder K. Sharma, Santa Chawla, M.M. Malik, M.S. Qureshi Journal of Alloys and Compounds 509 (2011) 5942

[196] Munisamy Subramanian, Kasilingam Senthilkumar, Masaki Tanemura, Tetsuo Soga, and Takehiko Hihara Jpn. J. Appl. Phys. 52 (2013) 01AC14

[197] M. Subramanian, P. Thakur, M. Tanemura, T. Hihara, V. Ganesan, T. Soga, K. H. Chae, R. Jayavel, and T. Jimbo J. Appl. Phys. 108 (2010) 053904

[198] Y. Zhang, Y. Liu, L. Wu, E. Xie, J. Chen, J. Phys. D: Appl. Phys. 42 (2009) 085106

[199] X. Wang, X. G. Kong, G. Y. Shan, Y. Yu, Y. J. Sun, L. Y. Feng, K. F. Chao, S. Z. Lu, and Y. J. Li, J. Phys. Chem. B 108 (48) (2004) 18408–18413

[200] Schmidt, T.; Mu¨ller, G.; Spanhel, L.; Kerkel, K.; Fouchel, A. Chem. Mater. 10 (1998) 65.

[201] Kohls, M.; Bonanni, M.; Spanhel, L. Su, D. S.; Giersig, M. Appl. Phys. Lett. 81 (2002) 3858.

[202] Liu, S. M.; Liu, F. Q.; Guo, H. Q.; Zhang, Z. H.; Wang, Z. G. Phys. Lett. A 271 (2000) 128.

[203] Liu, S. M.; Liu, F. Q.; Wang, Z. G. Chem. Phys. Lett. 343 (2000) 489.

[204] Yongsheng Liu, Wenqin Luo, Renfu Li, Haomiao Zhu, and Xueyuan Chen Opt. Express 17 9 (2009) 9748-9753

[205] Y.-K. Park, J.-I. Han, M.-G. Kwak, H. Yang, S.-H. Ju, and W.-S. Cho Appl. Phys. Let. 72 (1998) 668

[206] .Zeng, J. Yuan, Z. Wang, L. Zhang, Adv. Mater. 19 (2007) 4510

[207] Liang-Chiun Chao, Jian-Wei Huang, Chung-Wen Chang PHYSICA B 404 (2009) 1304

[208] W. Shockley and J. K. Queisser, J. Appl. Phys. 32 (1961) 510

[209] M. A. Green, K. Emery, Y. Hishikawa, W. Warta, Progress in Photovoltaics: Research and Applications 18 (2010) 144-150

[210] B. M. van der Ende, L. Aarts, A. Meijerink, Phys. Chem. Chem. Phys 11 (2009) 11081-11095

[211] B.S. Richards, Sol. Energy mater. Solar cells 90 (2006) 2329-2337

[212] H. J. Hovel, R. T. Hodgson, J. M. Woodale, Solar Energy Materials 2 (1979) 19-29

[213] A. Goetzberger, W. Greubel, Appl. Phys. 14 (1977) 123

[214] T. Trupke, M. A. Green, P. Würfel, J. Appl. Phys.92 (2002) 1668

[215] C. Strumpel, M. McCann, G. Beaucarne, V. Arkhipov, A. Slaoui, V. Svrcek, C. del Canizo, I. Tobias, Solar Energy Materials and Solar Cells 91 (2007) 238-249

[216] V. Švrček, A. Slaoui, J.-C. Muller, Thin Solid Films 451 (2004) 384

[217] Y. Jestin, Down-Shifting of the Incident Light for Photovoltaic Applications. (2012) In: Sayigh A, (ed.) Comprehensive Renewable Energy, Vol 1, pp. 563–585. Oxford: Elsevier

[218] Y, Xie, C. Yuan, J. Chem. Technol. Biotech 80 (2005) 954

[219] W. Li, S. Ismat Shah, C. P. Huang, O. Jung and C. Ni, Mater. Sci. Eng. B 96 (2002) 247

[220] Oh-Jin Jung, Sam-Hyeok Kim, Kyung-Hoon Cheong, W. Li, and S. Ismat Shah, Bull. Korean Chem Soc 24 (2003) 49

[221] Yibing Xie, Chunwei Yuan Appl. Surface Sci. 221 (2004) 17

[222] Y. Luan, P. Fu, X. Dai, Surf. Rev. Lett. 13 (2006) 429–438.

[223] Hou Meifang, Li Fangba, Li Ruifeng, Wan Hongfu, Zhou Guoyi and Xie Kechang, J. Rare Earths 22 (2004) 542

[224] Yue-Hua Xu, Chao Chen, Xue-Ling Yang, Xin Li, Bing-Feng Wang, Appl Surf Sci, 255 (2009), 8624

[225] Xie Y, Yuan C & Li X, Mater Sci Eng B 117 (2005) 325

[226] Yibing Xiea, Chunwei Yuana, Xiang zhong Li Colloids Surf A 252 (2005) 87

[227] Z. Gao, Y. Feng, F. Cui, Z. Hua, J. Zhou, Y. Zhu and J. Shi, J. Mol. Catal. A: Chem., 2011, 336, 51

[228] Yuhong Zhang, Huaxing Zhang, Yongxi Xu and Yanguang Wang J. Mater Chem 13 (2003) 2261

[229] H. Zhang, Y. Zhang, Y. Xu, Y. Wang, Acta Chimi. Sin. 61 (2003) 1813

[230] K. M. Joshi and V. S. Shrivastava, Applied nanoscience, "Photocatalytic degradation of Chromium (VI) from wastewater using nanomaterials like TiO_2, ZnO, and CdS" 04/2012; 1(3):147-155. DOI: 10.1007/s13204-011-0023-2.

[231] Gianluca Accorsi, "Trivalent Lanthanide Ions: Luminescence and Applications" PhD thesis, 2007

Chapter 2

Chapter 2

Synthesis, Methods and Materials Characterization

"It doesn't matter how beautiful your theory is, it doesn't matter how smart you are.
If it doesn't agree with experiment, it's wrong"
-Richard Feynman

2.1   INTRODUCTION

Much of the research interest is focused on the development of nanomaterials based on wide band gap semiconductors doped with the trivalent lanthanide ions as they constitute unique applications in optoelectronic and light emitting devices, plasma display panels, photovoltaic and so on [1]. Thin film processing technology is pervading unique breakthrough in developing these nanomaterials on molecular and atomic scale. Extensive progress in each of those applications depends upon the flexibility and controllability in depositing thin films – varying the thickness range from few nm to several micrometres with specified physicochemical properties.

 In this chapter, we described the details on the growth techniques used in the preparation of Neodymium - doped Titania, Zinc Oxide and Alumina thin films and the extensive characterization techniques employed to study and understand their physicochemical properties.

2.2 THIN FILM DEPOSITION METHODS

Thin films of rare earth ion doped semiconducting metal oxides can be prepared by a wide range of preparation techniques, mainly classified into (i) Physical Vapour Deposition (PVD) methods and (ii) Chemical Vapour Deposition (CVD). PVD methods include DC (Direct Current) and RF (Radio Frequency) Sputtering, Pulsed Laser Deposition (PLD), Electron Beam Evaporation, Thermal Evaporation, Molecular Beam Epitaxy (MBE) etc. Thin film preparation by chemical route includes Chemical vapour deposition (CVD) and their derivatives like metal organic chemical vapour deposition (MOCVD) and halide vapour phase epitaxy (HVPE), low pressure CVD (LPCVD), atmospheric pressure CVD (APCVD), Sol-gel, electro deposition etc. Among all the PVD techniques, the RF sputtering, industrial viable technique has superiority over the other techniques in the following aspects:

- To deposit electrically conducting, semiconducting and insulating coatings

- good control on nucleation and growth of thin films

- better adhesion can be achieved and maximum uniformity in the thickness and composition,

- relatively low temperature process.

A detailed explanation on the principle, working, advantages and application of sputter deposition are given in the book by [2, 3]. In the present study, the Neodymium - doped Titania, Zinc Oxide and Alumina thin films thin film depositions are carried out using RF co-sputtering technique.

2.3   THIN FILMS PREPARATION

2.3.1 RF SPUTTERING – BASIC PRINCIPLES

Sputtering is one of the most versatile technique developed rapidly over the last decade, as the process of choice for the deposition of a wide range of industrially viable coatings where higher purity, homogeneity and device quality films are required.

Sputtering is a process in which atoms, molecules or ions are ejected from a target surface (cathode) by bombarding it with a heavy ion (resulting in momentum transfer processes) such as argon, krypton, etc [2]. In the phenomena of sputtering, usually the incident particles are ions, which can be accelerated easily by applying the electric potential. A high negative voltage is applied to the target (which acts as a cathode), while substrate holder kept as anode. Substrates are placed in a vacuum chamber, connected to the chamber walls and to the ground or itself held at fixed potential facing towards the target material.
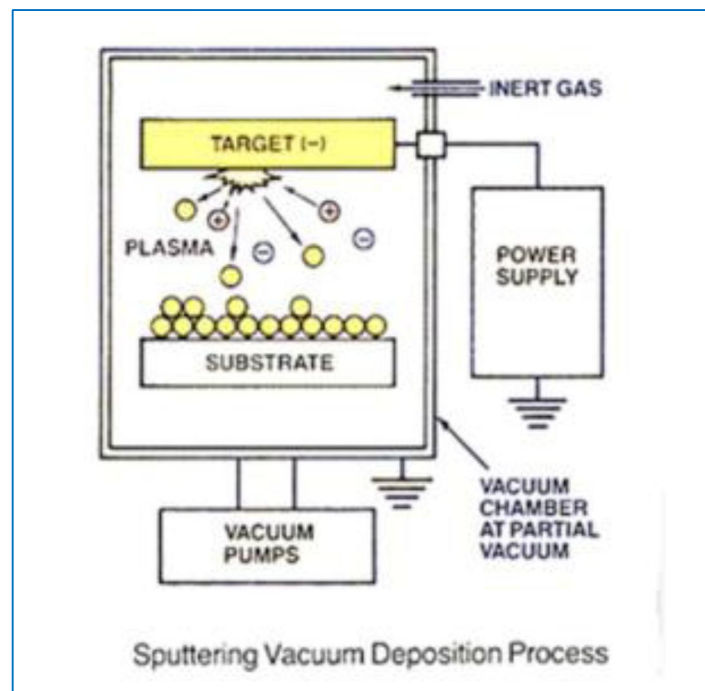
Figure 2.1: *The principle of RF Sputtering*

Figure 2.1 shows the basic principle of RF sputtering technique. Under the applied high voltage, the gas is ionized and plasma is initiated between the cathode and the anode. The positive ions of the plasma (from ionized Ar) are accelerated towards the negatively charged target and impinge on its surface. The mobility of the incident atoms arriving at the substrate is highly dependent on sputtering parameters especially on the pressure inside the chamber and on the power applied to the target. In addition to the sputtered (neutral) material ejected from the bombarded surface, other processes take place during sputtering which also influence the growth of films. They are secondary electron emission emitted from the cathode due to ion bombardment, which may cause further ionisation of the neutralised species, secondary positive or negative ion emission, emission of photon radiation, chemical dissociation, reflection and backscattering of the incident particles.

Non-conducting materials cannot be sputtered directly with an applied dc voltage due to the positive charge accumulation on the target surface. Thanks to the RF voltage supply any kind of insulating/conducting material can be treated or deposited. RF frequencies used for sputter deposition are in the range of 0.5–30 MHz, but usually the applied frequency (industrially/commercially) of 13.56 MHz that is often being used. The usefulness of RF methods for sputtering non-conducting materials is based upon the fact that a self-bias voltage, negative with respect to the plasma floating potential, develops on any surface that is capacitively coupled to a glow discharge. In a low gas pressure discharge, electrons have a greater velocity than the ions, which are several thousand times heavier. Objects plunged inside the plasma sustain a more important electron bombardment than ion bombardment, and therefore they charge negatively until the ion current and electron current are equal. At the RF powered cathode, the constantly negative potential that appears is called *self-bias*.

2.3.2 SUBSTRATE CLEANING

Substrate cleaning is an important step in preparing high quality thin films and also for high adherence to the substrate. In the present study, we have used silicon (100) and quartz substrates for all the analysis. Firstly all the samples were cleaned by normal water. Then the quartz and silicon substrates separately immersed and rinsed using deionized water. These substrates were again cleaned by an ultrasonic cleaner in a deionised water bath. Secondly, these substrates were cleaned by an ultrasonic cleaner in an isopropyl alcohol bath for 15 minutes and then washed thoroughly by deionized water and were allowed to dry with nitrogen flush. The main aim of cleaning the substrates by isopropanol is to remove the inorganic/organic impurities respectively. Ultrasonic cleaning was done to remove any other foreign particles stays on the surface of the substrates.

2.4   GROWTH CONDITIONS AND SAMPLE PREPARATION

2.4.1 BRIEF DESCRIPTION ABOUT THE EQUIPMENT

A pictorial view of the apparatus used for depositing Nd- doped TiO_2, ZnO and Al_2O_3 thin films is shown in Figure 2.2. Thin films were deposited in a 13.56 MHz RF sputtering enabled with the co-sputtering cathode assembly, which contains one target for oxide material [TiO_2, ZnO and Al_2O_3] of target size 10cm diameter and one magnetron cathode (for metallic target [Nd]) of target size 5cm. The pumping system includes a turbo molecular pump (for high vacuum) and rotary pump for pumping. The system was also equipped with RF and DC power supplies, various gauges, gas feed through controlled by mass flow controllers in a digital command module. The substrates can be replaced in the deposition chamber without breaking the main chamber vacuum inside, thanks to the introduction chamber enabled with gate load lock separated with a secondary turbo molecular pump. The distance between the

substrate and the target can be varied for both the target assembly. Infrared lamps can heat the substrates up to 400°C. The substrates are placed on a rotating substrate holder in horizontal position and the rotation is controlled by a stepper motor. The reactor base pressure achieved for the deposition in this system is (2-4) x10^{-6} Pa.
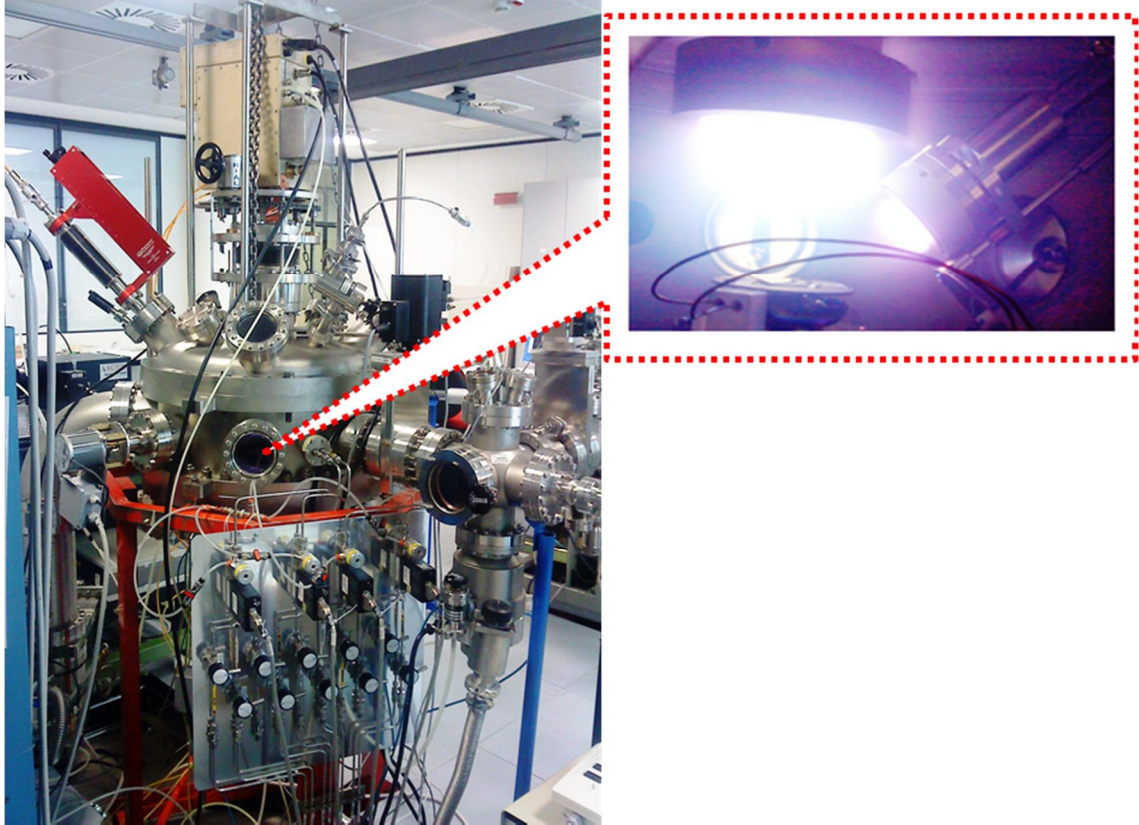
Figure 2.2: *A photograph of vacuum system used in the present study and plasma generated during the RF co-sputtering process.*

Nd -doped TiO$_2$, ZnO and Alumina thin films were deposited by varying different parameters described below.

2.4.2 PREPARATION OF Nd -DOPED TiO$_2$ THIN FILMS

The undoped- and Neodymium-doped titanium dioxide thin films were deposited by radio frequency (13.56 MHz) co-sputtering. High purity, a commercially available TiO$_2$ disc (99.999%) with 10cm diameter (Goodfellow) and metallic neodymium (99.99%) were used as cathodes and sputtered in pure argon atmosphere, by keeping

the argon flow rate constant at 30 sccm.. Separate power supplies (Advanced Energy RFX 600A and Advanced Energy CESAR) were connected to each target providing independent target power control. Multilayers of such films were also deposited by using these two targets assembly alternatively.

2.4.3 PREPARATION OF Nd -DOPED ZnO THIN FILMS

Pure and neodymium-doped ZnO films were deposited by radio frequency (13.56 MHz) co-sputtering. High purity, commercially available ZnO (purity= 99.999%, diameter= 10cm) target and metallic Nd target (5cm) equipped with a magnetron were sputtered simultaneously in a pure argon plasma. The reactor base pressure was kept at 4×10^{-6} Pa, while the depositions were operated at 6.6 Pa working pressure by keeping the argon flow rate constant at 30sccm.

2.4.4 PREPARATION OF Nd -DOPED ALUMINA THIN FILMS

Nd – doped alumina thin films were deposited by RF co-sputtering using Al_2O_3 disk target (99.999% purity) with 10 cm diameter (Goodfellow) and metallic neodymium (99.99%) were used as cathodes and sputtered in pure argon atmosphere, by keeping the argon flow rate constant at 30 sccm.

Other specific sample preparation and parameters will be discussed inside the corresponding chapters.

2.4.5 THERMAL ANNEALING OF THE FILMS

Ex-situ post-deposition annealing treatments were performed for all the samples of Nd –doped titania, ZnO and Alumina thin films in ambient air using a tubular furnace controlled by a temperature controller. For the annealing temperature effect studies, the films were annealed for six hours at a range of temperatures from 300°C to 800°C in air ambient.

2.5   THIN FILM CHARACTERISATION

This section describes the overall techniques used to characterize the thin films of neodymium- doped with TiO_2, Zinc Oxide and Alumina. The chemical composition of the films were analysed by using Auger Electron Spectroscopy (AES), X- ray Fluorescence (XRF) and X-ray Photoelectron Spectroscopy (XPS). The use of a multi-technique analysis approach (AES and XRF) helped to characterize the films for their chemical composition, especially for the low doping concentration. The films were also characterized for their structural properties using X-ray Diffraction (XRD) and Raman Spectroscopy analysis. Morphological properties of films were investigated by Scanning Electron Microscopy (SEM) and Atomic Force Microscopy (AFM) technique. The optical properties of the films studied using UV-Vis-near IR spectroscopy. Complete analyses on the near infra-red photoluminescence (PL) properties under resonant and non-resonant excitation were investigated using photoluminescence spectroscopy.

2.5.1 FILM THICKNESS MEASUREMENT

Film thickness determination was performed using a Surface Profiler (KLA Tencor Instruments). The profiler scans a tip over the sample surface while recording its vertical position. The tip is pressed on the surface with a constant force (2 *mg*). The samples were partially masked during the deposition process resulting in a small area of uncoated substrate neighboring with the coated part. Measurements paths started in the uncoated area and crossed the step created between the bare substrate and the coated one. The height difference measured between the two surfaces gives the film thickness. The film thickness is the average over more measurements (more than 5 usually).

2.5.2 STRUCTURAL CHARACTERISATION

2.5.2.1 X-RAY DIFFRACTION STUDIES

X-ray diffraction (XRD) is one of the most powerful and versatile non-destructive technique used for analyzing the structural properties of crystalline solid materials (such as grain size, phase composition, crystal orientation, and defects). Consider different layers of regularly spaced atoms, separated by a distance d and a monochromatic beam of wavelength (l) proximate to d, incidents on the atomic planes. θ is the angle between the incident and the diffracted beams direction and the atomic planes. There will be positive interaction (scattering in phase) only when the path difference of scattered waves from two neighboring atomic planes equals a whole number of wavelengths l. If the diffracted angle is equivalent to the incident one, this difference is given by $2d \sin\theta$ and the condition for diffraction can be written in the form:

$$n\lambda = 2d \sin\theta \qquad (2.1)$$

This condition, where d is the distance between crystal planes, 2θ the Bragg angle, n is the integer, and λ the wavelength of the X-ray, is known as *the Bragg's law* which is the fundamental equation of the X-ray diffraction from crystalline solid materials [4].

The diffraction pattern, that includes position (in 2θ angle scale) and intensities of the diffracted peaks, is obtained by varying the incidence angle.

Position (d) and intensity (I) of the diffracted peaks act as a distinctive "fingerprint" which provides several information about the samples:

- Identification of crystalline compounds (even in a complex sample) can be obtained by comparing the acquired pattern with the International Centre for Diffraction Data (ICDD) database [5].
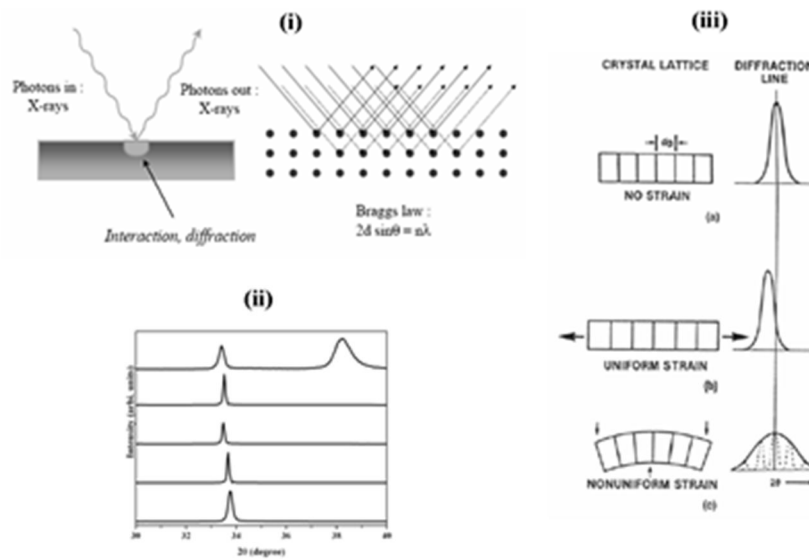
Figure 2.3: *X-ray reflection characteristic of the material, and the changes in peak shape due to different strains (adapted from the Reference* [6]*)*

- 2θ angles analysis allow to calculate the interplanar atomic distance (d-spacing)

- The (d) position of the diffracted peaks gives information about the atoms arrangement within the crystalline compound (unit cell size or lattice parameter)

- intensity can be used to evaluate the type and nature of the atoms

- Full width at half maximum (FWHM) of the peaks is used to determine crystalline size and micro-strain in the sample

Quantitative analysis of crystalline phases can also be performed. A number of different methods have been proposed and successfully applied also when multi-component crystalline phases quantification is required. External standard, reference-intensity-ratio (RIR) and Rietveld methods are probably the most accurate and reliable.

Two possible geometries can be used to acquire an XRD spectrum: the *Bragg-Brentano* and the *Seeman- Bohlin configuration*.

In the conventional Bragg-Brentano (also called θ -2θ) X-ray diffraction geometry, the sample rotates with an angular speed *w* in the centre of the focusing circle, while the source and the counter lies on the circumference of the same focusing circle. The source is fixed and the counter moves along the circumference with an angular speed of 2*w*; as a result the angle formed by the primary beam and the normal to the surface is equal to the angle between the normal to the surface and the counter and the Bragg's law is always maintained.

In the Seeman-Bohlin (also known as the *Grazing Angle configuration*), on the other hand, focused beam, sample and counter lies on the same focusing circle. The detector only rotates through the angular range, keeping the incident angle and the beam path length constant while the source and the sample are fixed. In this condition the Bragg's law is always maintained. By restricting the incidence angle to low values, the X-ray penetration depth can be limited to few hundreds of Angstrom and thin films and layers characterization can be performed. The low angle increases the path length of the incident X-ray beam through the sample and the investigation becomes more surface sensitive reducing the substrate contribution.

In the present study, the phase structures of the films were investigated using an Italstructures APD2000 X-ray diffractometer. The crystallinity and the phase structure of pure and Nd doped titania thin films were investigated using a Seeman–Bohlin (grazing angle) configuration and measurements were carried out by employing *CuKα* (λ= 1.5406Å) radiation at an incident angle of 3°, in steps of 0.02° operated at 40kV and 30mA. Crystallite size (D) and lattice strain (η) in the films were calculated using

$$B_{size+strain} \cos\theta = \frac{K\lambda}{\langle D \rangle} + \eta \sin\theta \qquad (2.2)$$

where λ is the X – ray wavelength equal to 0.15405 nm for Cu Kα radiation, $B_{size+strain}$ is the full width at half maximum (FWHM) of the peak considered (in rad), θ is the Bragg angle and $\langle D \rangle$ is the average crystallite size. K is approximately equal to 0.9 [4]. Here $B_{size+strain}$ is supposed to be induced by both low crystallite size and strain. The crystallite diameter and the film internal strain were determined by means of the Williamson-Hall plot of $B\cos\theta$ in function of $\sin\theta$. Lattice constants a and c of the films are calculated using the formula,

$$\frac{1}{d^2} = \frac{(h^2+k^2)}{a^2} + \frac{l^2}{c^2} \qquad (2.3)$$

where d is the interplanar distance and h, k, l are Miller indices.

For Nd-doped ZnO samples, we used the Bragg-Brentano X-ray diffractometer with $CuK\alpha$ (λ =1.5406 Å) radiation. In order to increase the sensitivity of the θ:2θ geometry, the incident and diffracted beams were made quasi-parallel by means of a Göbel Mirror optics on the incident beam and a soller slit along the detector side. XRD patterns were acquired using scan rate of 0.02° 2θ step at 40 kV, 30 mA over a 2θ angle range of 20°- 80°.

Crystallites size (D) was obtained according to the Scherrer's equation

$$D = 0.9 \frac{\lambda}{\beta \cos \Theta} \qquad (2.4)$$

where λ is the X-ray wavelength, β the Full Width at Half Maximum (FWHM) of the considered peak and θ is the Bragg angle [7]. The c-axis length was on the other hand calculated by the equation

$$c = \frac{\lambda}{sin\theta} \qquad (2.5)$$

where λ is the X-ray wavelength and θ is the Bragg diffraction angle in degree [8].

2.5.2.2 RAMAN SPECTROSCOPY STUDIES

Raman spectroscopy is another valuable technique used to study the lattice vibrations and their interactions with other excitations. Raman spectroscopy is primarily a structural characterization tool used to study the crystalline phase transformations, lattice distortions, the doping stress/strain states, oxygen defects and molecular properties from their vibrational transitions. The interaction of external photons (electric field) with solid or matter leads to polarization. This induced polarization represented by two phenomena, one represents the elastic scattering and the other inelastic scattering (Raman Scattering) which consists of Stokes (phonon generation) and anti-stokes (phonon annihilation) term of elementary excitations, as schematized in figure 2.4
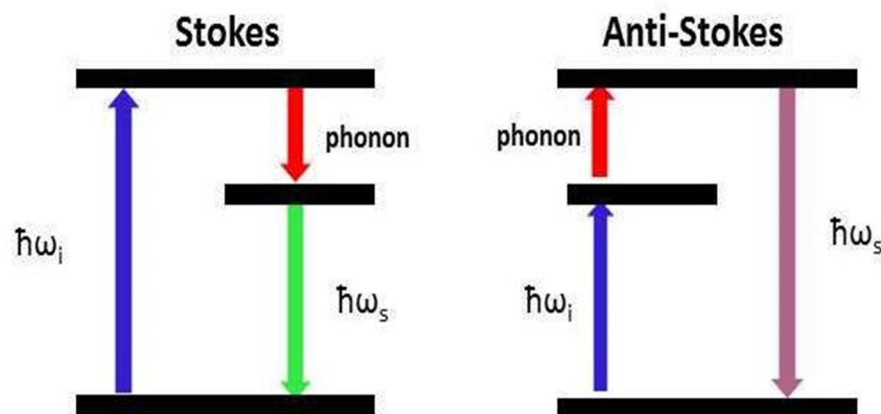
Figure 2.4: *Energy level diagram for Raman scattering; Stokes and anti-Stokes Raman scattering*

The frequency difference between the scattered light and the monochromatic excitation source is conventionally called Raman shift.

Raman Spectra of undoped and neodymium-doped titania thin films in the wavenumber region 20-700cm^{-1} were measured in backscattering geometry at room temperature (300K) using a triple-axis Raman spectrometer (Horiba-Jobin Yvon, model T64000) set in double-subtractive/single configuration and equipped with

holographic gratings having 1800 lines/mm. The spectra were measured, in turn, by exciting at the wavelength 514.5 nm line of Argon ion gas laser. The laser power on the sample surface was 10mW and it kept as a constant during all the measurements. The laser beam was focused onto the sample surface over a region of about 2μm in size, and the scattered radiation from this region was collected by the same objective used to focus the incident laser beam. After the filtering by the fore double monochromator, the scattered radiation was detected at the spectrometer output by a multichannel charge-coupled-device (CCD) detector, with 1024x256 pixels, cooled by liquid nitrogen. The spectral resolution was better than $0.7cm^{-1}$/pixel. A wave number calibration of the spectrometer was made by exploiting the emission lines of a Ne spectral lamp as reference. Repeated micro-Raman measurements were performed from different regions of the sample surface and the spectra showed a very good reproducibility. Raman measurements were made in collaboration with the Department of Informatics, Universita di Verona, Italy.

2.5.3 CHEMICAL COMPOSITIONAL ANALYSIS

2.5.3.1 AUGER ELECTRON SPECTROSCOPY (AES)

Auger Electron Spectroscopy (AES) is one of the most widely used analytical techniques for chemical analysis of the outermost layers of a material (surface or interface). Auger electrons result from an atomic rearrangement involving three electrons and following the creation of a core hole. A sketch of the Auger process is shown in fig 2.5. Though the latter can be generated in a number of different ways, i.e. by energetic electrons or ions as well as by X-rays, in a dedicated instrument electron beams are always employed. This is because the ability to finely focus and handle electrons beam directly gives the technique a high lateral resolution. Excited

Auger electrons are analyzed according to their kinetic energy, which is in turn a fingerprint of the emitting element [9].

Elemental identification is possible as well as quantification of elements relative abundance (0.5-1% is the typical detection limit for most elements). Information on the chemical state of surface is additionally derived from line-shape analysis of Auger transitions involving valence electrons. All elements in the periodic table (except hydrogen and helium) are detected over a wide energy range (generally 0 to 2000 eV) with moderate matrix effects.
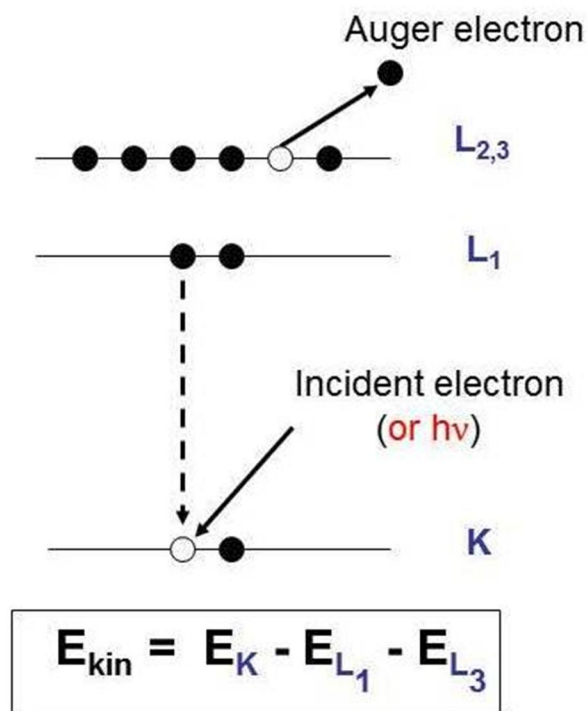
Figure 2.5: *Schematic diagram of an Auger process*

Characteristic of the technique is its high surface sensitive (few monolayers) due to the limited mean free path of AES secondary electrons. By combining Auger analysis with ion etching of the surface, a composition profile of elements as a function of

depth may be achieved. The depth profile raw data consist of peak-to-peak elemental signals as a function of the sputtering time but a more commonly used in-depth composition image is given by the elemental concentration as a function of the erosion depth. Therefore, a conversion of the measured sputtering time into sputtering depth and that of the acquired signal intensities to elemental concentration are required. In order to determine the erosion rate, a reference material of certificate thickness is used.

AES depth profiles were carried out using a Physical Electronics 4200 system, equipped with a variable resolution cylindrical mirror analyzer (CMA, energy resolution 0.6%) and a coaxial electron gun. Auger spectra were excited using a 5KeV electron beam that scanned an area of 400 μm^2, while film etching was performed by a 2KeV Ar^+ beam. The argon pressure during the measurements was kept at 10 mPa and the ion beam was rastered over an area of 1 mm^2. The C KLL (271 eV), O KLL (503 eV), Zn LMM (994 eV), Nd MNN (91 eV) and Ti LMM (387eV) transitions were monitored for the film characterization while Si LMM (89 eV) for probing the signal coming from the silicon substrate [10]. The depth distribution of the elements was recorded as a function of the sputtered depth, assessed on the basis of the erosion time and the film thickness. The elements signal intensity was measured from the peak-to-peak heights in derivative spectra after correction with their specific sensitivity factors.

2.5.3.2 X-RAY PHOTOELECTRON SPECTROSCOPY (XPS)

X-ray photoelectron spectroscopy (XPS), alternatively named electron spectroscopy for chemical analysis (ESCA), is now a well-established surface analysis technique capable of providing elemental and chemical state information from the outer 5 to 10 nm of a solid surface. The technique is based on the photoelectric effect, discovered

by Hertz in 1887, where the emission of electrons from a material occurs under photon irradiation. When an X-ray of known energy (hν), generally, with laboratory-based equipment either Al Kα at 1486.7eV or Mg Kα at 1253.6eV, interacts with an atom, a photoelectron can be emitted via the photoelectric effect according to the scheme in figure 2.6. The emitted electron's kinetic energy (KE) can be measured and the atomic core level binding energy (BE) relative to the Fermi level (E_F) of the sample can be determined using the following equation:

$$(BE) = \hbar v - (KE) - \varphi_{sp} \qquad (2.6)$$

where Φsp is the work function of the spectrometer. The various core level binding energies observed in a spectrum can be used to identify all the elements of the periodic table except for hydrogen and helium [9].
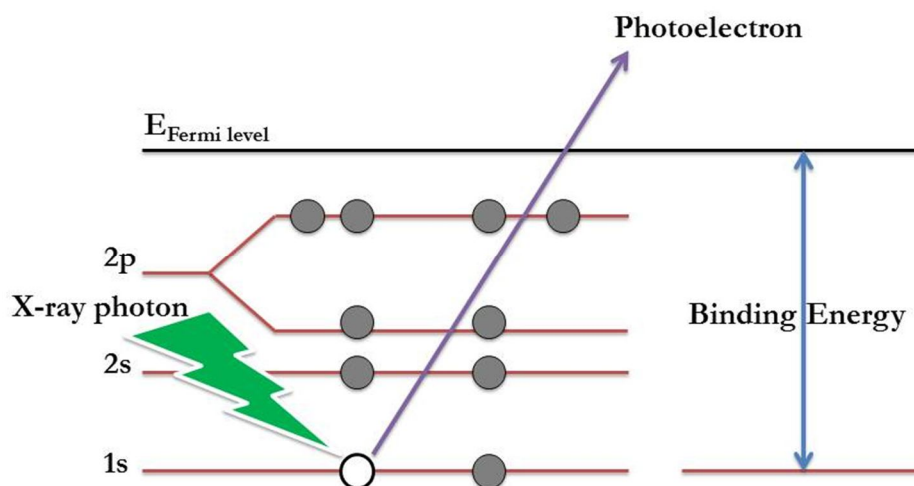
Figure 2.6: *A scheme of X- ray photoelectron spectroscopy process*

Chemical state information can also be extracted because binding energies are sensitive to the chemical environment of the atom. Chemical environments that deshield the atom of interest (i.e. are bound to strongly electron withdrawing groups) will cause the core electrons of that atom to have increased binding energies. Conversely, decreased binding energies will be measured for core electrons of atoms

that withdraw electrons from their neighboring atoms. In this way the degree(s) of oxidation of each atomic species can be measured. For Nd –doped TiO_2 thin films, the XPS studies were performed on samples using a SCIENTA ESCA 200 spectrometer with a monochromatic Al$K\alpha$ X-ray source (1486.6 eV). The experiments were performed under ultrahigh vacuum ($2x10^{-8}$ Pa) conditions without any additional in situ cleaning procedure. Photoemission spectra showed that carbon and water are the only surface contaminants for all of the investigated films. The spectra of C *1s*, O *1s* and Ti *2p*, Nd *4d* core lines were acquired at 150 *eV* pass energy (resolution of 0.4 *eV*). The chemical composition of doped TiO_2 films was determined, using the Scienta atomic sensitivity factors for the different core levels.

In the case of Nd –doped ZnO thin films (different concentrations of Nd doping) XPS spectra were recorded with a KRATOS AXIS UltraDLD instrument equipped with an hemispherical analyzer and a monochromatic Al Kα (1486.6 eV) X-ray source. The experiments were performed under ultrahigh vacuum ($2x10^{-8}$ Pa) conditions without any additional in situ cleaning procedure. The core lines (C1s, O1s, Zn2p, Nd4d) were acquired at 20 eV pass energy, which leads to an energy resolution of $\sim$0.4 eV. After a Shirley-type background subtraction, the XPS spectra were fitted using a non-linear least-squares fitting program adopting a Gaussian–Lorentzian peak shape.

During the XPS analysis, due to the low electrical conductivity of the samples, an electrostatic charge always builds at the surface. Compensation of this surface charging was performed by bombarding the surface with an electron flood gun during the analyses. The spectra needed to be corrected for the BE scale and this was performed using as reference the C1s spectrum. Since the deposited films were exposed to air, the C1s peak must include a significant amount of carbon due to ambient contamination. After deconvolution of the C1s core line therefore, the main

peak at 285 eV corresponding to hydrocarbon contamination was used as internal reference to calibrate the spectra and correct their binding energy (BE) shift, either under flood electron gun application or without.

2.5.3.3 X-RAY FLUORESCENCE SPECTROSCOPY (XRF)

X-Ray Fluorescence Analysis (XRF) exploits the characteristic emission of atoms after an inner-shell vacancy induced by a photoelectric absorption. A sketch of the microscopic principle is given in Figure 2.7.
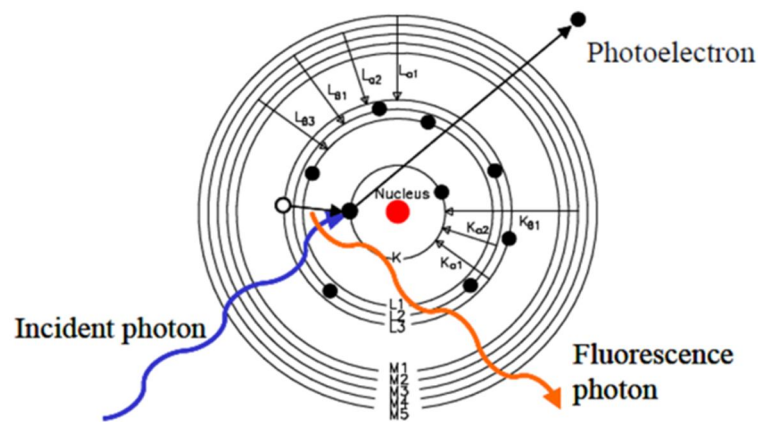
Figure 2.7: *Schematic sketch of microscopic principle*

Any XRF experiment can be divided into a few general steps. A source of high energy photons irradiates the sample; the radiation emitted by the sample is collected and separated with respect to its energy or wavelength. The photons of the characteristic lines are counted and related to the concentration of the elements in the sample. In Energy dispersive X-Ray fluorescence the emitted photons are separated according to their energy in a solid state detector. A typical XRF setup is shown in Figure 2.8.
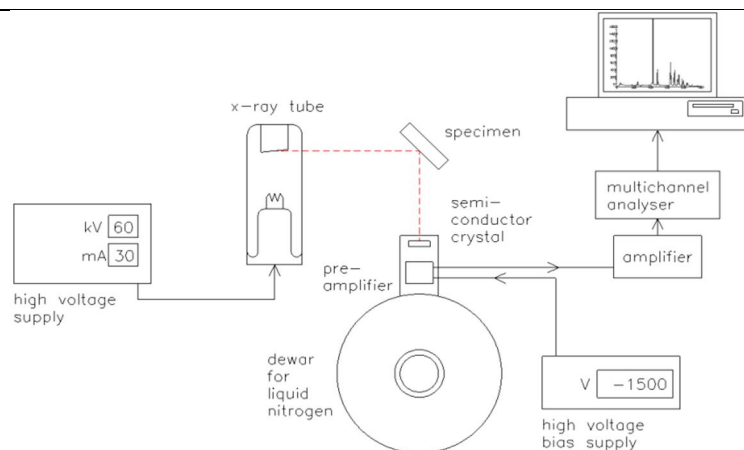
Figure 2.8: *Typical XRF set up*

In the case of determination of low concentration of neodymium in titania or ZnO matrix, X-Ray Fluorescence spectra (XRF) have been acquired on a theta-theta diffractometer (TNX phoenix) equipped with a monochromatic parallel beam Mo*Kα* (λ = 0.71Å) source and a Silicon drift detector (SDD - KETEK 50mm^2). The primary beam was set at 30° of incidence relative to the sample surface. The fluorescence intensity of the elements was acquired by placing the SDD detector at a distance of 15mm above the surface of the sample with the cold finger at 90° relative to the sample surface. Acquisition time depended on the concentration of Nd and was varied from 200 to 40000 seconds. The deadtime of the acquisition system was between 5 and 7% for all samples. XRF measurements were made in collaboration with MINAlab, FBK, Trento, Italy.

2.5.4 MORPHOLOGICAL STUDIES

2.5.4.1 SCANNING ELECTRON MICROSCOPY (SEM)

Scanning electron microscopy (SEM) is used for surface characterization. When the focussed beam of electrons impinge on the sample, interaction between the incident beam and the constituent atoms in the sample produce variety of signals such as characteristic X-rays (in the μm range), backscattered electrons (10s of nm to 100s of nm), cathodoluminescence, Auger electrons, secondary electrons (in the nm range)

81

will be generated. The detector collects the emitted secondary or backscattered electrons and converts it into signals, amplified and fed them to the viewing screen to produce the image. The secondary electrons were used to study the topographical observation of surface while the backscattered electrons were used to study the compositional observation of surface. Elemental analysis can be studied through the characteristic emitted X-rays. In the present investigation, Secondary Electron images of the samples were acquired by using a Field Emission SEM (JEOL JSM 7401F) operated at 5 kV. Secondary electron only was detected to maximize lateral resolution. SEM analyses were made in collaboration with MINAlab, FBK, Trento, Italy.
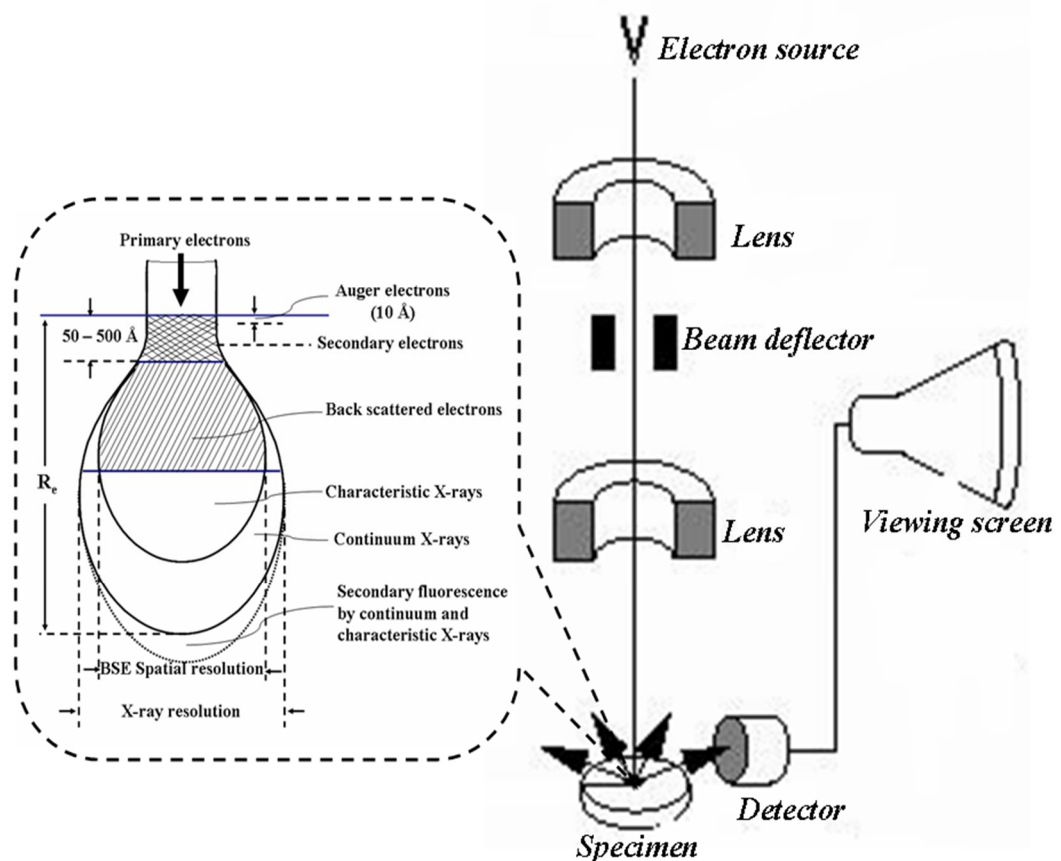
Figure 2.9: *The ray diagram of SEM with an insert of interaction of X-rays with the specimen.*

2.5.4.2 ATOMIC FORCE MICROSCOPY (AFM)

AFM is a versatile and non destructive surface analysis technique, in which both conducting and non- conducting samples can be analysed. Normally, AFM works on number of modes, but in general the two primary modes of operation is (1) contact mode (static) (2) non-contact mode (dynamic). The AFM consists of a microscale cantilever with a sharp tip (also called as probe) at the end used to scan the sample surface. The tip will be slowly scanned across the prescribed dimension on the sample surface either in the contact mode or non-contact mode. The force between the tip and the atoms on sample surface causes bending in the cantilever. The magnitude of this bending depends on the tip atoms and the atoms on the surface and the Van der Waals force existing between them. In contact mode, the first tip contact surface is always kept constant maintaining a constant deflection during the time of scan. These deflections were recorded by using the optical system coupled with photodetectors. The signals from the photodetectors were used to probe the surface topography of the samples. In the dynamic mode, the tip is oscillated at resonant frequency and the amplitude of oscillation is kept constant. The horizontal and the vertical movements of the tip were controlled by the piezoelectric motors.

The 3D profile of the surface morphology on a nanoscale was studied by Atomic Force Microscopy (AFM) in contact mode imaging with a SIS Ultra Object Instrument. The roughness was measured as root mean square value over an area of 4x4 μm.

2.5.5 OPTICAL PROPERTIES MEASUREMENTS

2.5.5.1 UV-VIS-NIR SPECTROPHOTOMETRY

The transmittance (T), defined as the ratio of total transmitted energy to the incident energy when a light beam passes through thin films of uniform thickness, has been

mostly used to derive the optical parameters like absorption coefficient (α) and band gap (E_g) of the materials. The optical properties (Transmittance, Absorbance and the band gap) of neodymium –doped TiO_2 and ZnO were studied using UV-Vis-NIR spectroscopy. A double beam spectrophotometer (Model - JASCO V-670), single monochromator design covering a wavelength range from 190 to 2700 nm was employed to record the optical transmittance and reflectance spectra of the deposited films at normal light incidence. An Al mirror was used as 100% reflectance reference material.

The optical band gap energy is the minimum energy required to excite an electron from the valence band to conduction band by an allowed transition. The optical band gap of the transmitting thin films were calculated by Tauc's equation [11]

$$\alpha h\nu = B(h\nu - E_g)^m \qquad (2.7)$$

where hν is the incident photon energy, B is a constant, E_g is the bandgap energy, the exponent *m* is characteristic of the type of optical transition process (m= 2 for indirect allowed transition and m=0.5 for a direct allowed one) and α, the absorption coefficient can be determined near the fundamental absorption edge using the relation

$$\alpha = \frac{1}{t}\ln\left[\frac{(1-R^2)}{T}\right] \qquad (2.8)$$

where t is the film thickness, T and R are the corresponding transmittance and reflectance respectively. The allowed indirect bandgap energies can be obtained from the extrapolation of the linear region of $(\alpha h\nu)^{1/2}$ as a function of photon energy (hν) to the horizontal X-axis.

2.5.6 PHOTOLUMINESCENCE SPECTROSCOPY

Photoluminescence spectroscopy is a non-destructive technique used to study the electronic structure of the materials. Photoluminescence is a process in which the

substance absorbs the incident photons (i.e) electromagnetic radiations and re emits the photons. Quantum mechanically, when the sample is excited with the sufficient energy of incident photons, the electrons in the materials gets excited towards the higher energy states. This is called as photo-excitation. These electrons eventually relax and return to the ground states with or without the emission of photons. If radiative relaxation occurs (with emission of photons), the process is called photoluminescence (see the schematic sketch in figure 2.10). The PL emission spectra can be used to identify interfaces, defects, impurity levels, disorders in the material. In order to measure the emission spectra, the excitation wavelength of the sample is fixed and the intensity of the PL emission were collected as a function of wavelength.
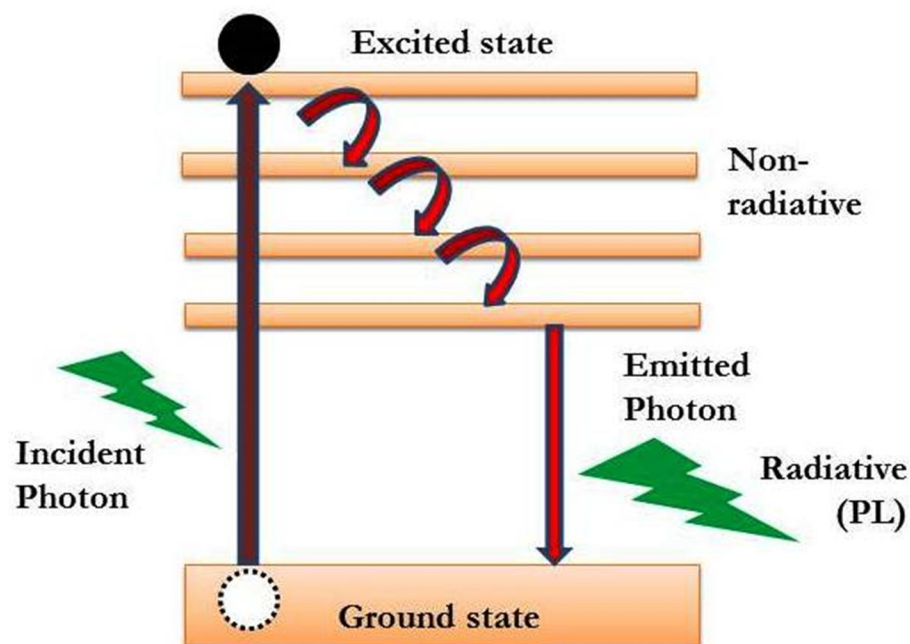
Figure 2.10: *Schematic representation of emission of luminescence photon*

In the case of PL excitation spectra, the emission wavelength (high intensity) is kept constant and the intensity of the PL emission monitored as a function of excitation wavelength. The only excitation line which gives rise to the fixed emission wavelength will give signal in the excitation spectrum.

The excitation, emission and decay characteristics of neodymium- doped TiO_2, ZnO and Alumina thin films were characterized by using photoluminescence spectroscopy technique. In the present study, photoluminescence emission measurements were performed using the 514.5, 496 and 476 nm lines of a coherent Innova Sabre (Ar^+) argon ion laser and the third harmonic of pulsed Nd-YAG laser for UV excitation (355 nm).The luminescence spectrum in the region of transition was detected by using a photomultiplier (PMT) and a silicon detector. All measurements were carried out at room temperature. PL emission measurements were made in collaboration with CNR-IFN, CSMFO Lab, Department of Physics, University of Trento, Italy.
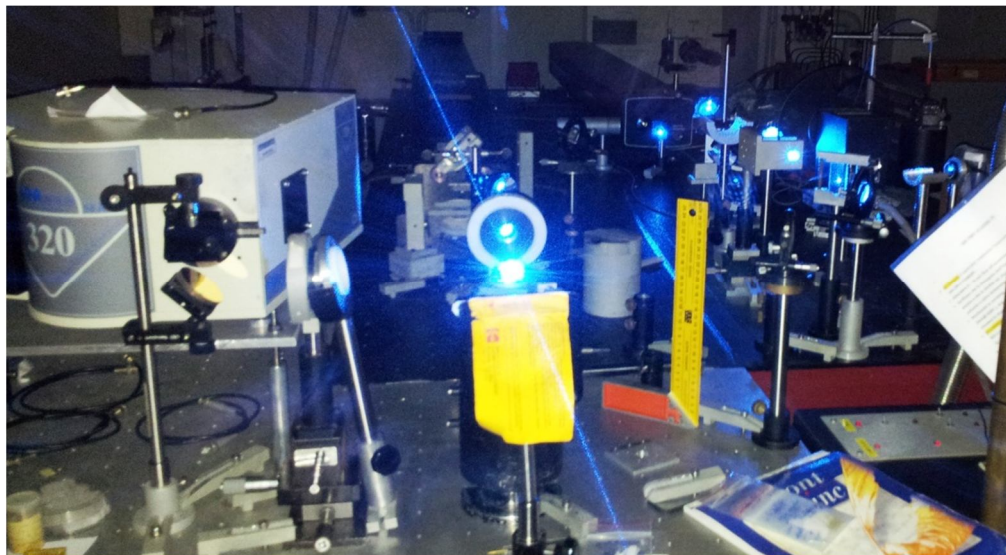
Figure 2.11: *Photoluminescence instrumentation set up equipped with YAG laser for 355 nm excitation*

Photoluminescence Excitation and Emission investigations were carried out using Horiba Jobin-Vyon Nanolog Spectrofluorometer system. For the PLE measurements, a standard 450W intense broadband continuous wavelength Xenon (Xe) lamp was used as a bright excitation source from UV to near-IR. The PL emission signal were

collected by using photomultiplier tube (PMT Model-Hamamatsu R928P) for visible light until 900nm and a liquid nitrogen cooled IGA array (Model-Symphony II InGaAs array detector) for 800-1600 nm infra-red emission detection. All the measurements were performed at room temperature.

The Luminescence decay measurements of Nd^{3+} ion were performed using (Xe) Xenon pulsed lamp as the excitation source. Decay curves were obtained recording the signal with a Horiba Jobin-Vyon Nanolog spectrofluorometer equipped with a photomultiplier detector (Hamamatsu R928P). The decay curve was fitted with a double exponential function using the equation,

$$I = A_1 \exp\left(\frac{-t}{\tau_1}\right) + A_2 \exp\left(\frac{-t}{\tau_2}\right) \qquad (2.9)$$

from which can be derived τ_1 and τ_2, the decay lifetimes. A_1 and A_2 are constants. PL Excitation and Emission characteristics and decay time measurements were made in collaboration with Department of Informatics, University of Verona, Italy.

2.5.7 WETTABILITY PROPERTY MEASUREMENT

Wetting indicates the tendency of a liquid to cover a solid surface. The degree of wetting (wettability) is determined by a balance between adhesive and cohesive forces. Adhesive forces between the liquid and solid cause a liquid drop to spread across the surface. Cohesive forces within the liquid cause the drop to ball up and avoid contact with the surface. The wettability of a material can be measured using the sessile contact angle technique, in which a drop of a liquid is deposited on the sample surface and the angle between the solid surface and the tangent to the drop profile at the drop edge is measured. The contact angle (θ) is the angle at which the liquid-vapor interface meets the solid-liquid interface [13]. The contact angle is determined by the resultant between adhesive and cohesive forces. The tendency of a

drop to spread out over a flat, solid surface increases as the contact angle decreases. Thus, the contact angle provides an inverse measure of wettability.
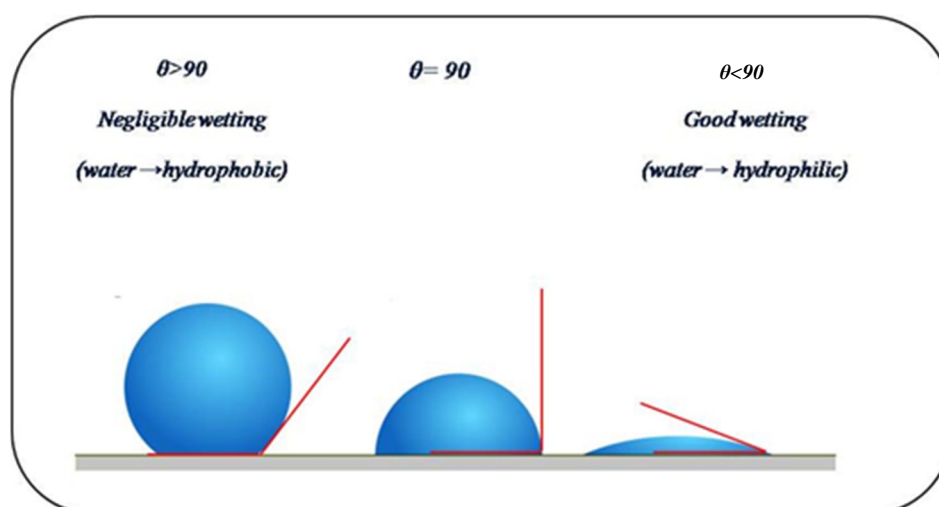
Figure 2.12: *Schematic representation of contact angle of sessile drop on the substrate [adapted from the reference 12].*

A contact angle less than 90° (low contact angle) usually indicates that wetting of the surface is very favorable, and the fluid will spread over a large area of the surface. Contact angles greater than 90° (high contact angle) generally means that wetting of the surface is unfavorable so the fluid will minimize contact with the surface and form a compact liquid droplet. For water, a wettable surface may also be termed hydrophilic and a non-wettable surface as hydrophobic. Super hydrophobic surfaces have contact angles greater than 150°, showing almost no contact between the liquid drop and the surface. This is sometimes referred to as the "Lotus effect".

2.5.8 PHOTOCATALYTIC ACTIVITY

Photocatalytic measurements were made in collaboration with LGPPTS laboratory, UPMC (Paris) as part of co-tutelle program. The photocatalytic property of the pure and Neodymium –doped titania thin films are studied by the oxidation of Methylene

Blue (MB) dye. Fig 2.13 shows the chemical structure of MB. MB is used as an indicator in this process.
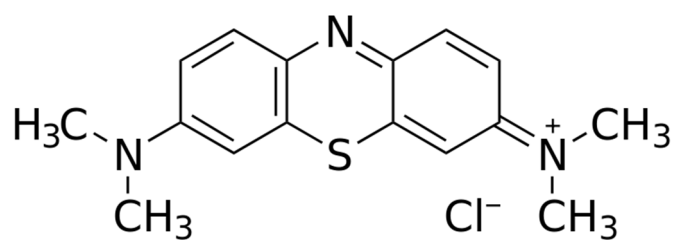
Figure 2.13: *Chemical Structure of Methylene Blue*

The Photocatalytic activity of TiO_2 and Nd doped TiO_2 thin films is evaluated by the degradation of aqueous Methylene Blue dye solution under UV 254 nm wavelength [8 watts] irradiation. In each run, a thin film sample is immersed (such that the incident light falls onto the surface of the catalyst through the MB solution) into 4 ml aqueous MB solution with a concentration of 10mg/L using distilled water. The distance between the lamp and the sample is ~ 5 cm for all the experiments.
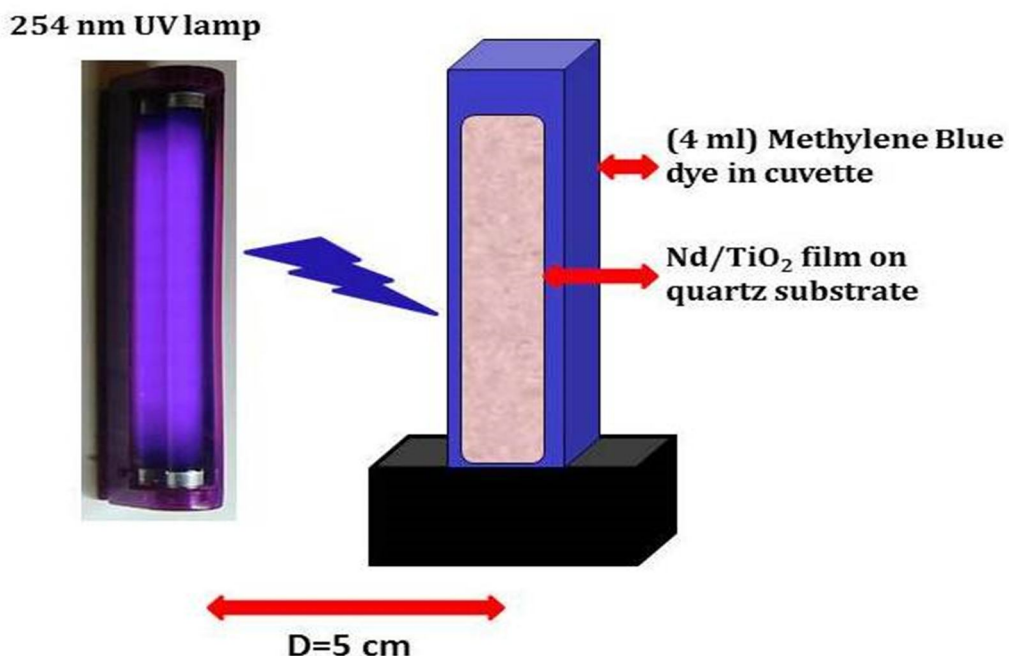
Figure 2.14: *Schematic set up of Photocatalytic experiment*

Prior to the experiment, the optical absorption intensity of MB dye at 664.05 nm is recorded for different concentration. The oxidation of the dye (de-coloration) due to the photocatalytic activity is measured periodically every 10 minutes by Ocean Optics Maya Pro 2000 spectrometer and the spectra were collected at the interval of every 30 minutes.

2.6 CONCLUSIONS

In this chapter we have provided an overview of thin film growth techniques and the basic parameters that have been used for the preparation of neodymium–doped Titania, Zinc oxide and Alumina thin films are described. The thin films were deposited using RF co-sputtering technique, possibly followed by a post growth annealing treatment. The principles and the conditions of the techniques used to characterize the Chemical, Structural, Morphological, Optical and Photoluminescence properties of the thin films are briefly described.

REFERENCES

[1].   A. J. Steckl, J. H. Park, J. M. Zavada, Mater. Today 10 (2007) 20–27

[2].   R. F. Bunshah, Handbook of deposition technologies for films and coatings- science, Technology and Applications, Noyes publications, 1994

[3].   Westwood. W. D. (2003) Sputter Deposition, AVS Publication, New York.

[4].   B. D. Cullity, Elements of X-ray Diffraction, Addison-Wesley,Reading, 1978

[5].   PDF-database. JCPDS, International centre for diffraction data (ICDD), 1601 Park Lane, Swarthmore, PA 19081, USA

[6].   Krishna Valleti, "Investigations on an innovative rotating cylindrical magnetron cathode and on tantalum based hard coatings", PhD Thesis, 2008, IITMadras

[7].   H.P. Klug, L.E. Alexander, X-ray Diffraction Procedures for Polycrystalline and Amorphous Materials, 2nd ed, John Wiley & Sons, New York, 1974

[8].   M. Subramanian, P. Thakur, S. Gautam, K. H. Chae, M. Tanemura, T. Hihara, S. Vijayalakshmi, T. Soga, S. S. Kim, K. Asokan, R. Jayavel, , J. Phys. D : Appl. Phys. **42** (2009) 105410

[9].   Surface Analysis by Auger and X-ray Photoelectron Spectroscopy.", Edited by David Briggs and John T. Grant., p.84, 2003

[10].   L. E. Davis, N. C. MacDonald, P. W. Palmberg, G. E. Riach, R. E. Weber, Handbook of Auger Electron Spectroscopy: A reference book of standard data for identification and interpretation of Auger electron spectroscopy data, 2nd ed., Physical Electronics Division, Perkin Elmer Corporation, 1978.

[11].   Pankove, J.I. Optical properties in semiconductors, Prentice-hall, New Jersey, 1971.

[12].   http://pam.fbk.eu/en/SESSILECONTACTANGLE

[13].   J. C. Berg (1993) Wettability 1st Edn, Vol. 1, Marcel Dekker Inc., New York

Chapter 3

Chapter 3

Neodymium effects on the structural, morphological, optical and photoluminescence properties of titania films

> *"The important thing in science is not so much to obtain new facts*
> *as to discover new ways of thinking about them"*
> *-Sir W. L. Bragg*

3.1 INTRODUCTION

In this chapter, the results of an investigation on structural, chemical, optical and photoluminescence properties on Nd incorporation in nanocrystalline TiO_2 thin film matrix at different concentrations are presented. Only doping with low concentrations is generally pursued in order to avoid dopant clustering and luminescence quenching. The point is that very few investigations were focused on the incorporation of neodymium in titania. The doped TiO_2 films were grown by RF sputter deposition and a lack of knowledge subsists in literature concerning sputter deposited neodymium-doped titania and in particular the neodymium concentration limit in the host matrix beyond which no photon frequency conversion effects occurs, such as frequency down-shifting. To our knowledge, there has been no analysis in this matrix concerning the experimental investigation on the influence of doping limit, for such a series of concentrations were studied. The use of a multi-technique analysis approach helped to characterize the films for their chemical composition, especially for the low Nd

concentrations. The films were also characterized for their near-infrared photoluminescence under both resonant and non-resonant excitation. In the latter case, an efficient energy transfer between the matrix and the rare-earth ion was evidenced. The joint study of the optical and structural properties allowed to clarify the location site nature of the neodymium in the titania films.

3.2 THE SAMPLE PREPARATION AND CHARACTERISATION

A constant power of 82 watts was applied to the TiO_2 cathode for all the deposition processes, corresponding to a self-bias voltage (V_{TiO2}) of -850V. In order to obtain different neodymium compositions in the films, a power in the range 3 -7 Watts was applied to the Nd target, corresponding to a self-bias voltage (V_{Nd}) in a range from -36V to -70 V. Table 3.1 summarizes the deposition conditions and the sample numbering which, from S1 to S5, follows the power applied onto Nd target, except for sample S2. The latter was prepared by exploiting the cross-contamination process which occurs when two facing targets are co-sputtered. Usually cross-contamination is a disturbing factor, however in this case it plays a positive role in incorporating very low concentration of Nd in titania matrix. As 3 Watts, the lowest useful power to apply to our Nd target, did not allow to achieve very low Nd concentration in TiO_2, the process of cross-contamination was used for that purpose. For this doing, (1) both the target surfaces were sputter cleaned in argon for 30 min, (2) the titania target was faced towards the Nd target and covered by neodymium, sputtered with power of 7 watts for 9 hrs, and finally (3) the Nd-contaminated titania cathode was run in the sputtering regime, with the Nd target kept unpowered. The samples were mounted on the rotating substrate holder support, water-cooled at room temperature, and at a distance of 4 cm from the TiO_2 cathode. All the depositions were carried out at 4 Pa working pressure. Films were deposited onto Silicon (100), 1 mm thick quartz and

soda lime glass substrates. Beforehand these were ultrasonically cleaned with isopropyl alcohol, de-ionized water for 15 minutes each, finally flushed with nitrogen (N2) gas and then introduced into the growth chamber. All the films were deposited for 9 hours at room temperature. Ex-situ post-deposition annealing treatments were made for six hours in ambient air, at a temperature of 600°C, reached with a heating rate of 5°C/min. All the grown samples are analyzed for their structural, chemical, optical and photoluminescence properties by using characterization techniques described in chapter II. The films thickness has been determined with a KLA – Tencor P-6 Stylus profilometer. The plasma parameters and the measured film thicknesses are given in Table 3.1.

Film label	Cathodes	Power on TiO_2 cathode (Watt)	self-bias on TiO_2 cathode, V_{TiO2} (V)	Power on Nd cathode (Watt)	self-bias on Nd target, V_{Nd} (V)	Film thickness (μm)
S1	TiO_2	82	-850	0	0	0.87 ±0.05
S2	Composite TiO_2-Nd	82	-850	0	0	1.05 ±0.02
S3	TiO_2 and Nd	82	-850	3	-36	1.43 ±0.01
S4	TiO_2 and Nd	82	-850	5	-47	1.73 ±0.02
S5	TiO_2 and Nd	82	-850	7	-70	2.55 ±0.06

Table 3.1: *Plasma conditions, film labeling and thicknesses of pure titania and neodymium-containing titania films.*

3.3   FILM GROWTH RATE

The variation of the film deposition rate as a function of the applied power to Nd target is shown in figure 3.1. From the figure, it is clear that the deposition rate increases with the power applied to the neodymium target. The maximum growth rate

was found to be 4.72 nm/min, as the power applied to Nd target was 7W. The increase in growth rate can be explained by the fact that the contribution of powered Nd cathode increased the ion density of the discharge.
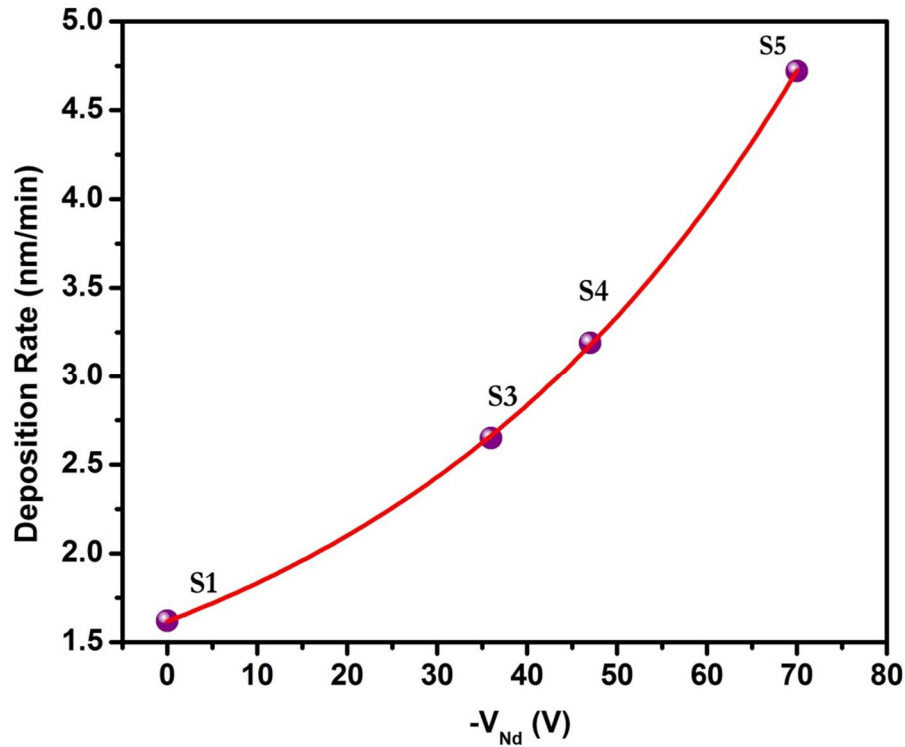
Figure 3.1: *Film growth rate for co-sputtered at room temperature Nd- TiO$_2$ deposited in Ar plasma as a function of the self-bias on Nd target ,V$_{Nd}$, with a constant V$_{TiO2}$. The data are also identified by the sample labeling.*

3.4 FILM COMPOSITION FROM XPS AND AES ANALYSES

3.4.1 XPS ANALYSIS OF UN-DOPED AND Nd-CONTAINING FILMS:

XPS analysis was performed on the samples surface, without any preliminary ion-etching.

Figure. 3.2 (a and b) shows the Ti2p and O1s core level spectra respectively, acquired on an un-doped titania film after annealing and deconvoluted into individual peaks after a Shirley background subtraction. The Ti2p core level spectrum consists of Ti2p$_{3/2}$ and Ti2p$_{1/2}$ contributions located at 459.48 eV and 465.2 eV respectively. The

peaks are well-fitted with symmetric gaussian-lorentzian functions. The Ti2p3/2 BE agrees well with published data for Ti^{4+} states in TiO_2 (*459.2 eV* for anatase and rutile in [1] and reference therein for example).

The corresponding O1s displayed in Figure.3.2 (b) can be fitted with three peaks: the major one O_I at 530.71 eV pertaining to O^{2-} ions in titanium oxide [1 and references therein] and the two others at 531.71 eV (O_{II}) and at 532.55 eV (O_{III}). The atomic ratio O_I /Ti, calculated on the basis of the areas under the O_I and $Ti2p_{3/2}$ peaks is found as 1.88. This gives the ratio of oxygen to titanium atoms involved in Ti-O oxide bonds. The deviation from the ideal stoichiometry TiO_2 (quantified as *x* in TiO_{2-x}) can be due to structural defects as O vacancies, as the XPS analysis probes the surface region of the samples. The formation of Ti-OH bonds due to H_2O dissociative adsorption can be expected too, this way healing the O vacancies [2]. In many transition metals, Ti-OH bonds give rise to a peak whose energy is close to the O_{II} peak one [3,4]. The Ti-OH bonds are difficult to quantify from the second component of the O *1s* spectrum (O_{II}). The O_{II} contribution could stem from OH groups bonded to carbon too [5]. Peak O_{III} is reported to be due to C-O bondings from carbonaceous surface contamination [5].
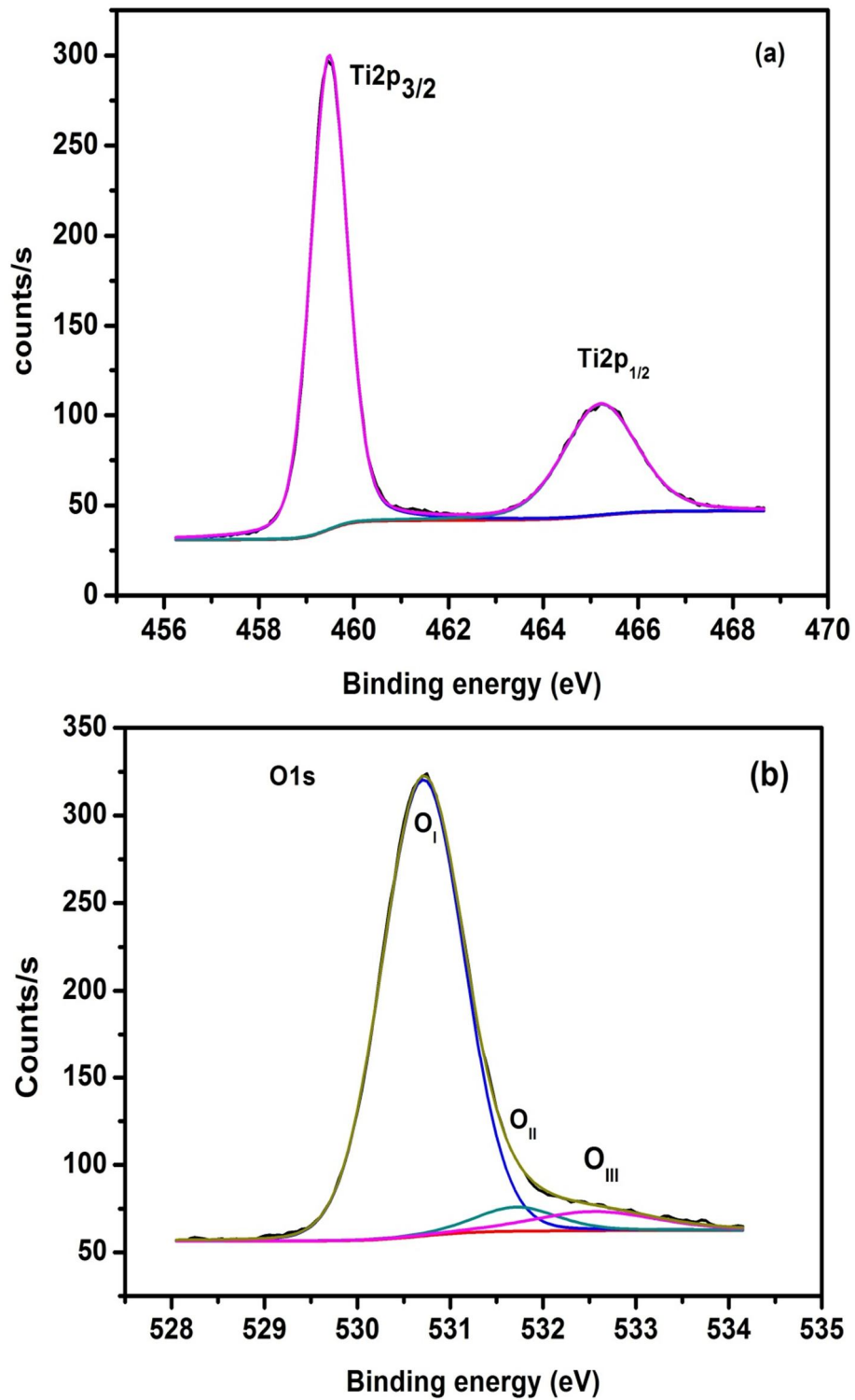
Figure 3.2: *(a) Ti2p and (b) O1s spectra for un-doped titania film*

The Ti2p, O1s and Nd 4d core level spectra acquired on the sample S3 are displayed

in Fig. 3.3 (a-c) respectively.

The Ti2p was fitted by two peaks corresponding to Ti2p3/2 and Ti2p1/2, no other contribution was necessary for the fit, as can be seen in Fig. 3.3 (a). The Ti2p3/2 core level signal occurred at 458.57 eV while, similarly to the un-doped film case, three contributors were necessary to fit the O1s peak. The main peak, O_I, is located at 529.92 eV, O_{II} at 531.15 eV and O_{III} at 532.16 eV (Fig. 3.3 (b)).

The O_I /Ti atomic ratio was calculated as 2.15, a value above the ideal stoichiometry in TiO_2. This means that oxygen atoms contributing to the O_I peak could partly pertain to Nd-O bonds. In fact the O1s photoelectron relative to oxygen in Nd_2O_3 would appear at a BE close to O_I, at 530.6 eV [1]. The corresponding Nd 3d level would be at 982.8 [1]. For the present samples, considering the Nd 3d peak was problematic as it overlaps with the OKLL Auger peak of oxygen. This led us to follow the Nd 4d core level, instead. This spectrum was acquired and it is displayed in Fig.3.3 (c). It was fitted with a single broad peak, centred at 121.98 eV. This BE value is close to 120.8 eV, the one reported for Nd in the Nd^{3+} state, like in Nd_2O_3 [1]. Nd was found in an atomic ratio to titanium, Nd/Ti = 0.037. In order to conclude about the formation of Nd_2O_3 oxide, we considered the O_I/(Ti+Nd) atomic ratio and calculated the maximum value that this ratio would take if two oxide phases co-exist, with the respective ideal stoichiometry, TiO_2 and Nd_2O_3. The O_I/(Ti+Nd) ratio value should be minor than 2 in that case. The calculated value from the acquired spectra was slightly major than this value, being equal to 2.08, while with the Nd/Ti ratio given above, the maximum value of O_I/(Ti+Nd) should be 1.98. This means that neodymium was not incorporated in an oxide phase, but that the Nd^{3+} state detected by XPS is rather an indication of Nd location in substitutional sites in titania. The chemical composition can be described as $Ti_{1-0.070}$ $Nd_{0.034}$ O_2, which also put in evidence that this substitution occurred with a defect creation in titania, in the present

case titanium vacancies. It is known that doping of semi-conductor oxides results in charge compensation effects which are expressed in the creation of structural defects such as oxygen vacancies or cation vacancies, this is the case of donor doping and acceptor doping respectively. In the case of Nd^{3+} in titania, we may expect the formation of Ti vacancies.

The O_I/Ti, O_I/(Ti+Nd) as well as the Nd/Ti atomic ratio values, as obtained for all the samples, determined on the basis of the O_I, Ti2p$_{3/2}$ and Nd4d peak areas and corrected by the relative sensitivity factors, are given in Table 3.2. Here, as recorded above, in the O_I/Ti and O_I/(Ti+Nd) ratio calculation, only the oxygen atoms involved in Ti-O and possibly in Nd-O bondings in oxides are considered. For sample S2, the Nd content was below the detection limit of the XPS analysis, it was determined by another technique, as reported later in the subsequent sections.
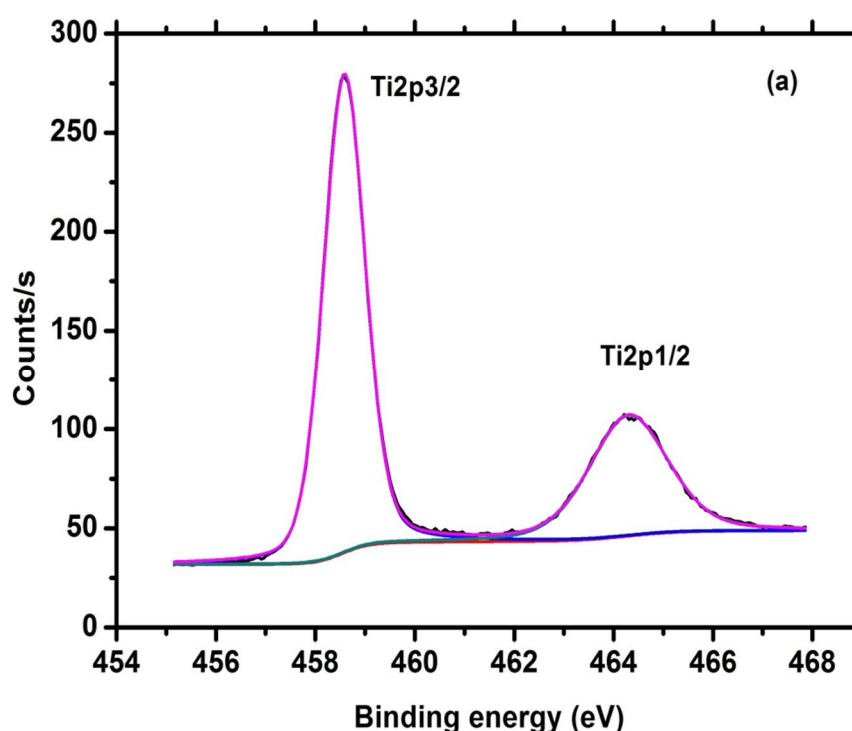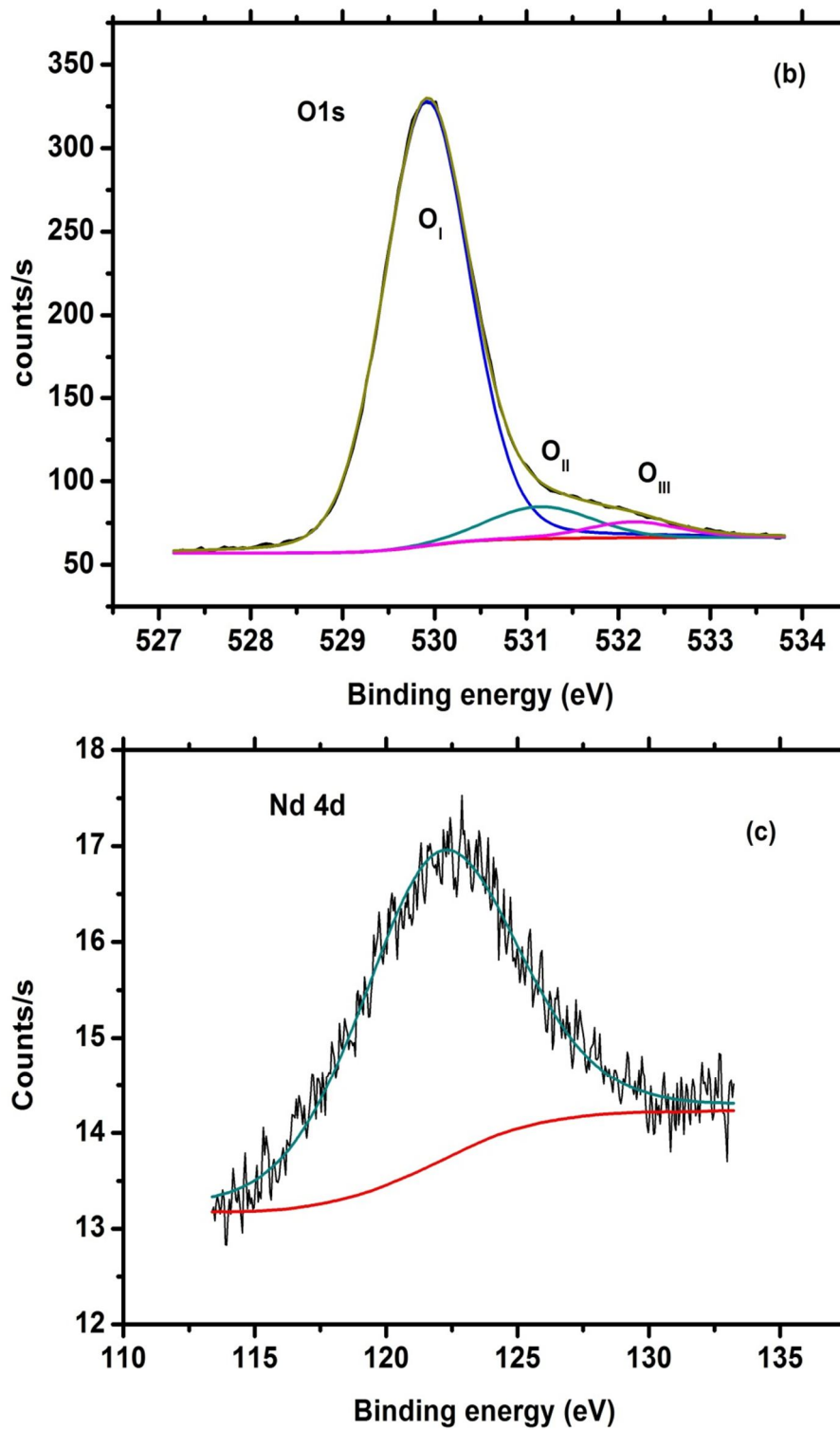
Figure 3.3: *(a) Ti2p, (b) O1s and (c) Nd4d spectra for an Nd-containing titania film (sample S3).*

It comes from the results summarized in the table that a slight increase of the applied power to the Nd target has a considerable effect on the Nd incorporation in the films. Correspondingly, the O_I/Ti atomic ratio increases too: the pure titania film (sample S1) was clearly oxygen-deficient, a deficiency which disappeared in sample S2 down to revert to oxygen excess in samples S3-S5. In these samples, oxygen was not only bonded to Ti, but Nd-O also were created.

Film label	Power on Nd target (Watt)	Self-bias on Nd V_{Nd} (V)	Nd/Ti atomic ratio from XPS (%)	O_I/Ti atomic ratio from XPS	O_I/(Nd+Ti) atomic ratio from XPS	Nd/Ti atomic ratio from AES (%)	Nd / Ti atomic ratio From XRF (%)	O/(Nd+Ti) atomic ratio from AES
S1	0	0	0	1.88	1.88	0	0	1.10
S2	0	0	N/A	2.01	2.01*	N/A	0.9	N/A
S3	3	-36	3.7	2.15	2.08	5.5	-	1.35
S4	5	-47	25	2.32	1.86	43.0	-	1.05
S5	7	-70	45	2.59	1.79	100	-	1.00

(NA) in the table denotes that the data are not available by XPS and AES, below the detection limit.
*The very low value of Nd concentration with respect to Ti in S2 would not greatly affect the O_I/(Ti+Nd) atomic ratio, so it is expected that the value is practically the same as for S1.

Table 3.2: *Elemental analysis by XPS, AES and XRF of pure and Nd-containing titania films, annealed at 600°C.*

Moreover, in contrast with sample S3, the O_I/(Ti+Nd) ratio is lower than 2 in S4 and S5, which may indicate the formation of two oxide phases (titania and neodymium oxide). In Figure 3.4 (a), the experimentally obtained values for such ratio are plotted versus the values calculated for the ideal case of the presence of the 2 oxides, for the three samples S3-S5. For clarity, a bisector line is also drawn. What can be seen is that sample S3 is above this line, while S4 and S5 stay below.
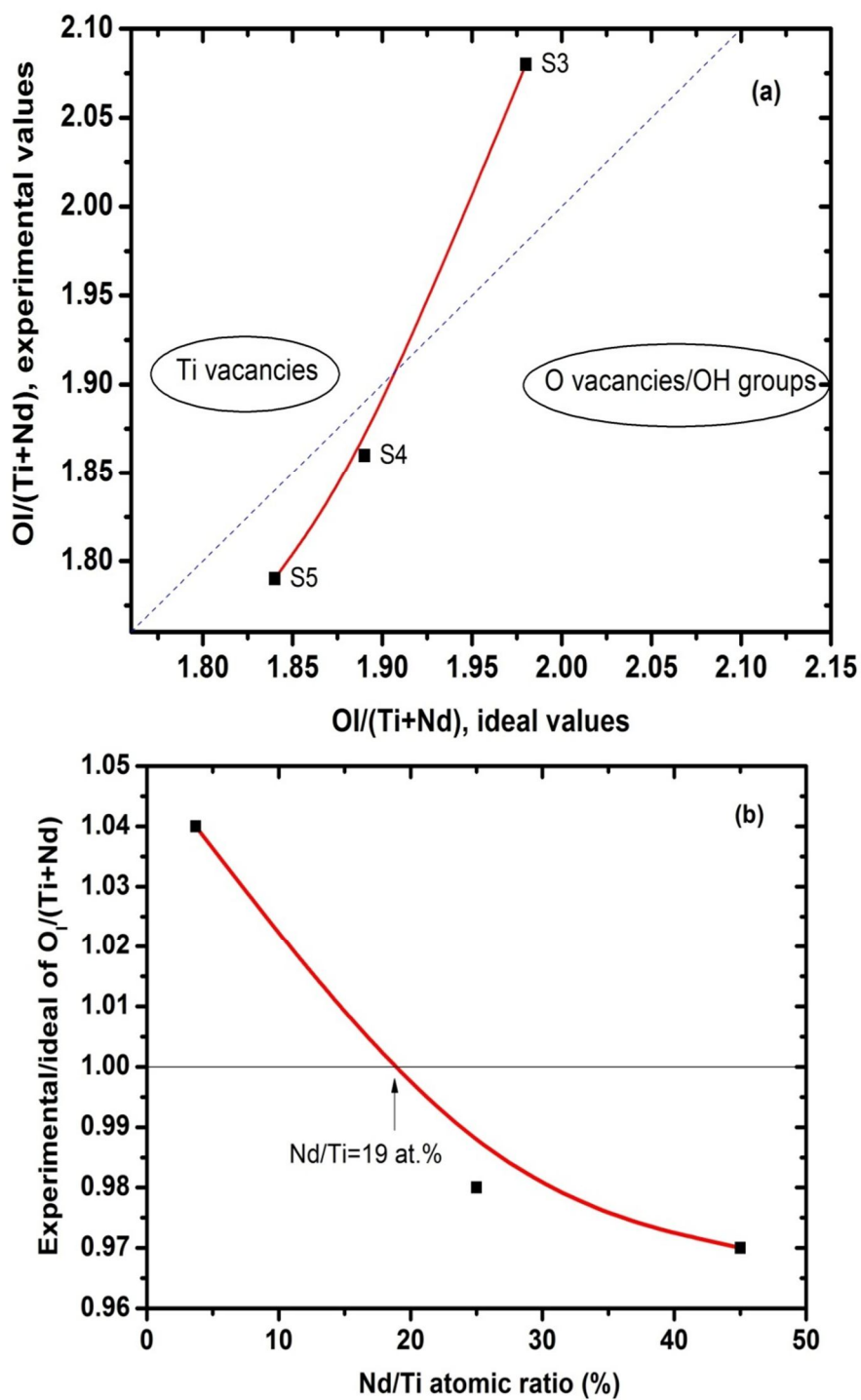
Figure 3.4: *(a) experimental versus ideal $O_I/(Ti+Nd)$ atomic ratios and (b) $O_I/(Ti+Nd)$ experimental/ideal value ratio in function of Nd/Ti atomic ratio.*

The bisector line divide the plot in two areas: the one above the line would describe films with excess oxygen in the oxide-like bonds, i.e. films with cation (Ti) vacancies,

in opposition with the area below the line which would pertain to films with oxygen deficiency, i.e. films with oxygen vacancies. In figure 3.4 (b) the deviation from ideality in case of 2 oxide phases for the $O_I/(Ti+Nd)$ ratio value is plotted in function of the Nd/Ti ratio, which gives an approximate Nd concentration threshold for neodymium oxide formation. It appears that if present in a ratio to titanium above ~19 at.%, neodymium oxide more likely forms as a distinct phase, with more or less oxygen vacancies. It should be noted that the missing oxygen in the Ti-O bondings can also be involved in Ti-OH hydroxyl groups.

3.4.2 AES ANALYSIS OF UN-DOPED AND Nd-CONTAINING FILMS:

The element concentration depth profiles for all detected elements determined by AES depth profiling for samples grown on silicon substrate are shown in Figure 3.5. Figure shows the AES depth profiles, acquired respectively on the sample S2 (upper panel) and sample S4 (lower panel). AES technique was not able to detect the Nd concentration in sample S2 (sample prepared by cross contamination) for its low content; another method was used, as discussed in the following section.

Depth profiling by AES is very useful to control the depth distribution homogeneity of the elements which compose the film chemical composition. The depth profiling was conducted down to the interface, through the whole film thickness (1 μm and 1.73 μm for S2 and S4 respectively), however well-known artifacts occurred for such prolonged ion-bombardment which includes ion-beam mixing at interface with the substrate and other effects relative to ion-beam induced heating and roughening. So we limited the depth profiles to 800 nm depth, over which a fair homogeneity of the elemental depth distribution can be observed.
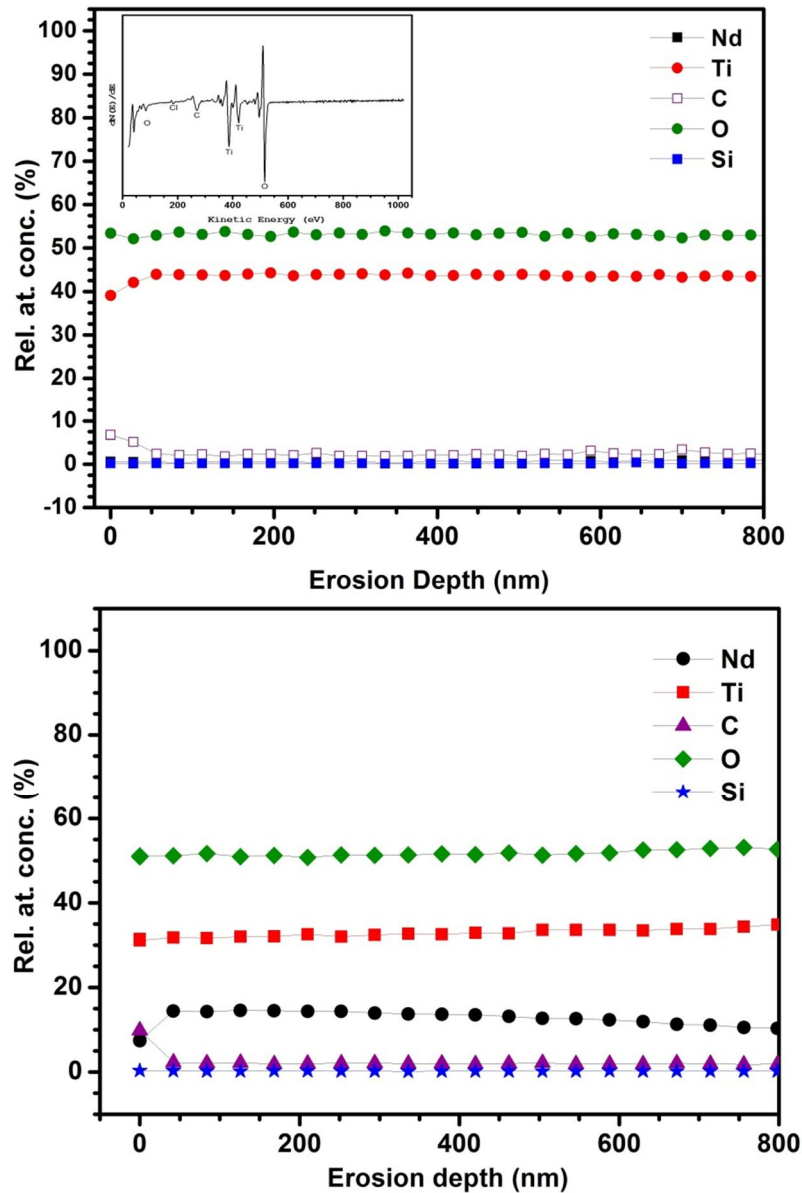
Figure 3.5: *AES depth profiles, acquired on (upper panel) sample S2 and (lower panel) sample S4. Inset is a typical large scan Auger survey spectrum, showing the differential peaks relative to the Auger transitions of the different elements.*

Apart from the surface carbon contaminant, the average relative atomic concentrations of neodymium, titanium and oxygen for all the samples were determined. They are summarized in Table 3.2. with Nd/Ti and O/(Nd+Ti), the relative atomic ratios for the pure and Nd-containing films.

Significant differences can be seen between the results obtained by AES and XPS, for the Nd/Ti ratio and in a more pronounced way for the O/(Nd+Ti) ratio. This is due to side-effects of ion bombardment used for profiling and the electron beam used for the analysis itself. In fact, AES analysis of multi-component material, when combined with energetic ion erosion (depth profile) is often affected by non-negligible effects related to both electron irradiation and ion bombardment. In 3d transition metal oxides likeTiO_2, the electron beam often induces stimulated oxygen desorption. The desorption process originates from the production of a core hole on the cation, followed by an inter-atomic Auger process and desorption of oxygen via the Coulomb explosion [6]. The loss of oxygen produces reduction phenomena of the surface oxide leading to a not negligible alteration of surface chemical composition and under-estimation of film stoichiometry. This electron beam induced oxide reduction results in changes in the line shape and peak position of the main Auger transitions of titanium, which impedes to obtain the description of the actual surface composition of the films. Energetic ion bombardment, beside the removal of the atoms, is also responsible for changes in the surface composition and morphology, creating an altered layer whose composition can be different from the volume beneath: oxygen preferential sputtering, leading to titanium surface enrichment, preferential sputtering effect on Ti and Nd yield too.
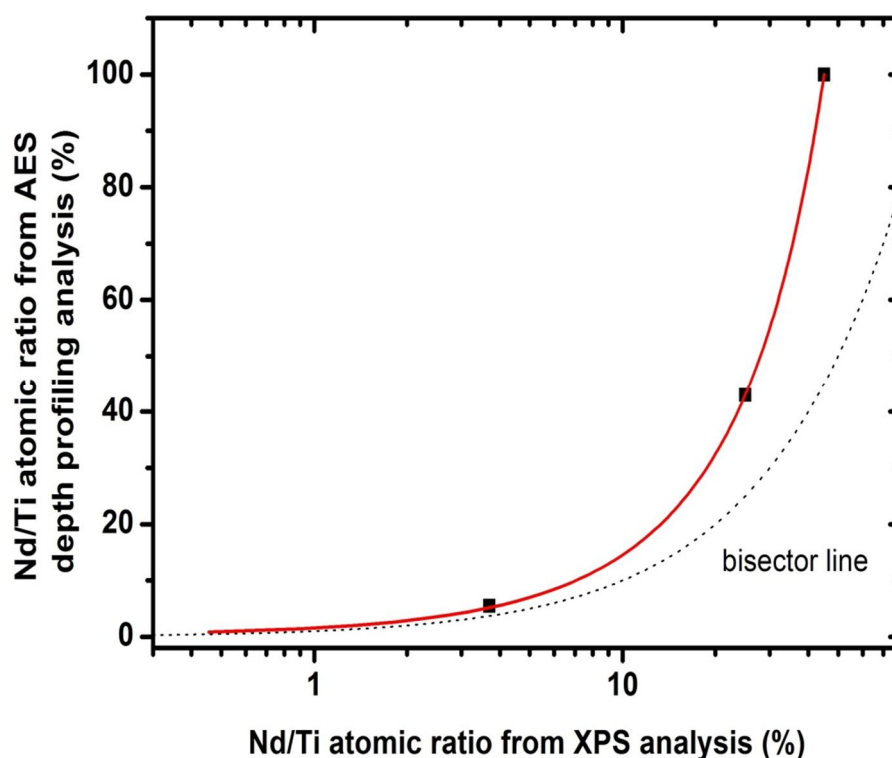
Figure 3.6: *Semi-logarthmic scale plot of Nd/Ti atomic ratio from AES versus Nd/Ti from XPS and of the bisector line.*

The differences between the XPS and AES results are well illustrated in Fig. 3.6, where the Nd/Ti ratio is plotted as AES values versus XPS values. The greatest deviation between the two kinds of results can be observed for the highest Nd concentrations. A bisector line is also drawn, on a semi-logarithmic scale to better estimate the departure of the AES results from the XPS ones. We can see that for the samples with Nd/Ti ratio ≤ ~4 at.%, the differences are much weaker. This coincides with the fact that for such low contents, Nd is more likely incorporated in titania lattice, while when a distinct phase of neodymium oxide is favored to form, the differential sputtering effect on Nd and Ti involved in their oxides becomes more important. No such great effect seems to operate when Nd is on the titania lattice sites. So, for low Nd contents, we expect a good correspondence between AES and

XPS analyses results.

An attempt have also been made in order to investigate the valence state of Nd in the films with high Nd concentration using AES, by analyzing the MNN transitions line shape and comparing them with that of neodymium and neodymium oxide. Unfortunately the difference between the MNN transition line shapes of Nd element (Nd^0) and in Nd_2O_3 (Nd^{3+}) found in (very scarce) literature are not significant and cannot constitute a precise mean to define the valence state of neodymium by AES.

3.5 QUANTIFICATION OF LOW NEODYMIUM CONTENT FROM XRF

The quantification of Nd doped TiO_2 sample (S2) was carried out by X- ray fluorescence. $TiK\alpha$ (KL_2 and KL_3 transitions) and $NdL\beta$ (L_1M_3 and L_2M_4 transitions) intensities were extracted by peak fitting with IAEA WinQXAS software [33, 34].

In order to make the XRF a semi-quantitative analysis, a calibration curve as constructed on the basis of Nd concentrations obtained by AES measurements performed on samples S3-S5 was used. Figure 3.7(a) shows the X-ray fluorescence spectra measured for sample S2 deposited on quartz substrate. The $NdL\beta$-to-$TiK\alpha$ counts ratio was plotted against the AES determined weight fractions in Figure 3.7(b). An exponential fit of the curve could be done, following the equation reported in the plot, from which an Nd/Ti atomic ratio could be derived for sample S2. The Nd/Ti atomic ratio, equal to 0.9 at.%, is reported in Table 3.2.

It is also important to note that a calibration of the XRF data against Nd/Ti XPS results gave a Nd/Ti ratio in sample S2 of 1.1 at.%, so close to the value given above.
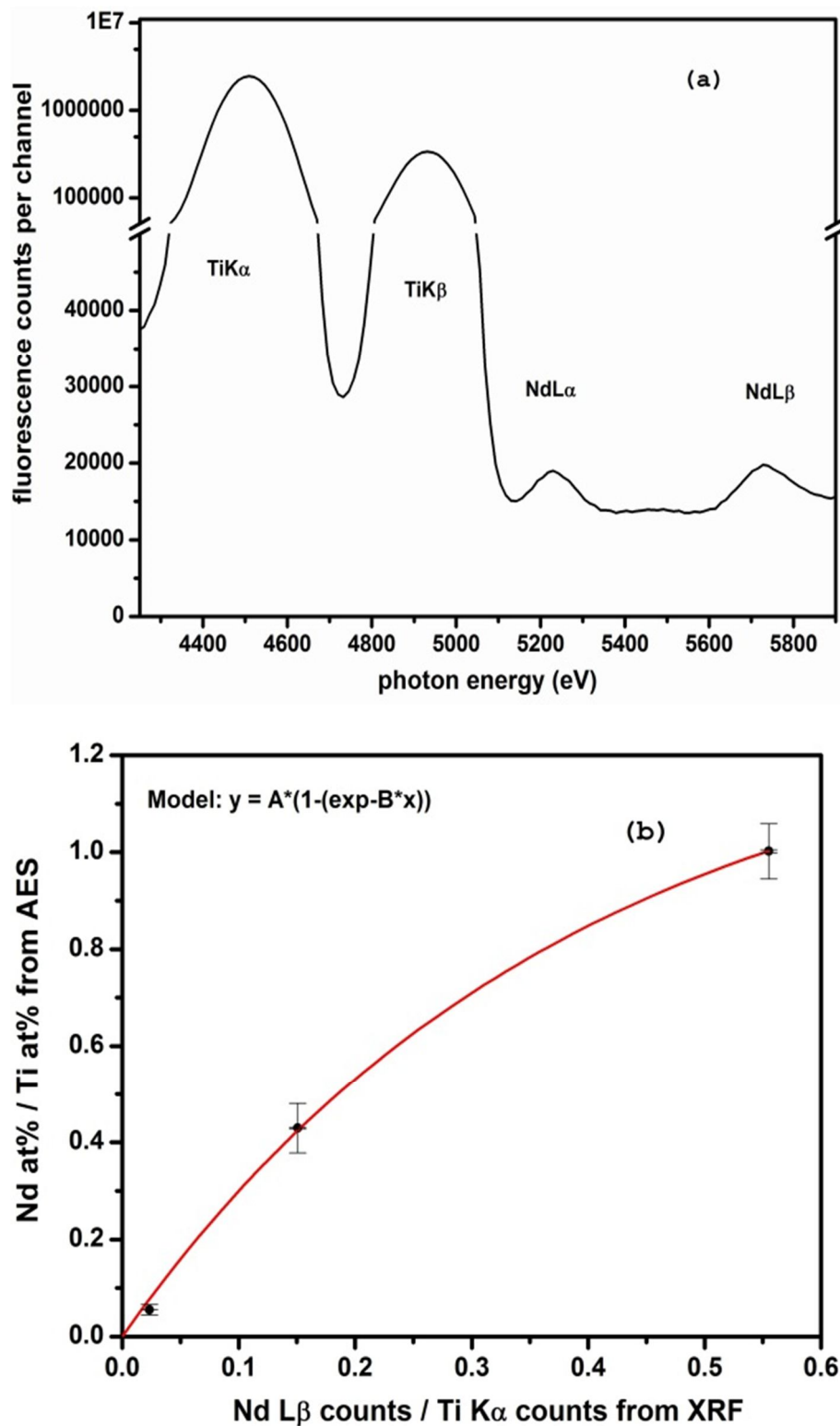
Figure 3.7: *X-ray fluorescence spectra for sample S2 grown on quartz substrate and (b) XRF calibration curve with Nd concentrations obtained by AES*

3.6 FILM STRUCTURE FROM XRD ANALYSIS

The as-grown titania films were amorphous, as indicated by the XRD analysis: no diffraction peak was observed. Figure 3.8 shows the XRD spectra obtained for undoped titania and for films with various amounts of neodymium grown on quartz substrates, after annealing at 600°C in ambient air atmosphere. As clearly seen from the XRD measurements, the neodymium doping induced remarkable modification in the structural properties of the films. Pure titania thin film exhibits a crystalline structure corresponding to an anatase structure, (ICDD card # 21-1272), indicated as "A". In addition to the main peak A(101) located at 2θ=25.36°, the peaks associated to the (103), (004) and (200) crystallographic planes were observed as well, although of very weak intensity. The strongest intensity of the (101) diffraction peak indicates a preferred oriented anatase polycrystalline structure. A very low incorporation of neodymium into the titania lattice produced dramatic changes in the crystallographic structure of the films. The XRD pattern of the film S2, deposited with Nd/Ti in an atomic ratio of 0.9%, exhibits both anatase and rutile structures, the latter indicated as "R". The figure also reveals that the peaks slightly broaden, indicating a deterioration of the crystallinity of the titania film. Much higher concentration of Nd (samples S3 and S4) produced a further intensity reduction and an increase of the FWHM of the peaks. The anatase and rutile relative amount changed remarkably with the Nd concentration: the intensity ratio between the A(101) and R(110) peaks varies from 1.27 for the 0.9 at.% of *Nd/Ti* ratio (sample S2) to 2.27 for the film with S3 (3.7 at.% *Nd/Ti*.

The R(110) peak at 2θ= 27.4° for the film with *Nd/Ti*= 25% (sample S4) becomes nearly indistinguishable, only the A(101) peak remains, although with a very low signal-to-noise ratio. For the highest concentration of Nd (sample S5), no A(101) or

R(110) signal was detected, the film appears more likely as an amorphous phase.

Additional peaks corresponding to Nd metal clusters or other mixed dopant oxides were not revealed by XRD analysis. The result shows that neodymium incorporation leads to the phase transformations (A → A+R) and also hinders crystal growth at higher dopant concentrations. Beside the peak broadening (FWHM=0.567°), the A(101) peak position shows a positive shift of 0.07° with respect to that for bulk Anatase (ICDD card # 21-1272 - shown as a vertical line in the figure 3.8), which increases with increasing the *Nd/Ti* atomic ratio from 0.9% to 25% (samples S2 to S4), indicating the creation of an internal strain induced by Nd incorporation in the TiO_2 matrix.

A Williamson-Hall plot, following equation (2.2) in Chapter 2 was applied for the (101) peak and other peaks of much lower intensity of anatase corresponding to A(103), A(004) and A(200) to determine the average crystallite size <D> and the strain (η). The (101) and (200) anatase reflections were used to calculate the lattice parameters using equation (2.3) in Chapter 2.
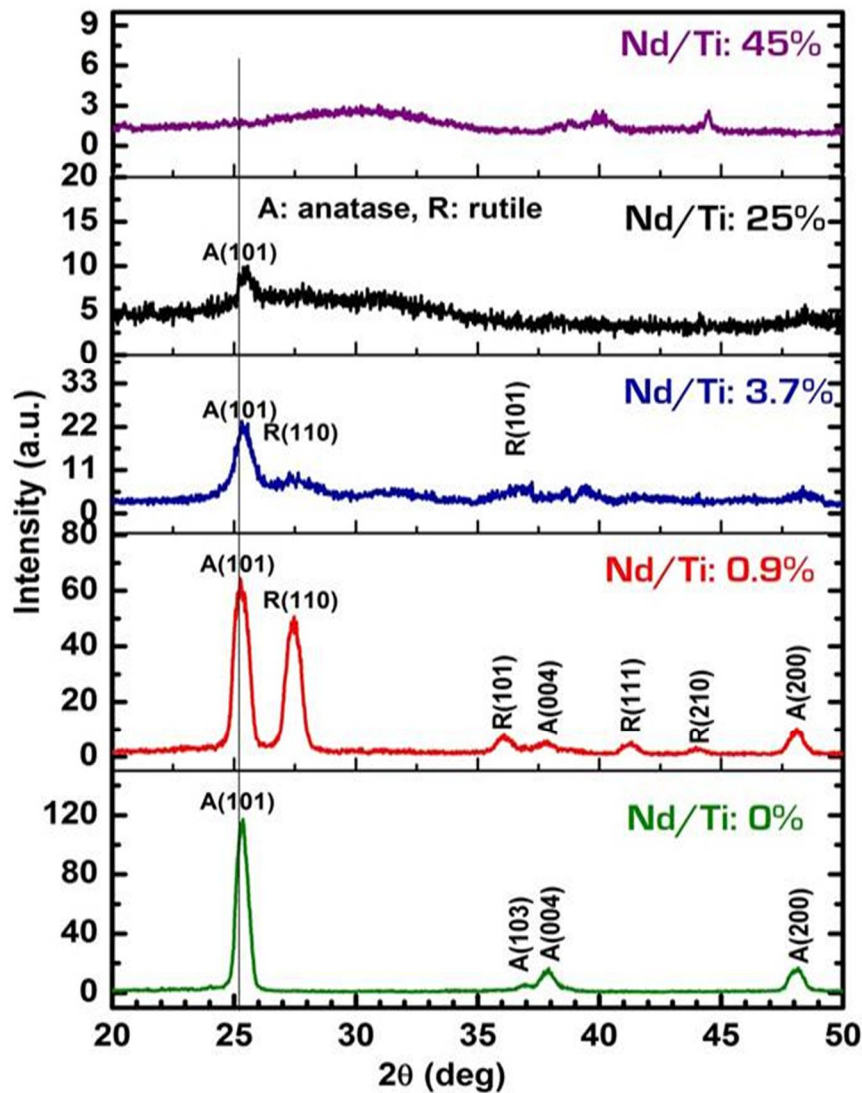
Figure 3.8: *X-ray diffraction (XRD) patterns of Pure and Nd doped TiO₂ samples grown on quartz substrates annealed at 600°C as a function of different neodymium concentrations. The vertical line represents the 2θ value for bulk anatase (ICDD card 21-1272). The XPS value of Nd/Ti ratio is given for each sample.*

Figure 3.9 shows the dependence of the calculated lattice parameters ("a" and "c") for anatase phase when varying the Nd concentration, along with their ratio c/a, the cell volume (V), <D> and η. A small amount of Nd changed significantly the "c" and "a" parameters. "c" abruptly increased and "a" decreased when Nd was introduced in a ratio of 0.9% to Ti. The maximum elongation of 'c' with respect to the value for un-doped film was about 0.22Å from 9.438Å (for 0% Nd) to 9.661Å (for Nd/Ti of 0.9at.%).
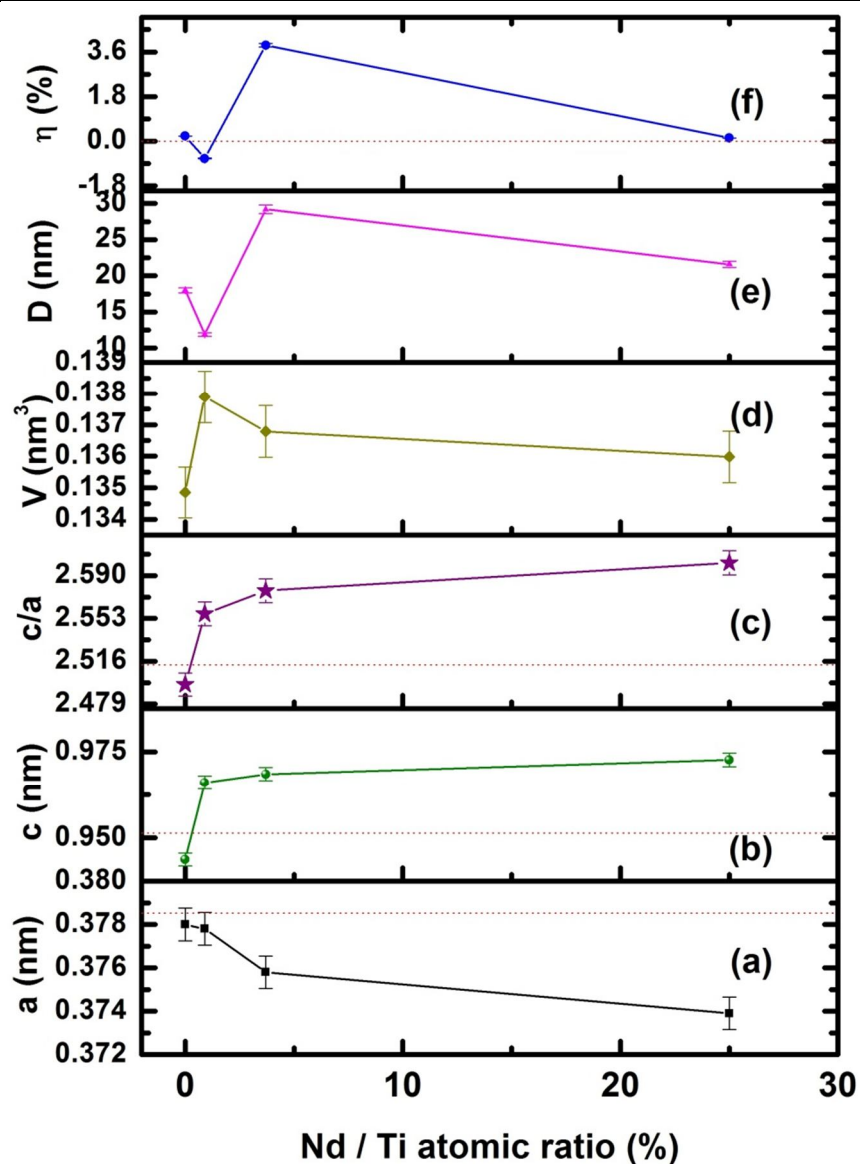
Figure 3.9: *Lattice parameters a (plot a), c (plot b) and c/a (plot c), cell volume V (plot (d), average crystallite size <D> (plot e) and internal strain η (plot f) for anatase with various Nd- doping levels (the dashed line indicates a, c, and c/a values for bulk anatase, from standard ICDD card (# 21-1272). The dotted line in plot (f) signs the zero-strain level).*

For further Nd addition, parameter "c" keeps slightly increasing and parameter "a" decreasing. Neodymium doping induced lattice distortion in titania, also evidenced by the increase of c/a ratio in plot (c) of Figure 3.9. Due to the large difference of the ionic radii between the dopant (Nd: 0.983Å) and the host Ti ions (Ti^{4+}:0.68 Å), the

113

strong lattice expansion along 'c' axis observed at lower Nd concentration indicates Nd enters the TiO_2 lattice substitutionally.

When the neodymium concentration increases, the lattice distortion, reflected in the c/a value, did not further noticeably increase suggesting that (i) Nd might segregate at the grain boundaries without further substitution of Ti^{4+} ions and or (ii) to accommodate an increase of substituted sites in TiO_2 lattice, new defects might be created around the Nd ions. The latter hypothesis is rather corroborated by the evolution of the cell volume, which was maximum for the film with a Nd/Ti of 0.9%, concomitantly with a compressive residual strain in the film, while for the more Nd - rich films, the cell volume tends to decrease as if the excess volume brought by Nd was compensated by a O or Ti vacancies.

The shifts in the 2θ values corresponding to the maximum intensity of the A(101) peak are well reflected in the variation of the residual strain with the Nd concentration plotted in Fig. 3.9 (plot f). The films S1, S3 and S4 exhibited a tensile strain, while S2 a compressive one. This also correlates with the variation of the cell volume of the anatase phase of the films, as shown in Fig.3.9-plot d. The higher cell volume value was for sample S2 and this can explain the occurrence of a compressive strain in the film. It should be kept in mind that many factors can contribute to the stress building in the sputter-deposited films: the film structure induced by the growth conditions (temperature, ion bombardment) and cell parameter mismatch between film and substrate generates an intrinsic stress while a thermal expansion coefficient mismatch in the film/substrate system leads to an extrinsic stress. The TiO_2 films grown onto silicon had a columnar structure (observed by scanning electron microscopy) [7]. Such structure is generally known to generate a tensile stress [8] The change of the final strain (stress) from tensile – to – compressive – to – tensile with increasing the

Nd concentration (observed in Fig. 3.9 (plot f), which is also correlated with the change of the anatase cell volume, can be a valuable indication of the effective incorporation of Nd in the anatase cell. On the other hand, the sign and intensity of the residual strain in the films influenced the grain growth. The larger the crystallite size, the higher the tensile strain. A compressive strain gave rise to the smallest crystallites. Moreover, in the films strained in tension (for pure TiO_2 and for Nd/Ti= 3.7 and 25%), rutile phase formation seems to be hindered (Figure 3.8), while the presence of compressive strain favored the anatase-to-rutile transformation (film S2 in Fig. 3.8 with $Nd/Ti = 0.9$ at.%).

3.7 Nd-EFFECT ON THE VIBRATIONAL PROPERTIES OF TITANIA FILMS: RAMAN SPECTROSCOPY STUDY

3.7.1 Assignment of Raman Bands

Raman spectroscopy, a light scattering process which can be used to obtain valuable information about the structural (such as crystalline phase transformations, lattice distortions), the doping induced stress/strain states, oxygen defects and molecular properties from their vibrational transitions. Detailed vibrational studies were carried out using Raman spectroscopic technique for understanding the effect of Nd incorporation on the structure of titania. Indeed, anatase phase has a body centered tetragonal structure with a space group of $I4_1/amd$ containing twelve atoms per unit cell. According to factor group analysis, anatase phase of titania has six Raman active modes: $A_{1g} + 2B_{1g} + 3E_g$, three infra-red active modes: $A_{2u} + 2E_u$ and one vibration mode B_{2u} which is silent.

Peak positions (cm^{-1}) [Present work] S1-PureTiO$_2$ - Anatase	Assignments	Peak positions from literature (cm^{-1}) Ohsaka et. al [1978] [9]
142.7	E_g	144
197.5	E_g	197
395.5	B_{1g}	399
516.2	A_{1g}, B_{1g}	519
639.2	E_g	639

Table 3.3: *Observed Raman peaks assignments of pure TiO$_2$ thin films grown on quartz substrates and annealed at 600°C*

Ohsaka 1978 [9] determined the following allowed Raman modes as well as their symmetry for a single crystal for anatase: 144, 197, 399, 513, 519 and 639 cm^{-1}. Rutile phase is tetragonal too, with two TiO$_2$ molecules per primitive cell with the space group of *P4$_2$/mnm*. Rutile has four Raman active modes: A_{1g} + B_{1g} + B_{2g} + E_g which appears at 143 (B_{1g}), 447 (E_g), 612 (A_{1g}) and 826cm^{-1} (B_{2g}). The vibrational modes of 447cm^{-1} (E_g) and 612cm^{-1} (A_{1g}) are considered as the characteristic peak of rutile TiO$_2$.

Figure 3.10 displays the Raman spectra of Pure and Nd doped TiO$_2$ samples grown on quartz substrates annealed at 600°C as a function of different neodymium concentrations with excitation line at 514.5 nm. The Raman spectra were deconvoluted into individual peaks; they clearly show that the effect of different Nd/Ti atomic ratio influences the titania phase transition. All the peaks were fitted with Gaussian-Lorenzian procedure in order to determine the contribution of two titania phases in each spectrum.
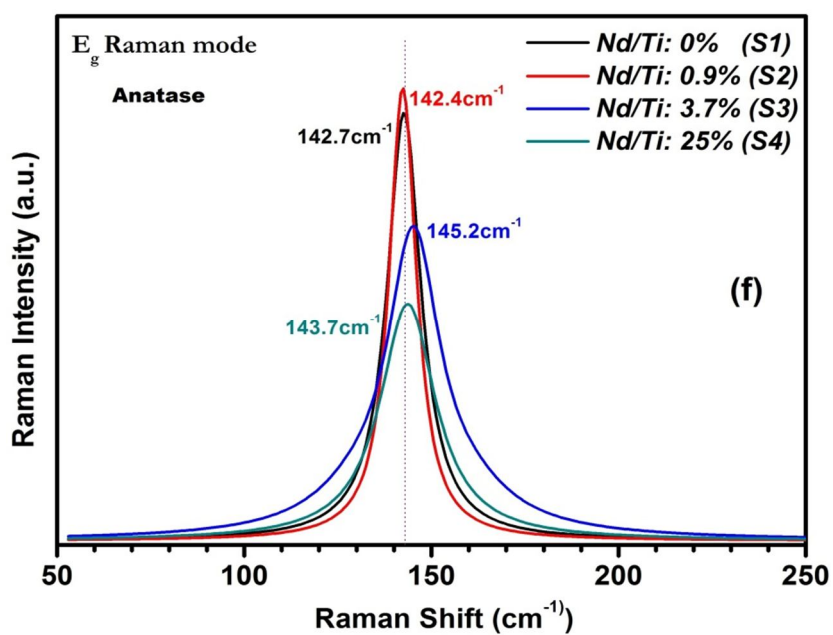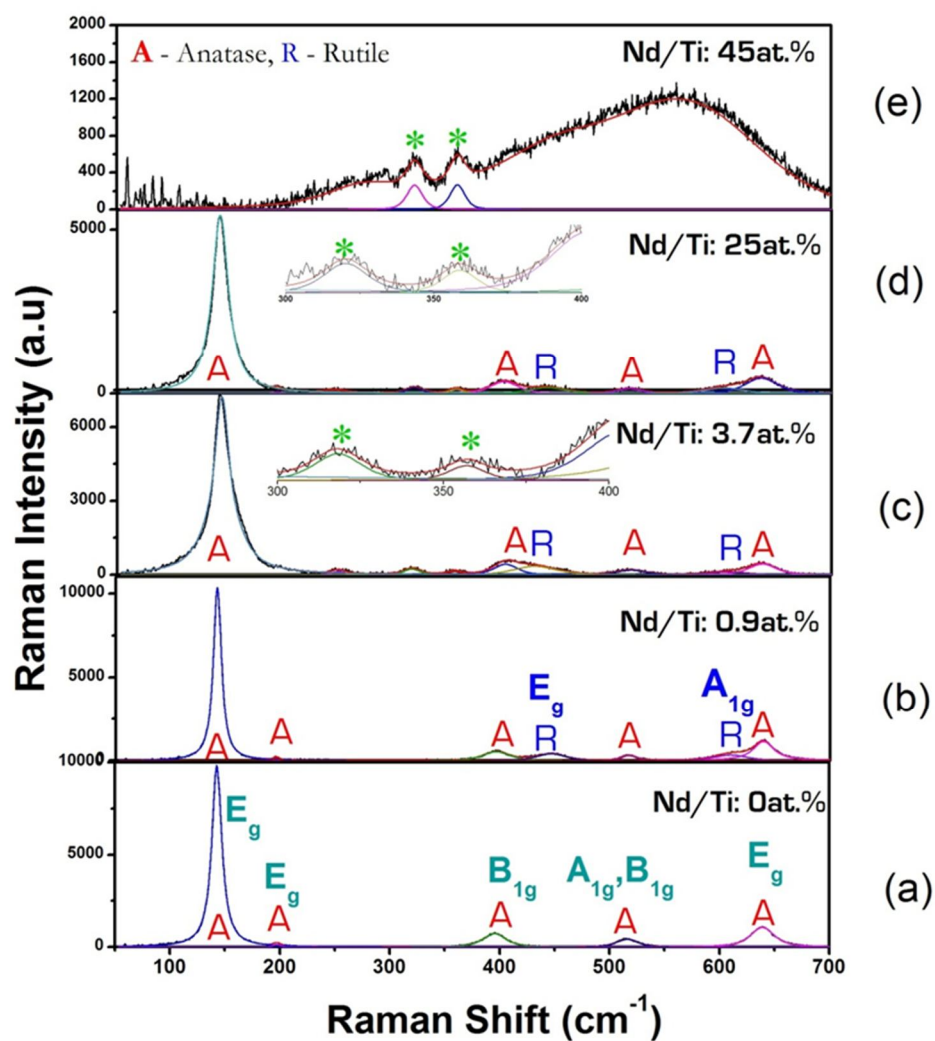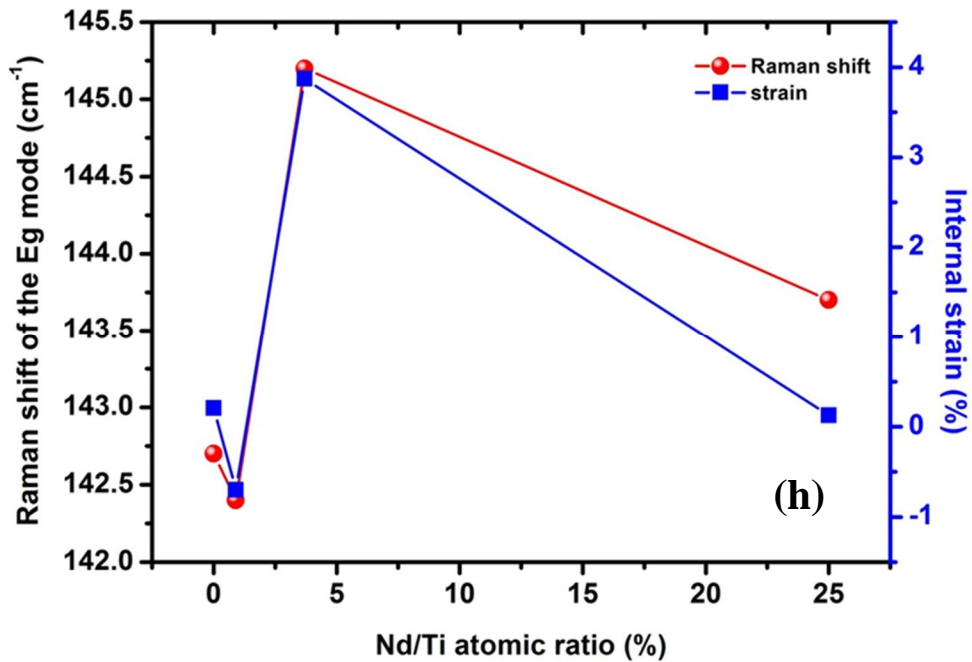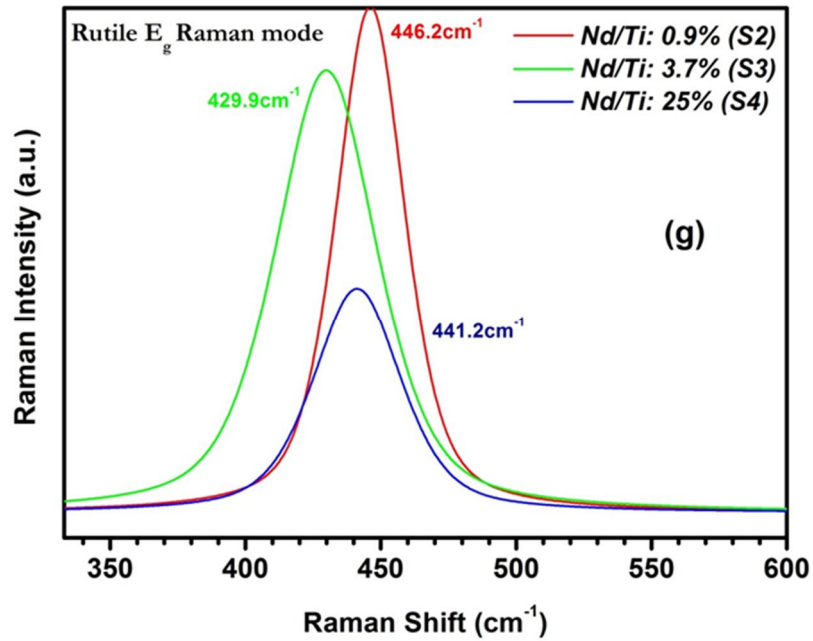
Figure 3.10: *Raman shift spectra of TiO$_2$ films with (a) 0at.%, (b) 0.9at.%, (c) 3.7at.%, (d) 25at.% and (e) 45at.% of Nd/Ti atomic ratio as calculated from XPS. The Raman modes marked in the figure are explained in the text. The figure also shows the peak shift in anatase (f) and rutile (g) of (E$_g$) Raman vibrational modes explicitly, and (h) Raman shift of the Eg mode of anatase and internal strain deduced from XRD analysis, in function of Nd/Ti ratio.*

3.7.2 Raman study of the Nd effect on phase structure of TiO_2 thin films

Pure Titania (S1) exhibits the characteristic Raman fingerprint vibrational modes of anatase phase (142.7, 197.5, 395.5, 516.2 and 639.2 cm^{-1}) and these results are consistent with XRD analysis. The strongest E_g (142.7) mode is the most characteristic peak of anatase phase; it corresponds to the stretching vibration of Ti-O bonds in the plane of Ti-O-Ti-O of the elementary cell. This mode is very sensitive to any disorder in the local oxygen sub- lattice resulting from the thermal and or grain size induced non-stoichiometry. The B_{1g} (395.5) band is originated by symmetric bending vibration of O-Ti-O and the A_{1g} mode (516.2) is associated to anti-symmetric bending vibration of O-Ti-O bond [10]. A very low incorporation of neodymium (Nd/Ti at. ratio= 0.9%), into the titania lattice produced remarkable changes in the crystallographic structure of the films. The appearance of two broad bands of rutile phase is observed at 446.2 and 609.5 cm^{-1} (spectrum b) which are attributed to the E_g and A_{1g} vibrational modes of titania. These findings clearly show a partial phase transformation of anatase to rutile phase in TiO_2. When Nd content is varied from 3.7 to 45% of Nd/Ti at.ratio (spectra c to e), an abrupt change in the structure was observed. From the figure 3.10 (f), it is clear that there is a deterioration of crystalline quality of the films, (revealed by the intensity quenching of the E_g mode of anatase), a shift in the peak position to the lower and higher wavenumbers. Besides the characteristic bands of anatase and rutile, very weak bands are also visible for the films S3 (318.2, 357.1 cm^{-1}); S4 (320.3, 358.8 cm^{-1}) and S5 (320.9, 359.9 cm^{-1}) which is marked as "*" in Figure 3.10(c-e), where the corresponding bands were magnified for clarity. A complex broad band at 248.6cm^{-1} was observed for the sample S4 (25 at.% of Nd/Ti), it can be arising from the two phonon scattering and indicating a high

level of anharmonicity (disordered induced) in the rutile phase[11] . As there is a shift in the peak position of the above mentioned corresponding bands, there is a controversy in assigning the weak broad bands as observed for the films S3, S4 and S5. Maria *et al* [12] proposed that these bands (at 322 and 363cm^{-1}) have been associated with defects in the TiO_2 nanocrystalline phase. Jing et al. [13] and Tompsett at al. [11] assigned that the band at 320 cm^{-1} to a weak two-phonon scattering band occurs in the anatase phase and a first overtone of B_{1g} at 395.5 cm^{-1}. Additionally, some of the authors Golubovic *et al.* [14], Yi Hu *et al.* [15] and Paola *et al.* [16] reported that the Raman modes at 320 and 362 cm^{-1} ascribed to the evolution of brookite phase of titania. In the films with higher doping concentration, broadband peak with very low intensities of these modes indicates great disorder and partial amorphization of brookite phase. Even if XPS analysis results indicate the formation of neodymium oxide, no peaks due to Nd_2O_3 were observed in the range 107-436 cm^{-1} where stretching and bending modes are expected. However the corresponding wavelength numbers would overlap with the anatase ones [17, 18] and thus difficult to detect. Figure 3.10 (f and g) also shows the wavenumber shift of Raman band for anatase (E_g) and rutile (E_g) mode separately respectively, as it came from the fit of the acquired spectra. Increase in the Nd concentration (from Nd/Ti ratio 0.9 to 25 at.%) reveals a noticeable wavenumber shift (for E_g anatase) and also the peak broadening in comparison with pure titania. The peak broadening of the E_g mode might be due to the nonstoichiometry induced by either oxygen deficiency or substitution of Nd in the titania host lattice [19]. A shift towards higher wavenumbers of the peak energy is observed for the higher doping concentration varied from Nd/Ti at.ratio 3.7 to 25% along with the remarkable drop in the Raman intensity. On the other hand, for the low doping concentration ratio (0.9% of Nd/Ti at.ratio), the E_g mode shows a slight shift

to lower wavenumbers suggesting the relaxation of Ti-O bond. This shift is also in accordance with those of shift in the 2theta peak positions analysed by XRD. These changes in the Raman band position can be ascribed to the structural disorder resulting from the introduction of oxygen vacancies and dopant ions [20]. Finally, the full width at half maximum (FWHM) of the Eg of both the anatase and rutile peaks varies abruptly. The maximum broadening is observed for the film with 3.7% Nd/Ti at.ratio. Taking into consideration of large difference in the ionic radii between Nd^{3+} ions (0.983A) and Ti^{4+} (0.605A), it is known that Nd atoms cannot easily enter into the lattice sites of titania and also Nd^{3+} induces lattice strain in the titania lattice, which may hinders the growth of TiO_2 crystallites.

There are several factors that can influence the Raman shift of the E_g mode, namely, phonon confinement, temperature, defects and the strain induced to the lattice distortion in TiO_2 lattice. In this case, the shift due to phonon confinement can be neglected as the average crystallite dimension is more than 20 nm. As reported by Sahoo et al.[21], defects in the nanostructure can also cause the shifts of the Raman peaks and significant broadening of Raman line shape. We can also anticipate that for higher doping concentrations defects to cause the shifting of Raman peak position (for 3.7 and 25 at.% Nd/Ti ratio), as there is a significant change in the FWHM with the change in the peak position. In Fig. 3.10 (h) the Raman shift of the Eg mode of anatase is plotted together with the internal strain determined from XRD analysis, in function of Nd/Ti ratio. A clear correlation can be observed between the two parameters. As well-known, the Raman shift variation is related to the bi-axial strain. The evolution of the E_g mode frequency observed in figure 3.10 (h) means an opposite trend of this bi-axial strain determined by XRD. The latter is linked to the normal stress, i.e., the one in the film growth direction. The bi-axial strain is build due

to a difference between the thermal expansion coefficient of the films which underwent thermal annealing.

3.8 Nd EFFECT ON SURFACE MORPHOLOGY

Figure 3.11 shows the three dimensional atomic force microscopy images (scan area: 4µm x 4µm) obtained in contact mode for the neodymium -doped TiO_2 thin films grown on quartz substrates after annealing at 600°C.
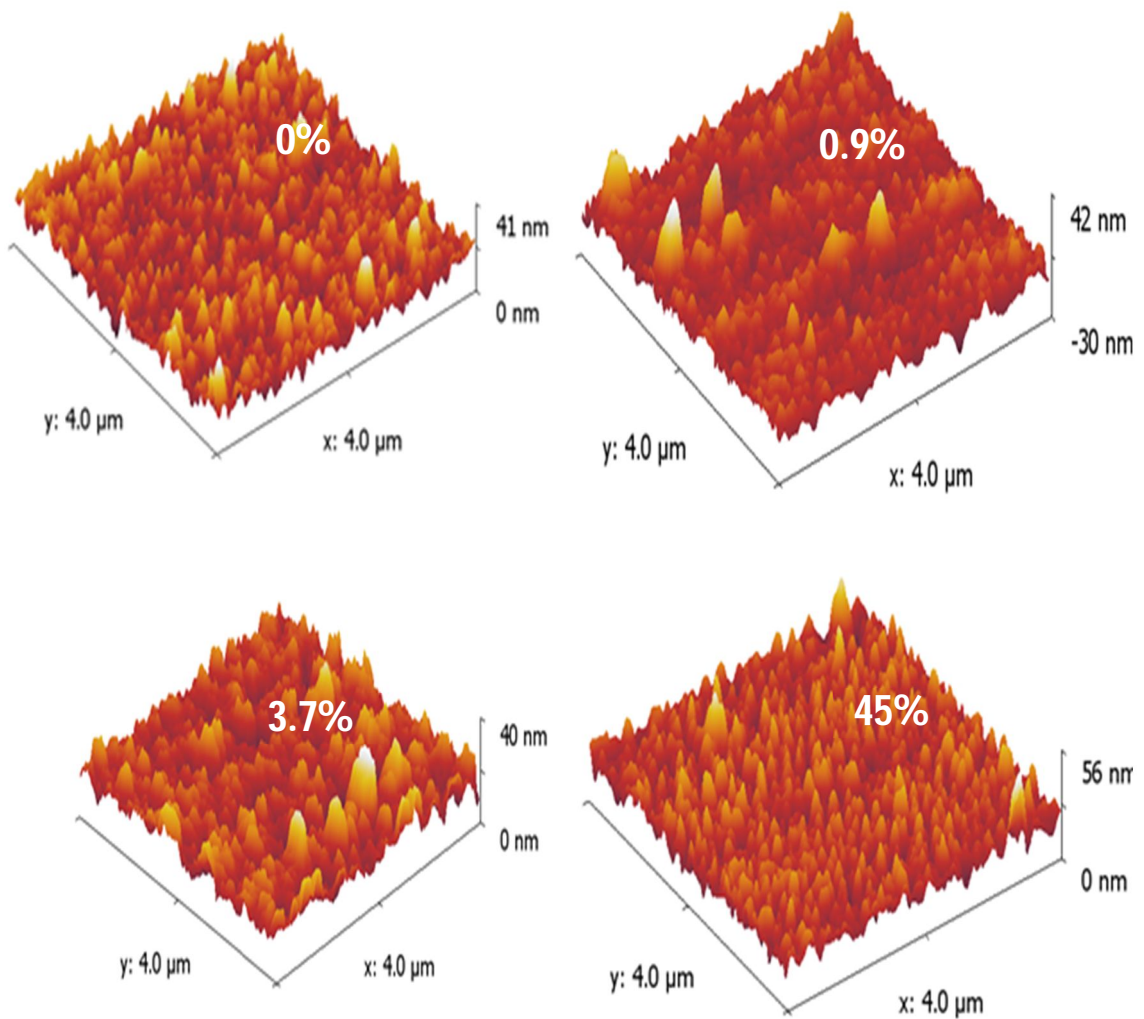
Figure 3.11: *Three dimensional AFM Images of Undoped (0%), and doped TiO_2 with Nd/Ti ratio of 0.9%, 3.7% and 45% on quartz substrates.*

Samples	Column diameter dimension (nm)	RMS (nm)
S1	223 ± 18	3.97
S2	153 ± 29	4.22
S3	322 ± 43	4.07
S5	164 ± 40	4.99

Table 3.4: *RMS values and column diameter dimensions as measured by AFM on the S1, S2, S3 and S5 films deposited on quartz substrates.*

The surface roughness and also the grain size of the pure and Nd- doped TiO_2 were measured. All the films result in the apparent generation of small amount of porosity (<10%) with the grains of uniform distribution. The tower-like grains can be related to the columnar-growth nanostructure of the layer. Based on these images, the analyzed average dimension of columns and the surface roughness (given as RMS – root mean square value) were depicted in the Table 3.4. The average roughness value of pure TiO_2 was found to be 3.97 nm while samples of neodymium incorporated TiO_2 showed a roughness between 4 and 5 nm.

The average value of column diameter reaches its maximum crystallite dimension in the case of 3.7% *Nd/Ti* ratio, with a dimension of 322 ± 43 nm, while the other films showed a column diameter dimension between 150 nm and 235 nm. The columns dimension is related to the crystallite size as calculated by XRD. The bigger the crystallite size, the larger the columnar head dimension. The dimension of the crystallites depends on *Nd/Ti* concentration. The maximum dimension of crystallite, as for columnar head, is reached with a concentration of *Nd/Ti* of 3.7%.

3.9 Nd EFFECT ON OPTICAL PROPERTIES FROM TRANSMITTANCE AND REFLECTANCE MEASUREMENTS

The optical analyses of the films deposited on quartz substrates and annealed at 600ºC were explored in order to study their optical bandgap. Pure TiO_2 exhibits a strong

absorption cut –off in the UV region around 370 nm which can be related to the band-gap absorption of titania. Figure 3.12(a, b, c) shows the absorbance, transmittance and reflectance spectra of the annealed films respectively. All the films were transparent with an optical transmittance of $\geqslant$ 70% in the visible region. The variation in transmittance and in the extrema number is related to the increase in the thickness of the film and the progressive incorporation of Nd into the films.
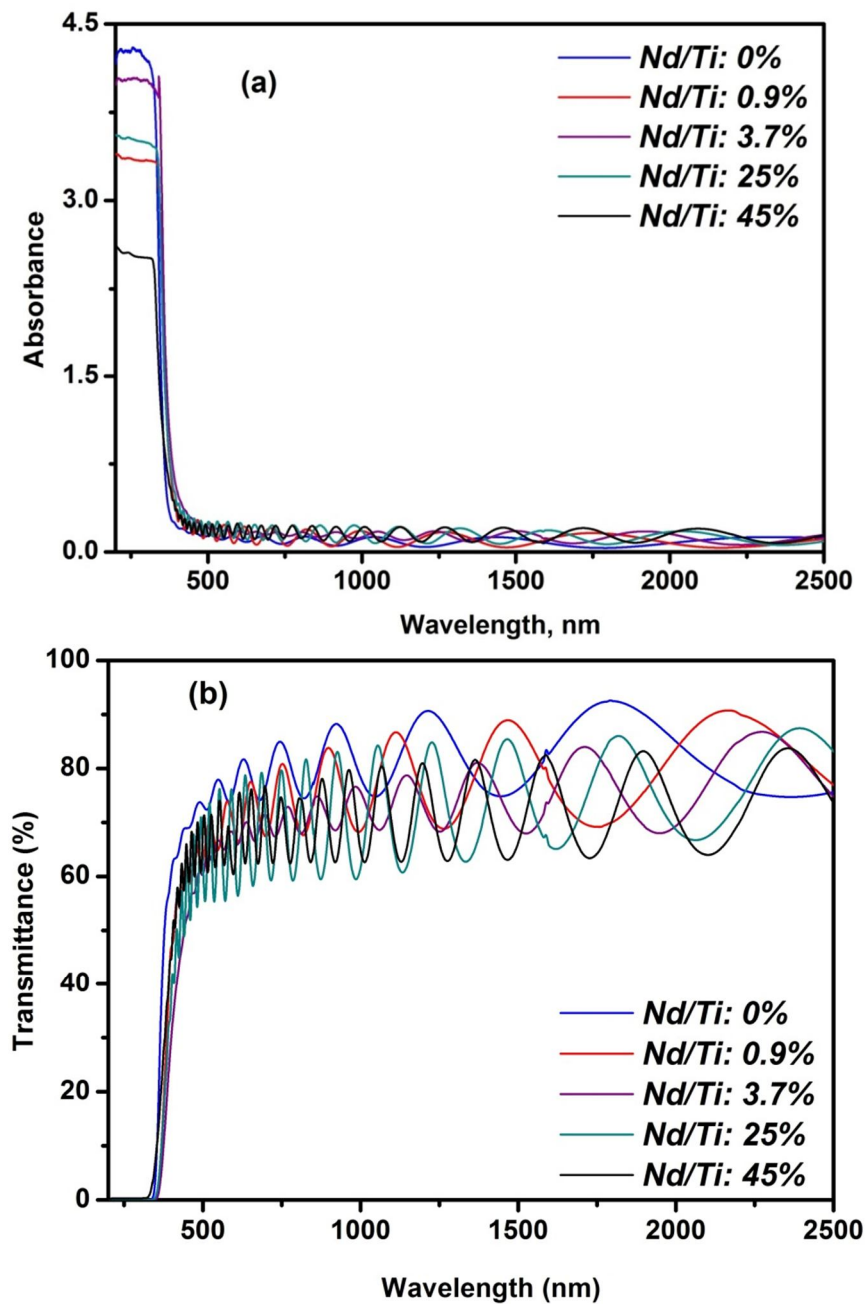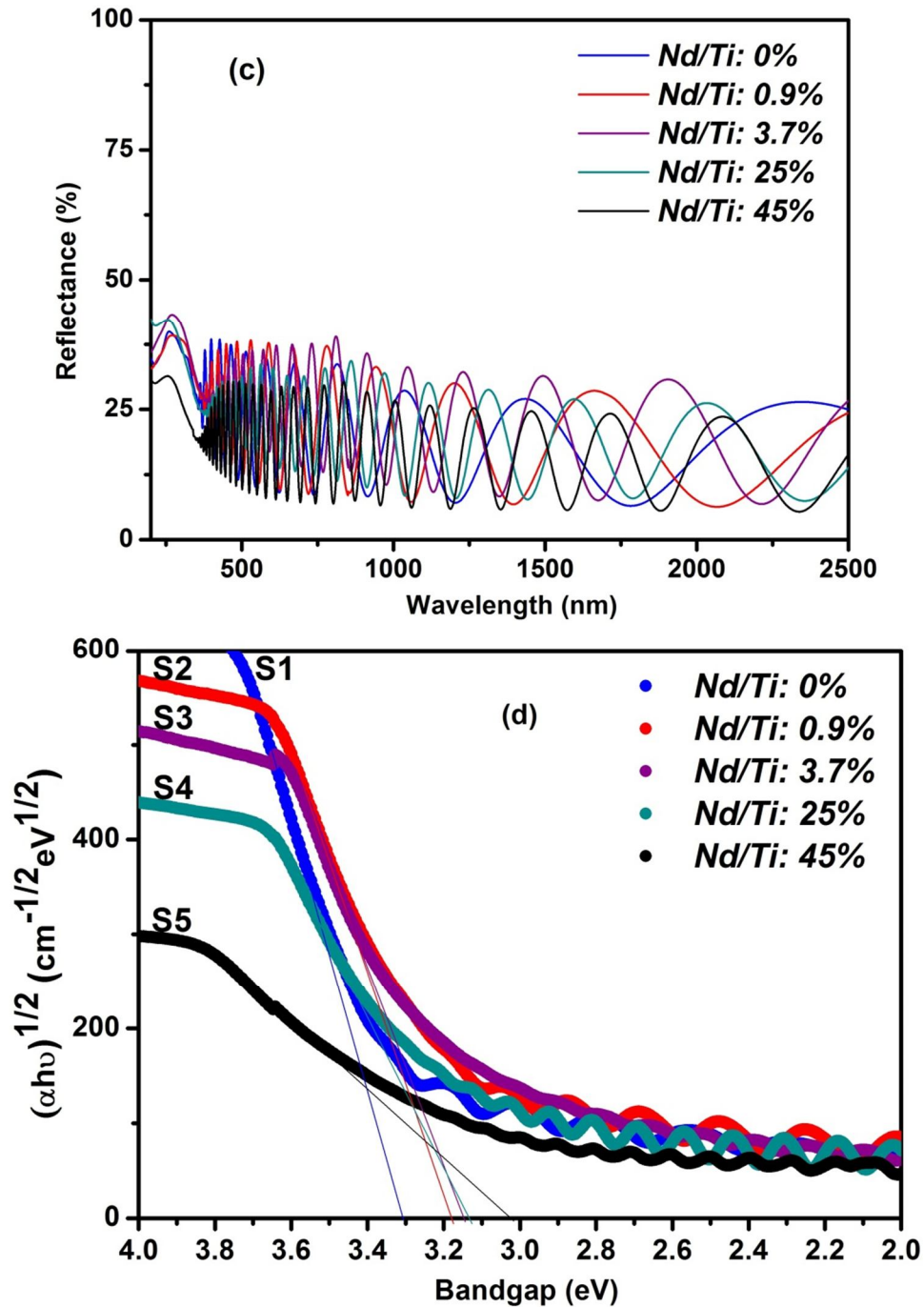
Figure 3.12: *UV –visible near IR spectra of Nd doped TiO₂ films on quartz substrates (a) Absorbance (b) Optical Transmittance (c) Reflectance and (d) bandgap plot of (αhν) ¹/² vs. photon energy (hν)*

With the increase in the dopant concentration, the absorption edge extended towards longer wavelengths. The Tauc's plot (following equation 2.7 of chapter 2, with m=2, corresponding to indirect gap), shown in figure 3.12(d) illustrates these red shifts as

Nd concentration in the matrix is increased. The optical band gap decreases from 3.3 to 3.02 eV as the Nd to Ti ratio increases from 0 to *Nd/Ti*= 45 %. This phenomenon is consistent with the works of Zhao et al. [22] and of Li et al. [23] which reported similar red-shifts of the band gap of TiO_2 nanoparticles induced by Nd^{3+} doping. Such bandgap narrowing was attributed to new unoccupied electron states into the gap below the conduction band edge due to the location of Nd ions in substitutional sites in the TiO_2 matrix.
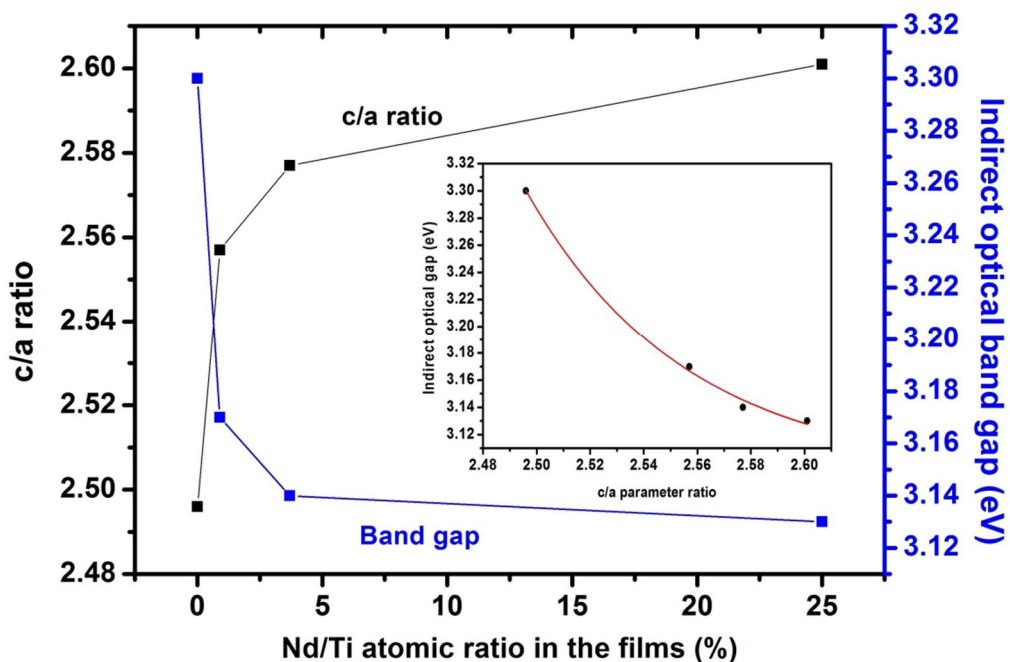
Figure 3.13: *Variation of the optical bandgap and the c/a parameter ratio in function of the Nd/Ti atomic ratio in the films.*

In fact, the reduction of the bandgap with increasing Nd incorporation in the films was found to correlate well with the lattice distortions reflected in the c/a parameter ratio, as shown in Figure 3.13, where both c/a and the gap are plotted in function of Nd/Ti in the films: the higher c/a, the lower the optical gap, as also illustrated in the inset. In turn the c/a parameter ratio is strongly determined by the "c" parameter value, as can be seen in Figure 3.9 (plot b), itself related to the Nd incorporation in the TiO_2 lattice.

3.10 Nd EFFECT ON THE NIR PHOTO-LUMINESCENCE PROPERTIES

Photoluminescence (PL) investigations of intra-configurational 4f emission from Nd ion in titania host were systematically studied by different excitation regimes: (1) direct excitation of the ion at different excitation wavelengths: green (514.5 nm), blue green (496 nm) and blue (476 nm) at constant power and (2) non resonant or indirect excitation in UV (355 nm). In a first step, we investigated the optical activity of the incorporated Nd in the host titania. Room temperature PL emission spectra were recorded for doped TiO_2 thin films doped with different concentrations of Nd at the excitation wavelength of 514.5 nm (2.41 eV) which is located in the non-absorbing region of the titania matrix (see Fig. 3.12 (a)). Strong near infra-red PL was observed pertaining to the transitions from the $^4F_{3/2}$ state to the $^4I_{9/2}$ (around 904 nm) and $^4I_{11/2}$ (around 1094 nm) states, respectively, as shown in figure 3.14(a). Whatever the excitation wavelength, no Nd related PL luminescence was observed in the as-deposited samples, but only in the annealed samples. Since the excitation wavelength in this case is below the bandgap, we conclude that the excitation is a direct from the ground state to one of the upper excited states around 514.5nm ($^4G_{7/2}$, $^4G_{9/2}$). Thereafter, the electrons decay back to the $^4F_{3/2}$ state, from which they relax down to the ^4I_J (J=9/2, 11/2, 13/2) states, with the emission of photons of characteristic wavelengths.
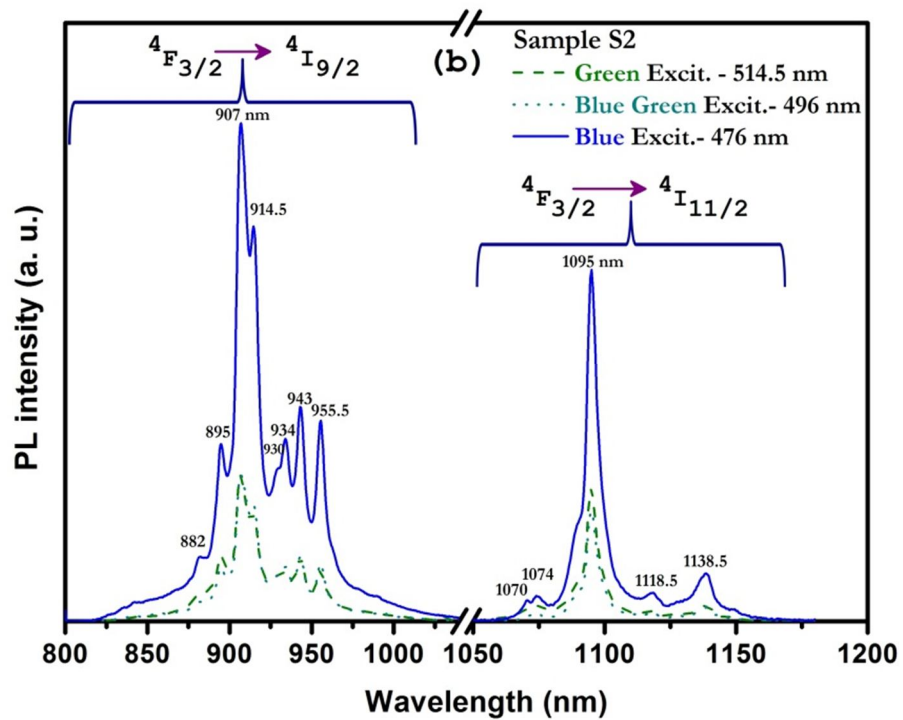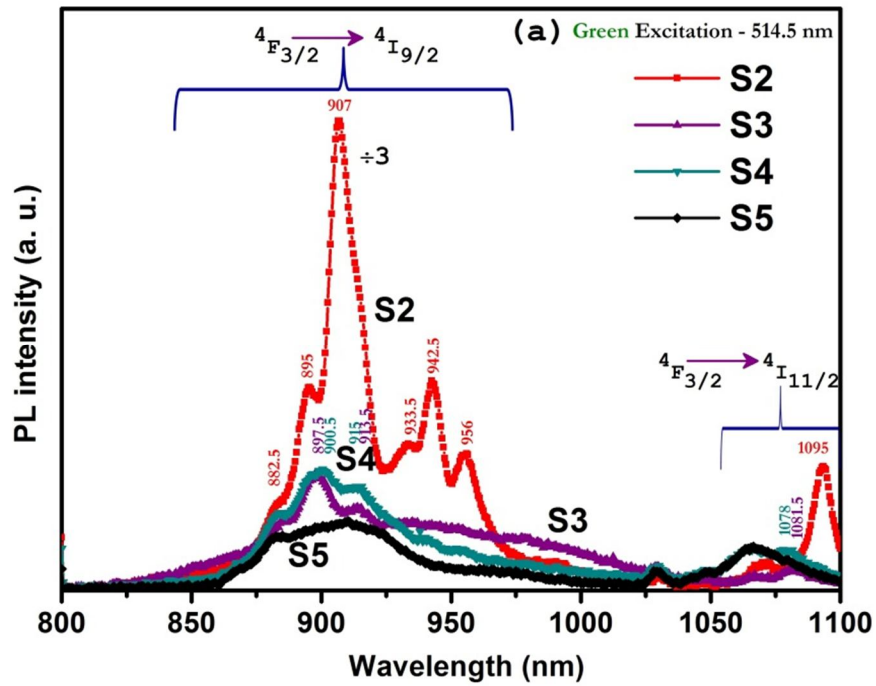
Figure 3.14: *Photoluminescence Spectra of Nd doped TiO₂ films on quartz substrates (a) Direct Excitation – laser Green line 514.5 nm for different concentrations and (b) Excitation –different laser wavelengths: 514.5, 496 and 476 nm for doped TiO₂ films with Nd/Ti= 0.9% (sample S2).*

For all the samples, the excitation power was 1.1 W, except for the film S2 with *Nd/Ti*= 0.9% for which a power of only 0.32 W was used. As the luminescence of the sample S2 was much stronger than for the other samples, the excitation power was reduced in order not to saturate the detectors (both the PMT and Si detector). The spectra of all the Nd-doped films are displayed in Figure 3.14(a) (spectrum for film S2 reduced by a factor 3) and can be compared. The spectrum was reduced because the signal intensity of the sample S2 was much higher than for the other samples. Actually even when the excitation power was reduced to 0.32 W the signal was still about three times stronger than for the other samples. In the series S3-S5, the PL intensity at ~ 900 nm decreases with the increase in the Nd concentration, this indicates that with the increase of Nd content, the quenching effect becomes important. In the same series, broad emission bands are observed. On the contrary, for the lowest Nd concentration (*Nd/Ti*= 0.9%, sample S2), the PL spectrum reveals the fine splitting effect. The $^4F_{3/2}$ to $^4I_{11/2}$ transition, at ~1094 nm is depressed in intensity due to the low response of the detector in this spectral region. Figure 3.14 (b) presents the PL spectra as a function of various excitation wavelengths at constant incident power (0.56 W) for sample S2. Neither shifting in the peak positions nor broadening was observed in the PL emission while the intensity of the emission peak gradually increases with the increase of the excitation energy. The PL intensity is much stronger for the excitation wavelength 476 nm (2.6 eV); while no great change was observed in the splitting of the emission line. Upon different excitation energy levels, eight PL lines in the $^4F_{3/2}$ to $^4I_{9/2}$ band and five PL lines in the region $^4F_{3/2}$ to $^4I_{11/2}$ were observed.
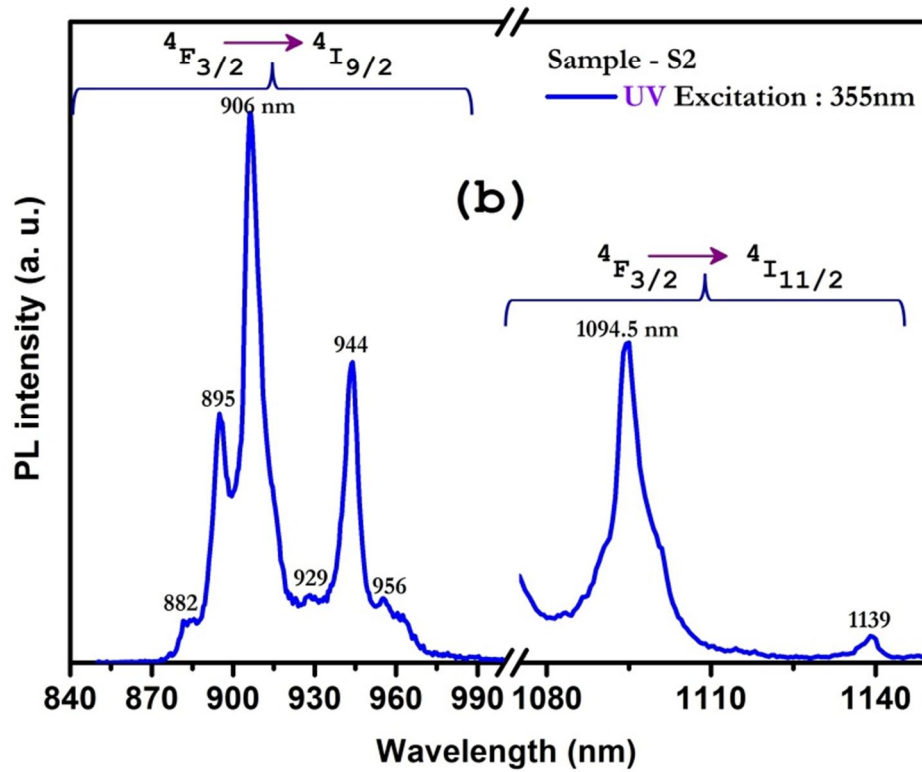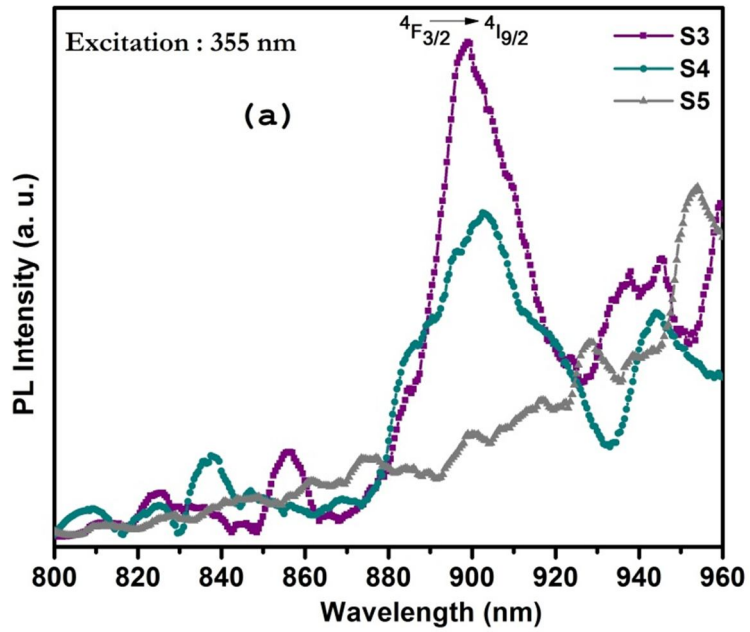
Figure 3.15: *Photoluminescence Spectra of Nd doped TiO₂ films on quartz substrates under Indirect Excitation – at 355 nm sample S3 and S4 (a) and (b) for sample S2 (b).*

The Nd-doped films were further tested for frequency down-shifting effect, by excitation in UV, at energies above the band gap of the titania matrix (at 355 nm, 3.49

eV). Figure 3.15(a) shows the PL emission spectra in the near IR region upon excitation at 355 nm (under a power less than 0.01 W) for samples S3 and S4. Characteristic NIR luminescence band centered at 902 nm ($^4F_{3/2}$ to $^4I_{9/2}$) was observed for the sample S3 (*Nd/Ti*= 3.7%). The observation of this emission upon excitation shows the existence of efficient energy transfer (ET) process from the electron-hole pairs created in the titania host matrix to the Nd ions. Only broad emission bands were observed. The same can be said for the sample S4; the spectrum is even broader. There is a complete absence of well resolved crystal-field-split (CF) Stark lines. This may be due to poor incorporation and inhomogeneities in the rare earth ion environment [24, 25]. As we see when the concentration is increased as going from sample S3 to sample S5 (*Nd/Ti* increasing from 3.7 % to 45%), the predominant PL emission intensity was drastically lowered to become undetectable for sample S5. This can be attributed to the quenching effect at high Nd concentrations, resulting from the enhanced cross-relaxation process. Upon excitation at 355 nm, the Nd PL peak at ~1094 nm ($^4F_{3/2}$ to $^4I_{11/2}$) could not be observed because the fundamental harmonic of the Nd-YAG laser falls at 1064 nm (as the excitation was done with the third harmonic of the laser at 355 nm) and in the luminescence setup used for this work, we were not able to completely remove the unwanted fundamental harmonic of the laser which completely overshadows the much weaker PL signal. The PL spectrum obtained for sample S2 was different in terms of both signal intensity which was much higher and the Stark splitting which was more pronounced. This can be explained by the fact that the Nd concentration is beyond the optimum doping limit for the samples S3, S4 having the *Nd/Ti* atomic ratio 3.7% and 25%, which led to luminescence quenching. Figure 3.15(b) shows the representative emission spectra recorded in NIR for sample S2 excited at 355 nm with a pumping power less than

10mW on the sample. Although the excitation power was considerably reduced, this sample showed strong luminescence. Two emission bands centered at 906 nm and 1094.5 nm corresponding to the $^4F_{3/2}$ to $^4I_{9/2}$ and $^4I_{11/2}$ transitions with fine CF splitting are distinguishable. The $^4F_{3/2}$ to $^4I_{9/2}$ transition covers the region 870 – 970 nm region with six well resolved components and the region from 1040 – 1150 nm is covered by $^4F_{3/2}$ to $^4I_{11/2}$ transition with three resolved Stark splittings. Here the luminescence peak for the $^4F_{3/2}$ to $^4I_{11/2}$ transition appears at 1094.5 nm due to the different chemical environment of the Nd ions in the matrix. In this process, the tetragonal titania will act as an effective light harvester to absorb UV photons and subsequently transfer energy to Nd and thereby results in the typical luminescence of Nd ion. Similarly, Fix et al. recently reported on luminescence properties of Nd-doped $SrTiO_3$, showing the Nd-related near-infrared luminescence bands and a photon down-shifting process through energy transfer from the $SrTiO_3$ host matrix by exciting at 325 nm [26]. This implies that excitation energy transfer from the matrix to the rare-earth dopant can be achieved by exciting with energy close to the band gap energy of the host and within proper doping limits. Luo et al. also reported as the most intense band for the above transition appeared at 1093.7 nm when Nd^{3+} is incorporated in the anatase titania nanocrystals [27]. Although the transition from $^4F_{3/2}$ to $^4I_{11/2}$ is known as the strongest transition of Nd, the 906 nm emission line showed very strong intensity and the same was observed in the case of Nd-doped Si nanoclusters [28].

The PL emission spectra made with 355 nm excitation differs greatly from spectra with other excitation wavelengths 514.5, 496 and 476 nm for sample S2. There are noticeable differences in the peak locations, line shapes, PL intensities and the crystal field splitting effects. This indicates the existence of multiple luminescence centers of Nd ions within the TiO_2 matrix [29].

Different resonant direct excitations (at 476, 496 and 514.5 nm) with the transition of Nd can selectively excite particular Nd sites in TiO_2 matrix whereas the 355 nm excited emission spectra is the superposition of all emissions from various subsets of Nd sites in titania. Therefore, multiple luminescent site emissions of Nd are detected upon excitation above the titania bandgap. The emission pattern is different from that of Nd in Nd_2O_3 nanocrystals [30] in respect to peak positions and shapes, which suggests that, when present, Nd_2O_3 should be in an amorphous phase, as XRD didn't detect it. The reason for showing these two spectra (Fig 3.15(a) and 3.15(b)) separately is because for the samples S3 and S4 the signal intensity was much lower than for the sample S2. So in order to put them in the same figure we would have to reduce the spectrum of S2 by a large factor (it is difficult to compare the spectra since the excitation power was very low and difficult to measure [due to lack of appropriate power meter as the power is less than 10mW], but we would say that the factor is at least 10).

Taking into account the PL properties analyzed above, the possible argument of efficient energy transfer (from host titania to Nd ion) can be proposed via defect related levels. There are number of models treating the energy transfer from the host to RE ions. Frindell *et al.* [31][and Xin *et al.* [32] proposed a model for the energy transfer via relaxation to defect states on titania before the energy is transferred to rare earth ion. In this study the predominant energy mediating defects of reduced titania might be the existence of oxygen deficiencies by the substitutional doping of Nd in the TiO_2 lattice, as the evolution of the anatase cell parameter and volume with Nd incorporation suggested too (Figure 3.9). Hence we presume the energy transfer process between reduced TiO_{2-x} and Nd as follows: the above-band-gap excitation of titania leads to the transition of electrons in TiO_2 matrix from valence band to

conduction band. The energy of recombination of electron-hole pair generated in titania host is transferred non-radiatively to the excited states of the Nd ions, followed by nonradiative relaxation to $^4F_{3/2}$ of Nd, thereby NIR emissions of Nd take place. Alternatively, some of the electrons in the conduction band can also be trapped by the defects in titania; hence on recombination of electrons in the defect state with the photo generated holes can also transfer its energy to the excited states of the Nd ions. In this case, the energy transfer from the matrix to the acceptor ion is not a simple level to level transition, but is a more complicated energy transfer involving defect states inside the band gap. To be able to estimate the transfer efficiency we would have to measure the dependence of the luminescence decay for such as defects related state in the presence and absence of neodymium.

3.11 CONCLUSIONS

In summary, the influence of Nd doping on the nanostructured titania thin film properties (structural, chemical, optical and photoluminescence properties) deposited by RF sputtering at room temperature were investigated. The following conclusions were drawn from this study:

A. from the structural and optical point of view:

(a) It is observed that the doping with low concentration of Nd induces the co-existence of both anatase and rutile phases even with the addition of large amount of neodymium in titania matrix (up to 25% *Nd/Ti* atomic ratio).

(b) Incorporation of low concentration of neodymium (0.9% *Nd/Ti* atomic ratio) leads to a remarkable lattice distortion along the c-axis in anatase which reveals that Nd ions are in substitutional site, further increase in the Nd concentration (from *Nd/Ti* equals 3.7 at.% to 45 at.%) resulted in an increasing amorphization. For large Nd

amounts, the incorporation of Nd is more likely in the amorphous phase of titania and forming an oxide (more likely amorphous) phase. The formation of neodymium oxide phase was not evidenced, though not excluded.

(c) For higher Nd concentration, there is no remarkable change in the c/a ratio of anatase at the same time we found that crystallization is hindered completely of the rutile phase.

(d) Addition of neodymium dopant also shows significant variation in terms of absorbance and the bandgap of the material. Specifically, redshift of the absorption band edge and the bandgap reduction was observed in the case of low concentration (0.9% *Nd/Ti* at. ratio) which concludes that Nd ions are in the substitutional site.

B. From the photoluminescence study:

(a) The PL properties both in resonant and non-resonant excitation have been investigated. In general the downshifting luminescence emission intensity depends upon the doping concentration, crystal structure and size dependent properties.

(b) An appreciable effect have been observed under the indirect excitation of titania (through UV), the maximum NIR PL emission intensity through an effective defect mediated energy transfer from the host titania matrix with resolved crystal field splitting was obtained for low doping concentration (0.9% *Nd/Ti* at. ratio) of Nd ions as in the substitutional site. Quenching of PL emission intensity was observed for higher doping concentration of Nd ions (from 3.7 at.% - 45 at.% *Nd/Ti* ratio) because of cross relaxation process and also the poor incorporation of neodymium into the TiO_2 matrix, which is an imperative for the occurrence of efficient energy transfer.

REFERENCES

[1].   J. F. Moulder, W. F. Stickle, P. E. Sobol, K. D. Bomber, "*Handbook of X-ray Photoelectron Spectroscopy*", (J. Chastaing, R. C. King Jr., Eds., Physical Electronics, Inc. Eden Prairie, 1995)

[2].   N. Laidani, P. Cheyssac, J. Perrière, R. Bartali, G. Gottardi, I. Luciu, V. Micheli *Journal of Physics D: Applied Physics* 43 (48), 2010, 485402

[3].   T. L. Barr, *J. Phys. Chem.* **82** (16), (1978), 1801

[4].   H. M. Liao, R. N. S. Sodhi and T. W. Coyle, *J. Vac. Sci. Technol. A* **11**(5) (1993) 2681

[5].   G. Beamson and D. Briggs, "*High Resolution XPS of Organic Polymers, The Scienta ESCA300 Database*", (John Wiley &Sons, West Sussex, 1992)

[6].   C. G. Pantano and Theodore E. Madey, *Electron Beam Damage in Auger Electron Spectroscopy; Application of Surface Science* **7** (1981) 115 - 141, North-Holland Publishing Company

[7].   Ioana Luciu, "RF plasma synthesis and characterization of thin films for transparent conductors", PhD thesis, March 2012, University of Trento.

[8].   R. Koch, *Surf. Coat. Technol.*, **204**, (2010), 1973.

[9].   Toshiaki Ohsaka, Fujio Izumi and Yoshinori Fujiki, *J. of Raman Spectroscopy*, **7**, (1978), 321

[10].   Fang Tian, Yupeng Zhang, Jun Zhang and Chunxu Pan, *J. Phys Chem C* **116**, (2012), 7515

[11].   G. A. Tompsett, G. A. Bowmaker, R. P. Cooney, J. B. Metson, K. A. Rodgers and J. M. Seakins, *J. of Raman Spectroscopy* **26**, (1995), 57

[12].   Francisco MSP and Mastelaro VR *Chem Mater* ., **14**(6), (2012), 2514

[13].   Jing Zhang, Meijun Li, Zhaochi Feng, Jun Chen, and Can Li *J. Phys. Chem. B* **110** (2), (2006), 927–935

[14].   A. Golubović, M. Šćepanović, A. Kremenović, S. Aškrabić, V. Berec, Z. Dohčević-Mitrović and Z. V. Popović *J. of Sol-Gel Science and Technology* **49**, (2009), 311

[15].   Yi Hu, H.-L Tsai and C.-L Huang, *J. of the European Ceramic Society* **23**, (2003), 691–696

[16].   A. Di Paola, M. Addamo, M. Bellardita, E. Cazzanelli and L. Palmisano *Thin solid films* **515**, (2007), 3527

[17].   S. Jandl, J.-P. Rheault, M. Poirier, A. Ait-Ouali, A. M. Lejus, and D. Vivien *Phys. Rev. B* **56**, (1997), 11600–11603

[18]. Wei-Xing Xu, Shu Zhu, Xian-Cai Fu and Qiang Chen *Appl. Surf. Sci* **148**, (1999), 253

[19]. A. Ali, E. Yassitepe, I. Ruzybayev, S. Ismat Shah, and A. S. Bhatti, *J. Appl. Phys*. **112**, (2012), 113505

[20]. Hirotaka Fujimori, Masatomo Yashima, Masato Kakihana and Masahiro Yoshimura, *J. of American Ceramic Society* **81**, (1998), 2885

[21]. Satyaprakash Sahoo, G. L. Sharma and Ram. S. Katiyar,*J. of Raman Spectroscopy* **43**, (2012), 72

[22]. D. Zhao, T. Peng, J. Xiao, C. Yan and X. Ke, *Mater. Lett*., **61**, (2007), 105

[23]. W. Li, Y. Wang, H. Lin, S. Ismat Shah, C. P. Huang, D. J. Doren, S. A. Rykov, J. G. Chen and M. A. Barteau, *Appl. Phys. Lett*., *83,(2003) 4143*

[24]. J. Yin, L. Xiang and X. Zhao, *Appl. Phys. Lett*., **90**, (2007), 113112

[25]. Y.-P. Du, Y.-W. Zhang, L.-D. Sun and C.-H. Yan, *J. Phys. Chem. C*, **112**, (2008), 12234

[26]. T. Fix, H. Rinnert, M. G. Blamire, A. Slaoui and J. L. MacManus-Driscoll, *Sol. Energy Mater. Sol. Cells*, **102**, (2012), 71

[27]. W. Luo, R. Li and X. Chen, *J. Phys. Chem. C*, **113**, (2009), 8772

[28]. A. N. MacDonald, A. Hryciw, F. Lenz and A. Meldrum, *Appl. Phys. Lett*., **89**, (2006), 173132

[29]. G. D. Metcalfe, E. D. Readinger, H. Shen, N. T. Woodward, V. Dierolf and M. Wraback, *J. Appl. Phys*., **105**, (2009), 053101

[30]. R. Yu, K. Yu, W. Wei, X. Xu, X. Qiu, S. Liu, W. Huang, G. Tang, H. Ford and B. Peng, *Adv. Mater*., **19**, (2007), 838.

[31]. K. L. Frindell, M. H. Bartl, M. R. Robinson, G. C. Bazan, A. Popitsch and G. D. Stucky, *J. Solid state Chem.,* **172**, (2003), 81

[32]. H. Xin, R. Ma, L. Wang, Y. Ebina, K. Takada and T. Sasaki, *Appl. Phys. Lett*., **85**, (2004), 4187.

[33]. WINQXAS Ver. 1.3, Software Package for Energy Dispersive X-Ray Fluorescence Analysis, IAEA Evaluation Report 2002

[34]. http://www.iaea.org/OurWork/ST/NA/NAAL/pci/ins/xrf/pciXRFdown.php

Chapter 4

Chapter 4

Neodymium effects on the structural, Chemical, Morpholol gical, Optical and Photoluminescence properties of Zinc Oxide thin films

"Desire is the starting point of all achievement, not a hope, not a wish, but a keen pulsating desire which transcends everything"

-Napolean Hill

4.1 INTRODUCTION

Doping is commonly used for altering phase structure, electronic structure, surface and bulk chemical and physical properties of a material depending on the pursued application. A crucial prerequisite for a successful doping is actually an accurate control over the dopant concentration in the host material. Moreover, since the physical and chemical properties of the host matrix have been proved to be influenced by the level of foreign elements incorporation, a full characterization of the material over an adequate range of dopant concentrations is recommended [1].

In the first part of this chapter, the effects of different amounts of Nd atoms incorporation on the structural, chemical, morphological, optical and photoluminescence properties of RF sputtered ZnO thin films were studied

Nevertheless, detailed literature survey shows that few reports are there focusing on the incorporation of Nd atoms into ZnO films by RF sputtering [1, 2]. Besides, due to the large mismatch in ionic radius and charge imbalance between Nd^{3+} and Zn^{2+}, the successful incorporation of neodymium ions into the ZnO lattice has always been rather challenging [3]. Therefore, a study was conducted to describe the influence of incorporated Nd concentration on ZnO thin films properties, in particular to determine the Nd concentration limit in the host matrix beyond which dopant clustering may occur. The co-sputtering process appears to be successful in doping the ZnO matrix at low Nd concentration, while much higher dopant levels produce dramatic changes in the microstructure of the films and eventually the formation of two co-existing phases.

4.2 THE SAMPLE PREPARATION AND CHARACTERISATION

Undoped- and neodymium-doped ZnO films were deposited by radio frequency (13.56 MHz) co-sputtering. High purity, commercially available ZnO target (purity= 99.999%, diameter = 10cm) and metallic Nd target equipped with a magnetron (diameter = 5 cm) were sputtered simultaneously in a pure argon plasma. The reactor base pressure was kept at $4x10^{-6}$ Pa while the depositions were operated at 6.6 Pa working pressure by keeping the argon flow rate constant at 30sccm. A constant self-bias voltage (V_{ZnO}) of -550 V for an average power of 44±2 Watt was kept fixed on the ZnO cathode for all the deposition processes. On the contrary, to obtain different levels of Nd doping in the films, the power applied to the Nd cathode (W_{Nd}) was varied from 0 up to 7 Watts, corresponding to a self-bias voltage (V_{Nd}) ranging between 0 and -67V. The deposition time was 7 hours for all the samples at room temperature and ex-situ post annealing treatment were made at 600ºC for six hours in

air ambient.

4.2.1 FILM GROWTH RATE

The growth rate for Nd-ZnO films deposited at -550V, in Ar plasma, at various self-bias voltages applied to Nd target is shown in Figure 4.1. The film deposition rate depends on the several growth parameters, especially on the working pressure (which decides the mean free path of the active species) and the applied voltage (which determines the maximum energy with which the sputtered particles can be carried towards the substrate). Here the deposition pressure was kept constant. The electrical power and self-bias voltage conditions, the film labeling and thickness values are summarized in Table 4.1.

Films	Power on ZnO target	Self-bias voltage on ZnO target V_{ZnO} (V)	Power on Nd target	Self-bias voltage on Nd target V_{Nd} (V)	Thickness (micron)
S1	40	-550	0	0	0.85
S2	43	-550	1	-19	0.91
S3a	46	-550	3	-36	1.08
S3b	45	-550	3	-39	1.10
S4	45	-550	5	-55	1.45
S5	46	-550	7	-67	1.89

Table 4.1: *Plasma conditions (power, self-bias voltages), film labeling and thickness values.*

The average deposition rate values for each plasma condition are plotted in Fig. 4.1 as a function of V_{Nd}. The deposition rate increases with increasing the self-bias voltage on the Nd target, showing an exponential behavior. This trend can be explained considering that the powered Nd cathode contributed in increasing the ion density of the whole discharge. It can be noticed that, even if the applied power to ZnO target is much lower than that in the case of titania film deposition (-850 V), the deposition

rates are of the same order, ZnO sputtering yield is much higher than that of TiO_2.
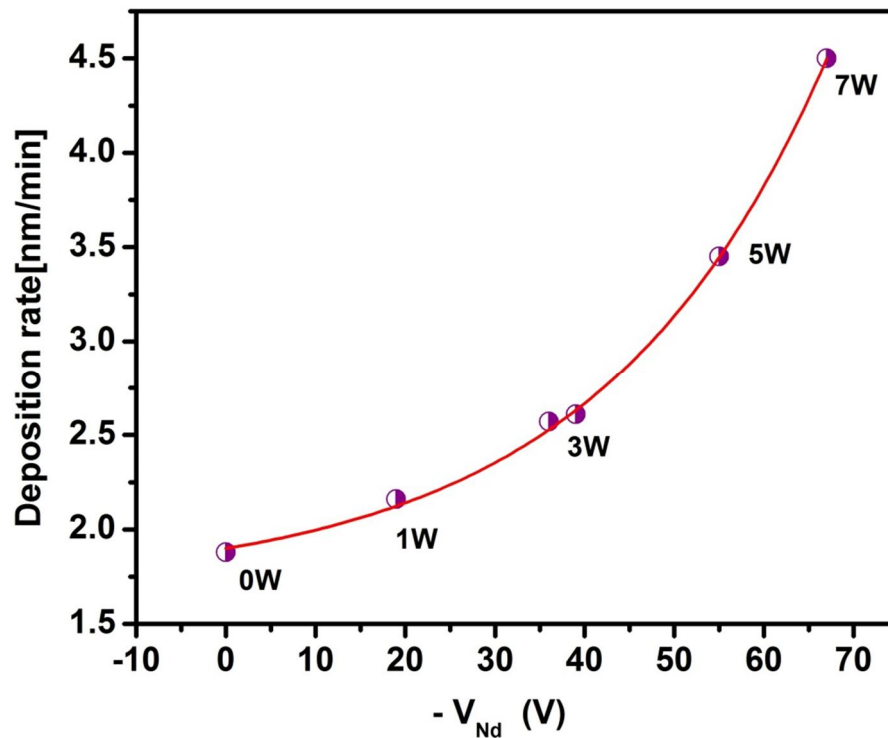
Figure 4.1: *Film growth rate for co-sputtered Nd- ZnO films as a function of the self-bias voltage at Nd target, V_{Nd}. The relative electrical powers are given in the plot.*

4.2.2 FILM COMPOSITION FROM AES

After post-growth annealing, the films were checked throughout their thickness by Auger depth profiling, in order to assess their composition uniformity and stoichiometry. In Fig. 4.2(a, b and c), AES depth profiles of three samples S1, S3b and S5, deposited onto Si substrates respectively with $V_{Nd} = 0$, -3 and -67 V, are plotted.

All of them exhibit a rather sharp interface region towards the substrate and an homogeneous composition throughout their thickness. The high erosion rate of ZnO made faster a complete depth profiling, down to the substrate-film interface, without artificially distorted profile which can result from prolonged Ar ion-irradiation (heating and ion-beam mixing, induced roughness), in contrast with titania films.
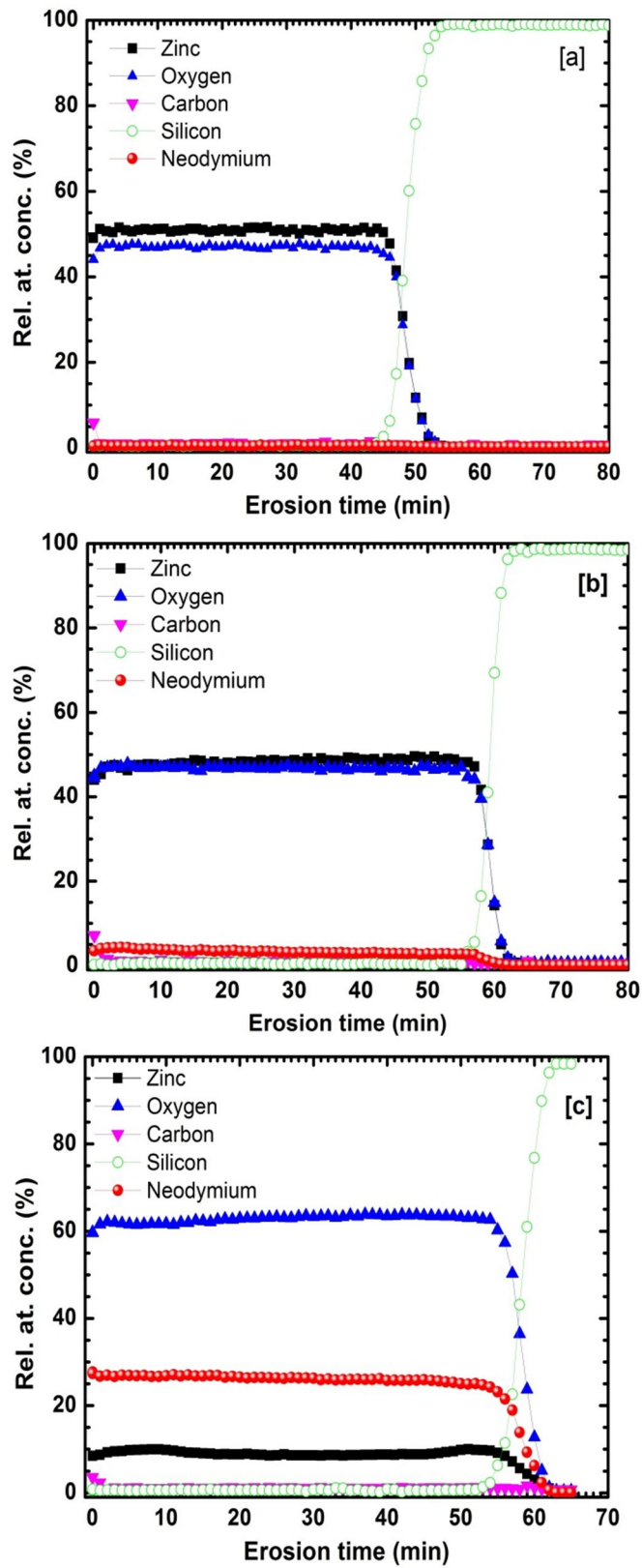
Figure 4.2: *AES depth profiles, acquired respectively on samples (a) S1, (b) S3b and (c) S5.*

A negligible carbon contamination has been recorded in all the films, with the exception of the surface region where a certain amount of adventitious carbon is always present due to air exposition. The obtained elemental compositions, calculated as an average over the bulk of the films (surface and film/substrate interface regions excluded) and expressed in relative atomic percentages, are listed in Table 4.2 for all the deposited samples.

Films	[Zn] at.% from AES	[O] at.% from AES	[Nd] at% from AES	[C] at.% from AES	Nd/Zn from AES	O/(Zn+Nd) from AES
S1	50.9	47.1	0.00	2	0.00	0.92
S2	51.2	47.3	0.00	1.5	0.00	0.92
S3a	50.1	47.72	0.9	1.28	0.02	0.93
S3b	48.4	46.8	3.3	1.5	0.07	0.90
S4	19.5	57.2	21.8	1.5	1.12	1.38
S5	9.1	62.9	26.3	1.7	2.89	1.77

Table 4.2: *Elemental composition and atomic ratios obtained by AES analysis, averaged over the films thickness for all the films deposited with negative V_{Nd} in the range 0-67V.*

As can be seen from data reported in Table 4.2 and Fig.4.2, the Nd signal (absent for sample S1 (Fig.4.2(a)) becomes detectable by AES starting from samples deposited with a V_{Nd} starting from -39V (sample S3) to more negative values, it grows to be dominant with respect to Zn signal in Fig. 4.2(c). More likely the film S2 deposited with $V_{Nd} = $ -19V did not contain Nd. This low voltage on the Nd target cannot lead to a significant sputtering yield, the energy displacement threshold for many elemental materials being typically around 25 eV.

The Nd/Zn atomic ratio concentration in Nd-ZnO films plotted as a function of V_{Nd} is shown in Figure 4.3 and the corresponding values are given in Table 4.2. An

exponential fit of the plot could be performed. The Nd/Zn ratio increases with increase in V_{Nd}.
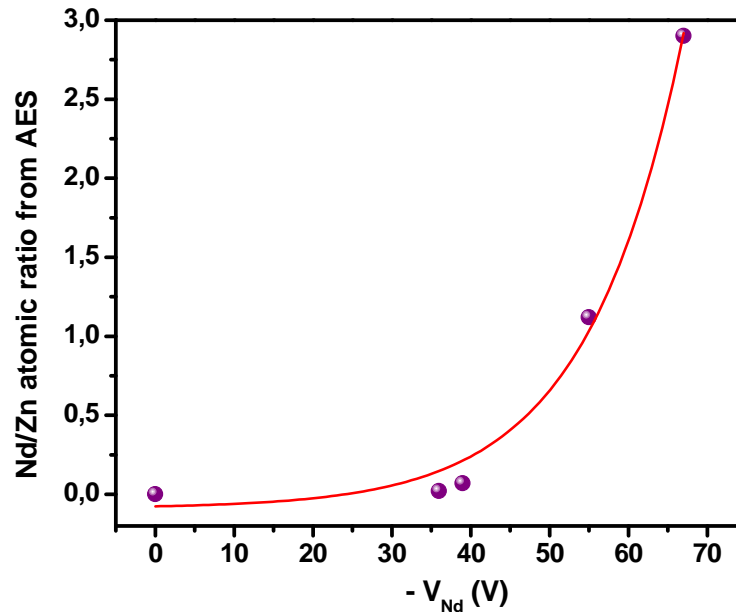
Figure 4.3: *Nd/Zn atomic ratio in Nd doped ZnO films plotted as a function of voltage self-bias applied at Nd target (-550V on ZnO)*

We can also observe that pure ZnO sample appears to be slightly sub-stoichiometric, with an O/Zn ratio equal to 0.92. Close to 0.9 is also the value of the O/(Nd + Zn) ratio obtained in all the films deposited with low power applied on the Nd target (samples S1-S3)) which are those where the Nd concentration is low ([Nd] $\leqslant$ 3.3 at.%). This is most probably due to the fact that at low doping levels neodymium atoms succeed to enter the host ZnO matrix by substituting into the Zn^{2+} sites. Further evidence of this deduction will come from XRD analyses as well.

On the contrary, increasing the dopant concentration further than 21 at.% (samples S4 and S5) results in an increase of the O/(Nd+Zn) atomic ratio up to 1.77, well beyond the unit value expected for a zincite-like structure. This implies that high Nd doping level in the material lead to the formation of a different oxide phase involving

neodymium, which can coexist and eventually become dominant with respect to the original host ZnO matrix. We suppose that a proper identification of such a phase is Nd_2O_3. The analysis of the line shape of the AES O KLL peak can help confirming our hypothesis.

In Fig.4.4 the AES O KLL spectra acquired in the derivative mode on (a) a bulk ZnO standard, (b) a bulk Nd_2O_3 standard, (c) a pure ZnO film (sample S1), (d) on ZnO:Nd film with Nd = 3.3at.% (sample S3b) and (e) on ZnO:Nd film with the highest Nd content (sample S5) respectively are plotted. In the figure, three parameters are evidenced: $\Delta1$ refers to the kinetic energy (KE) difference between the main negative excursion and the main positive excursion of the O KLL peak, $\Delta2$ is the KE difference between the main negative excursion and the small shoulder at 508 eV in ZnO (spectrum (a)) and $\Delta3$ is the KE difference between the main negative peak position and plasmon loss peak located at 488 eV in ZnO spectrum (a) and 489.5 in Nd_2O_3 spectrum (b).

It is evident that the O KLL peak acquired on the undoped ZnO and the ZnO:Nd film deposited at V_{Nd}= -39V (sample S3b) exhibits almost the same line shape as the ZnO standard (as shown in spectra (a), (c) and (d)). The spectra reveal the two distinct features at 508 and 511.5 eV, which are distinguishing zinc oxide. Conversely, the O KLL peak acquired on the Nd-richest ZnO film (spectrum (e)) shows a structure characterized by a narrow peak at 512 eV which is peculiar (for both shape and position) to that of a neodymium oxide (spectrum (b)). This means Nd atoms were not incorporated in ZnO structure anymore, but rather synthesizing a mixed phase where Nd_2O_3 is prevailing over ZnO. The O KLL spectrum relative to the standard Nd_2O_3 sample was shifted towards low KE, which is due to a higher electrostatic charge building given by its insulating nature.

(a) ZnO standard

(b) Nd$_2$O$_3$ standard

(c) film S1
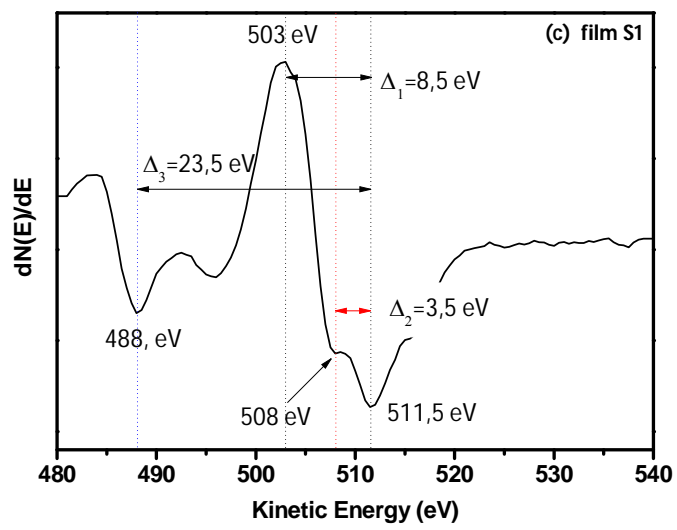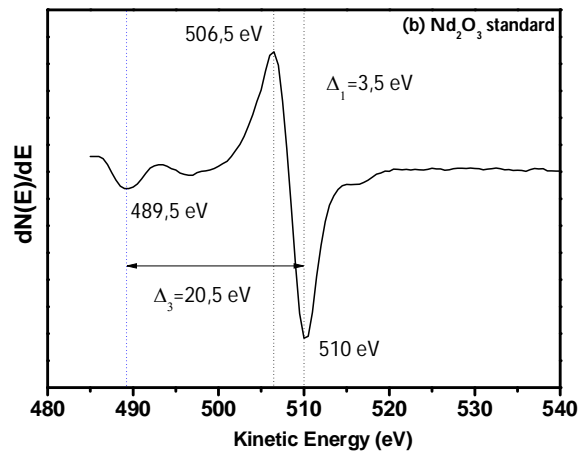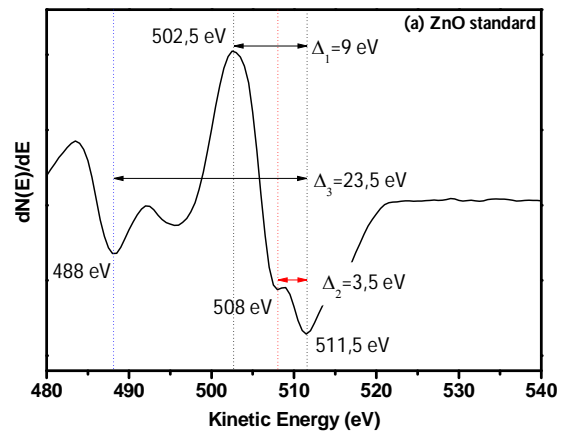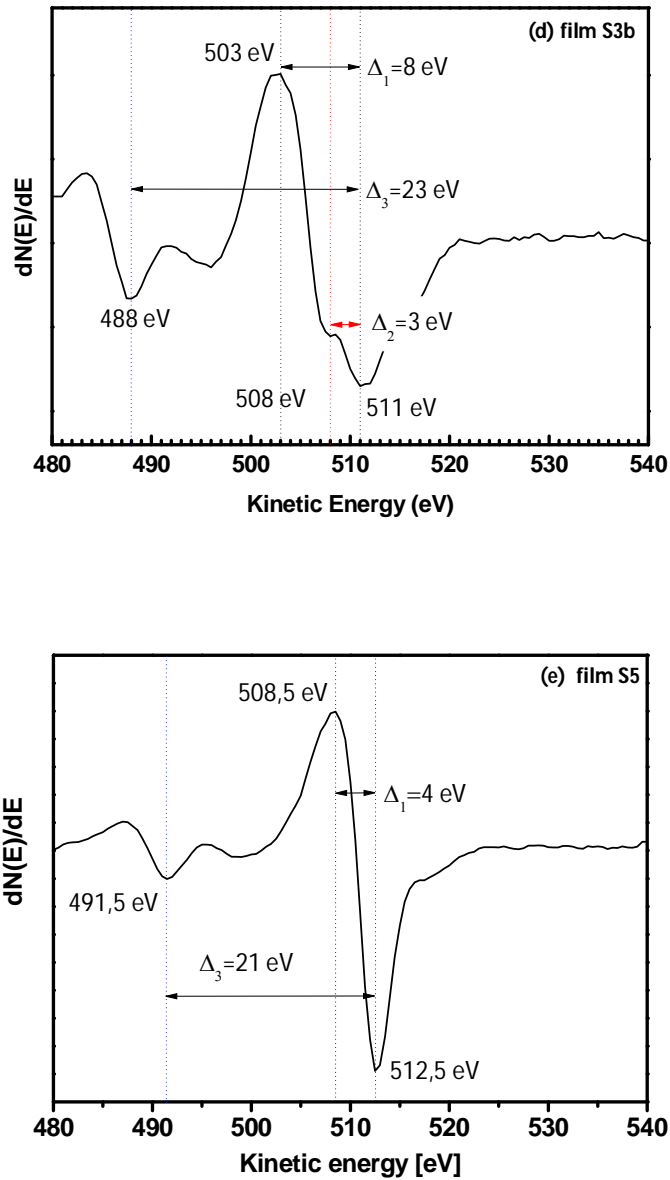
Figure 4.4: *AES line shape of O KLL peak acquired on a (a) ZnO standard, (b) Nd$_2$O$_3$ standard, (c) pure ZnO film (V_{Nd} =0, sample S1), (d) on a ZnO:Nd film deposited with V_{Nd} = -39V (sample S3b) and (e) ZnO:Nd film deposited with V_{Nd} = -67V (sample S5).*

4.2.3 CHEMICAL STRUCTURE FROM XPS

XPS analyses of the films surface were performed on all the samples deposited on silicon substrates after post-growth annealing at 600ºC in air ambient and regarded the core levels Zn2p, O1s, Nd4d, C1s and survey regions. Fig. 4.5 shows a survey spectrum acquired on a pure ZnO film (S1) and on the sample S5 (V_{Nd} = −67V).

Figure 4.6 shows the O1s core line (all in left panels) and Zn2p core line (right panels) acquired on sample S1, S3b, S4 and S5.
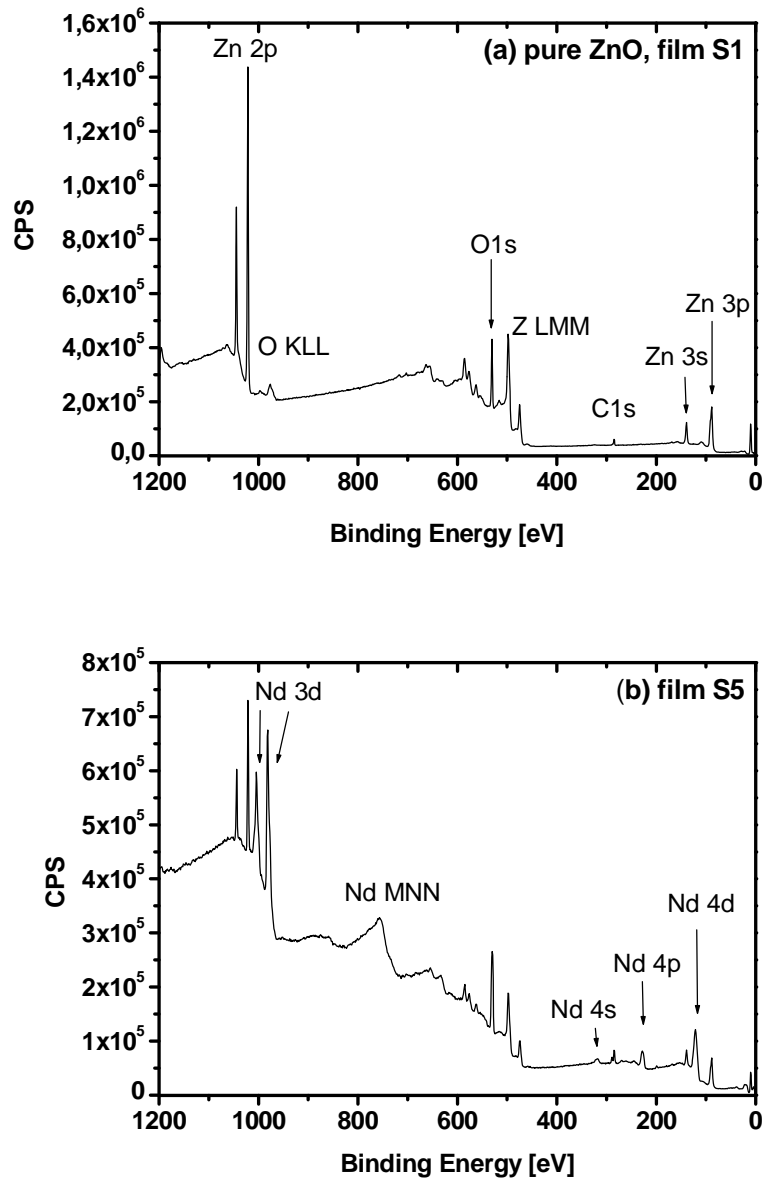
Figure 4.5: *XPS spectra: survey of (a) pure ZnO thin film (S1) and (b) of film S5.*

Finally, Fig. 4.7 shows the Nd 4d core-line for the samples S3b, S4 and S5. From the surveys (fig. 4.5) in panel (a) and (b) it is immediately evident the remarkable variation in the composition of the samples with the two extreme Nd concentrations

of our experimental range: the first showing a pure zinc oxide surface, the second a surface characterized by the presence of strong neodymium signal in addition to those of zinc and oxygen. The XPS core lines of Zn2p3/2, O1s and Nd4d were studied in detail for all the samples shown in Table 4.2 and the results are summarized in Table 4.3. In all samples carbon content was in the range 18-20 at.% (not shown). In the same way of AES analyses, XPS could not reveal and quantify Nd signal in samples S2.
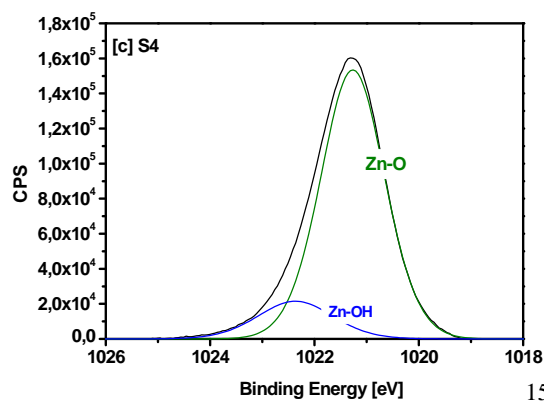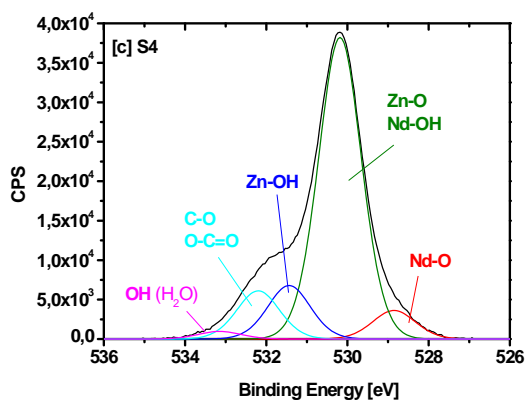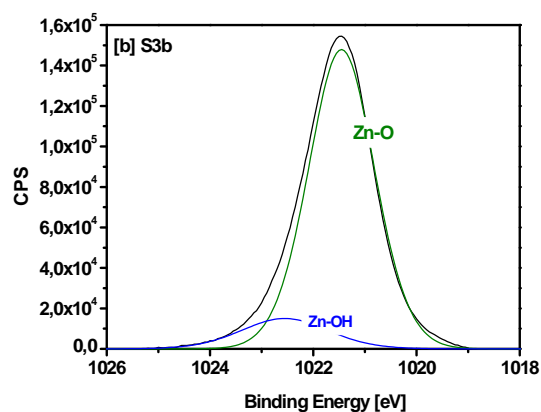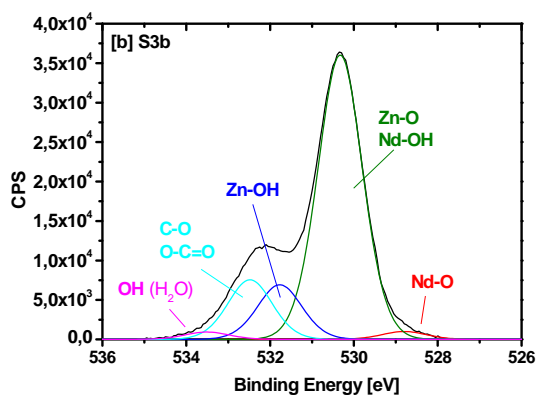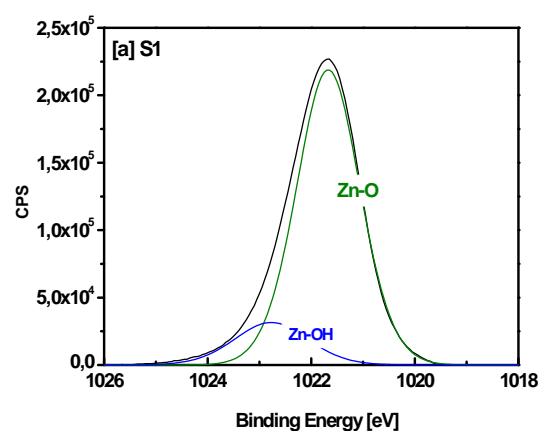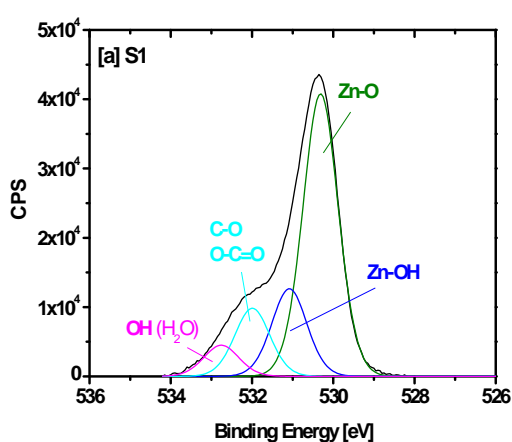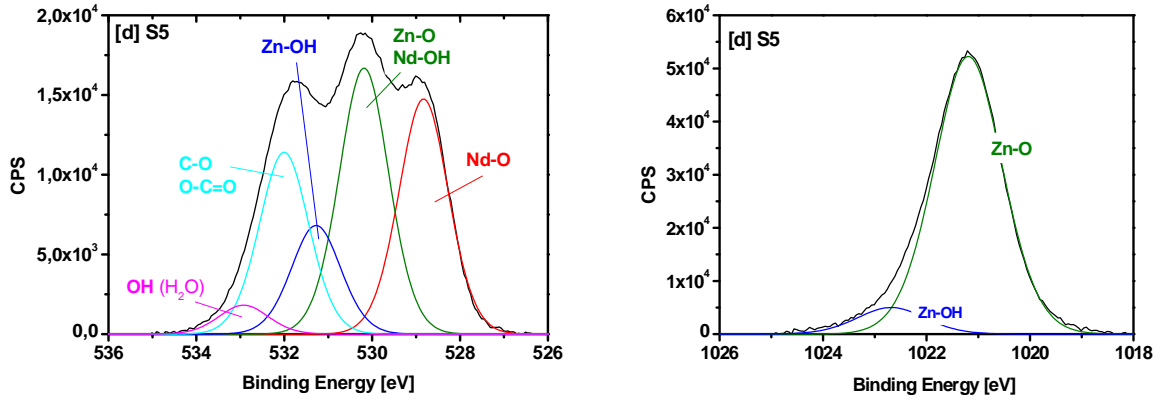
Figure 4.6: *O1s spectra (Left panels) and Zn2p spectra (Right panels) of annealed pure ZnO film S1[a] and ZnO:Nd films S3b[b], S4 [c] and S5[d].*

As already reported in Chapter 3, usually the elemental quantification is performed on the basis of the peak area relative to the most intense core line, which in the case of Nd would be the Nd3d core level. However, due to the overlapping between the Nd3d and the OKLL peaks, the Nd4d core level was acquired as an alternative. The surface chemical composition was obtained for the ZnO and ZnO:Nd films and the obtained values are listed in Table 4.3 together with the corresponding Nd/Zn ratio. The detailed deconvolution of the O1s, Zn2p and Nd4d core lines is summarized in Table 4.4 showing the binding energies (BEs) of the various components. The results for film S3a are also included in both tables.

As can be seen from figure 4.6 (right panels), the introduction of neodymium in the films has no significant influence on the XPS spectra in the Zn2p level. After correction of the core levels binding energy (BE) shift due to surface electrostatic charging (by calibration with respect to the C1s main peak put at 285 eV), for pure ZnO film the Zn 2p3/2 peak was always fitted with two components: the main one,

located at 1021.6 eV, corresponding to zinc bound to oxygen in zinc oxide and a weaker shoulder, shifted by 1.1 eV toward high binding energies with respect to the first component, attributed to zinc hydroxide, situated at 1022.7 eV [4-7]. No great changes were observed for the BEs of Zn2p for the ZnO:Nd films.

Films	V_{bias} on Nd [V]	O1s [at. %]	Zn2p [at. %]	Nd [at.%]	Nd/Zn
S1	0	56.60	43.40	-	-
S3a	-36	57.55	41.96	0.49	0.01
S3b	-39	69.26	27.98	2.76	0.10
S4	-55	67.81	26.87	5.32	0.20
S5	-67	69.88	9.71	20.41	2.10

Table 4.3: *XPS quantification of C1s, O1s, Zn2p and Nd4d atomic concentration in the Nd doped zinc oxide thin films*

Films		O1s					Zn 2p		Nd 4d
	V_{RF} on Nd [V]	Nd-O [eV]	Zn-O Nd-OH [eV]	Zn-OH [eV]	C-O O-C=O [eV]	OH (H_2O) [eV]	Zn-O [eV]	Zn-OH [eV]	Nd-O [eV]
S1	0	-	530.3	531.1	532	532.8	1021.6	1022.7	-
S3a	-36	-	530.3	531.4	532.3	-	1021.6	-	123.2
S3b	-39	528.8	530.3	531.6	532.4	533.5	1021.5	1022.5	122.1
S4	-55	528.9	530.2	531.4	532.2	533.1	1021.3	1022.4	121.8
S5	-67	528.8	530.2	531.3	532	532.9	1021.2	1022.6	121.1

Table 4.4: *Deconvolution details of O1s, Zn2p and Nd4d XPS core levels along with their BE (eV) for the annealed Nd- doped ZnO thin films.*

A more meaningful description of the effects exerted by different levels of dopant incorporation on the chemical structure of the films can be derived instead from the

deconvolution of the O1s peak, (Fig. 4.6, left panels a–d). Independently of the Nd content, the O1s peak appears always dominated by the component Zn-O at 530.2 eV due to oxygen atoms involved in the ZnO host matrix. A second component assigned to zinc hydroxide species (Zn-OH) and placed at 531.3 eV, was found to exist in between the dominant ZnO and the higher BE components associated to oxygen atoms participating in C-O/O-C=O bounds and to OH adsorbed water originating from surface contamination. It is well known, in fact, that in many transition metals hydroxylation occurs, giving rise to a peak (due to metal-OH bond formation) whose energy is in accordance with ours [6,7,8]. Finally, an additional component (labeled as Nd-O and placed at about 529 eV) arises at the lower BE side of the O1s peak as soon as the Nd signal becomes detectable by XPS (Fig. 4.6, panels b-d). This component is completely separated from the main one due to oxygen involved in the ZnO würtzite structure (530.2 eV) and can be assigned to oxygen atoms bound to Nd [9, 10, 11].

As shown in Figure 4.7, the Nd4d peak BE position, found in the range 122.1 -121.1 eV, is in good agreement with an oxidation state of Nd^{3+} [9, 10, 11], in all samples, suggesting that the Nd atoms could be either incorporated in ZnO structure in such state or be present in the form of its oxide (Nd_2O_3). In fact, AES results (Table 4.2) showed that the oxygen concentration in the films and the O/(Zn + Nd) atomic ration started to vary strongly only for samples S4 and S5. It is more likely that a mixed phase ZnO- Nd_2O_3 formed for the latter.

To conclude the description of the XPS spectra in Fig. 4.6, it is interesting to note that for the sample S5, which had the highest Nd concentration ((d), left panel), the intensity of the O1s peak due to Nd-O bounds (BE= 528.8eV) is lower than that of the main component Zn-O (BE= 530.2eV). This is in contrast with what expected on the base of the quantification results (Table 4.3), from which we know that Nd/Zn ratio is

2.1 for this sample. The discrepancy can be explained in view of the oxygen excess, which was clearly revealed also by AES depth profiles, which can reasonably be attributed to the adsorption of water on the samples. The component placed at 533 eV, normally reported to pertain to adsorbed molecular H_2O [7, 12, 13] confirms this
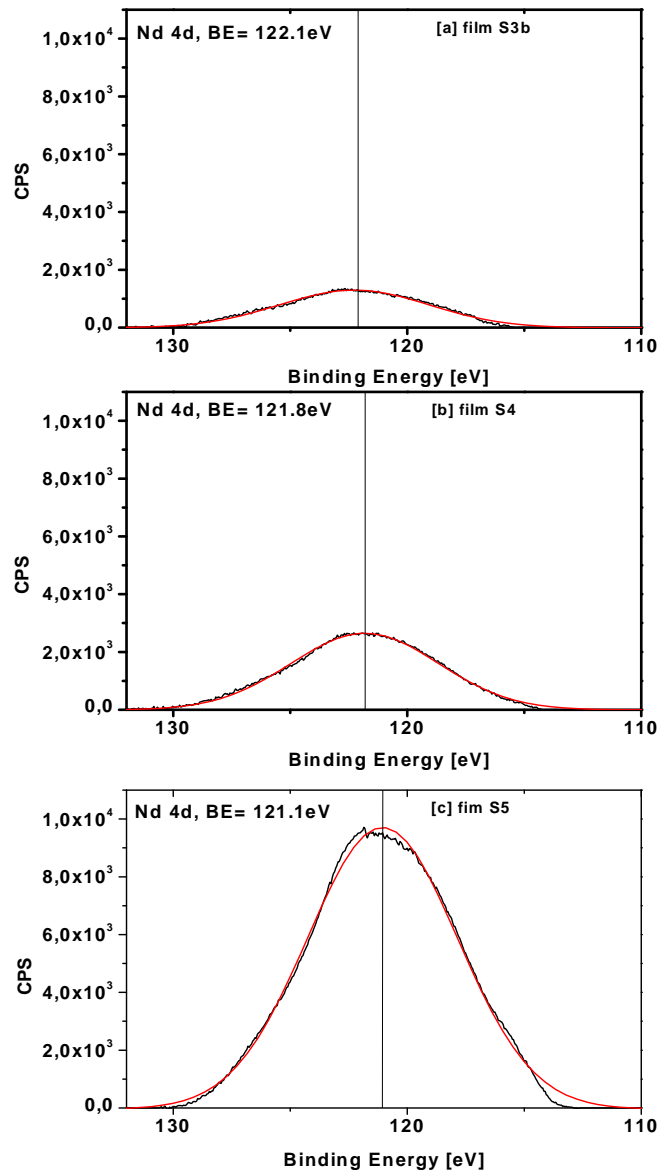
Figure 4.7: XPS *Nd 4d core-levels for annealed Nd-doped ZnO films: (a) film S3b, (b) film S4, (c) film S5.*

supposition. It is just the existence of adsorbed water which can promote the formation of $Nd(OH)_3$ by the reaction $Nd_2O_3 + 3\ H_2O \rightarrow 2\ Nd(OH)_3$ in the oxide film

[10]. Oxygen atoms involved in neodymium hydroxide give a signal which overlaps with the ZnO component, whose intensity results this way enhanced.

This is well-illutrated in Fig. 4.8(a) where the atomic ratio $O_{Zn-O, Nd-OH}/Zn$ is plotted for all the films in function of Nd/Zn atomic ratio. Let's name $O_{Zn-O, Nd-OH}/Zn$ ratio as O_I/Zn. For pure ZnO film, its value was equal to 0.97 (indicated by a dotted line). When Nd is incorporated in the films, O_I/Zn increased to reach high values, 2.3 for sample S5, departing from the ideal value of 1, which is a clear indication of Nd –OH bonds contribution to this value. Moreover, the contribution of Zn-O bondings are more likely to decrease when Nd concentration increases, as indicated by the evolution of the O_{Zn-OH}/Zn atomic ratio: the higher Nd/Zn (the lower Zn concentration), the higher O_{Zn-OH}/Zn. In the films where Nd is predominant, Zn hydroxylated states are increasingly important. The hydroxylated states are probably located at boundaries, where hydration may occur easily. This could be possible if such films contain a larger number of grain boundaries in their structure, given by a nanocrystalline structure.
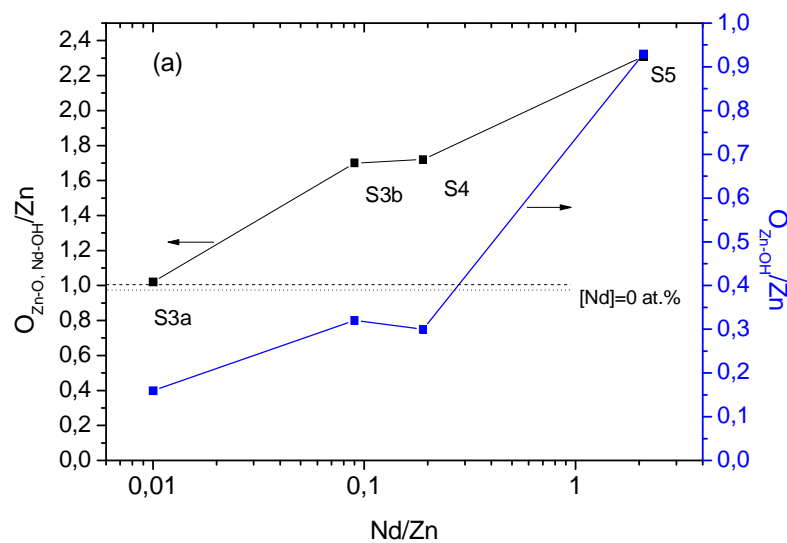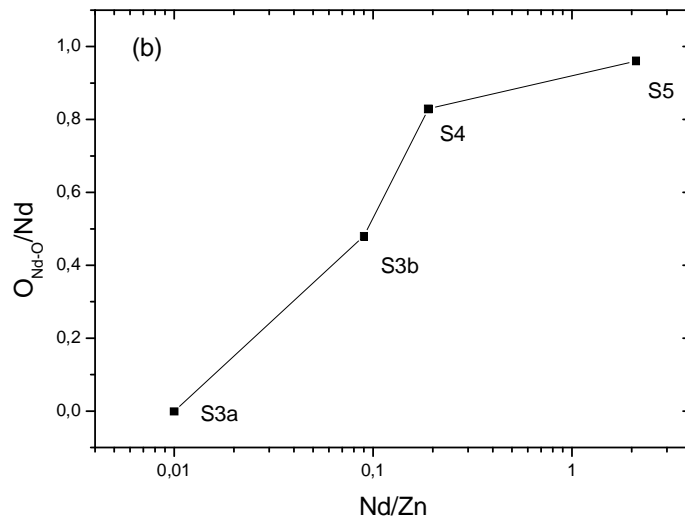
Figure 4.8: *Evolution in function of Nd/Zn atomic ratio of (a) the $O_{Zn\text{-}O,\ Nd\text{-}OH}$ / Zn and $O_{Zn\text{-}OH}$ / Zn atomic ratios and (b) the $O_{Nd\text{-}O}$ / Nd atomic ratio. The analyzed films are also indicated.*

Opposite results were obtained for Nd chemical states: with increasing Nd content in the films, oxygen bound to Nd was increasingly involved in neodymium oxide bondings (Nd-O), as shown in Fig. 4.8(b) where the $O_{Nd\text{-}O}$/Nd atomic ratio evolution in function of Nd/Zn ratio.

4.2.4 FILM STRUCTURE FROM XRD AND SEM ANALYSIS

Figure 4.9 (a) shows the diffraction patterns acquired on as-deposited (before annealing) films of pure and Nd- doped ZnO samples grown on quartz substrates as a function of different neodymium concentrations. The analyzed films were S1, S2, S3b, S4 and S5. The XRD analysis geometry employed for these samples was the Bragg-Brentano one. All the samples were analyzed this way, except sample S3a. As clearly seen the as-deposited films were revealing their crystalline nature for low Nd concentration. All the films deposited with V_{Nd}= -39 V and below crystallized in the

characteristic hexagonal würtzite type phase of ZnO and appear to be highly textured, presenting mainly one dominant preferred orientation along the [0 0 2] axis ($2\theta=$ 34.4º, in accordance with the ICDD 36-1451 card). A magnified scale of Y-axis is used here in order to reveal lower intensity peaks. A peak pertaining to the (0 0 4) reflection can this way be recognized, as well as two small peaks placed at 2θ around 31º and 37.1º likely due to the presence of $Zn(OH)_2$ (ICDD 20-1435 card) impurities, as revealed also by XPS analyses. When increasing V_{Nd} to −39 V, two other small peaks corresponding to the (1 0 1) and (1 1 2) directions of the ZnO würtzite structure become visible, but no reflections attributable to Nd containing phases can be observed. This means that the films do not contain any secondary phases and that neodymium atoms are successfully incorporated into the hexagonal ZnO lattice. The film crystallinity worsened in the Nd-richest films (films S4 and S5) as evidenced by the decrease in the peak intensity and broadening. Two new peaks appeared at 2θ around 45° and 30°, they pertain to $Nd(OH)_3$, though the second one might be also due to Nd_2O_3 phase (ICDD card nos. 21-0579, 28-0671, 06-0601). Zinc oxide signal is very suppressed in these films.

Post deposition annealing at 600ºC was performed with the aim of improving the crystal quality of their structure and the data discussed below refer to the annealed samples. The diffraction patterns are displayed in Fig. 4.9 (b).

(a) BEFORE ANNEALING
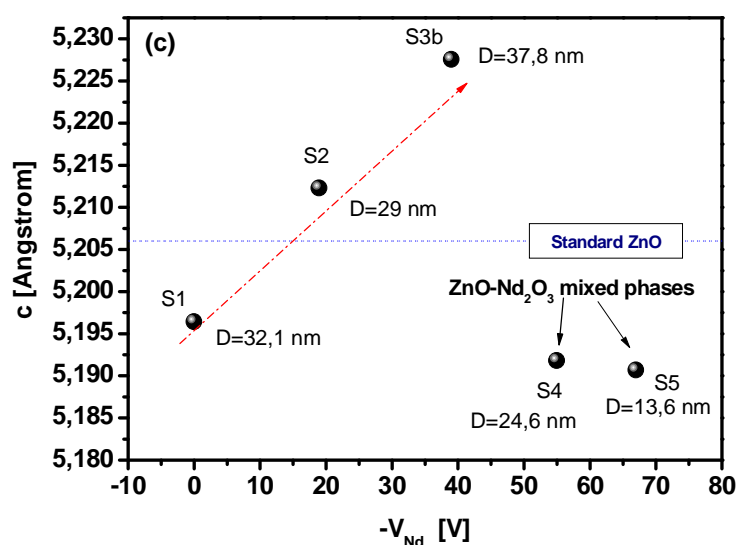
(b) AFTER ANNEALING

Figure 4.9: *Diffraction patterns of ZnO:Nd films deposited as a function of increasing neodymium comcentration for both before (a) and after annealing (b). The ZnO main crystallographic planes are identified in the plots; the Y scale was magnified to reveal the lowest intensity peaks. (c) Lattice 'c' parameter variation for ZnO:Nd samples deposited as a function of neodymium concentrations. The blue dotted line represents the 'c' parameter value of standard ZnO from ICDD card #36-1451.The red dashed line is to guide the eye. The grain size, D, values are also indicated for each sample.*

The lattice parameters (" a″ and " c″) of the films were calculated using the equation (2.5 in chapter 2) by considering the peaks corresponding to (002) and (110) planes. Due to the absence of (110) peak, the lattice parameter "a" cannot be estimated. At the same time, what can be observed is a slight shift in the position of the (0 0 2) peak toward lower angle side with increasing dopant level in the films. This shift allowed to calculate the corresponding variation in the c-axis length [1], which is plotted toward the bias applied on the Nd target in Fig. 4.9(c). The increase of this parameter for samples with low dopant content indicates that ZnO lattice expands along the c-axis when Nd atoms enter the matrix and substitute into the Zn^{2+} sites. Such an expansion can be qualitatively understood considering the size of the

ions involved in the doping process: the ionic radius of Nd^{3+} (0.995Å) is much larger than that of Zn^{2+} (0.74Å), which creates lattice strain and consequently increases the lattice parameter [14, 2, 15].

On the other hand, for films deposited with V_{Nd} more negative than -39 V, a strong reduction of the (0 0 2) peak intensity occurs, together with an abrupt decrease in the average crystallite size D, as shown in Fig. 4.9 (c). This indicates that the high level of Nd incorporation in the films restrains ZnO crystallites growth leading eventually to a visible deterioration of the ZnO wurtzite structure [14, 2, 15]. For a value of 0.19 and 2.1of Nd/Zn ratio (samples S4 and S5), the XRD peaks attributable to possible phases of Nd_2O_3 and $Nd(OH)_3$ become more intense and narrower than before annealing (Fig. 4.9 (b)). This means that at higher Nd concentrations, the crystal growth in zinc oxide was completely hindered and the Nd atoms were segregated from ZnO forming a co-existing nano-crystalline phase of Nd_2O_3 and $Nd(OH)_3$ in the films [10, 16, 17], in good agreement with the XPS analysis results.

The scanning electron micrographs presented for the samples after post-growth annealing at temperature (600ºC) in Fig. 4.10 closely reflect the above described structural changes. Pure ZnO films show a rather rough surface with large crystallites (Fig. 4.10-a) whereas at high concentration of Nd in the film, the material appears with grains of visibly reduced dimensions (Fig. 4.10-b).
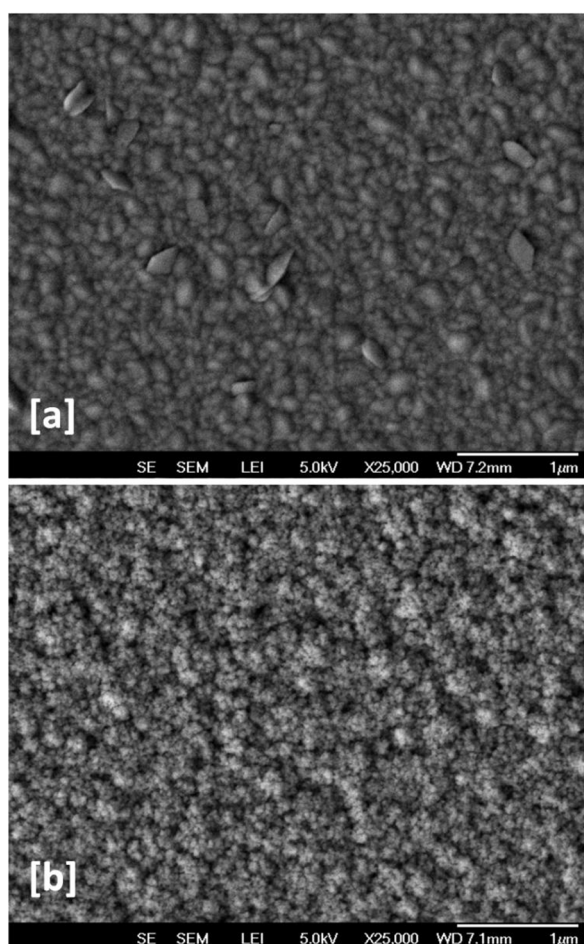
Figure 4.10: *SEM micrographs of (a) a pure ZnO film (sample S1) and (b) sample S5.*

4.2.5 Nd EFFECT ON PHOTOLUMINESCENCE PROPERTIES OF ZnO FILMS: EMISSION SPECTRA

The NIR luminescence spectra were measured for ZnO films with different Nd concentrations by exciting at two different wavelengths, resonantly using 476nm (Blue) of the Ar ion laser and also 355nm (Non-resonant through UV) of the Nd-YAG laser. The analyzed films containing Nd were S2, S3b, S4 and S5. In order to check whether the incorporated Nd ions are optically active in the matrix, direct excitation (in non-absorbing wavelength region of zinc oxide) were performed. We acquired the luminescence spectra at 902 nm and 1080 nm, pertaining to the transitions from the

excited level of the Nd^{3+} ion $^4F_{3/2}$ to $^4I_{9/2}$ and $^4I_{11/2}$, respectively. The relative spectra, normalized to the maximum intensity, are displayed in Fig. 4.11. As shown in the figure, upon excitation with the 476nm argon line, the emission bands originating from the lowest excited levels are observed in the spectral region between 800 – 1100 nm. The spectra were collected using a Si detector.
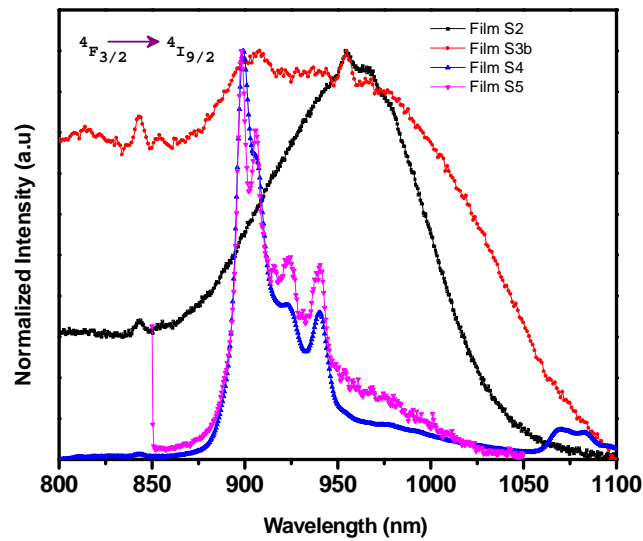
Figure 4.11: *Near-IR PL emission spectra of ZnO thin films (a) S2 (b) S3b (c) S4 and S5 (resonant excitation with 476 nm laser line).*

It can be noticed from the spectra, that as far as the films S2 and S3b are concerned, they exhibit characteristic broad NIR luminescence bands centered at 902 nm ($^4F_{3/2}$ to $^4I_{9/2}$). The results are totally different for the films S4 and S5. Intense and narrow bands were obtained in the range 859-950 nm and another band of lower intensity between 1050 and 110 nm. The spectrum is even more resolved for the sample S5. It is worth to know that in such films which contain a high amount of Nd (Nd/Zn = 0.19 and 2.1), even being in an oxide state, exhibits so well-defined spectra. This contrasts with the Nd-doped titania films. In the latter, in order to have good photoluminescence characteristics, Nd concentrations needed to be greatly reduced. A

162

very low Nd concentrations (Nd/Ti = 0.9 at.%) was necessary in titania matrix to obtain intense, sharp and resolved bands.

The appearance of luminescence upon excitation at 476nm motivated us to investigate the photoluminescence properties of the Nd-doped ZnO films through the host zinc oxide matrix, using 355 nm excitation (non-resonant excitation). However, it resulted that no photoluminescence emission was observed for any of the films containing Nd in a ratio to Zn as Nd/Zn $\geq$ 0.1. Therefore, it is recognized that only direct excitation of Nd^{3+} ions could be observed, and no efficient energy transfer occurs between activator and host matrix.

4.2.6 PHOTOLUMINESCENCE PROPERTIES OF LOW-Nd ZnO FILMS (Nd/ZnO< 0.1)

From the results given in the previous section, it comes that an interesting aspect of the problem is to find the optimal conditions of Nd-doping of the zinc oxide matrix for a efficient photon frequency down-shifting function. A detailed study was performed to investigate the photoluminescence properties by exciting resonantly (by 476 nm) and also through UV - (355 nm) non-resonant Nd excitation in ZnO: Nd films with very low Nd concentration.

Doping with relatively low (optimum) concentration is the center of interest and it is generally pursued in order to avoid separate cluster formation of neighboring dopants and also taking into consideration of luminescence quenching. The structural and compositional changes at the nanoscale level will strongly influence the photoluminescence emission characteristics of the material. Based on the former analyses, the lowest Nd concentration in the films was obtained when the self-bias voltage on Nd target was equal to -36V (Nd/Zn = 0.01 as in sample S3a). This

represents the lowest useful condition which can be used to grow ZnO films containing Nd by co-sputtering of ZnO and Nd targets. However such condition was not easily reproducible due to the fact the electrical power had to be fixed at only 3W, which is close to the lower limit of the power supply equipment used for this work. Second, a further lowering of V_{Nd} did not lead to Nd sputtering at all, being in voltage conditions close to or below the sputtering threshold. Therefore, we searched designing an alternative approach in order to optimize the deposition process with the reproducible stability and also to achieve a very low doping concentration and high luminescence intensity.

For this reason, in order to have a better control over the optical properties and the optimal concentrations, a bi-layer film approach was adopted with the sequence ZnO:Nd / ZnO, by fixing V_{Nd} equal to -41 volts (for a 4W power) and co-sputtering Nd and ZnO from the two targets for 30 min to grow a first layer (of a thickness of 80 nm) onto quartz substrates. The film deposition proceeded then with sputtering of only the ZnO target to grow a second layer on top of it. The properties of the films with this architecture were studied and compared with that of samples S1 (pure ZnO film) and S3a (ZnO:Nd grown with V_{Nd}= -36V, see Table 4.1). A film architecture sketch is displayed in Figure 4.12, labeling the bilayer film as sample S6.

All the samples were deposited for 450 minutes at room temperature to have overall average thickness of about 1 µm thick. After deposition, ex situ post-deposition annealing treatments were made for all the samples in ambient air at 600°C for six hours at a heating rate of 5°C/min.
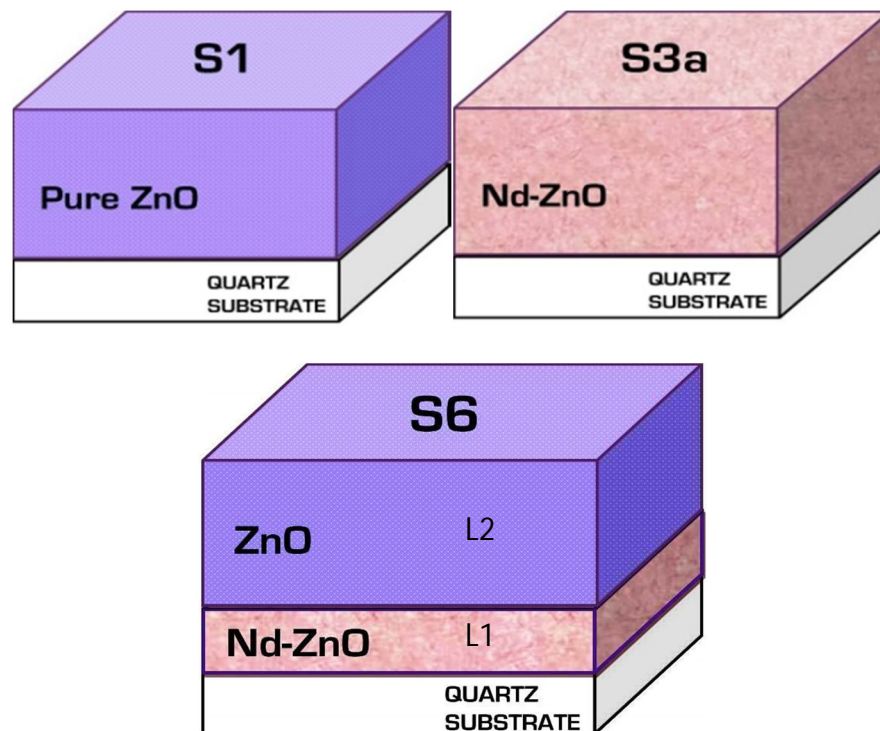
Figure 4.12: *Schematic illustration of the sample S1, S3a and S6.*

The initial Nd concentration in layer L1 (displayed in Fig. 4.12, sample S6) could be estimated on the basis of the evolution of the Nd/Zn atomic ration in function of V_{Nd}, shown in Fig. 4.13. The plot is based on the XPS results analysis of samples S3a, S3b, S4 and S5. For a V_{Nd} of -41 V, an approximate value of Nd/Zn of 0.10 can be extracted from an interpolated plot, which would correspond to a Nd concentration [Nd] ~ 4.7 at.% in layer L1. In the annealed bilayer films, Nd was expected to be further diluted in the pure ZnO layer on top of it to reach a very low concentration through the film, although it iss difficult to determine the depth concerned by Nd diffusion.
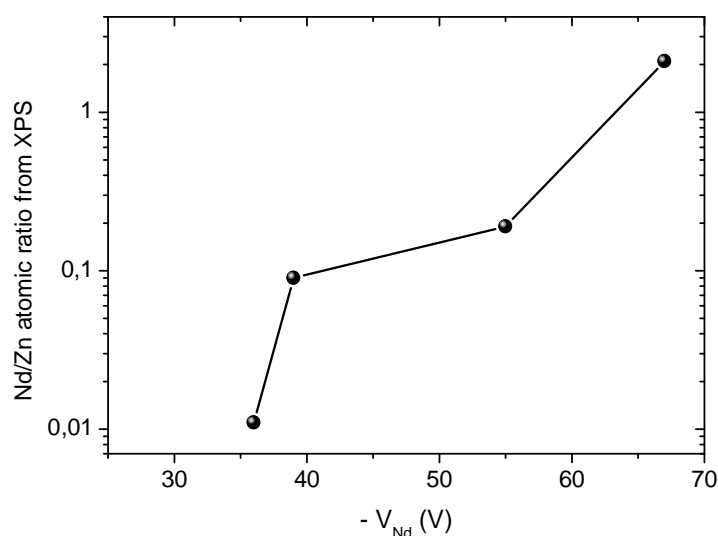
Figure 4.13: *Nd/Zn atomic ratio in function of the self-bias voltage at Nd target, values obtained by XPS. The line is to guide the eye.*

4.2.7 QUANTIFICATION OF LOW NEODYMIUM CONTENTS FROM AES AND XRF IN THE BI-LAYER FILM.

As already reported in Table 4.2, the average relative atomic concentration of Nd in Sample S3a was found by AES to be 0.9 at. %, corresponding to a Nd/Zn ratio equal to 0.02. Nd in the bilayer sample S6 was not detected by AES after annealing. An estimation of its concentration has been obtained by X-Ray Fluorescence Analysis. As in the case of Nd-doped titania films, combined use of analytical techniques such as Auger Electron Spectroscopy and X-Ray Fluorescence analysis allowed to estimate the low Nd concentration also for this sample.

Figure 4.14 shows the XRF spectra of samples S3a and S6. The ZnKα (KL_2, KL_3 transitions) and NdLβ (L_1M_3, L_2M_4 transitions) intensities were extracted by peak fitting with IAEA WinQXAS software [18, 19] and used for the quantification. Acquisition times for samples S6 and S3a were 44000 sec and 2000sec respectively.
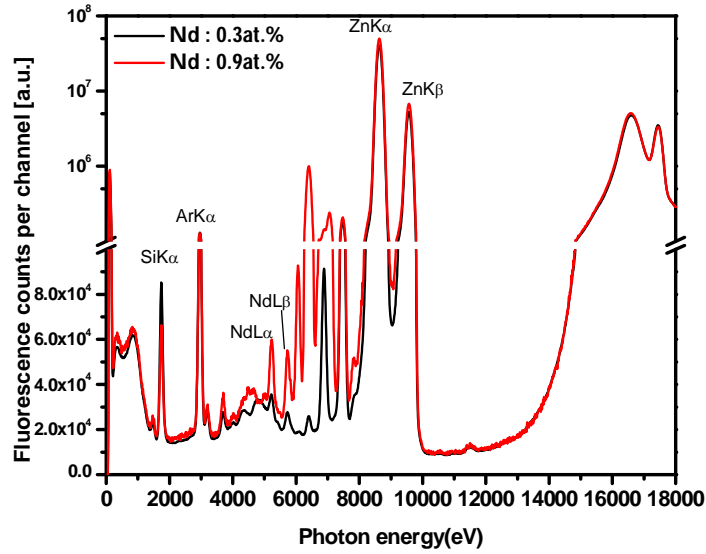
Figure 4.14: *X-ray fluorescence spectra (XRF) for sample (T3-0.3at.% and T2-0.9at.%). Spectra are normalized to the same livetime.*

Samples S6 and S3a present the same matrix (ZnO), not altered by the low concentration of Nd. In this dilute regime a linear behavior of the Nd/Zn fluorescence counts is expected [20]. Hence a one point calibration was performed using sample S3a as standard and calculating the concentration of Nd in sample S6 according to equation, which was estimated to be 0.3at.% in ZnO matrix.

$$CS6 = \frac{\left(\dfrac{Ndcounts}{Zncounts}\right)_{S6}}{\left(\dfrac{Ndcounts}{Zncounts}\right)_{S3a}} C_{S3a}$$

Values of the measured XRF counts are given in Table 4.5. It is worth noting that this value is in fair agreement with the one obtained by approximating a Nd concentration in all the film, found as [Nd] = 0.33 at., by considering the Zn and O atoms number in the whole bi-layer thickness. It was obtained by dividing [Nd] in layer L1 by the thickness ratio L1/(L1+L2).

Samples analyzed by XRF

Transition	S3a	S6
NdLβ counts	12493	84190
ZnKα counts	33363937	590531083

Quantification by AES and XRF

V_bias on Nd target [V]	at.% [Nd]	at.% [Zn]	at.% [O]	at.% [C]	at. ratio (Nd/Nd+Zn)
Sample S3a	from AES 0.9	50.1	47.72	0.77	0.02
Sample S6	from XRF 0.3				

Table 4.5: *Elemental quantification by AES and XRF for Nd doped Zinc Oxide thin films*

4.2.8 FILM STRUCTURE FROM XRD ANALYSIS

Figure 4.15 shows a comparison of the XRD patterns obtained for annealed films of undoped ZnO with those obtained for films doped with low concentrations of neodymium in a grazing angle incidence (3°) configuration. All films were nanocrystalline and the diffraction peaks can be indexed to hexagonal Wurtzite structure. The most prominent peak observed in all the films corresponds to (1 0 1) plane. In addition to the dominant peak, other reflections such as (1 0 0), (0 0 2), (1 0 2), (1 1 0), (1 0 3), (2 0 0), (1 1 2) and (2 0 1) crystallographic planes have also been observed but with relatively lower intensities (ICDD card # 36 - 1451). No other impurity peaks corresponding to Nd metal clusters or other oxide compounds such as

(Zn, Nd_2O_3, Zn $(OH)_2$, mixed composite phase of ZnO- Nd_2O_3) were detected in any of the samples, which imply that the doped Nd atoms were well incorporated into the lattice sites of hexagonal ZnO host matrix.

The figure shows the variation in the peak intensities and the peaks corresponding to (100) and (200) plane became indistinguishable upon Nd incorporation. Substantially in comparison with the pure ZnO film, increasing the neodymium concentrations caused a slight shift in the 2θ position of the peak (101) towards lower diffraction angles. This shift in the position of the peak arises from an increase of local strain around impurity or from lattice defects related to the impurity atoms [21]. One of the main obstacle in order to have effective incorporation of Nd ions into ZnO lattice is the great mismatch of ionic radii between the dopant (Nd^{3+}) and the host Zn ions in order to replace the Zn^{2+} sites by Nd atoms. The significant features in the XRD pattern of the Nd doped samples are the reduction in the intensity and increase in the full width half maximum (FWHM). The most dominant peak (101) of sample S6 (0.3at. %) and S3a (0.9at. %) with respect to sample S1 are broader (gradual increase in FWHM), which results from the change in the crystallite size and /or random lattice strain. The (101) peak broadening with the incorporation of Nd atoms in ZnO, is in agreement with [22], which may be caused by the increase in the lattice strain contribution in addition with the grain boundary defects, which in turn reflects in the decrease of intensity of the corresponding peaks.
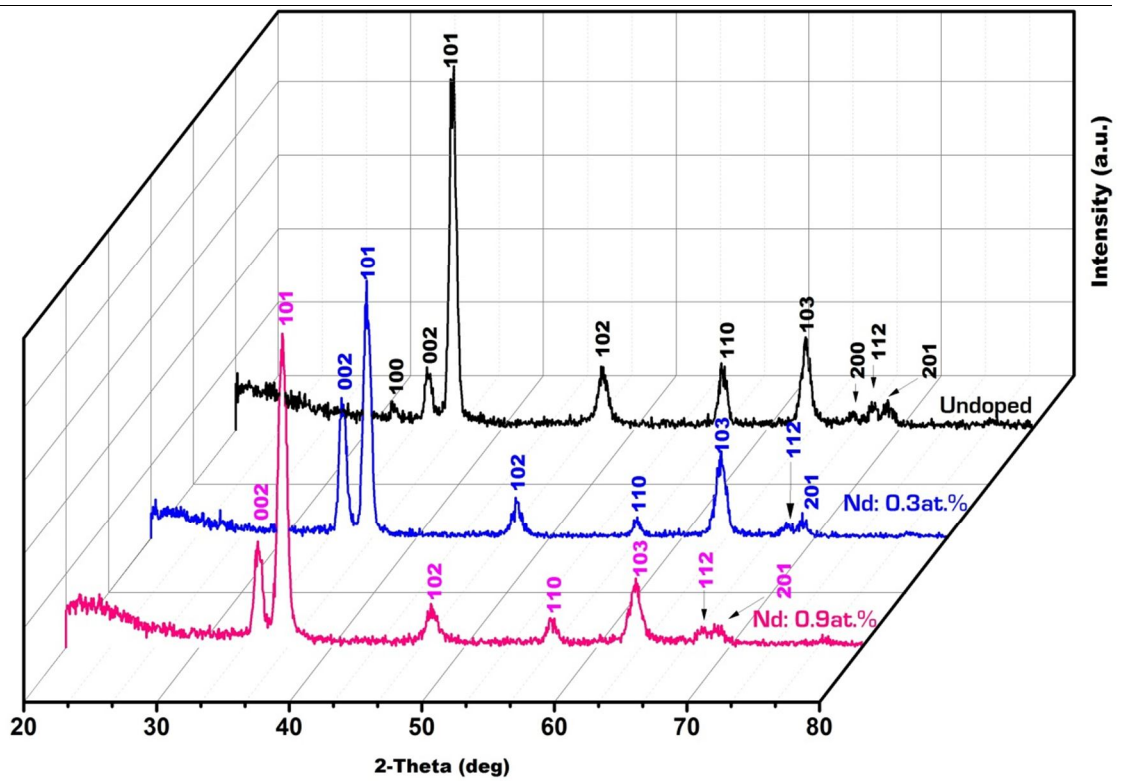
Figure 4.15: *X-ray diffraction (XRD) patterns of Pure and Nd³⁺ doped ZnO samples annealed at 600°C as a function of different neodymium concentration*

Nd [at.%]	Highest peak position 2θ [deg]	FWHM	Crystallite size D [nm]	Lattice Parameter [Å]		Internal Strain [η] %
				a	c	
0	36.37	0.563	23.6 ± 4.5	3.243	5.194	0.74 ± 0.30
0.3	36.30	0.615	38.1 ± 23	3.247	5.201	1.93 ± 0.52
0.9	36.30	0.704	30.9 ± 17.3	3.247	5.20	1.95 ± 0.59

Table 4.6: *Summary of XRD data for Pure and Nd doped zinc oxide thin films*

Taking into consideration the lattice constants for the hexagonal structure (a=b≠c), lattice parameters ("a" and "c") of the films were calculated using the equation

below, by considering the peaks corresponding to (002) and (110) planes,

$$\frac{1}{d^2} = \frac{4}{3a^2}(h^2 + hk + k^2) + \frac{l^2}{c^2}$$

Due to the incorporation of very low concentration of Nd in the ZnO matrix, there is only slight change in the lattice parameters were observed (lattice expansion along 'c' axis and 'a' even though much less evident) in comparison with the pure ZnO which confirms the probable existence of Nd ions in ZnO lattice in the interstitial sites. The incorporated Nd atoms into the crystal lattice of ZnO induce the strain into the system resulting in alteration of the lattice periodicity and decrease of crystal symmetry. The lattice strain caused by the large mismatch was found to be tensile (i.e., positive values). The larger the size of the crystallites, higher the tensile strain. The increase in tensile strain suggests that Nd ions induce the lattice distortion on doping with ZnO matrix. This reflects the fact that on doping with low concentration of neodymium, the film undergoes lattice disorder due to the incorporation of the Nd^{3+} ions into the Zn^{2+} sites, leading to the increase in the lattice strain.

4.2.9 FILM STRUCTURE FROM RAMAN SPECTROSCOPY

4.2.9.1 Assignment of Raman bands

Raman scattering spectroscopy is a non-destructive characterization method to study the phase and purity and the vibrational properties of ZnO including doping stress/strain in the material, and the phonon interactions. ZnO crystallizes in hexagonal structure belongs to wurtzite type with the space group C_{6v}^4 (P6$_3$mc) with two formula units per primitive cell as all atoms occupy C_{3v} sites. Each Zn is tetrahedrally surrounded by four oxygen atoms. According to group theory, the optical phonons irreducible representation is given by $1A_1 + 2B_1 + 1E_1 + 2E_2$. Among

these optical modes, A_1 and E_1 symmetry are polar and can split into two namely transversal acoustic (TO) and longitudinal optical (LO) modes. The A_1 mode is Raman active while the B_1 and E_1 modes are both Raman inactive. Non polar modes of phonons E_2 symmetry exhibits two frequency modes, E_2^{high} and E_2^{low}. The former E_2^{high} frequency mode is associated with oxygen atoms while the latter E_2^{low} is associated with vibrations of heavy Zinc sublattice.
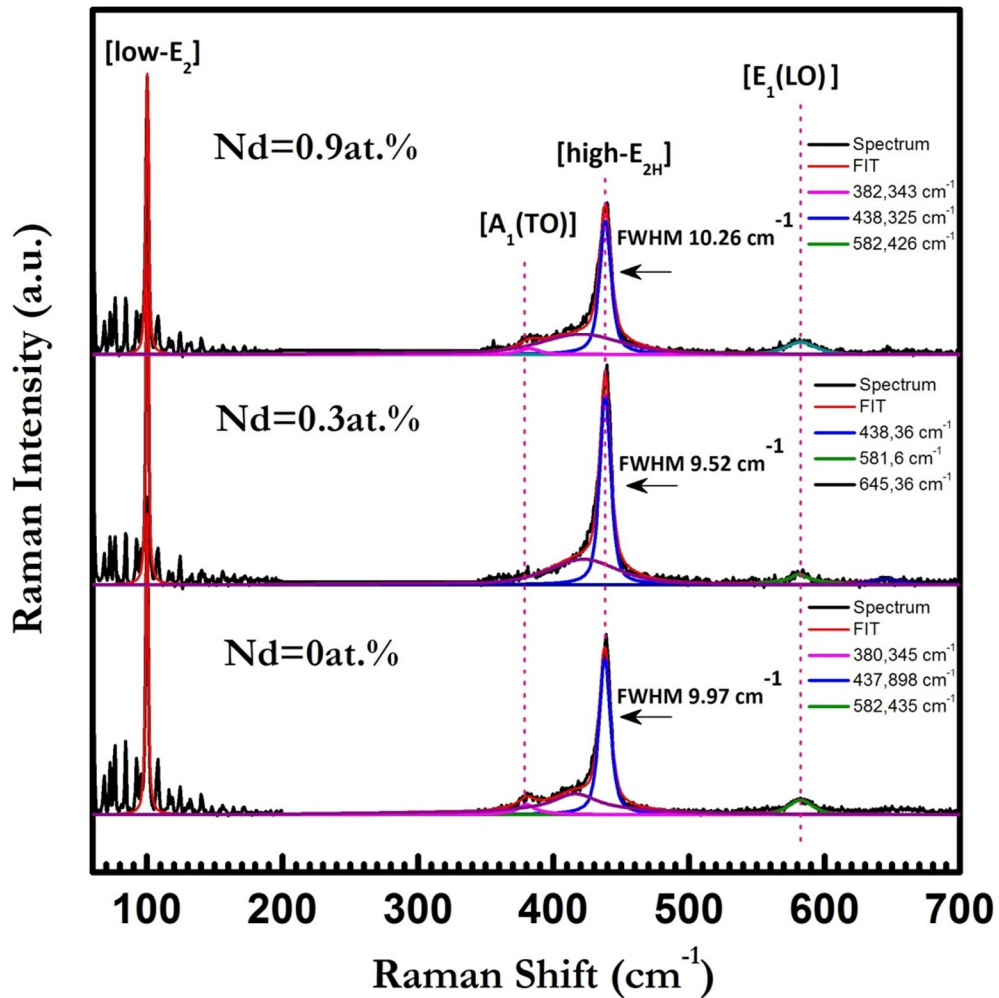
Figure 4.16: *Visible Raman spectra of ZnO thin films containing 0at.% (film S1),0.3at.% (film S6) and 0.9at.% of Nd (film S3a), acquired with the laser excitation line at 514.5 nm. The legends give the peak positions obtained from the fit of the E_2^{high} and $E_1(LO)$ peaks.*

From the Figure 4.16 one can observe a total of five Raman peaks of different

intensities for film S1: two intense peaks at 100 cm^{-1} and 437.89 cm^{-1} and a weaker one at 582.43 cm^{-1}. Peak deconvolution was performed using Gaussian- Lorenzian peak fit into individual components which position is given in the legend. One of the most intense narrow peak (FWHM ~2cm^{-1}) observed at 100.2 cm^{-1}[E_2^{low}], ascribed to the vibrations of Zinc sublattice in ZnO. The strong intensity of the peak at 437.89 cm^{-1}assigned to E_2^{high} mode indicates good crystallinity. The presence of E_2^{high} mode in all the samples reveals that Nd doping does not alters the wurtzite structure of ZnO.

Peak positions (cm-1) Sample S1 – Pure ZnO	Peak assignments	Peak positions from literature (cm-1) for ZnO [23]
100.2	E_2^{low}	99
380.34	A$_1$(TO)	378
415.37	E$_1$(TO)	410
437.89	E_2^{high}	438
582.43	E$_1$(LO)	590

Table 4.7: *Observed Raman peaks assignments for the pure ZnO thin films annealed at 600°C in comparison with the literature data.*

Nd at. conc. (%)	Peak positions (cm^{-1}) For E_2^{high}Raman mode	FWHM (cm^{-1})	Δω (shift in E_2^{high} mode w.r.to bulk ZnO)	Calculated strain based on the shift in E_2^{high} mode
0	437.9	9.97	-0.6	-0.09
0.3	438.36	9.52	-0.04	-0.007
0.9	438.32	10.26	-0.1	-0.01

Table 4.8: *Raman peak positions and FWHM of E_2^{high} mode for annealed pure (S1) and Nd- doped ZnO thin films /S3a and S6). The parameters are explained in the text.*

The peak at 582.43cm^{-1} E$_1$(LO) mode is attributed to the impurities and structural defects like oxygen vacancies [V$_o$] and or excess Zn at lattice sites and interstitial positions [24]. The wavenumber red-shift and the increase in the full width at half maximum (FWHM) of the E_2^{high} mode suggest the contribution of several factors like phonon confinement, defects, strain caused by doping and annealing. Here the phonon confinement can be ruled out as the crystallite dimension is more than 30 nm. Here we can anticipate that shift and broadening can be due to the defects in ZnO and strain caused due to lattice distortion, as the FWHM of E_2^{high} increased in comparison with the pure ZnO film with the increase in the Nd concentration. This is because of the large ionic radii of Nd^{3+} compared to Zn, new lattice defects might be created when Nd substitutes the Zn^{2+} ions. An increase in the relative intensity of E$_2$ mode for 0.9at.% of Nd is observed due to the larger particle size calculated from XRD. The strain induced can be calculated from the shift of E$_2$ high mode peak position. Grubel et al [25, 26] have reported the influence of biaxial strains on the vibrational and exciton energies in wurtzite type ZnO. Considering the peak position of E$_2$ high and the strain along c, ε$_{cc}$,

$$\Delta \omega = \left[b - a \left(\frac{C_{33}}{C_{13}} \right) \right] \varepsilon_{cc}$$

where a and b are the phonon deformation potential parameters and C$_{13}$ and C$_{33}$ are the elastic constants and Δω is the difference between the peak position of bulk ZnO (438.4 cm^{-1}) and obtained E$_2$ mode peak position for the samples. The quantity (i.e., slope) inside the brackets was calculated by Grubel *et al* [25] and it is found to be 527 ± 25cm^{-1}. The calculated Δω and the strain value are given in the table 4.8. From the table, Raman peak position (E$_2$ high) shows a maximum red shift as compared to the undoped ZnO, which means that the tensile strain dominates over the compressive

one on Nd doping, which is in accordance with the internal strain calculated from the XRD.

4.2.10 OPTICAL PROPERTIES: TRANSMITTANCE, BANDGAP ESTIMATION

The optical analyses on these films were systematically performed in order to determine the optical bandgap of the films. The optical transmission and reflectance spectra in the wavelength range 200 - 2500 nm for the annealed films are shown in Figure 4.17. The average optical transmission in the visible region is high (75-80%), but the transmission decreases substantially at short wavelengths reflecting the absorption edge of the film.

The oscillating shape on the spectra is due to the film thickness and consequently with the interference effect in the layer. The average value of reflectance of the films is about 10-20% in the visible region. The films shows a strong absorption onset at ~380 nm, which corresponds to the excitonic transition of ZnO.
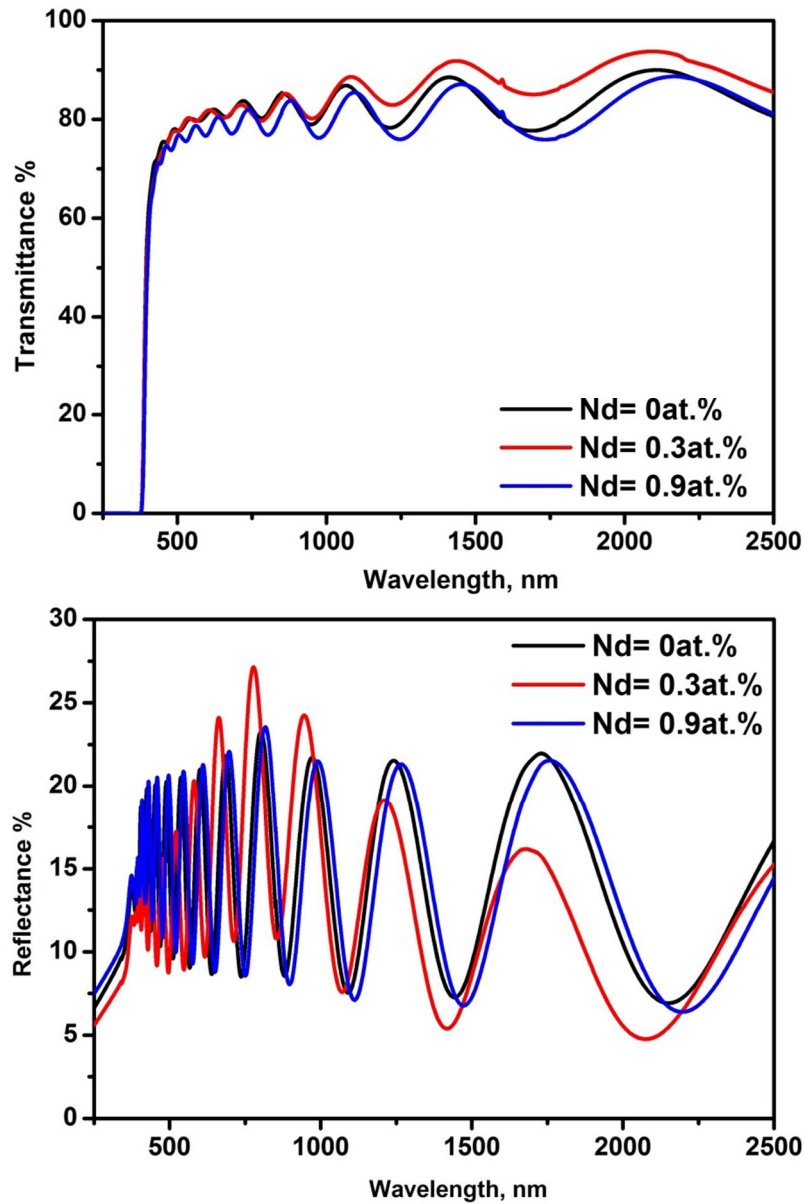
Figure 4.17: *UV –visible near IR spectra of Nd doped ZnO films on quartz substrates - Optical Transmittance and the reflectance spectra of the corresponding films*

It is seen that the fundamental absorption edge extended towards longer wavelength (red-shifted) as the neodymium concentration increased. The energy of the direct band gap values were calculated by using Tauc's equation. From the results of Tauc's plot shown in Figure 4.18, the optical bandgap for the ZnO thin films varies with neodymium concentration for the samples.
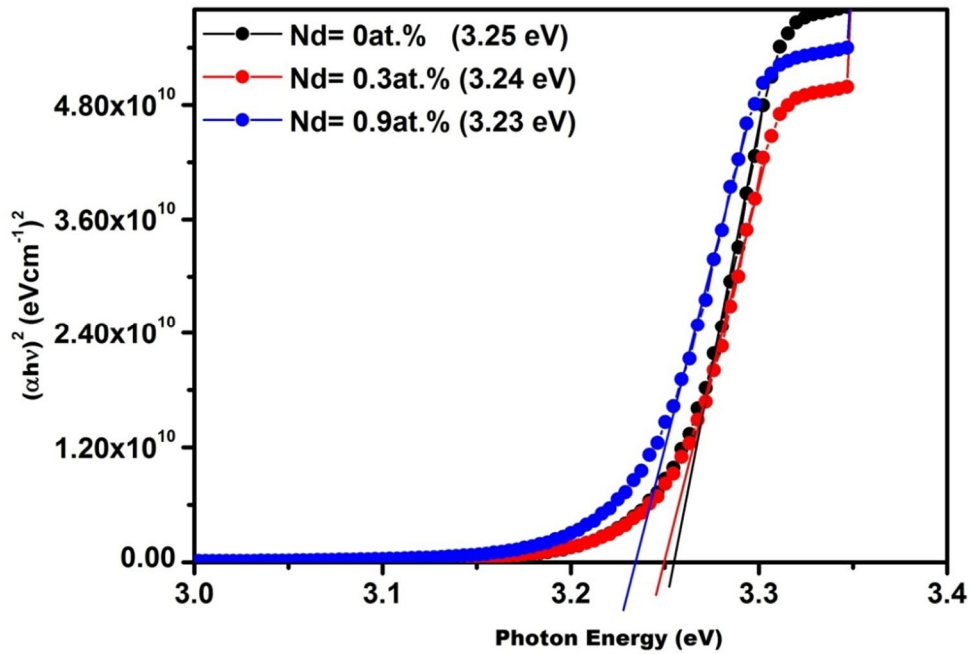
Figure 4.18: *UV –visible near IR spectra of Nd^{3+} doped ZnO films on quartz substrates - Estimation of bandgap $(\alpha h\nu)^2$ vs. hν*

A slight change in the band gap energy (E_g - 0.02eV) was observed as increase in the doping concentration as 3.25, 3.24 and 3.23 eV which corresponds to very small bandgap narrowing when Nd is incorporated in ZnO film. This red shift is much less than what reported earlier by Li *et al* in TiO$_2$ (0.55eV) and Liu *et al* in ZnO (0.06eV) matrix [27, 28]. In the latter case, the results were explained by the introduction of new unoccupied energy level into the bandgap (close to the lower edge of conduction band edge) of ZnO energy levels. These results are in contradiction with the recent report [29] showing a bandgap increase with increasing the Nd content in ZnO matrix synthesized by sol-gel route, with a doping ratio (Nd/[Nd+Zn]) varying from 1% to 5%. This was mainly attributed to the quantum size effect as well as the strong interaction between the surface oxides of Zn and Nd. This suggests that there is an optimum doping limit, annealing temperature and environment in order to attain the effective band gap narrowing.

4.2.11 PHOTOLUMINESCENCE PROPERTIES - EMISSION SPECTRA UNDER VISIBLE & UV- EXCITATION

In order to check whether the incorporated Nd ions are optically active, the near-IR emission spectra were acquired at room temperature for ZnO films doped with low concentrations of neodymium. The photoluminescence (PL) properties of these samples under excitation at two different wavelengths: laser blue line (476nm, 2.6eV) and UV excitation (355nm, 3.49eV) were investigated. Under a band-to-band optical excitation the neodymium doped ZnO material emitted NIR luminescence characteristic of Nd ions in a trivalent charge state. Figure 4.19 illustrates the PL emission spectra of the annealed ZnO:Nd with [Nd] =0.3at.% (sample S6) and 0.9at.% (S3a) measured under the 476nm argon line excitation (below bandgap pumping).
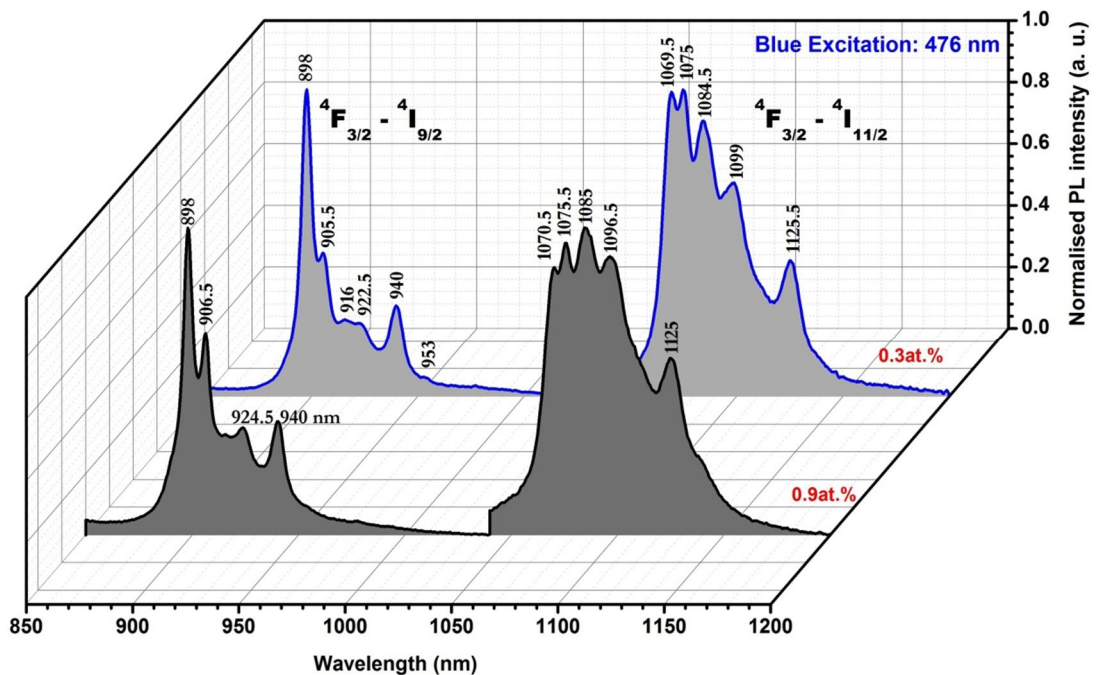
Figure 4.19: *Near-IR PL emission spectra of ZnO thin films doped with (a) 0.3at.% and (b) 0.9at.% of Nd excited at 476 nm (Resonant Excitation)*

For both the samples, the excitation power of 200mW was used. Sharply structured PL emission bands of Nd^{3+} ions were observed corresponding to the optical transitions from the levels $^4F_{3/2}$ to $^4I_{9/2}$ and $^4F_{3/2}$ to $^4I_{11/2}$ respectively. The band observed in the region 850-960 nm corresponds to the transition of $^4F_{3/2}$ to $^4I_{9/2}$ and consists of six well resolved components centered around 898 nm. The band observed in the region 1050-1200 nm is attributed to the transition of $^4F_{3/2}$ to $^4I_{11/2}$ with five well resolved Stark splitting. These resolved components indicate that the Nd ions occupy a few well-defined lattice sites. The obtained emission patterns indicate that the local structure of Nd^{3+} ions in ZnO matrix differs from that of the Nd_2O_3 phase [30]. The 476 nm photon is resonant with the transitions of Nd^{3+} ions from the ground state to one of the excited state centered around $^2G_{9/2}$. This can be attributed to the fact that resonant excitation directly excites the Nd ions giving rise to a sharp emission line with high intensity.

The appearance of PL emission spectra upon resonant excitation with 476 nm argon line motivated us to excite the zinc oxide host through UV-355 nm (3.49eV- above the bandgap of ZnO) to investigate the possibility of a frequency downshifting effect through the energy transfer between the host and the rare earth ions. Figure 4.20 illustrates the PL emission spectra in the near IR region upon excitation at 355 nm of YAG laser line with a pumping power of 10mW. Appreciable spectral feature was observed by exciting ZnO with photons of energy higher than the band gap leads to the broadband NIR luminescence covering the region 880 - 960 nm pertaining to the optical transitions $^4F_{3/2}$ to $^4I_{9/2}$ levels. This indicates that, through non resonant excitation, near infra-red Nd^{3+} emissions can be achieved via an non-radiative energy transfer process presumably through defects from ZnO to Nd^{3+} ions as there is no direct absorption of Nd^{3+} at 355 nm.
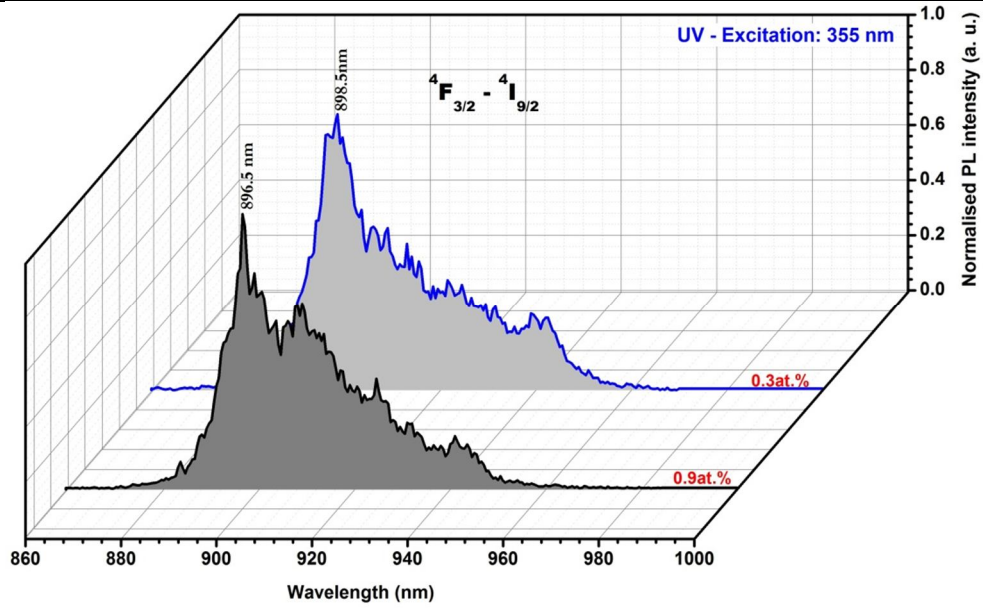
Figure 4.20: *Near-IR PL emission spectra of ZnO thin films doped with (a) 0.3at.%, (b) 0.9at.% of Nd excited at 355 nm (Non-Resonant Excitation)*

The second PL emission band of Nd^{3+} ion corresponding to the transition $^4F_{3/2}$ to $^4I_{11/2}$ (1050-1100 nm) cannot be observed because the fundamental harmonic of the Nd-YAG laser falls exactly at 1064 nm, which completely overshadows the much weaker PL signal. Moreover, after the careful observation of these two resonant and non-resonant excitations, the emission patterns are completely different in respect to shape and positions, indicating the non-uniform crystalline local structure surrounding around Nd^{3+} ions. Therefore the obtained emission spectra when exciting at 355 nm might be the superposition of all emissions from various subsets of Nd^{3+} which in turn confirms the existence of different luminescence centers of Nd^{3+} in ZnO matrix. However since the signal intensity upon excitation at 355nm was very low we cannot be certain if this broadening of the pattern is not just due to the noise of the detector.

No Nd^{3+} emission was observed for the as-deposited samples, probably due to quenching caused by high energy vibrations of impurities such as H_2O adsorbed at the surface [31]. There are a number of models treating the energy transfer (ET) from host

to incorporated RE impurities. They illustrate the mechanism of energy transfer from ZnO host to RE^{3+} through defect mediated energy transfer process. After the formation of an electron-hole pair in ZnO host upon excitation, exciton recombination will transfer its energy presumably to the Zn related defects. Some excited defects transfer their energy non-radiatively to one of the excited state of Nd, followed by subsequent non-radiative relaxation eventually leading to NIR emissions of Nd^{3+}. In this case, the defects might be the oxygen vacancies $[V_o]$, Oxygen interstitials $[O_i]$, Zinc vacancies $[V_{Zn}]$ or Zinc interstitials $[Zn_i]$ which can also acts as luminescent center and also as a luminescence quencher [32, 33] in competition with the NIR emissions of Nd^{3+}. This might also limits the energy transfer efficiency and the NIR photoluminescence intensity.

4.3   CONCLUSIONS

The effect of neodymium on the microstructure and chemical structure of ZnO thin films prepared by RF co-sputtering were studied. A detailed characterization of the pure and doped ZnO films, performed by AES, XPS, XRD techniques, allowed a complete description of the material evolution in function of the Nd doping level. In fact, marked structural modifications turned up together with variations in the films composition. In particular, at low Nd atomic concentration (Nd/Zn $\leq$ 10%) Nd atoms appeared to be successfully incorporated into the ZnO matrix, whose crystalline structure was maintained. A deterioration of the wurtzite phase was observed on the contrary with increasing Nd doping level to have Nd/Zn above 10%, which inhibits growth of ZnO crystallites. The study allowed in other words to determine the Nd concentration limit in the host matrix beyond which dopant clustering may occur. Nd atoms segregation consisted in the precipitation of a different Nd-containing phase,

which we could identify as Nd_2O_3 and hydroxylated oxide. In such films, the PL spectra under visible excitation were intense and well-resolved. However, no NIR emission was observed under UV light excitation.

Obviously, an adequate approach is absolutely essential in finding the optimal doping concentrations and explaining the relationship between the optimal doping ratio and their photoluminescence performance. Nd- doped ZnO thin films with two different low concentrations ([Nd] = 0.3at.% and 0.9at.% of Nd) were prepared and their optical and near-infra red photoluminescence properties were investigated. No abrupt changes were observed in terms of crystallinity point of view, all the films were with wurtzite structure like the un-doped ones. Evolution of the local lattice distortion (increase in the lattice strain and small variation in the lattice parameter) with the low Nd concentration allowed us to clarify the most probable location of the rare earth ions in the structure. Furthermore PL measurements of the deposited films gave promising results, in particular, exciting with energy slightly above the bandgap of zinc oxide (355 nm) results in the NIR luminescence, which suggests a possibility of energy transfer process from the host matrix which is yet to be studied. However, we have shown the optimal deposition conditions in order to achieve NIR luminescence exciting in UV with the possibility of energy transfer from the matrix, which can serve as a solid background for further investigations. The evidence and the mechanism of the energy transfer characteristics based on PL excitation and emission spectra, and life time characteristics will be discussed in the next chapter.

REFERENCES

[1]. M. Subramanian, P. Thakur, S. Gautam, K.H. Chae, M. Tanemura, T. Hihara, S. Vijayalakshmi, T. Soga, S.S. Kim, K. Asokan, R. Jayavel, *Journal of Physics D:Applied Physics* 42 (2009) 105410–105415.

[2]. Z.Y. Huang, P. Luo, M. Chen, S.R. Pan, D.H. Chen, *Materials Letters* 65 (2011) 2345–2347

[3]. Y. Liu, W. Luo, R. Li, H. Zhu, X. Chen, *Optics Express* 17 (12) (2009) 9748–9753.

[4]. H.T. Cao, Z.L. Pei, J. Gong, C. Sun, R.F. Huang, L.S. Wen, *Journal of Solid State Chemistry* 177 (2004) 1480–1487.

[5]. N. Asakuma, T. Fukui, M. Toki, K. Awazu, H. Imai, *Thin Solid Films* 445 (2003) 284–287.

[6]. S. Ben Amor, M. Jacquet, P. Fioux, M. Nardin, *Applied Surface Science* 255 (2009) 5052–5061.

[7]. U. Meier, C. Pettenkofer, *Applied Surface Science* 252 (2005) 1139–1146.

[8]. N. Laidani, P. Cheyssac, J. Perriere, R. Bartali, G. Gottardi, I. Luciu, V. Micheli, *Journal of Physics D: Applied Physics* 43 (2010) 485402–485413.

[9]. M. Yuan, J. Zhang, S. Yan, G. Luo, Q. Xu, X. Wang, C. Li, *Journal of Alloys and Compounds* 509 (2011) 6227–6235.

[10]. X.M. Wang, X.Q. Zeng, G.S. Wu, S.S. Yao, L.B. Li, *Applied Surface Science* 253 (2007) 9017–9023.

[11]. Y. Uwamino, Y. Ishizuka, H. Yamatera, *Journal of Electron Spectroscopy and Related Phenomena* 34 (1984) 69.

[12]. W.P. Yang, D. Costa, P. Marcus, *Journal of the Electrochemical Society* 141 (1994) 2669.

[13]. H.P. Marques, A.R. Canario, A.M.C. Moutinho, O.M.N.D. Teodoro, *Applied Surface Science* 255 (2009) 7389

[14]. B. Roy, S. Chakrabarty, O. Mondal, M. Pal, A. Dutta, *Materials Characterization* 70 (2012) 1–7.

[15]. R. Saleh, S.P. Prakoso, A. Fishli, *Journal of Magnetism and Magnetic Materials* 324 (2012) 665–670.

[16]. R. Yu, K. Yu, W. Wei, X. Xu, X. Qiu, S. Liu, W. Huang, G. Tang, H. Ford, B. Peng, *Advanced Materials* 19 (2007) 838–842.

[17]. L. Zhao, Z. Wang, D. Han, D. Tao, G. Guo, *Materials Research Bulletin* 44 (2009) 984–988.

[18].   WINQXAS Ver. 1.3, Software Package for Energy Dispersive X-Ray Fluorescence Analysis, IAEA Evaluation Report 2002.

[19].   http://www.iaea.org/OurWork/ST/NA/NAAL/pci/ins/xrf/pciXRFdown.php

[20].   R. Pandiyan, V. Micheli, D. Ristic, R. Bartali, G. Pepponi, M. Barozzi, G. Gottardi, M. Ferrari and N. Laidani, *J. Mater. Chem.* **2012**, *22*, 22424–22432.

[21].   Z. Sofiani, B. Derkowska, P. Dalasiński, M. Wojdyła, S. Dabos-Seignon, M. Alaoui Lamrani, L. Dghoughi, W. Bała, M. Addou and B. Sahraoui, *Opt. Commun.* 267 (2006) 433-439

[22]   Surender Kumar and P.D. Sahare, *J. Rare Earth* 30 (2012) 761-768

[23].   R. Cusco, E. Alarcon-Llado, J. Ibanez, L. Artus, J. Jimenez, B. Wang, M. J. Callahan, *Phys. Rev. B* 75 (2007) 165202.

[24].   M. Scepanovic, M. Grujic-Brojcin, K. Vojisavljevic, S. Bernik, T. Sreckovic, *J. Raman Spectrosc.* 41 (2010) 914-921

[25].   Th. Gruber, G. M. Prinz, C. Kirchner, R. Kling, F. Reuss, W. Limmer, and A. Waag *J. Appl. Phys.* 96 (2004) 289

[26].   Sahoo, Satyaprakash, Sharma, G. L. Katiyar, Ram. S. *J. Raman Spectrosc.* 43, 72, (2012)

[27].   W. Li, Y. Wang, H. Lin, S. Ismat Shah, C. P. Huang, D. J. Doren, S. A. Rykov, J. G. Chen *and* M. A. Barteau, *Appl. Phys. Lett. 83 (2003) 4143-4145.*

[28].   Y. Liu, W. Luo, R. Li, X. Chen, *J. Nanosci. Nanotechnol.* 10 (2010) 1871-1876

[29].   F. Xian and X. Li, *Opt. Laser Technol.* 45 (2013) 508-512

[30].   R. Yu, K. Yu, W. Wei, X. Xu, X. Qiu, S. Liu, W. Huang, G. Tang, H. Ford and B. Peng, *Adv. Mater.* 19 (2007) 838–842

[31].   Y. Liu, W. Luo, R. Li, H. Zhu and X. Chen, *Opt. Express* 17 (2009) 9748-9753.

[32]   K. Vanheusden, W. Warren, C. Seager, D. Tallant, J. Voigt, *J. Appl. Phys.* 79 (1996) 7983.

[33]   J. Lim, K. Shin, H.W. Kim, C. Lee, *J. Lumin.* 109 (2004) 181.

Chapter 5

Chapter 5
Study of the matrix-sensitized photoluminescence mechanism of nd³⁺ ion

"It is most necessary to avoid rusticity in any way,
whether in material, design, or execution"
-George Edmund Street

5.1 INTRODUCTION

This chapter reports the investigation results of the activation process of luminescent Nd^{3+} ions by the electronic structure of titanium dioxide and zinc oxide matrices. Some of the spectroscopic analyses presented in this thesis (in Chapters 3 and 4 for TiO_2 and ZnO respectively) gave a glimpse of fundamental importance as well to understand the physical nature of energy transfer mechanism between the dopant ions and the host matrix. Understanding the mechanism of NIR PL emission is of great importance for controlling and also enhancing the optical properties of novel materials. Recently considerable effort has been made by many research groups in order to understand the mechanism behind the luminescence and the energy transfer in oxide nanomaterials. Some of them are based on resonant energy model [1], defect-mediated energy transfer model [2, 3, 4], bound exciton models [5, 6], shallow donor or acceptor models [7] etc. In this chapter, we investigate the energy transfer mechanism that occurs between Nd^{3+} and TiO_2 and Nd^{3+} and ZnO. For this aim, the samples subjected to analyses contained low concentrations of Nd^{3+} in both the matrix

(i.e. only for the samples observed with high PL emission, based on the previous results described in the Chapters 3 and 4), in order to avoid luminescence quenching. Firstly, the excitation wavelength dependence NIR photoluminescence emission were thoroughly studied by exciting these matrices with energy (or wavelength) values under non-resonant conditions with the $^4F_{3/2}$ level of Nd, i.e., indirect excitation through UV range from 300nm to 400nm. Secondly, analysis of the photoluminescence excitation (PLE) and emission spectra were studied, which revealed a clear evidence of an energy transfer existence between host matrix and rare earth ion. Further, the lifetime characteristics of the emitting state in the presence of energy transfer processes are clearly addressed. Finally, the dependence of the lifetime upon the different excitation energy in both systems has been discussed which provides further insight in the efficiency of the energy transfer process.

The investigation of the nature of the energy transfer mechanism between the host matrix and the Nd^{3+} ion was pursued by investigating the PL properties of another matrix, Al_2O_3, deposited by RF sputtering and which has a large band gap (~6eV in the case of γ-alumina). This chapter reports also the results on the spectroscopic investigations performed on the Neodymium doped Aluminium oxide (Al_2O_3) thin films, as an alternative host matrix deposited by RF co-sputtering.

5.2 THE SAMPLE PREPARATION AND CHARACTERIZATION

Based on the previous results from Chapter 3 (Nd –doped TiO_2) and Chapter 4 (Nd – doped ZnO), the samples prepared with low concentration of neodymium were taken as a choice for this study.

For the study of Nd –doped Titania, intense NIR photoluminescence emission were observed for the samples having concentration of Nd/Ti= 0.9% (doped Titania-S2

sample) and the one having concentration of Nd/Ti= 3.7% (doped Titania-S3 sample).

In the case of ZnO doped with Nd, two samples having the concentration of Nd = 0.3at.% (doped ZnO-S6) and 0.9at.% (doped ZnO-S3a) were chosen.

For the need of the present study, alumina films containing neodymium were also produced and analyzed. The alumina films were co-sputtered with Nd from two separate targets, in the same conditions of pressure and target-to-substrate distance as for TiO_2 and ZnO films. The applied power to Al_2O_3 target was of 105 Watts for a self-bias voltage of -850V, while for Nd a power of 3 Watts was applied for a self-bias voltage of 36V. The film thickness was of 1.120±0.035 and 1.588±0.08 microns for pure and Nd –doped Alumina films respectively.

All the titania and ZnO films of this study were analyzed after annealing at 600°C in air for 6 hours. The alumina films were annealed at 600 °C and 1050°C.

5.3. TiO$_2$: Nd FILMS

5.3.1 PHOTOLUMINESCENCE EXCITATION SPECTRA OF TiO$_2$:Nd FILMS

Nd^{3+} doped materials have proven to be one of the most efficient candidates for photonic devices such as planar waveguides, micro-chip lasers, fibre lasers etc [8, 9, 10]. Most recent research has been focused in the near infrared spectral region, ranges from 1000 to 1400nm, where Nd^{3+} ions present narrow radiative emission at 890, 1060 and 1350nm originating from the electronic transitions between the $4f^n$ levels, $^4F_{3/2}$ to $^4I_{9/2}$, $^4F_{3/2}$ to $^4I_{11/2}$ and $^4F_{3/2}$ to $^4I_{13/2}$ respectively [11], as schematically shown in Fig. 5.1. The PL emission spectra of TiO_2: Nd^{3+} upon different non-resonant (indirect) excitation of $^4F_{3/2}$ state energy, in the range 300 - 400 nm and for the samples having Nd amounts of *Nd/Ti*= 0.9% and 3.7% are displayed in Figure 5.2 (panel (a) and (b)

respectively). Experiments were carried out at different excitation wavelengths in order to determine the optimum wavelength at which efficient Nd^{3+} luminescence is observed from the films.
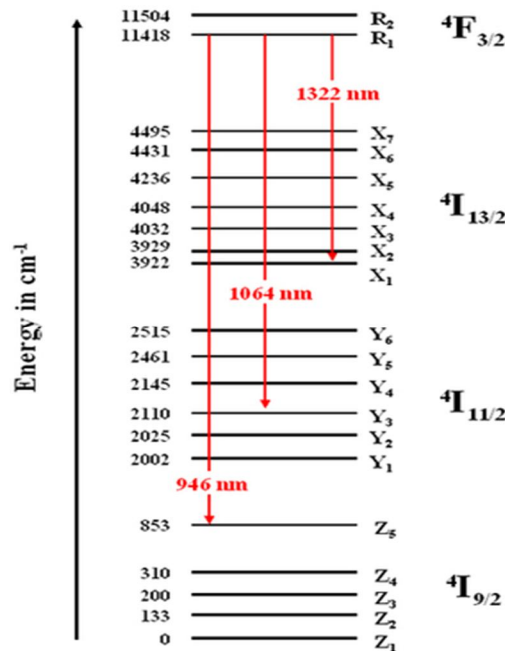
Figure 5.1: *Energy level diagram of Nd ion. The letter corresponds to the orbital quantum number, the superscript number gives the spin quantum number and the subscript fraction is the angular quantum number. Because of the crystal field splitting (Stark effect), the energy levels are split into sublevels, represented by letters with subscripts ($Z_1...R_2$) [Figure adapted from Reference 13]*

As already described in Chapter 3, for the film with *Nd/Ti*= 0.9%, the emission spectra of Nd^{3+} exhibits two luminescence bands centered around 906 nm and 1092 nm with a well resolved crystal field splitting (see Fig. 5.2), which depends on the symmetry of the coordination structure. The emission in the 1050 - 1150 nm range arising from the $^4F_{3/2} \rightarrow {}^4I_{11/2}$ dominated the whole emission spectrum. Six CF levels of $^4I_{9/2}$ (870 - 970 nm) transition and seven CF levels of $^4I_{11/2}$ (1050 - 1150 nm) transitions were identified and these splitting were generally consistent with the theoretically predicted multiplets of transitions from $^4F_{3/2}$ to $^4I_{9/2}$ and $^4I_{11/2}$ (5 and 6

189

lines) given by Kramers degeneracy [12]. These fine CF splitting firmly establish that Nd^{3+} ions embedded in fairly crystalline surroundings, even if the radii of Nd^{3+} is larger than the Ti^{4+} one.

These results suggest the association of Nd^{3+} emission with an energy transfer process from the titania host matrix to Nd^{3+} crystal states.

As can be seen in Fig. 5.2 (a), by varying the excitation energy, the peak positions did not change while their intensity significantly varied with the excitation wavelength. For the sample with *Nd/Ti*= 3.7% , the PL spectra acquired under all the excitation energy values in the wavelength range 300-400 nm exhibited two luminescence broad bands centered around 906 and 1092 nm (Fig. 5.2(b)). The spectra intensity was much lower, up to 40 times, than for the former film. The broadening of PL emission spectra reveals the non-uniformity of local crystalline environment (distorted lattice sites) around the Nd^{3+} ions. Structural disordering and surface defects are inevitable after the introduction of rare earth ions into the lattices of wide bandgap semiconductors [14]. This was evidenced in Chapter 3 through XRD analyses. Obviously, the contribution of clustering of Nd^{3+} could also contribute to the luminescence quenching through cross relaxation between neighboring Nd^{3+} ions. The same observation can be made for this sample, regarding the invariability of the peak positions when varying the excitation wavelength, in contrast with the peak intensity.

These results are better evidenced by the photoluminescence excitation (PLE) spectra acquired on the two samples and described below. Convincing evidence of the occurrence of photon conversion through energy transfer process can be obtained from the PL excitation spectra in comparison with the absorbance spectrum.

The room temperature PL excitation spectrum of Nd^{3+} doped TiO_2 sample with Nd/Ti = 0.9% was acquired in the 300 nm - 700 nm spectral region by monitoring the $^4F_{3/2}$

to $^4I_{9/2}$ transitions (at around 896 nm) of Nd^{3+} ion emission. It is displayed in Figure 5.3.
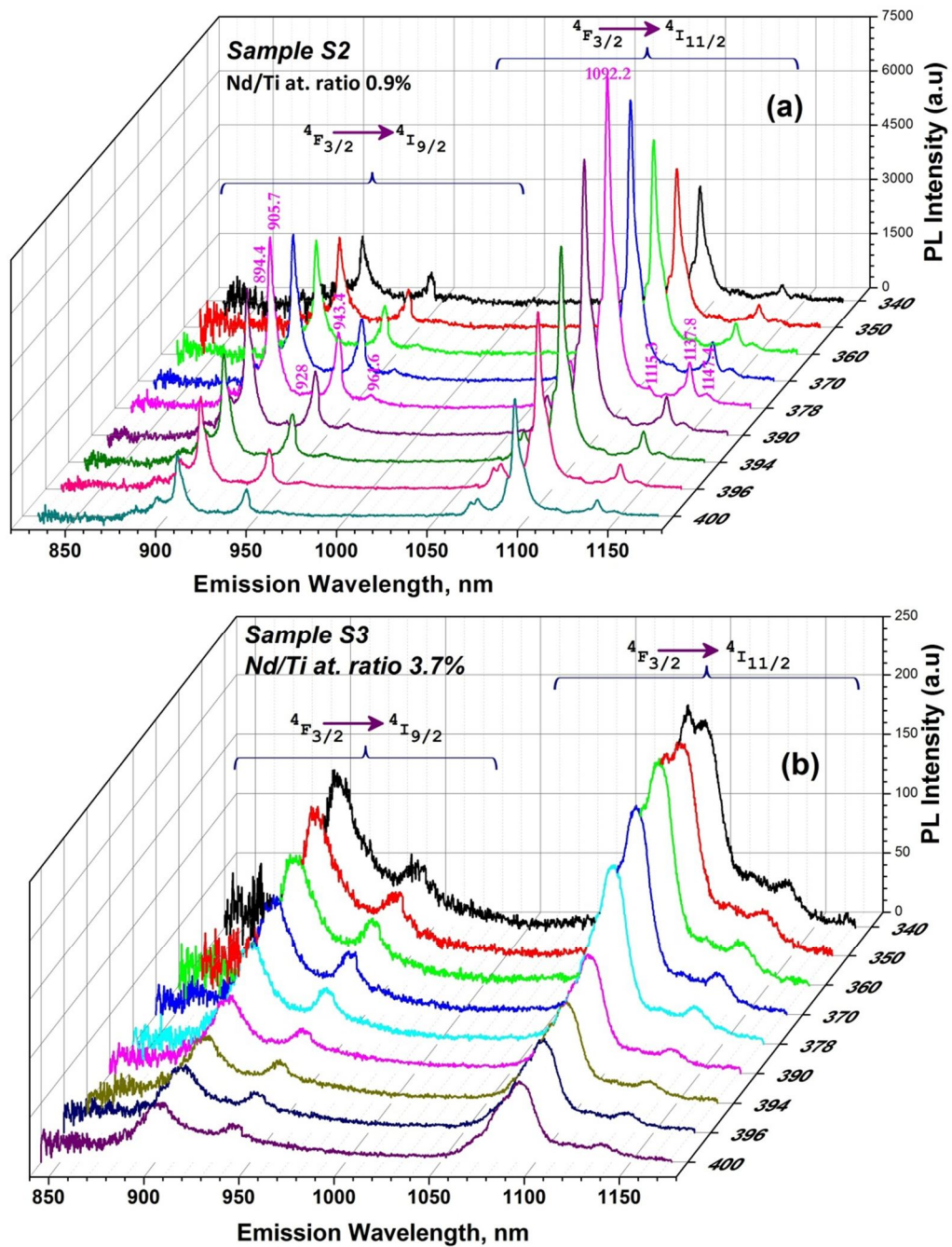
Figure 5.2: *Emission Spectra of TiO$_2$: Nd under non-resonant excitation (UV) from 300 – 400 nm for doped TiO$_2$ films with Nd/Ti= 0.9% & 3.7%*

The spectrum shows a most pronounced strong characteristic broad excitation band

centered at 378 nm (3.28 eV). A combination of absorption and photoluminescence excitation measurements showed that the band maximum coincides with the edge onset observed in the UV region of the optical absorbance spectrum of the sample, also plotted in Fig. 5.3, at 378 nm (3.26 eV). These observations confirm that the Nd^{3+} NIR emissions of the transitions $^4F_{3/2}$ to $^4I_{9/2}$ and $^4F_{3/2}$ to $^4I_{11/2}$ arose due to the indirect Nd^{3+} ions excitation mechanism through the energy transfer of electron-hole pairs created in the titania host matrix.

It is worth to note that the excitations lines which correspond to 4f-4f transitions of the neodymium ions in Visible region, were not detected in the excitation spectrum, probably be due to the fact that the non-resonant/ sensitized emissions is much more efficient than a direct excitation of Nd^{3+} [14].
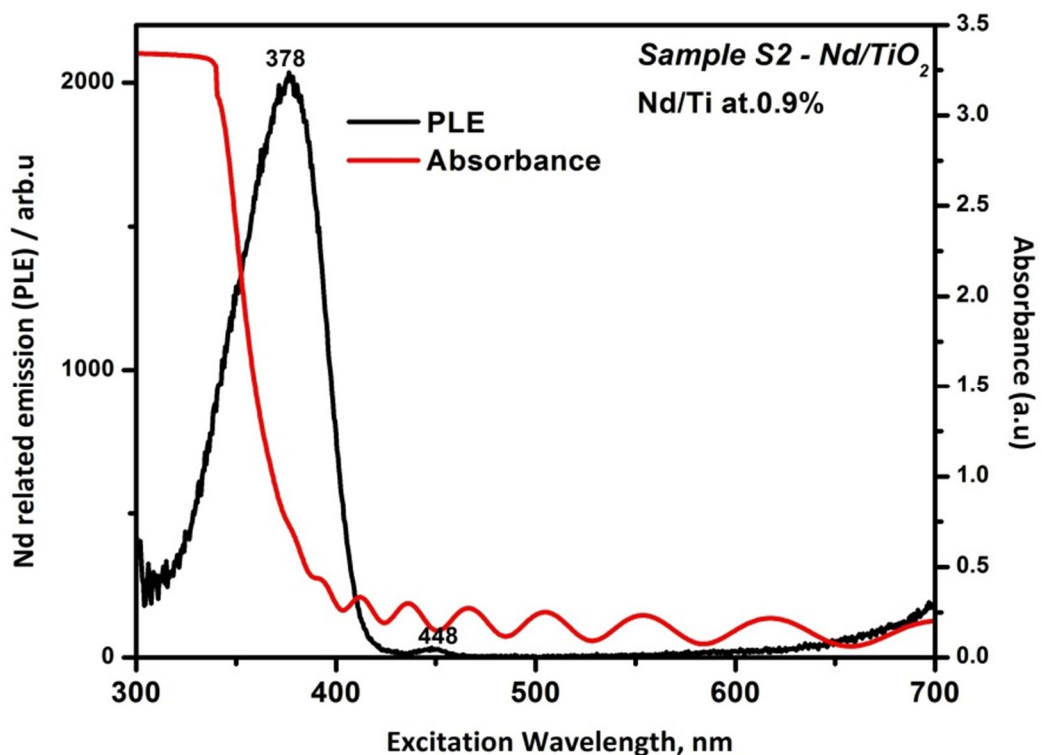
Figure 5.3: *Photoluminescence Excitation (PLE) monitoring the emission at 896 nm and the absorbance spectra of Nd/Ti= 0.9% .*

The host-to-rare earth energy transfer plays a crucial role in improving the emission efficiency for many technological applications. Frindell *et al.*, proposed a model based on the defect-mediated process via energy transfer [15]. In this model, the defects states act as intermediate channels to assist the energy transfer pathway between the host titania matrix and the rare earth ions (including Nd).
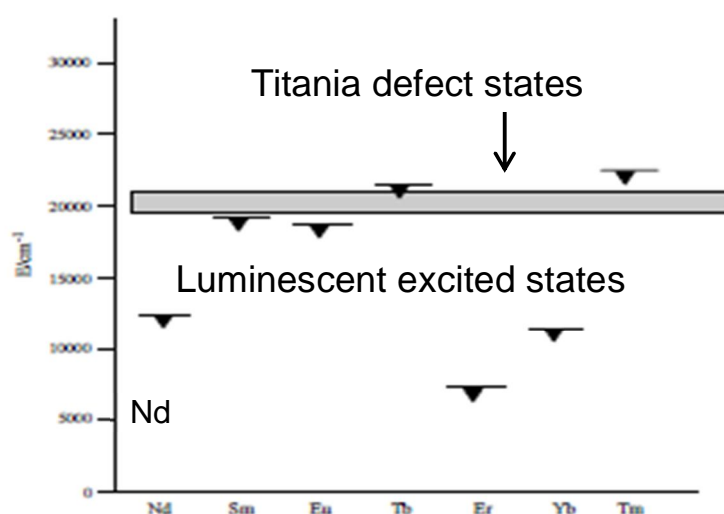
Figure 5.4: *Luminescence excited states of the lanthanide ions studied. The shaded area represents the proposed energy level of the titania defect states. Figure adapted from Reference [15]*

Assuming that the energy transfer occurs through wavefunction overlap between a donor (sensitizer) and acceptor (rare earth ion), i. e. a process following a Dexter-type mechanism of energy transfer, the defect energy level should be equal or higher than that of the emitting state of the rare earth ion in order to have a photoluminescence as depicted in Fig. 5.4 (adapted from [15]).

It has been reported that various types of defects states in the host matrix such as TiO_2

or ZnO play a crucial role in the energy transfer between the host and the dopant ion [16, 12].

5.3.2 DEFECT PROBING BY PHOTOLUMINESCENCE ANALYSIS IN VISIBLE RANGE

In order to check the existence the defects states in the films of the present study, photoluminescence was in this case exploited to detect and identify such defects. In turn, it provided a useful mean to clarify the role of the defects, if any, in the sensitizing process of Nd from the matrix for photoluminescence in NIR under excitation in UV.

- *Pure titania film:*

Light absorption in the visible can be due to lattice defects which create energy levels within the gap of titanium oxide. Regarding pure titania films, the most frequent defects are related to oxygen vacancies. However, although literature is abundant for the electronic structure of titanium oxide, many recent papers recognize that there still exists insufficient information on the optical properties of point defects. In a review made by Kuznetsov and Serpone [17], the absorption bands in the visible spectral region, in a range of 2.93- 2 eV (423-620 nm), are reported to be associated to O vacancies, which act as F-type color centers.

In effect, our un-doped titania films analyzed by XPS were oxygen deficient in their chemical composition (see Chapter 3). The stoichiometry of the oxide was $TiO_{1.88}$. Figure 5.5 (plot 1) illustrates the room temperature PL emission spectra excited at a wavelength of 378 nm that film. The selected excitation wavelength (378 nm) was the one giving the maximum NIR PL emission intensity shown in Fig 5.2 (a).
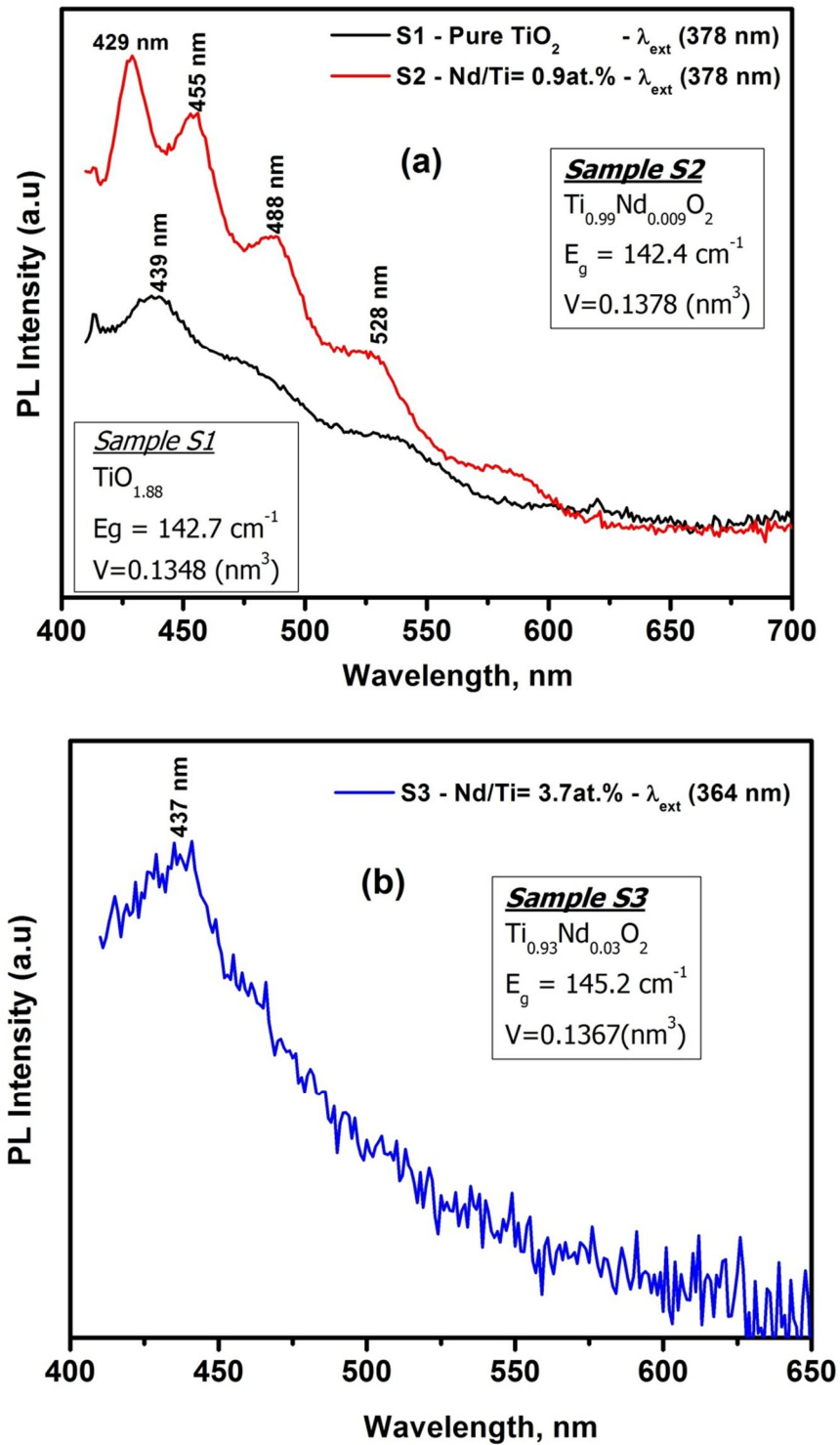
Figure 5.5: *(a) Photoluminescence Emission spectra in the visible range (a) Pure TiO₂ (Nd/Ti= 0%) and Nd/Ti= 0.9% (b) Nd/Ti= 3.7.%. PL spectra were measured with an excitation wavelength of 378 nm for the samples, pure TiO₂ and Nd/Ti= 0.9% and λ_ext of 364 nm for Nd/Ti= 3.7%.*

A broad emission band between 400 to 600 nm was observed. In this range, in general, PL emission of titania is attributed to three different physical origins: self-trapped excitons [18], oxygen vacancies [19] and surface defects [20]. The spectrum exhibits an emission band around 440 nm (2.8 eV), which could originate from a shallow trap level, as reported in [21], the emitting center identified with F^{++} center (doubly ionized O vacancy) [22]. A broad PL band in the visible region (500-600 nm) originating from the oxygen-vacancy-related defects was observed. De Haart and Blasse [23] reported that the small sharp peak at 413 nm (3.00 eV) is caused by the free exciton recombination. The weak signal at ~ 480 nm was reported as originating in surface states [15, 24, 25], but there is an increasingly convincing interpretation for this green-yellow emission feature as arising from radiative recombination of self-trapped excitons (STEs), localized on TiO_6 octahedra [26].

- *Nd-containing titania film with Nd/Ti = 0.9%:*

In Figure 5.5 (plot 2) the room temperature PL emission spectra relative to this film is displayed. The selected excitation wavelength was 378 nm as for the un-doped titania film.

More peaks and better-resolved than for pure titania appeared at 429 nm, 455 nm, ~488 nm and ~528 nm (2.9 eV, 2.7 eV, 2.5 eV and 2.3 eV respectively), with a small shoulder at ~590 nm. The peak at 439 nm, mainly present in plot 1 for pure titania, is absent in plot 2. The same can be said for all the other peaks of plot 1, except the one at ~480 nm, which is more intense in plot 2.

The assignment of the new peaks appearing for the Nd-containing film is rather difficult since both defect states in titania and Nd transitions can account for the emission in such range. In fact, the emission peak at 455 (reported at 457 nm) and 528 nm (reported at 537 nm) might be associated with oxygen related defect states [27].

However, considering their relatively high intensity and knowing the stoichiometry of the film, it seems less likely that the signal pertains to O vacancies. In this film, the oxide stoichiometry was $Ti_{0.99}Nd_{0.009}O_2$, i.e. a ratio O/Ti very close to 2, which means that oxygen vacancies are much less probable than in the un-doped titania film.

On the other hand, Nd itself can give rise to emission in visible range, corresponding to transitions from states $^4D_{3/2}$ to $^4I_{11/2}$, from $^2P_{3/2}$ to $^4I_{9/2}$, $^4D_{3/2}$ to $^4I_{11/2}$ or $^2P_{3/2}$ to $^4I_{9/2}$ and also from $^2P_{1/2}$ to $^4I_{9/2}$ [28]. Some reported emission peak wavelengths overlap with the ones observed in the plot 2: at 430 nm (429 nm in plot 2), 450 nm (455 nm in plot 2), 530 nm (~528 nm in plot 2) and 589 nm (~ 590 nm in plot 2). This fair correspondence suggests that the observed emission peaks pertain to Nd transitions.

It comes that, apart from peak at 488 nm related to surface states and/or STE, all the other emission peaks are more probably due to Nd transitions. The higher intensity of the surface states peak for this sample, with respect to the un-doped film, would be in agreement with a smaller grain size of the anatase phase, 18 nm versus 12 nm, as it comes from the XRD analysis (Chapter 3, Fig. 3.9 (e)). A smaller grain size will likely lead to a major density of surface states where non-radiative recombination e^-/h^+ can occur. However, the XRD analysis results also showed for this film both an increased lattice distortion and increased cell volume with respect to the un-doped film. This would be in agreement, too, with a higher intensity emission, related to a higher probability of exciton self-trapping.

- *Film with Nd/Ti = 3.7%*

The PL emission spectra in the Visible range is displayed in Fig. 5.5 (b). It was acquired under an excitation wavelength of 364 nm, which yielded the highest PL intensity spectra for this film (see Fig. 5.2(b)). The spectrum is featureless and noisy. No peaks pertaining to any of surface states/STEs were obtained, which can be

understood considering the much larger grain size of the anatase phase (29 nm) with respect to the un-doped and the low-Nd films described in the previous sections. No signal pertaining to Nd transitions was obtained. Only a noisy signal at ~437 nm was observed, at the same position as for the un-doped film (plot 1 in Fig. 5.5 (a)). This peak may be assigned to shallow traps states.

As discussed in Chapter 3, the Nd-containing films had a composition which depended of the Nd concentration, as illustrated in Fig. 3.4 (a) of that chapter. With Nd/Ti at.ratio = 3.7%, this film had a stoichiometry $Ti_{0.93}Nd_{0.03}O_2$, (or $Ti_{1-0.07}Nd_{0.03}O_2$) reflecting a deficiency in the Ti sub-lattice. So, in this film the major defects were Ti vacancies.

5.3.3 DISCUSSION ON THE ENERGY TRANSFER MECHANISM

In Frindell's model of the excitation energy transfer between a titania matrix and a rare-earth ion embedded in it, the UV light is absorbed by the titania with subsequent relaxation to defect states, followed by energy transfer to the rare-earth located close enough to the defect to have wave-function overlap. Self-trapped exciton can also be involved in the energy transfer process between the matrix and the Nd ion [29]. The presence of such defects was evidenced by the PL emission measurement in visible range at 488 nm. In rutile the excitons are free, while in anatase they are trapped in the TiO_6 octahedra and, thus, have a strong electron-phonon coupling giving a Stokes shift up to 1 eV. This is believed to be due to a lower packing density and distortion of the octahedra in anatase.

The question which rises is which of the STE defect, defect states such as O vacancies and the direct (resonant) transfer from the conduction band (CB) of the titania to a Nd^{3+} level (like $^4D_{1/2}$) is the UV energy transfer way. The three possible sceneries of

the excitation energy transfer are schematically depicted in Fig. 5.6. The first one consists of a direct resonant transfer from the CB of the titania to a high energy state of Nd^{3+}, followed by non-radiative relaxation down to the $^4F_{3/2}$ NIR emitting state. In the second scenery, the matrix relaxes after the UV photon absorption to a shallow defect, which then transfers the energy to one state of the ^4D or ^4G manifold through a Dexter mechanism, following the Frindell's model. In the third scenery, upon a UV photon absorption, the self-trapping of the exciton gives an intra-gap defect state, able to transfer energy to a Nd^{3+} state.
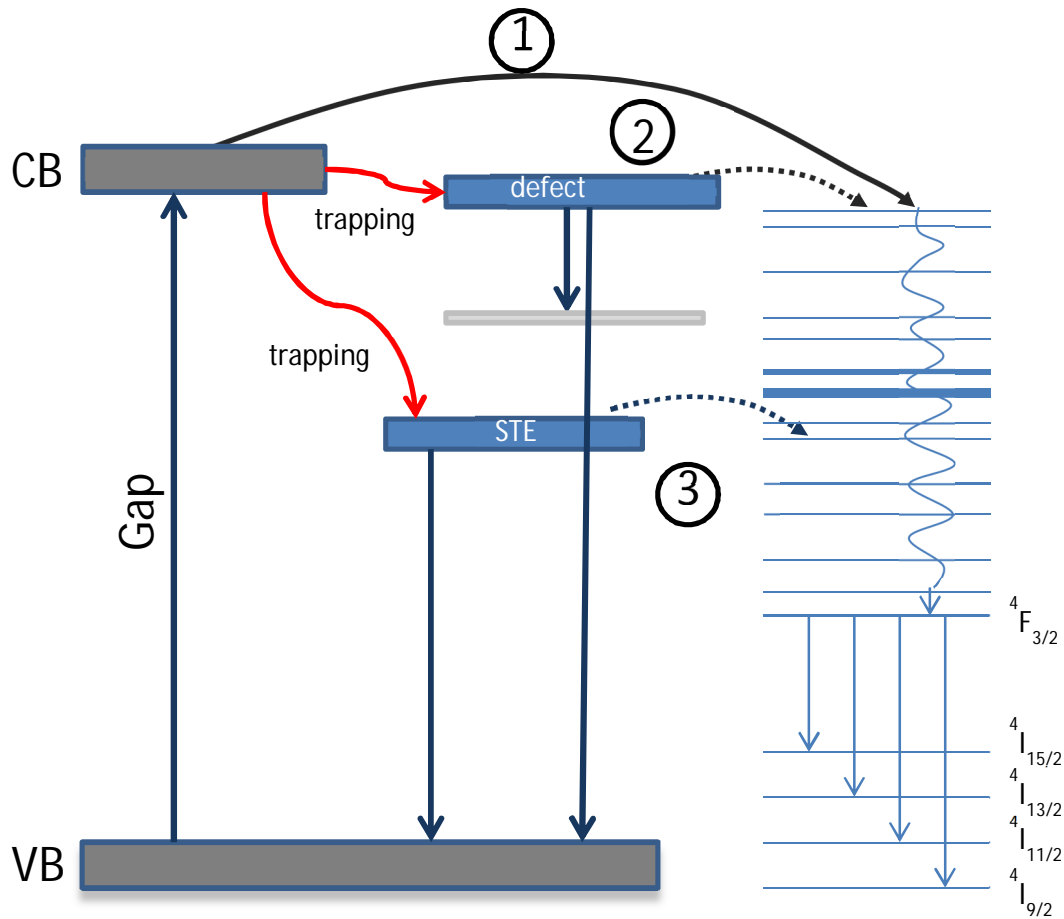
Figure 5.6: *UV-Energy transfer possible paths between the titania and the Nd^{3+} levels leading to NIR photoluminescence. Path (1) is for resonant energy model, (2) for defect-mediated model and (3) for self-trapped exciton (STE) model; VB and CB stand for valence band and conduction band respectively.*

The possible radiative relaxation of the STE state to ground state and that of the shallow defect trap to a lower defect state (for example from a F^{++} state to F^+ state or from F state to a F^+ state, in the case of O vacancies) or to ground state are also shown.

In order to answer the question about the most probable mechanism playing for the Nd-doped titania films of this study, some correlations should be made between the nature of structural defects, the relaxation energy of the titania lattice and the PL emission intensity.

The nature of the structural defects can be identified from the films stoichiometry, as discussed in the previous section. In Fig. 5.5 (a) and (b), for more clarity, the stoichiometry of the films is shown: the un-doped titania contains O vacancies, the 0.9%Nd/Ti- film should be free of O vacancies, while the 3.7% Nd/Ti-film contains Ti vacancies instead. In the latter film, no emission around 488 nm is expected and it was not observed in fact (Fig. 5.5 (b)). So, among the pure titania film and the 0.9% Nd/Ti-film, the former should exhibit the most intense emission around 488 nm. This was not observed, as this peak, on the contrary, was more intense and better resolved in the Nd-containing film (plot 2 in Fig. 5.5(a)). So, the peak at 488 nm appears as not pertaining to structural defect states, it is more likely to attribute to STEs.

The difference between the PL intensities observed for all the films, whatever in Visible or NIR, can be understood by considering the vibrational properties of the titania host. The value of the Raman shift of the E_g mode anatase (the mode giving the most intense peak, see Fig. 3.10 in Chapter 3) for the three samples is given in Fig. 5.5 (a) and (b). It is interesting to note that the film which exhibits the lowest Raman frequency (142.4 cm^{-1}) i.e. the 0.9%Nd/Ti-film, exhibits the most intense peak at 488 nm, transitions of Nd^{3+} in Visible range as well as intense NIR PL.

It is also interesting to note that for the un-doped film, the very modest peak at 488 nm, inversely followed the E_g Raman frequency too (it was higher, being equal to 142.7 cm^{-1}).

It comes that the lower the phonon frequency (energy), the higher the PL emission intensity and appearance of the STE emission. For the first aspect (highest PL emission), this is in agreement with the "energy gap law" reported by van Dijk and Schuurmans [30], following which the lower the phonon energy, the higher the radiative relaxation. Vice-versa, the higher the phonon energy, the higher the non-radiative relaxation probability.

As for the possible contribution of the STE to the excitation energy transfer to Nd^{3+}, as exciton self-trapping occurrence depends on the lattice relaxation energy, we expect that differences exist between this parameter values for the different films. In Chapter 3, the lattice distortion and the unit cell volume variation of the films with Nd-incorporation in the TiO$_2$ matrix were displayed in Fig. 3.10 in that Chapter and discussed. For a sake of clarity, the unit cell volume values corresponding to the films analyzed for PL in this section are shown in Fig. 5.5 (a) and (b). We can see that the highest the emission intensity at 488 nm is observed for the larger unit cell volume, i. e. for the 0.9% Nd/Ti-film. A larger cell volume also means a lower atom packing density, which together with the lattice distortion observed in the XRD results, might give rise to differences between the lattice relaxation energy in the three films. In fact, for example if anatase and rutile are considered and compared, it is known that exciton self-trapping can occur only in anatase, because of a lower packing density and octahedron distortion which allows a strong lattice relaxation.

In the film with Nd/Ti = 0.9%, composed of nearly stoichiometric oxide, the role of defect states would be minor. The energy transfer is more likely to be mediated by the

excitonic states, which energy (2.3 eV) is above that of the Nd emitting state $^4F_{3/2}$, as schematically illustrate in Fig. 5.6. Nonetheless, a direct transfer pathway between the CB of TiO_2 and a level state of Nd^{3+} cannot be excluded.

In the film with Nd/Ti = 3.7%, the absence of any feature in the PL spectrum does not allow to conclude about the role of the defects and the STE. This film should be dominated by O vacancies (see Fig. 3.4 in Chapter 3), in contrast with the absence of the peak at 488 nm in the Visible PL spectrum. The absence of such peak could also be due to the absence of exciton self-trapping. However, following the reasoning about the effect of the lattice distortion and the unit cell expansion on the exciton self-trapping possibility, this film should exhibit a STE defect state emission. In fact, the c/a lattice parameters ratio as well as a the cell volume were very close to those of the 0.9%Nd/Ti- film (see Fig. 3.10 in Chapter 3). For the 3.7%Nd/Ti –film it can only be stated that, whatever the intermediate defect (O vacancy or STE) state, the high phonon frequency can activate their non-radiative relaxation, which effect was observed for the Nd^{3+}NIR PL emission.

5.3.4 EXCITED STATE DYNAMICS- LUMINESCENCE LIFETIME CHARACTERISTICS

Luminescence lifetime (τ) is determined by radiative and non radiative decay rates, which is closely related to the crystalline environment around the dopant ions [14]. To get further insight on the dynamics of the energy transfer process between the host titania and Nd^{3+}, luminescence decay curve measurements were recorded for the $^4F_{3/2}$ → $^4I_{9/2}$ (896 nm) NIR emission from Nd^{3+} ion upon exciting with different wavelengths (from 350 - 400 nm). Figure 5.7(a) shows the luminescence decay curves of these emissions for TiO_2 doped with the Nd concentration such as *Nd/Ti*= 0.9a%,

as a function of different excitation wavelength (corresponding energy [eV] shown in the table). All data are measured at room temperature.

All emission from the Nd^{3+} states showed a noticeable rise time (build-up) at the initial stage followed by the decay of the emitting state.
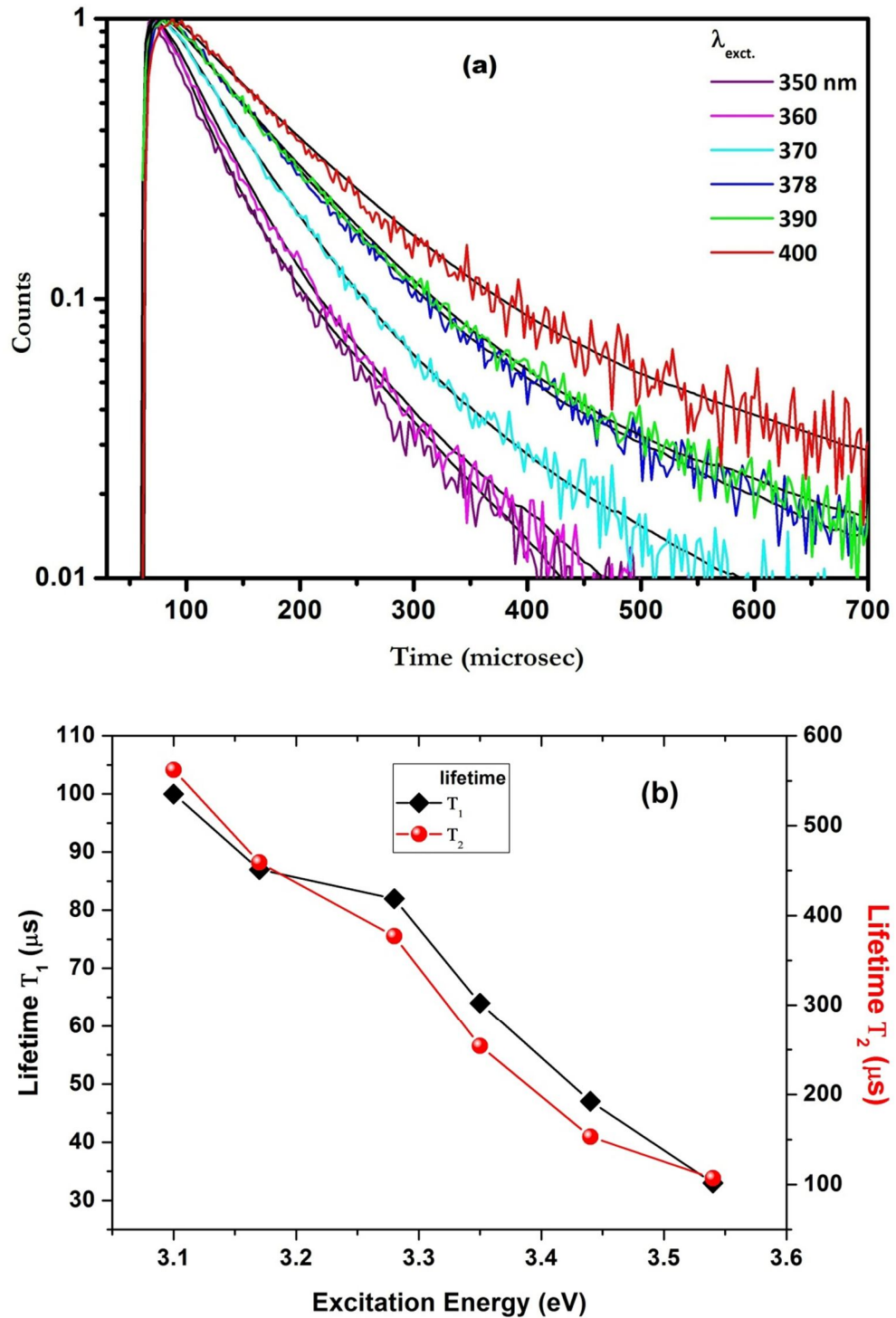
Figure 5.7: *Room temperature luminescence measurements decay measurements of*

Nd^{3+} emission at 896 nm ($^4F_{3/2}$ to $^4I_{9/2}$) of the sample having Nd/Ti= 0.9% upon excitation at different wavelengths (a) and plot of the lifetime in function of the excitation energy (b).

Excitation Wavelength (nm)	Excitation energy (eV)	τ_1 (µs)	τ_2 (µs)
350	3.54	33	107
360	3.44	47	153
370	3.35	64	254
378	3.28	82	377
390	3.17	87	459
400	3.1	100	562

Table 5.1: *Luminescence lifetimes deduced from double exponential fitting of the decay measurements of Nd^{3+} transition ($^4F_{3/2}$ to $^4I_{9/2}$) around 896 nm in TiO_2: Nd^{3+} for the sample Nd/Ti= 0.9%*

All these curves are well fitted with a double-exponential decay function and the characteristic decay time were deduced by using equation 2.9 in Chapter 2. It consists of a fast component and a slower component with a decay constant in the range of hundreds of microseconds timescale. For the samples with higher Nd^{3+} ion concentration such as Nd/Ti > 0.9 % (i.e. *Nd/Ti*= 3.7, 25 and 45%, the emission intensities were not measurable. The fitted values for the lifetimes are given in Table 5.1. They were found to increase monotonically with the increasing excitation wavelength for the both the short and long components, as can be clearly seen in Fig. 5.7(b). As we see, higher the excitation energy, shorter the life time. There are many factors that may influence the radiative lifetime of rare earth ions such as the non-

solid surrounding media and changes in the lattice constants [29].The shorter life time can be due to increase in the surface/structural defects states and to OH ions might act as a the channels of non-radiative relaxation, thus inducing rapid non-radiative transition.

5.4 ZNO:Nd FILMS

5.4.1 PHOTOLUMINESCENCE EXCITATION (PLE) & EMISSION SPECTRA

The PL emission spectra of Nd^{3+} doped ZnO thin films having Nd concentrations of Nd/Ti=0.3% and 0.9% under different non-resonant excitation wavelengths (320-400nm) are shown in Figure 5.8. Figure shows the PL spectra in the near IR region upon excitation at different non resonant excitation wavelength. A band at 902 nm was observed for the sample doped with Nd/Ti =0.3% and Nd/Ti =0.9% of Nd/Ti, suggesting a possible energy transfer from the zinc oxide matrix to the Nd^{3+} ions. It can be noticed from the spectra, for both samples, that the Nd doped films exhibit characteristic NIR luminescence bands centered at 902 nm ($^4F_{3/2}$ to $^4I_{9/2}$), but also it should be noted that only broad emission lines were observed. The broadening of PL emission spectra shows an increase in the non-uniformity of local structure around Nd^{3+} ions.
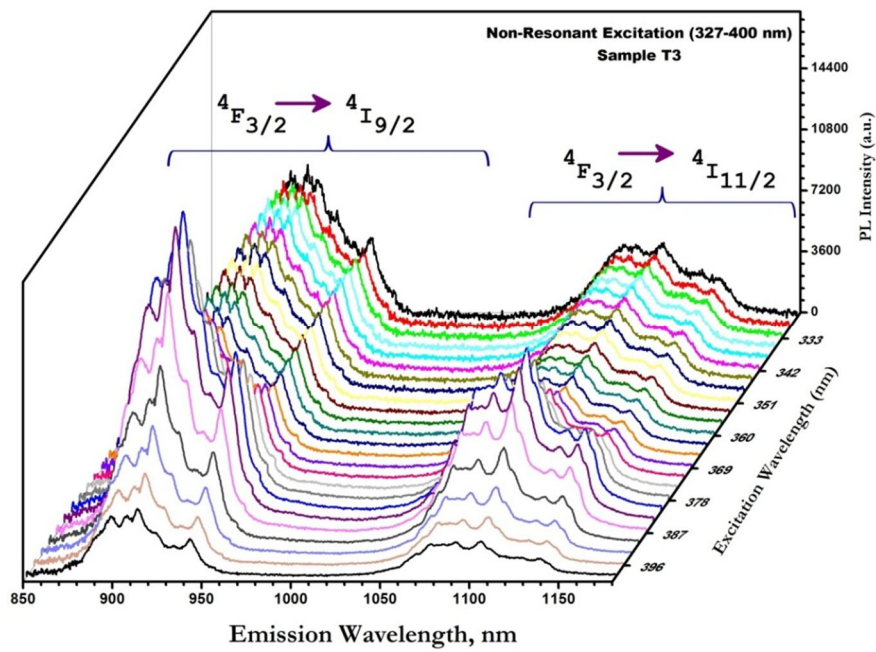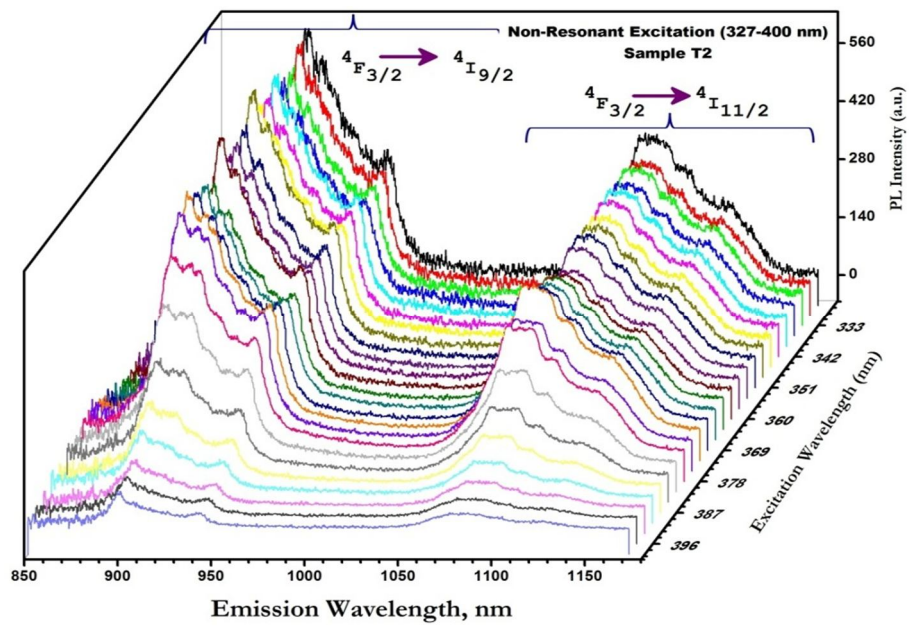
Figure 5.8: *NIR Photoluminescence emission spectra of ZnO thin film doped with T2(0.3 at.%) and T3(0.9at.%) of Nd by non-resonant excitation (from 300-400nm)*
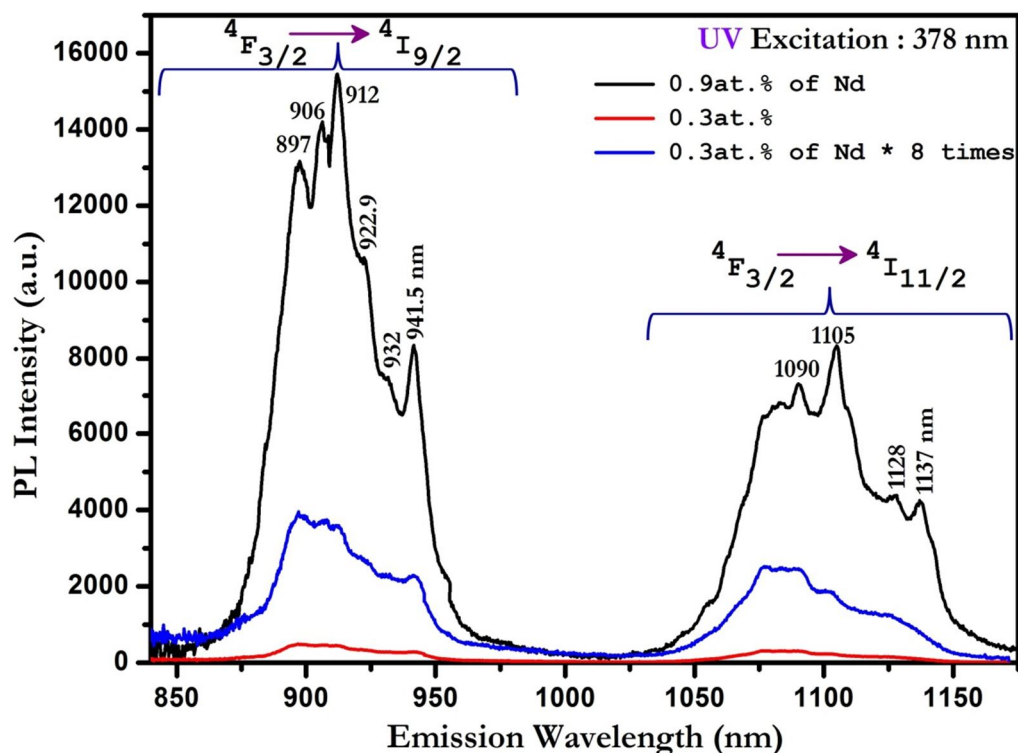
Figure 5.9: *NIR PL emission spectra of ZnO: Nd thin films under 378nm non-resonant excitation of films with Nd concentration equal to T2(0.3at.%) and T3(0.9 at.%.)*

To understand better the absorption and radiative transition mechanism responsible for the Nd^{3+} ions emission through energy transfer via absorption of ZnO host matrix, the PL excitation spectra of the Nd^{3+} emission were measured for the two samples with Nd concentration of 0.3 and 0.9 at.%. by monitoring the $^4F_{3/2}$ to $^4I_{9/2}$ transition around 896 nm. The PLE spectra, together with the absorption spectra are displayed in Fig. 5.10.
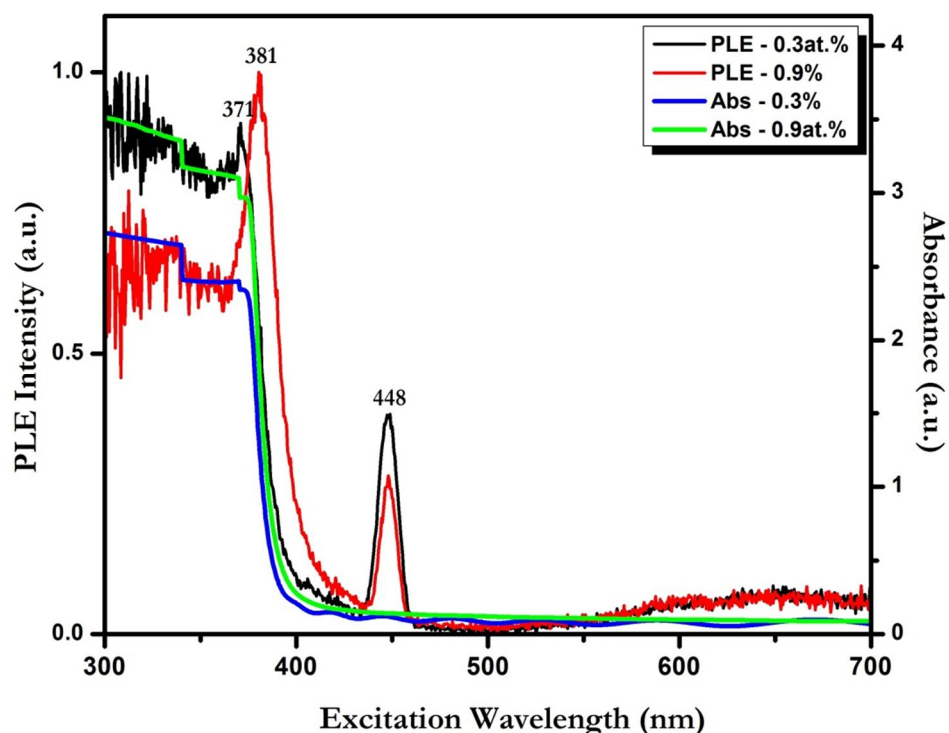
Figure 5.10: *Absorption spectra together with the PL Excitation spectra of the films obtained by monitoring the 896 nm emission [$^4F_{3/2}$ to $^4I_{9/2}$] of 0.3at.% and 0.9at.% of Nd^{3+} in ZnO.*

As can be seen from the figure, the excitation of the Nd^{3+} emission quite nicely follows the fundamental absorption band edge of Zinc oxide. The PL excitation spectrum is dominated by an intense UV broad band from 300 nm to 410 nm with a sharper feature peak centred at a wavelength of 371 (3.34eV) nm and 381 (3.25eV) nm for Nd concentration of 0.3 and 0.9 at.% respectively. This UV broad peak is attributed to the band gap and defects of zinc oxide and agrees close to the bandgap value calculated by using Tauc plot (Chapter 4). The value of the bandgap by Tauc plot is found to be 3.24 and 3.23eV for the 0.3% and the 0.9% Nd samples respectively. The peak at 448 nm corresponds to the second order of the monochromator, which is used to monitor the emission at 896 nm.

Like in the case of titania, these experimental results strongly suggests that the Nd^{3+} emissions can be achieved via an effective nonradiative energy transfer process from ZnO to Nd^{3+} ions.

5.4.2 LIFETIME CHARACTERISTICS

The decay profiles were measured under the indirect excitation (340, 378, 390 and 400 nm) by monitoring the Nd^{3+} around 896 nm ($^4F_{3/2}$ to $^4I_{9/2}$) are shown in Fig. 5.11. To estimate the decay times, the decay curves were fitted by a double exponential decay curve using the equation (2.9) in Chapter 2. The obtained life time values consist slow and the fast component are listed in the Table 5.2.
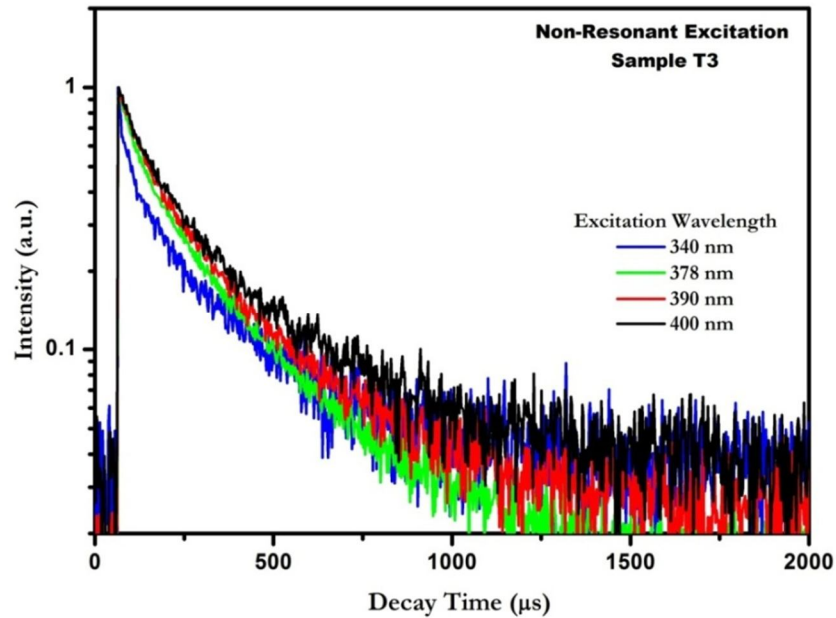
Figure 5.11: *Emission decay curve monitored within (896 nm) $^4F_{3/2}$ to $^4I_{9/2}$ transition under distinct excitation wavelengths.*

Excitation Wavelength (nm)	Excitation Energy (eV)	τ_1 (μs)	τ_2 (μs)
340	3.64	10	210
378	3.28	27	240
390	3.17	36	242
400	3.1	30	243

Table 5.2: *The parameters resulted from the double exponential fitting of ZnO: Nd for the transition $^4F_{3/2}$ to $^4I_{9/2}$ exciting under distinct wavelengths*

The decay value shows that the higher excitation energy exhibits a faster decay compared with the lower energy. The luminescence decay time was found to be dependent on excitation intensity. The noticeable rise edge in the initial stage has been observed which implies much slower non-radiative relaxation rate from $^4F_{5/2}$ to $^4F_{3/2}$ [31]. The multi-exponential decay can be due to the closely spaced energy levels of Nd^{3+} ions in various sites of ZnO matrix. The variation in the lifetime values upon different excitation energy might be attributed to the different energy transfer rates from the defects to the levels of Nd^{3+} ions.

5.5 LUMINESCENCE PROPERTIES OF ND DOPED ALUMINA (Al_2O_3) HOST MATRIX

Alternatively, to prove the existence of photon downshifting effects occurred from the bandgap absorption of Titania and Zinc oxide host matrix to Nd^{3+} ions, we also studied the luminescence properties of Nd –doped Alumina (Al_2O_3) matrix, having a wide bandgap of ~ 6eV, a non-absorber of UV photons. The deposition processes of these films are discussed in Chapter 2 in the section of experimental details. The thickness of the prepared sample for Pure Alumina 1.120 ±0.035 and Nd-doped sample is 1.588 ±0.08 microns respectively.

5.5.1 STRUCTURAL PROPERTIES OF ND DOPED ALUMINA THIN FILMS

Figure shows the X-ray diffraction pattern in grazing angle incidence configuration at 3° for pure Alumina (600°C) and Nd doped Alumina thin films annealed at 600°C and 1050°C in air ambient for six hours.

The pattern shows that the samples appear completely amorphous both before annealing and after annealing at 600°C. In the film annealed at 1050°C, a nanocrystalline γ-alumina phase formed, as indicated by the weak features at 2Theta = ~37, ~46 and ~67 °.
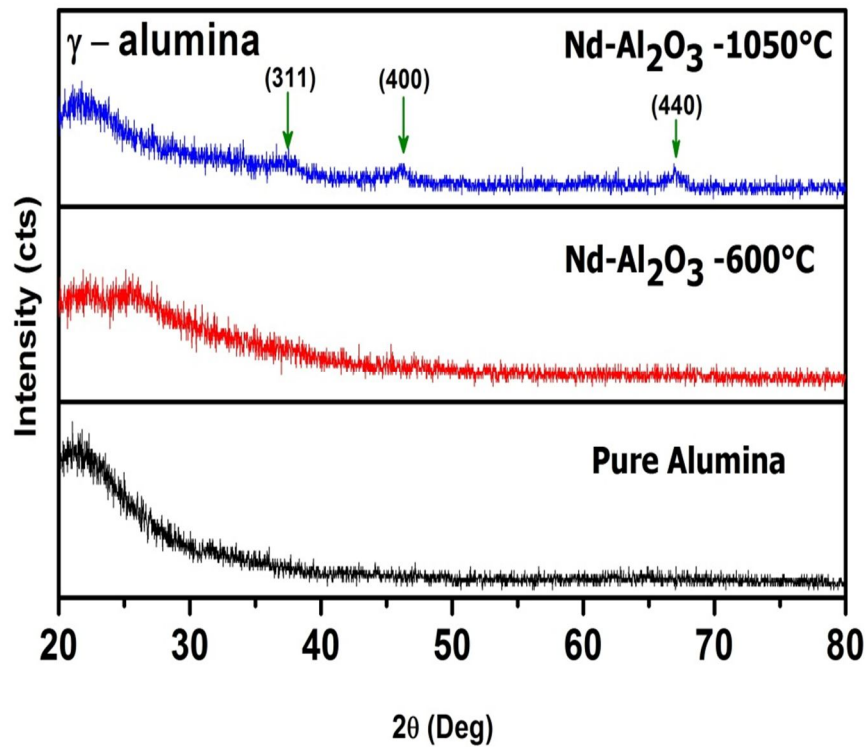
Figure 5.12: *Grazing angle incidence X-ray diffraction pattern for Pure Alumina (600°C) and Nd-doped Al₂O₃ thin films annealed at 600°C and 1050°C in air ambient.*

5.5.2 OPTICAL PROPERTIES OF ND DOPED ALUMINA THIN FILMS

The optical properties of the pure and Nd doped Al_2O_3 thin films were evaluated using UV-visible spectroscopy.
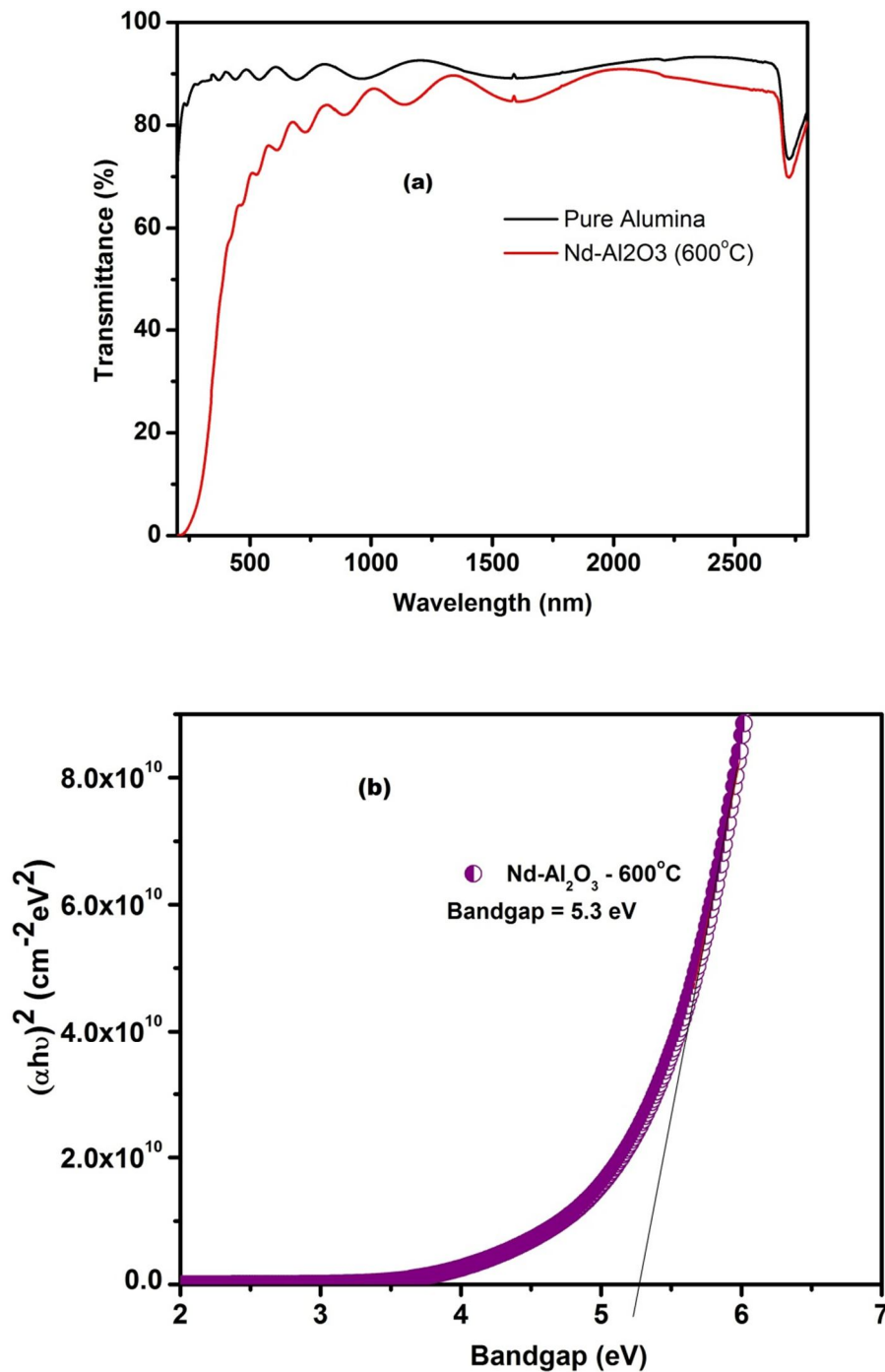
Figure 5.13: *(a) Optical transmittance for Pure and Nd doped Alumina and (b) Tauc's plot (αhυ)² in function of photon energy.*

The transmittance spectra show that the films are transparent with optical transparencies of 70-80% in the visible region (Fig. 5.13 (a)). None of the absorption peaks related to Nd can be observed. The optical band gap was estimated from a Tauc

plot of $(\alpha h\nu)^2$ in function of photon energy for Nd doped Al_2O_3 annealed at 600°C and the band gap values is found to be 5.3eV (Fig. 5.13 (b)).

5.5.3 PHOTOLUMINESCENCE PROPERTIES OF Nd DOPED ALUMINA THIN FILMS (BOTH DIRECT AND INDIRECT EXCITATION)

Direct Excitation

Figure shows the NIR PL emission spectra of Nd-doped Al_2O_3 thin films, annealed at 1050°C after an direct excitation of 476 nm (Blue) using argon laser with power 160mW of slit 1 mm.
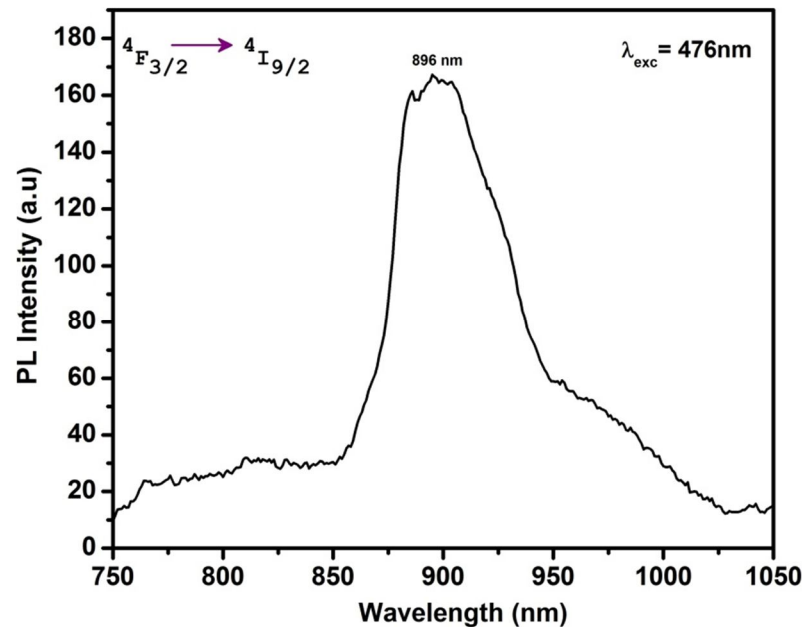
Figure 5.14: *PL emission spectra of Al₂O₃: Nd film under resonant excitation (476nm)*

Spectra show the weak inhomogeneous broad band of Nd^{3+} NIR luminescence with low intensity from 750 to 1050 nm corresponds to $^4F_{3/2}$ to $^4I_{9/2}$ transition. These broadening might be due to the location of Nd^{3+} ions in amorphous Al_2O_3 matrix. This reveals that the Nd^{3+} can be excited directly to one of the excited state.

Thereafter, the electrons decay back to the $^{4}F_{3/2}$ state, from which they relax down to the ^{4}I states, with the emission of photons of characteristic wavelengths.

Indirect (Non- resonant) Excitation

The Nd-doped films were further tested for frequency down-shifting effect by excitation in UV, at energies below the band gap of the Al_2O_3 matrix (from 300 to 400nm).
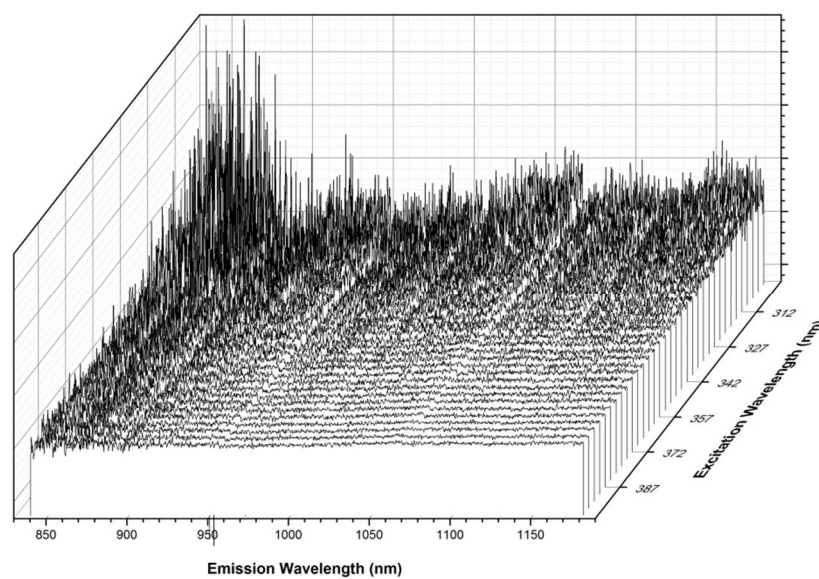
Figure 5.15: *PL emission spectra of Al_2O_3: Nd film under non-resonant excitation (UV) from 300-400nm*

Figure 5.15 shows the PL emission spectra in the near IR region upon excitation at 300 to 400nm. No PL signal was observed for any of the excitation energy. This confirms that the TiO_2 and ZnO matrices, with their peculiar bandgap value, acts as an efficient photon converter in absorbing UV photons from 300 to 400nm and the high intense photoluminescence can be achieved through efficient energy transfer characteristics.

5.6   CONCLUSIONS

The investigation on the nature of energy transfer mechanism between the host matrix and the Nd^{3+} was pursued investigating the PL properties (PLE and Emission). The PLE spectra shows a characteristic broad band excitation peak in the UV region which confirms that the Nd^{3+} emission arises due to the indirect excitation mechanism through energy transfer of electron pairs in the TiO_2 host. Interesting correlation made between the defect luminescence of the pure and Nd doped titania films to the variation in the vibrational properties from the Raman analysis. It is interesting to note that the film which exhibits the lowest Raman frequency (142.4 cm^{-1}) i.e. the 0.9%Nd/Ti-film, exhibits the most intense peak at 488 nm, transitions of Nd^{3+} in Visible range as well as intense NIR PL. The higher the PL emission intensity and appearance of the STE emission.

REFERENCES

[1]   H. Kühne, G. Weiser, E. I. Terukov, A. N. Kusnetsov, and V. Kh. Kudoyarova, *J. Appl. Phys.* 86, (1999), 896

[2]   W. Fuhs, I. Ulber, G. Weiser, M. S. Bresler, O. B. Gusev, A. N. Kuznetsov, V. Kh. Kudoyarova, E. I. Terukov, and I. N. Yassievich *Physical Review B* 56, (1997), 9545

[3]   Irina Yassievich, Mikhail Bresler, Oleg Gusev *J. of Non-Crystalline Solids*, 226, (1998), 192

[4]   Y. Abiko, N. Nakayama, K. Akimoto, T. Yao *Physica Status Solidi B* 229, (2002), 339

[5]   J. Palm, F. Gan, B. Zheng, J. Michel, and L. C. Kimerling *Physical Review B* 54, (1996), 17603

[6]   I. Tsimperidis and T. Gregorkiewicz H. H. P. Th. Bekman C. J. G. M. Langerak *Physical Review Letters* 81 (1998) 4748

[7]   T. Gregorkiewicz and D. T. X. Thao J. M. Langer H. H. P. Th. Bekman M. S. Bresler J. Michel and L. C. Kimerling *Physical Review B* 61 (2000) 5369

[8]   Bonar, J.R. Bebbington, J.A. ; Aitchison, J.S. ; Maxwell, G.D. ; Ainslie, B.J. *Electronics Letters* 30 (1994) 229

[9]   Lilia Coronato Courrol, Edison Puig Maldonado, Laércio Gomes, Nilson Dias Vieira Jr, Izilda Marcia Ranieri, Spero Penha Morato *Optical Materials*, 14 (2000) 81

[10]   E.O. Serqueira, N.O. Dantas, A.F.G. Monte, M.J.V. Bell *Journal of Non-Crystalline Solids*, 352 (2006) 3628

[11]   G. Lakshminarayana, Hucheng Yang, Jianrong Qiu *Journal of Alloys and Compounds*, 475 (2009) 569

[12]   Wenqin Luo , Renfu Li and Xueyuan Chen *J. Phys. Chem. C* 113 (2009) 8772

[13]   http://www.optique-ingenieur.org/en/courses/OPI_ang_M01_C01/co/Contenu_21.html

[14]   Y. Liu, W. Luo, H. Zhu, X. chen *Journal of Luminescence*, 131 (2011) 415

[15]   Karen L. Frindell, Michael H. Bartl, Matthew R. Robinson, Guillermo C. Bazan, Alois Popitsch, Galen D. Stucky, *Journal of Solid State Chemistry*, 172 (2003) 81

[16]   Takashi Tachikawa. Takamasa Ishigaki, Ji-Guang Li, Mamoru Fujitsuka and Tetsuro Majima, *Angew. Chem. Int. Ed.* 47 (2008) 5348

[17]   V. N. Kuznetsov, N. Serpone, *J. Phys. Chem.* 113 (2009) 15110

[18]   H. Tang, H. Berger, P.E. Schmid and F. Lévy, *Solid State Communications* 87 (1993)847

[19]   N. Serpone, D. Lawless and R. Khairutdinov, *Journal of Physical Chemistry* 99 (1995) 16646

[20]   L. Forss and M. Schubnell, *Applied Physics B: Photophys. Laser Chem.,* 56 (1993) 363

[21]   N. Serpone, D. Lawless and R. Khairutdinov, *Journal of Physical Chemistry*, 99 (1995) 16646

[22]   J. Chen, L. B. Lin, F.-Q. Jing, *J. Phys. Chem. Solids* 62(2001) 1257

[23]   L.G.J. de Haart and G. Blasse, *Journal of Solid State Chemistry* 61 (1986) 135

[24]   R.M. Kumar, S. Badrinarayanan, M. Sastry *Thin Solid Films* 358 (2000) 122

[25]   Y.C. Zhu, C.X. Ding J. *Solid State Chem.*, 145 (1999) 711

[26]   Watanbe and T. Hayashi, *J. of Luminescence* 112 (2005) 88

[27]   Y. Lei, L. D. Zhang, G. W. Meng, G. H. Li, X. Y. Zhang, C. H. Liang, W. Chen and S. X. Wang, *Applied Physical Letters* 78 (2001) 1125

[28]   F. Lahoz, I.R. Martín, U.R. Rodríguez-Mendoza, I. Iparraguirre, J. Azkargorta, A. Mendioroz, R. Balda, J. Fernández, V. Lavín *Optical Materials*, 27 (2005) 1762

[29]   E. Le Boulbar, E. Millon, E. Ntsoenzok, B. Hakim, W. Seiler, C. Boulmer-Leborgne, J. Perrière *Optical Materials* 34 (2012) 1419

[30]   J. M. F. Van Dijk and M. F. H. Schuurmans, *J. Chem. Phys* 78 (1983) 5317

[31]   Yongsheng Liu, Wenqin Luo, Renfu Li, Haomiao Zhu, and Xueyuan Chen, *Optics Express* 17 (2009) 9748

Chapter 6

Chapter 6

Applications on Photovoltaics and Photocatalysis

"All invention and progress come from finding a link
between two ideas that have never met."
-Theodore Zeldin

6.1 INTRODUCTION

Downshifting of high energy photons is among a series of methods proposed to increase solar cell efficiency. In this section the absorption and luminescent properties of luminescent photon-frequency down-shifter (DS) layers, based on the rare earth (Nd^{3+}) ions doped titanium dioxide matrix for conventional c-Si solar cells are presented. Titania shows strong absorption above the optical bandgap in which the spectral response of silicon solar cells is poor – and transfers the absorbed energy non-radiatively to rare earth ions. The luminescence properties of these doped wide bandgap oxide material is used to enhance the efficiency of photovoltaic devices. The estimation of the changes in the solar spectrum caused by the DS layer and finally the effect of these layers on the efficiency of c-Si solar cells were studied. Secondly, although TiO_2 is the most widely used photocatalyst, attention has been paid to rare earth ions doped titania and testing their efficiency to replace pure TiO_2 and enhance the photocatalytic conversions.

The work was based on the following investigation themes:

- the annealing temperature effects of the Nd^{3+} doped titania films in the range 300°C - 800°C for six hours;

- Exploration of doping possibility at very low Nd concentration in titania matrix by different architectures for the DS layer;

- in view of application point of view, testing the samples as a top DS layer on top of a crystalline silicon solar cell (laboratory made c-Si by MTLab, FBK), thus determining each sample's potential as an efficiency enhancer.

- the photoactivity properties of Nd –doped TiO_2 thin films: Photocatalytic degradation of Methylene Blue.

6.2 STUDY OF THE EFFECT OF ANNEALING TEMPERATURE ON THE FILM PROPERTIES

In the present section, the results of a study of the post- growth annealing effects on the properties of neodymium doped titania thin films are presented. Post-growth annealing treatments in air ambient were performed in a range of temperatures 300°C-800°C for six hours, with the aim to optimize the photoluminescence characteristics and the structural properties of the films. The influence of the annealing treatment on the structural changes (phase transformations) and optical properties was investigated. The photoluminescence emission features of Nd^{3+} ions (under both a direct excitation of the $^4F_{3/2}$ level and an indirect one by UV) are examined in order to obtain efficient NIR PL.

6.2.1 THE SAMPLE PREPARATION

In Chapter 3, it resulted that very low concentrations of Nd were necessary to obtain films with good photoluminescence properties, especially for a photon frequency down-shifting from UV to NIR. The study of the annealing temperature effects was performed on samples of very low Nd concentration, even lower than the 0.9 % value

considered in Chapter 3. In order to obtain that films, the same target cross-contamination process was exploited, but by lowering the Nd contamination level of the TiO_2 target, through a contamination time reduction.

Post-growth annealing of those films was carried out in an annealing furnace at $600°C$ for six hours, with a heating rate of $5°C/min$, in air ambient. The annealed films were studied by XRF (for chemical quantification of Nd content), XRD (for structural analysis - changes in the crystalline phase, lattice parameters), UV-Vis- NIR spectroscopy (for optical properties) and PL spectroscopy (for NIR photoluminescence emission characteristics).

6.2.2 CHEMICAL QUANTIFICATION OF LOW Nd CONTENT BY XRF STUDIES

XRF quantification was carried out by refinement of a sample model. A region of interest containing the characteristic lines of the main element (TiKα and TiKβ) and the lines of the dopant (Nd L lines) was simulated from first principles and intensities were normalised to the maximum of the line of the main component (Ti). The model of the sample was refined allowing the concentration of Nd to vary in a least squares minimisation loop and adding a polynomial background to the calculated intensities. The code was written in Python and the minimisation was performed with the package lmfit-py (http://newville.github.io/lmfit-py/#).

For the simulation a parallel incident beam with MoKα energy was assumed. X-Ray intensities were converted to broader lines with a Gaussian shape, low energy short and long tale and a step function as described by Van Gysel et al. [1].For the detector efficiency, escape effects and air absorption on the path sample-detector were also taken into account, considering 90 degrees incidence angle on the detector surface for

all detected photons [2]. In the calculation the effect of secondary fluorescence was not taken into account. The simulation code takes a stoichiometric formula as input (e.g. $TiO_2Nd_{0.001}$) with initial estimate for the Ti concentration and the film thickness. The TiO_2 density was assumed to be 4.23 g/cm^3. Fundamental parameters (photoelectric cross sections, total mass absorption coefficients, fluorescence yield, line energies, and relative emission probabilities) were taken from the X-raylib [3]. The estimated Nd concentration in these films is found to be 0.03at%.
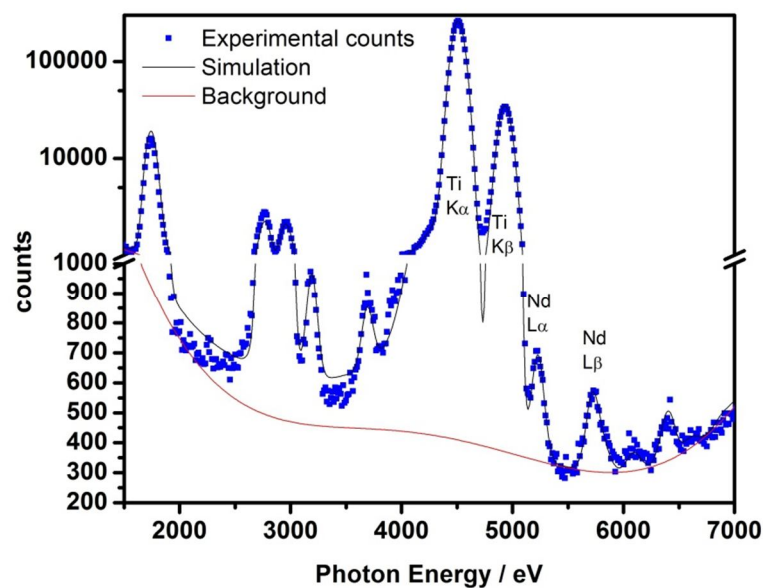
Figure 6.1: *X-ray fluorescence spectra for the film (annealed at 600°C) grown on quartz substrate*

6.2.3 Influence of post-growth annealing in air on the film crystal structure

The crystal structure and the degree of crystallinity of post-growth annealed Nd-doped TiO_2 films with a very low concentration of neodymium were investigated with X-ray diffraction analysis. The as-grown films were amorphous; no diffraction peaks were observed. Figure 6.2 shows the XRD patterns obtained for Nd- doped titania films grown on quartz substrates, after annealing at different temperatures.

(a)
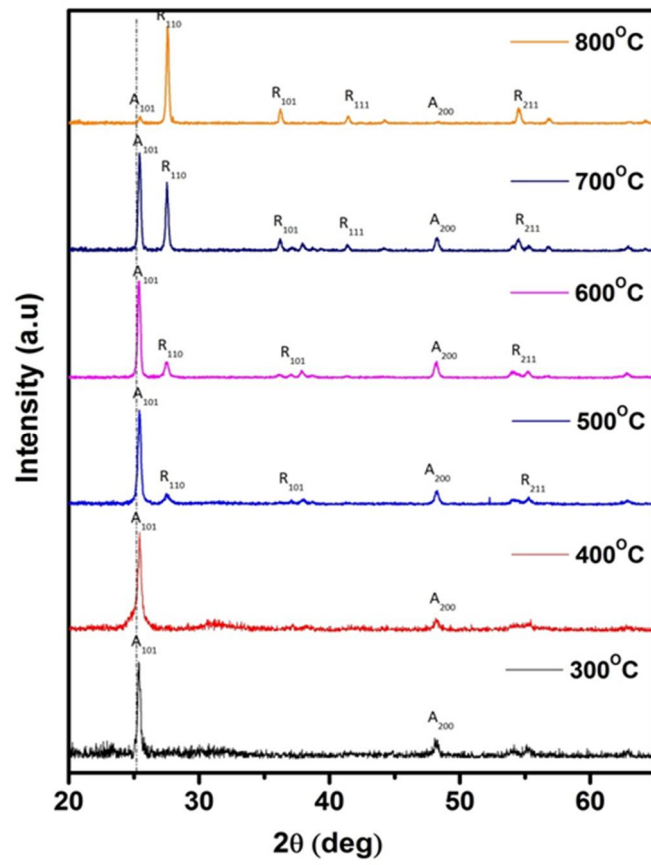
(b)
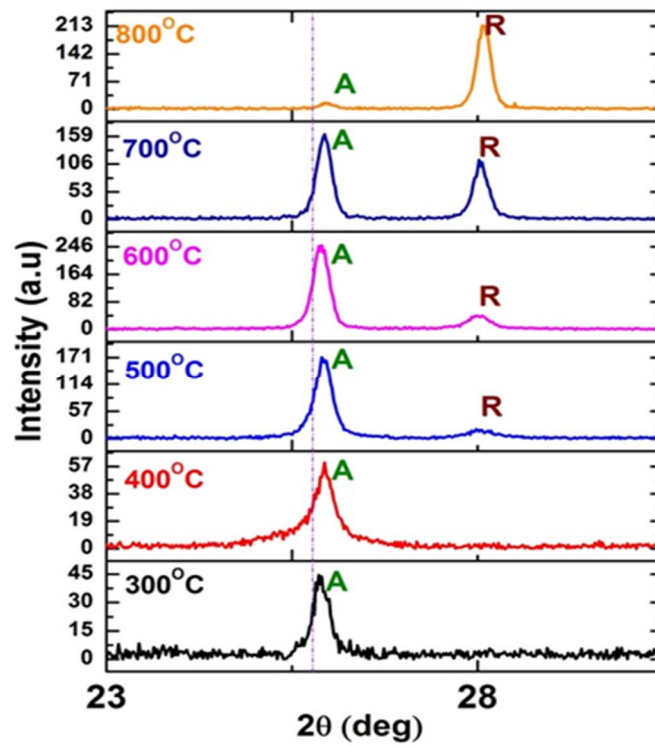
Figure 6.2: *Typical grazing angle incidence X-ray diffraction patterns on post-growth annealed (from $300^{\circ}C$ to $800^{\circ}C$ for six hours) Nd-doped TiO_2 films with [Nd]=0.03%. Panel (a) shows the diffraction pattern (2 theta from: 20°-65°) and panel (b) shows the enlarged diffraction pattern (from 2 theta: 23°-30°). The dotted line drawn is the guide to the eye for standard Anatase TiO_2 (ICDD #21-1272). A – Anatase; R- Rutile phase.*

Annealing resulted in diffraction peaks related only to the anatase and rutile phase structure, no other impurity based phases or any mixed oxide phases are detected for all the samples even annealing at high temperature of 800°C. The film annealed at 300°C crystallizes in the anatase phase of titanium dioxide. In addition to the dominant anatase A(101) located at 2θ=25.39°, additional crystallographic planes of A(103), A(004), A(200), A(105), A(211) and A(204) were observed as well with very low intensity. All diffraction patterns can be indexed as a tetragonal structure with a space group of $I4_1$/amd with a cell parameters of a=b=3.7852 and c= 9.5139 Å and a cell volume of 136.3 (JCPDS 21-1272). Evolution of rutile related peak R(110) at 2θ=27.56°and weak intensity peaks of R(101), R(111), R(211) began to appear for the films annealed at 500°C. At 500°C, the film undergoes the phase transformation from anatase to the thermodynamically stable rutile (A $\rightarrow$ A+R). Furthermore, figure depicts that the intensity of anatase (101) decreases when temperature increases from 500 to 800°C whereas the intensity of rutile (110) increases. It is assumed that anatase transforms to rutile at approximately 600°C in bulk materials [4, 5]. Wang et al. [6] reported that by varying annealing temperature from 70°C to 900°C in Nd –doped TiO_2 nanoparticles only anatase phase forms. The evolution of anatase to rutile phase transition happens at temperature 1100°C, which is high, compared to the critical temperature for the TiO_2 sample. However experimentally, factors such as particle size and morphology, impurities, surface chemistry, concentration of intrinsic defects,

temperature and the method of preparation have been observed to influence the transformation.
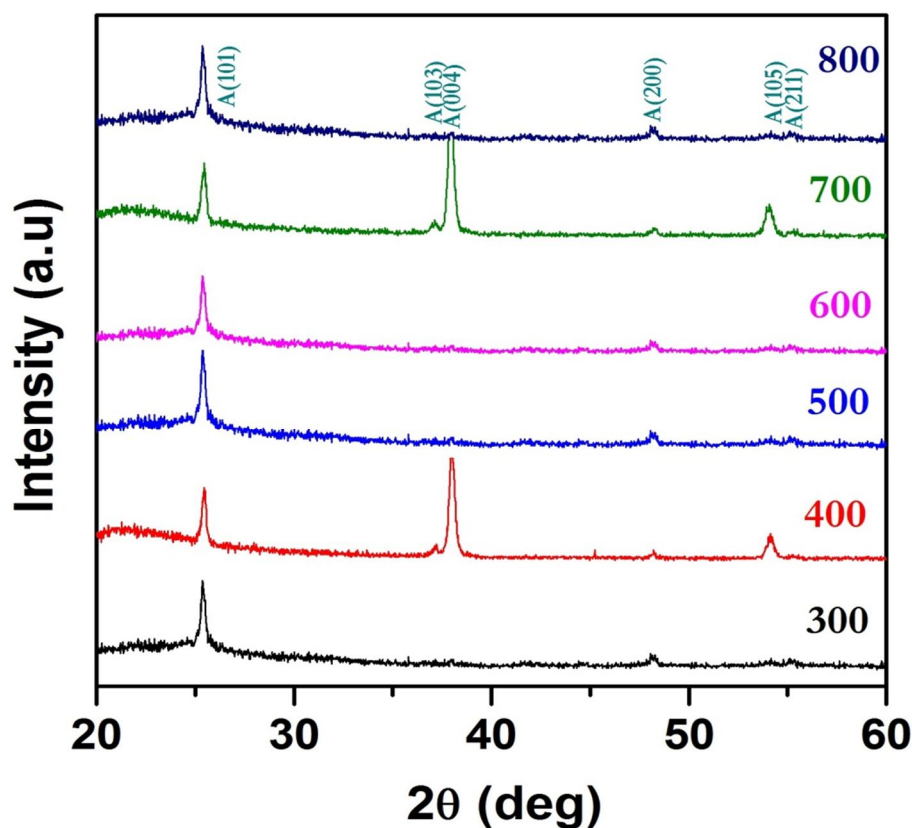
Figure 6.3: *Typical grazing angle incidence X-ray diffraction patterns on annealed pure TiO$_2$ film (from 300°C to 800°C for six hours). Anatase TiO$_2$ (ICDD #21-1272).*

Additionally, the XRD pattern of pure TiO$_2$ annealed at different temperatures are shown in Fig. 6.3. It can be seen that the patterns reveals only the pure anatase phase with dominant peak of A (101), as we increase the annealing temperature from 300°C to 800°C. Therefore, a very low incorporation of neodymium into the titania lattice produced remarkable changes in the crystallographic structure of the films as we increase the annealing temperature. The various structural parameters for Nd –doped TiO$_2$ thin films annealed at different temperatures (T$_A$) are calculated using the relevant formula and are systematically presented in table. In order to evaluate the change in crystallite size in the films with T$_A$, the FWHM value was derived from the

225

spectra around the reflection of anatase A(101). The spectra of samples (Nd –doped TiO$_2$) calcined at temperatures 300 and 400°C exhibits anatase (101) phase. The close peak intensity (from the table) of these samples indicates similar amount of crystalline material. Therefore, the amount of anatase phase is almost independent of the calcination temperature in the range of 300–400°C. From the table, considering the samples annealed at 500-700°C (having both anatase + rutile mixtures), the FWHM of anatase is seen to decrease from 0.2978 to 0.2371; correspondingly we can observe increase in the crystallite size (from 37.1 to 60 nm).

Annealing Temp. (°C)	A (101) 2θ position	R (110) 2θ position	A (101) FWHM	R(110) FWHM	Peak height A phase	Peak height R phase	a (Å)	c (Å)	c/a	V (Å³)	D A(101) (nm)	D R(110) (nm)
300	25.39	-	0.286	-	19.77	-	3.774	9.447	2.503	135	39.7	-
400	25.43	-	0.277	-	19.75	-	3.772	9.353	2.479	133	42.1	-
500	25.42	27.56	0.297	0.676	63.78	12.67	3.771	9.412	2.495	134	37.1	16.1
600	25.39	27.51	0.257	0.342	76.96	18.62	3.774	9.452	2.504	135	48.8	33
700	25.43	27.54	0.237	0.240	47.23	33.04	3.769	9.414	2.497	134	59.9	49.8
800	25.46	27.58	0.293	0.210	5.134	61.30	3.765	9.389	2.493	133	38	59.1
Anatase	25.28	-	ICDD CARD No. (21-1272)				3.785	9.514	2.513	136.3		
Rutile	-		ICDD CARD No. (21-1276)				4.593	2.958	0.644	62.4		

Table 6.1: *Lattice parameters from XRD - a(nm), c(nm), c/a ratio, cell volume V(Å³), Crystallite size <D> (nm) for the Nd –doped TiO$_2$ films annealed at different temperatures.*

Larger the crystallite size, narrower the peak broadening. On the other hand, at 800°C, there is a visible deterioration of anatase phase (rutile being the major phase) which influences the increase in the peak broadening (0.2937) and the crystallite size decreases. As we also see that, the 2theta values of anatase (101) peak shifts from the standard value, which indicates the presents of lattice defects associated with the impurity atoms and also due to the increase of the local strain in the lattice.

6.2.4 INFLUENCE OF ANNEALING TEMPERATURE ON THE FILM OPTICAL PROPERTIES

Post-deposition annealing strongly affects the optical transmission spectra and reflectance of the Nd –doped thin films. Figure 6.4 shows the optical transmission and reflectance spectra for the films annealed at different temperatures. Annealing in air changed the overall transmission characteristics, affecting the average transmission in the visible range. The transmittance of the films decreased with increasing the annealing temperature which reveals that the films are more absorbant at higher temperatures. Increase in the annealing temperature showed a progressive red shift in the fundamental absorption band edge in Nd –doped TiO_2 films. These red shifts in the band edge of the doped sample can be attributed to the charge transfer between the titania valence or conduction band and Nd ion 4f level [7].
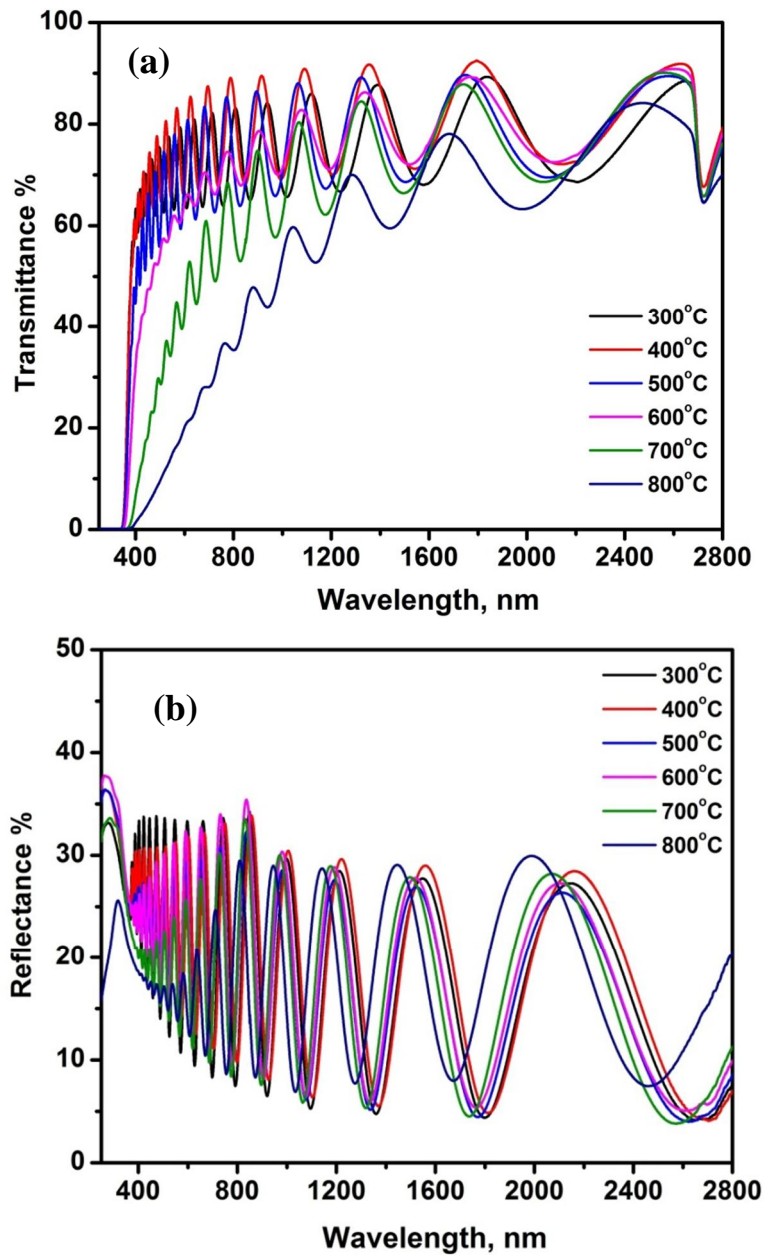
Figure 6.4: *UV –visible near IR spectra of Nd doped TiO₂ films on quartz substrates (a) Optical Transmittance and (b) Reflectance*

ESTIMATION OF OPTICAL BANDGAP

A given semiconductor can exhibit direct or indirect band to band transitions which depend on its crystal structure. It was found in the literature for TiO₂ anatase phase structure has the direct bandgap of 3.42 eV while the indirect bandgap is 3.46 eV [8].

The direct and indirect bandgap of rutile phase is 3.04 eV and 3.05 eV [9]. These transitions are all in UV region.

The optical bandgap energy of the films was obtained by using the Tauc plot, using the equation [Chapter 2, Equation 2.7]. Figure 6.5 shows the Tauc's plots (a) of $(\alpha h\nu)^2$ for direct gap and (b) of $(\alpha h\nu)^{1/2}$ for indirect gap, versus the photon energy (E) of the samples annealed at different temperatures and the optical band gaps of the films were determined by extrapolation. Both the direct and indirect bandgap decreased monotonically with increasing the annealing temperatures. The direct bandgap decreased from 3.51 to 2.99 eV whereas the indirect bandgap decreased from 3.25 to 2.30 eV respectively.
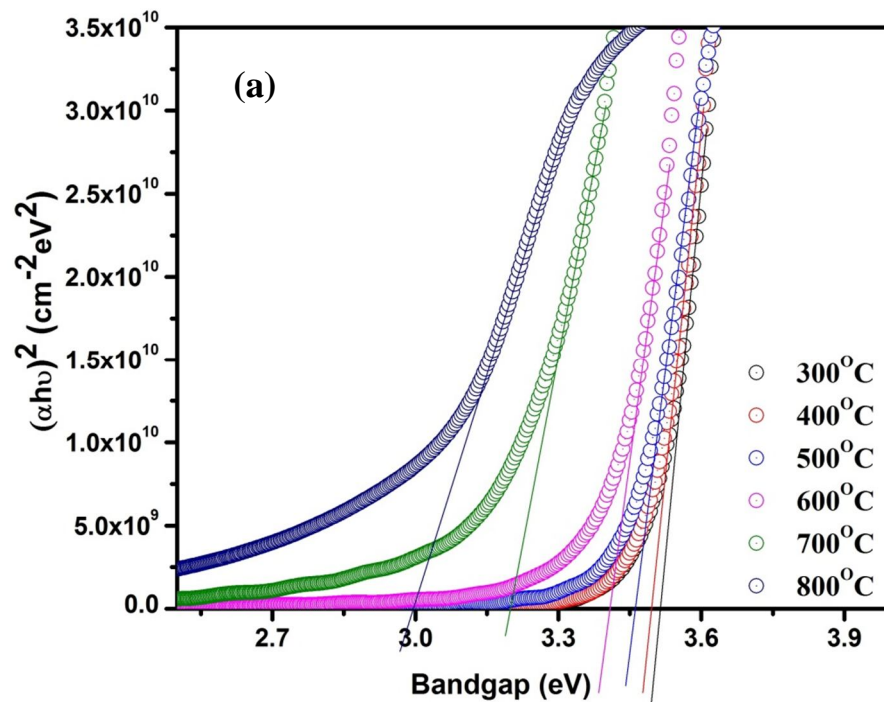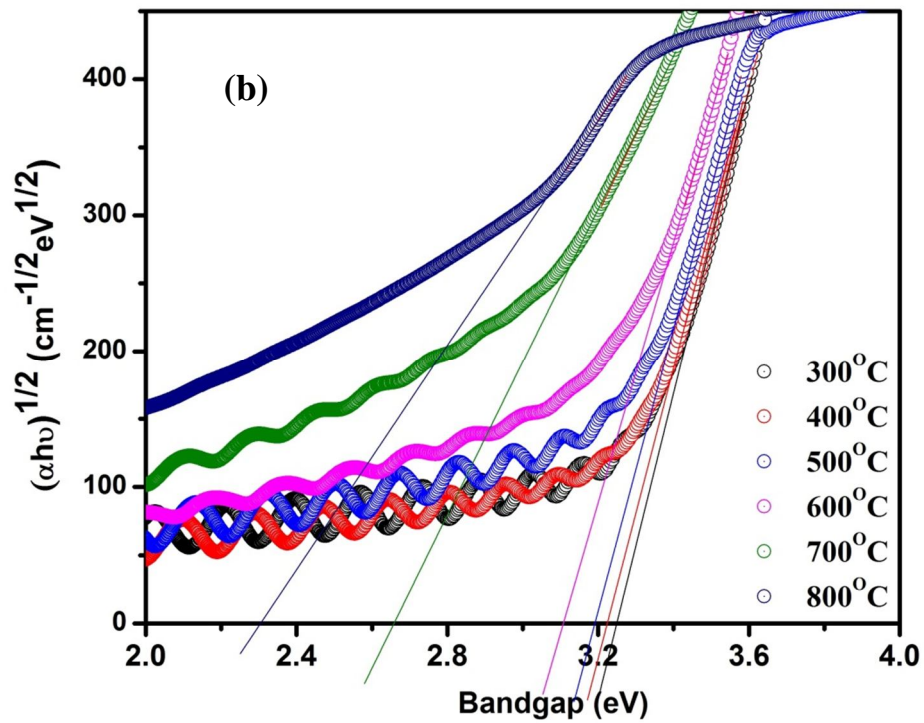
Figure 6.5: *(a) Direct and (b) indirect bandgap Tauc's plot of (αhυ) $^{1/2}$ vs. photon energy (hυ) for Nd –doped TiO$_2$ films (having Nd concentration 0.03at.%) annealed at different temperatures (from 300°C to 800°C for six hours)*

Annealing Temp.	Direct Bandgap	Indirect Bandgap
(°C)	(eV)	(eV)
300	3.51	3.25
400	3.49	3.22
500	3.46	3.18
600	3.40	3.10
700	3.19	2.65
800	2.99	2.30

Table 6.2: *Direct and indirect bandgap values obtained for Nd –doped TiO$_2$ films annealed at different temperatures (300°C to 800°C)*

6.2.5 ANNEALING TEMPERATURE EFFECT ON THE NEAR INFRA-RED PHOTOLUMINESCENCE PROPERTIES

Photoluminescence (PL) investigations of intra-configurational 4f emission from Nd^{3+} ion in titania host matrix annealed at different temperatures were systematically studied by two excitation regime: Direct excitation of $^4F_{3/2}$ - Blue line from a Argon ion laser (476 nm – 2.60 eV) and Non resonant with $^4F_{3/2}$ or Indirect excitation – through UV (355 nm) and their energy transfer. Figure 6.6 shows the evolution of room temperature near infra-red photoluminescence spectra of titania film doped with 0.03 at.% of Nd concentration as a function of the annealing temperature with excitation wavelength at 476nm. Like all other rare earth elements found in literature, thermal activation of Nd^{3+} enhances the luminescence intensity. All the samples annealed at various temperatures reveal the characteristic PL emission bands of Nd ions irrespective of their intensity. The sample annealed at 600°C displays a strong luminescence emission band centred at 908 nm and 1096 nm (Fig. 6.6 (a) and (b) respectively). The spectrum at 840-1000 nm was measured by a silicon detector (excitation power was kept constant at 150mW for all the samples), while the second part of the spectrum at 1040-1180 nm was measured by a PMT (excitation power was kept constant at 350mW for all the samples).
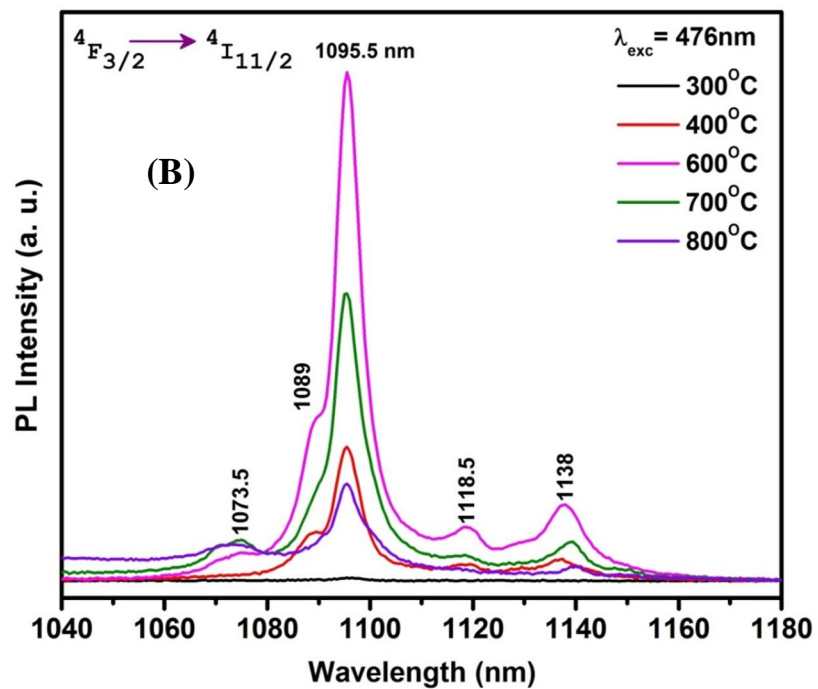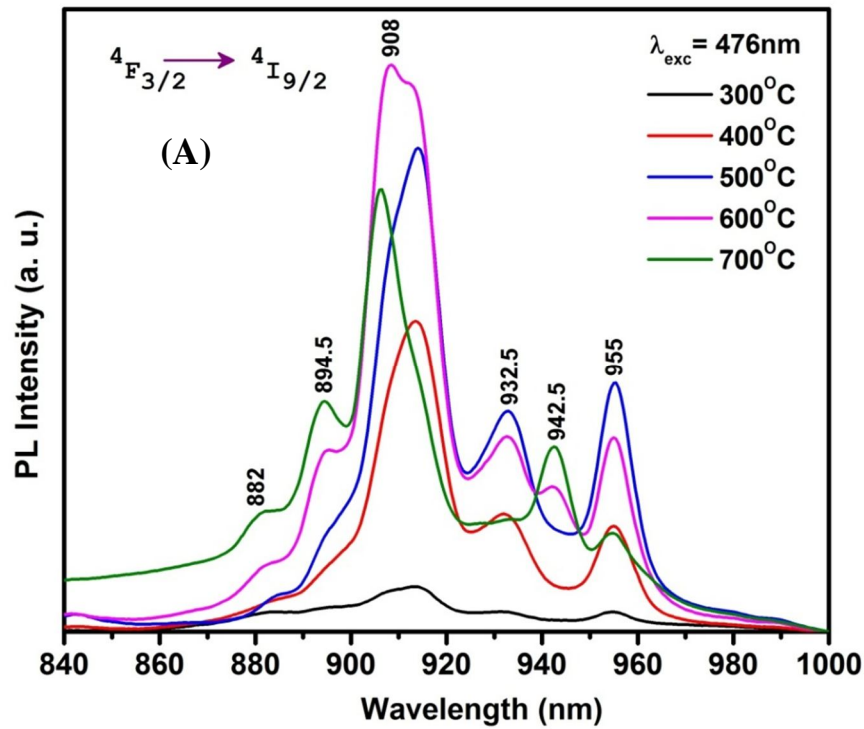
Figure 6.6: *PL emission Spectra of TiO₂: Nd under Resonant excitation (Direct) with 476nm for Nd -doped TiO₂ film annealed at different temperatures (from 300°C to 800°C)*

Six crystal field (CF) splitting for the transition $^4F_{3/2}$ to $^4I_{9/2}$ and five CF splitting for $^4F_{3/2}$ to $^4I_{11/2}$ transition were observed. The luminescence spectra indicates that Nd^{3+} ion is optically active at these two transitions ($^4F_{3/2} \rightarrow {}^4I_{9/2}$ and $^4F_{3/2} \rightarrow {}^4I_{11/2}$). A significant change in the PL intensity, shape and position of the emission band was observed with respect to the variation in the annealing temperature. Since the excitation wavelength in this case is lower than the bandgap of titania, we conclude that the excitation is direct from the ground state to one of the upper excited states around 476nm ($^4G_{9/2}$). Thereafter, the electrons decay back to the metastable state $^4F_{3/2}$, from which they relax down to the lower lying ^4I_J (J=9/2, 11/2, 13/2) states, with the emission of photons of characteristic wavelengths.

The NIR PL emission observed through direct excitation motivated us to determine their performance as spectral engineering photon frequency down-shifters by exciting through UV (355nm, indirect excitation) close to the bandgap of titania. Figure 6.7 (a and b) shows the evolution of room temperature near infra-red photoluminescence spectra of titania film doped with 0.03 at.% of Nd concentration as a function of the annealing temperature with excitation wavelength at 355nm line from a YAG laser at constant power of 2mW of slit 1mm. The annealing process has significant effect on the PL intensity.
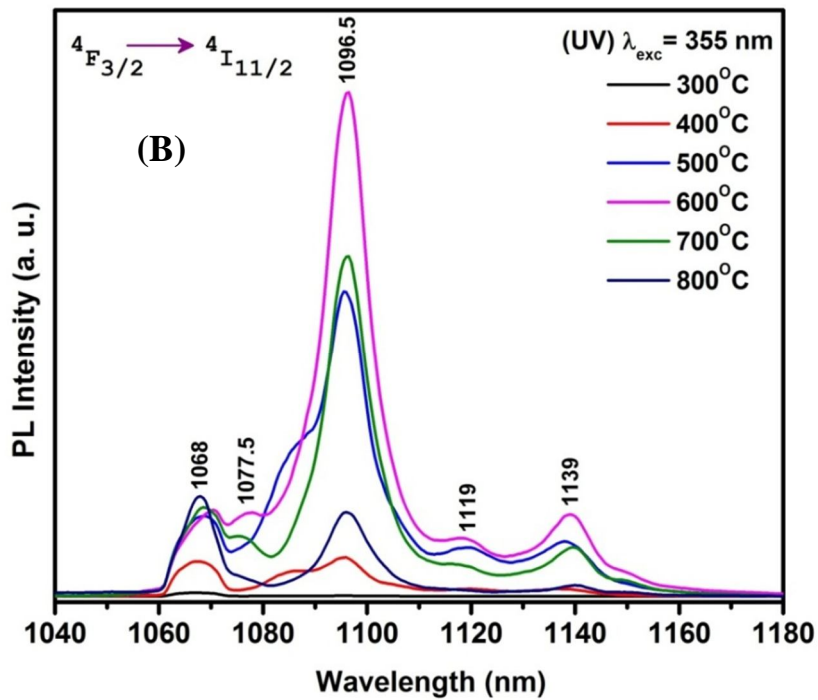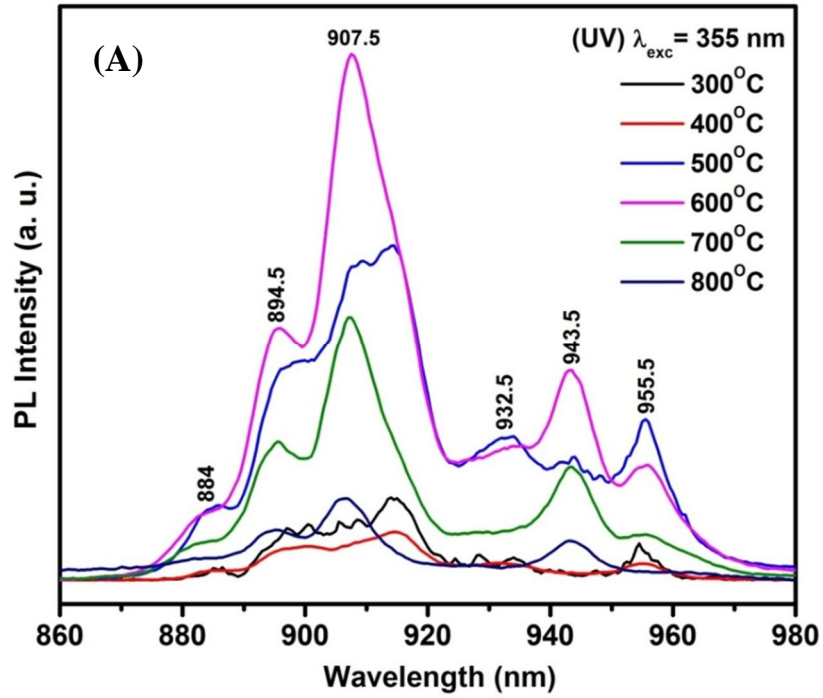
Figure 6.7: *PL emission Spectra of TiO$_2$: Nd under non-resonant excitation (UV) with 355nm for Nd -doped TiO$_2$ film annealed at different temperatures (from 300°C to 800°C)*

All the annealed samples exhibits NIR PL emission peaks of Nd^{3+} around 907.5 nm and 1096 nm, which are associated with the electronic transitions of $^4F_{3/2} \rightarrow {}^4I_{9/2}$ and $^4F_{3/2} \rightarrow {}^4I_{11/2}$. Firstly, the appearance of these strong near infra-red PL emission lines at non-resonant excitation above the band gap of titania host matrix clearly indicates that the indirect excitation mechanism of Nd^{3+} ions via energy transfer is significant. The emission pattern is different from that of Nd^{3+} ions in Nd_2O_3 in both the peak positions and shape, thus excluding the possibility of impurity phase and also the separate segregation of Nd_2O_3 [10]. Figure 6.7 (excited with 355nm) shows that the PL intensity of $^4F_{3/2} \rightarrow {}^4I_{11/2}$ transitions under 355 nm excitation wavelength firstly increases with the temperatures to the maximum and then drops with the further increase of temperature. Film annealed at 600°C exhibits the strongest luminescence from Nd^{3+} when excited at both 476 and 354 nm. The PL emission is reduced in intensity considerably when the annealing temperature is below and above 600°C. L. Li *et al* [11] reported [Eu/TiO$_2$] that the reduced emissions at lower temperature (around 400°C) can be due to small number of thermally generated anatase nanocrystals and a larger amount of hydroxyl groups. Li *et al* also reported that the reduction in the intensity higher than 400°C (till 900°C) can be also due to the energy shifts of the anatase conduction band edge and titania defect states caused by the particle size and the clustering of rare earth ions. This will also reduce the energy transfer efficiency between the host matrix and doped rare earth ions. Zeng *et al* [12] reported that the reduction in the intensity at higher annealing temperature can be also due to the temperature quenching effect, which includes the non radiative transitions, energy transfer between the two neighbouring ions, impurity centres or defects nearby.

6.3 EXPLORATION OF DIFFERENT FILM ARCHITECTURES FOR PL PHOTOLUMINESCENCE PROPERTIES OPTIMIZATION FOR PHOTO-VOLTAIC APPLICATION

In recent years, the efficient energy transfer from the oxide host matrix to RE ion has been attracting much interest in photovoltaics in order to adapt the solar spectrum through photon conversion for an effective utilization of high energy photons through non-radiative energy transfer, a process which can improve the silicon based solar cell efficiency. It was demonstarted in Chapter 3 that Nd doping concentration limit plays a crucial role in order to achieve high luminescence intensity through down-shifting. Since there is a technical limit to explore a wide range of very low Nd concentrations, linked to the difficulty of a fine tuning of the electrical power at the Nd target (the lowest useful power for Nd sputtering was 3W). Therefore, we searched an effective alternative approach in favor of achieving a more intense Nd-related photoluminescence emission in NIR through DS from UV. Taking this feature into consideration, we proposed a new stratregy in building up films with a multilayer architecture, in order to incorporate very low/optimal concentration of neodymium inside the titania matrix.

In this present section we focussed on the fabrication of these different architectuures and their characterization and potential application in photovoltaics.

Multi-layer film deposition

Different bilayer and multilayer thin films of titania doped with optimal concentrations of neodymium were deposited on quartz substrates. Their chemical composition, structural and near infra-red (NIR) photoluminescence properties were studied. The major step involved for the successful fabrication of mutilayers was to optimise the overall layer thickness and the optimal doping concentration limit in the

host titania matrix. The overall average thickness of each film was kept constant around 1μm. Secondly, as we knew the limitations of the dopant concentrations in order to avoid luminescence quenching effect, the optimal concentration of Nd ion was kept less than 1 at.% (Nd/Ti = 3.7%), a value above which photon downshifting process hardly occurs.

Pure and Neodymium doped titanium dioxide thin films has been prepared by radio frequency (13.56 MHz) sputtering by using TiO_2 target, by keeping the Argon flow rate constant at 30 sccm and a pressure of 4 Pa. The reactor base pressure was kept at $2x10^{-6}$ Pa. A self-bias voltage of -850 V at TiO_2 target (corresponding to a power of 82 watts) was kept fixed. In order to obtain different optimal neodymium compositions in the films, the power onto the Nd target was varied by keeping also the fixed thickness ratio. All the depositions were carried out at 4 Pa working pressure. All the films were deposited at room temperature and ex-situ post-deposition annealing treatments were made for six hours in ambient air, at a temperature of at 600°C, reached with a heating rate of 5°C/min.

6.3.1 SAMPLE DEPOSITION SCHEMATIC REPRESENTATION

The different bilayers & multilayer architecture stacks of TiO_2: Nd^{3+} were prepared by different approaches aiming to achieve optimal doping ratio Nd/Ti by keeping the overall layer thickness constant. The description of the plasma parameters for the different architecture demonstrated at fixed thickness ratio were depicted along with the measured film thicknesses in Table 6.3, together with the sample labelling. 4 types of film architectures were produced, they are displayed in the scheme in Fig. 6.8.

The schematic representation of these layers architecture along with the deposition parameters used were predicted below.
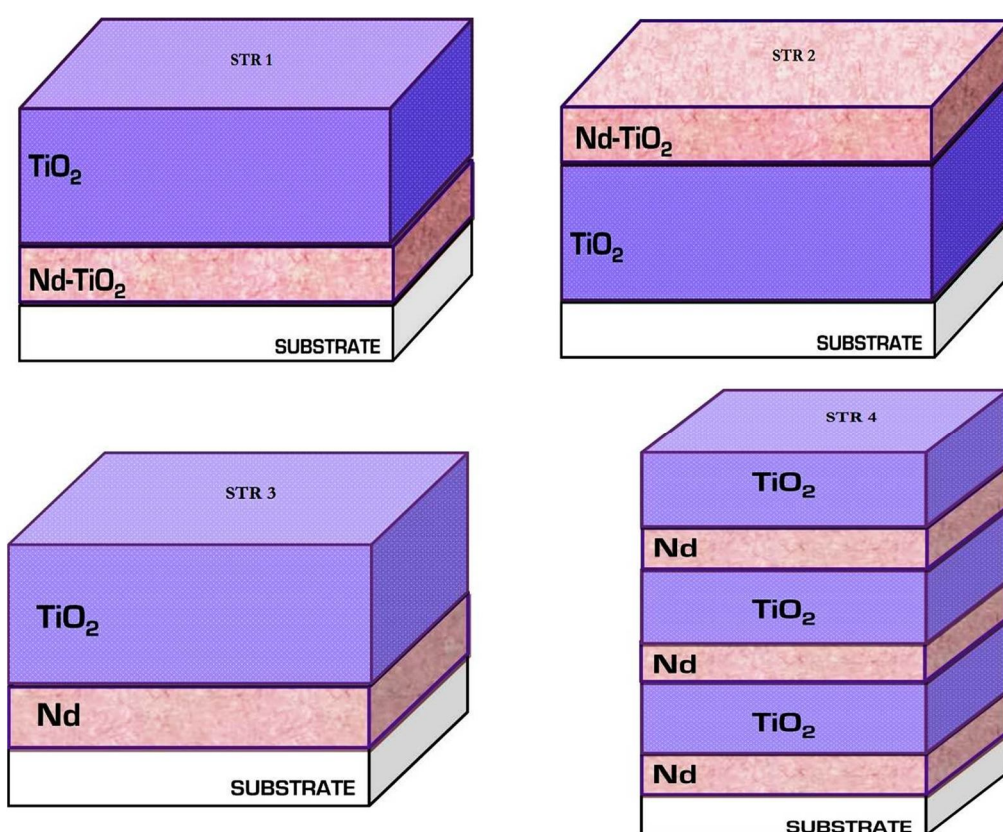
Figure 6.8: *Layer Architecture of the selected TiO₂: Nd samples #STR 1, #STR 2, #STR 3 and #STR 4 and the corresponding sample depostion parameters are described in Table 6.3.*

Sample Architectures	Deposition Conditions	Deposition Time	Average Total Thickness (μm)	Nd (%) Quantification from XRF
STR 1	Co-Sputtering – (Nd/TiO$_2$) TiO$_2$: -850 V, Nd : 4 Watts	30 mins	0.895 ± 0.026	0.1
	Single RF cathode - TiO$_2$	8 hours		
STR 2	Co-Sputtering - Nd/ TiO$_2$ TiO$_2$: -850 V, Nd : 4 Watts	30 mins	0.986 ± 0.014	0.25
	Single RF cathode - TiO$_2$	8 hours		

STR 3	Nd : 12 watts	4 mins	0.933 ± 0.025	0.22
	Single RF cathode - TiO$_2$	8 hours 56 mins		
STR 4	Nd : 12 watts	Each layer coated 1 min 20 secs	1.043 ± 0.011	0.26
	Single RF cathode - TiO$_2$	Each layer coated 3 hours		
	Single RF cathode - TiO$_2$	8 hours		

Table 6.3: *Deposition parameters for the different architecture layer for the samples (TiO$_2$: Nd) #STR 1, #STR 2, #STR 3, #STR 4*

6.3.2 STRUCTURAL ANALYSIS

Figure 6.9 shows the XRD pattern aquired by grazing angle incidence at 3° for different architectures of Nd –doped Titania thin films after post growth annealing at 600°C in air ambient. All the films exhibits pure anatase phase of titania and no trace of characteristics peaks was observed for other phases such as rutile or brookite. By means of Debye- Scherrer equation, the average size of all the architecture were estimated (varies between 19 -21 nm) and reported in Table 6.4 below. Comparing to the previous results (Chapter 3) for sample S1 of Pure TiO$_2$, the average size was found to be 18 nm. There is no abrupt change in the structural properties between different architectures and also in comparison with pure titania.
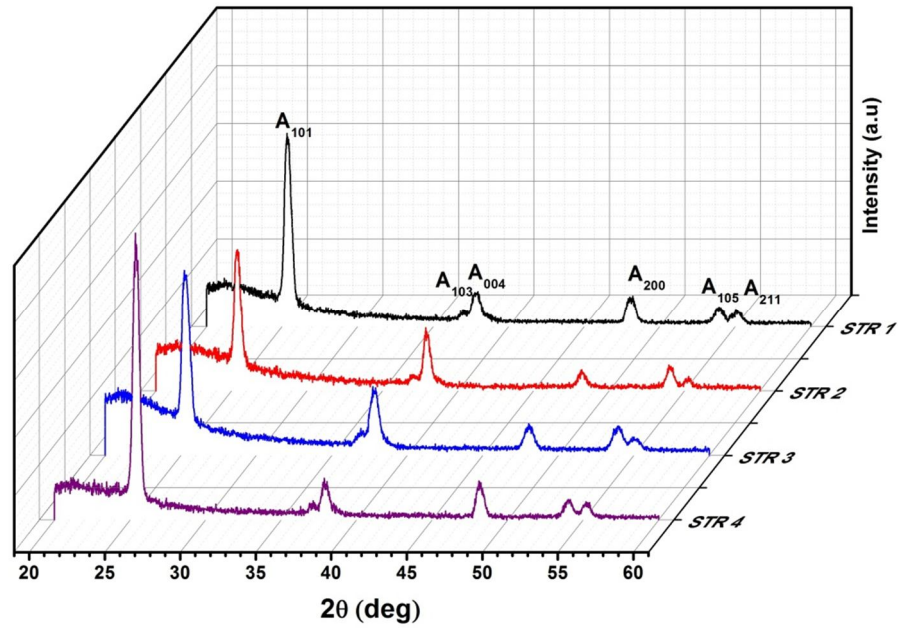
Figure 6.9: *X-ray diffraction pattern for different layer architecture TiO$_2$: Nd samples #STR 1, #STR 2, #STR 3 and #STR 4.*

Sample ID	Phase	2θ (deg) (101)	Crystallite Size (nm) (Sherrer)	d spacing [Å]	Lattice Parameter (Å) a	Lattice Parameter (Å) c	c/a	Volume (Å^3) V=a^{2}c
S1	A	25.33	18 (W.H)	-	3.780	9.438	2.496	134.85
STR 1	A	25.385	20	3.504	3.7807	9.3657	2.4772	133.87
STR 2	A	25.407	21	3.501	3.7725	9.4338	2.5006	134.26
STR 3	A	25.346	19	3.509	3.7836	9.4225	2.4903	134.99
STR 4	A	25.414	21	3.500	3.7750	9.3781	2.4842	133.64

A: Anatase, d$_{PDF}$ – standard interplanar distance, $\Delta d = [(d - d_{PDF}) / d_{PDF} \times 100\%]$; W.H – Williamson Hall plot

Table 6.4: *Lattice parameters (a, c and volume), crystallite size <D> for the different architecture layer for the samples (TiO$_2$: Nd) #STR 1, #STR 2, #STR 3 and #STR 4.*

6.3.3 PHOTOLUMINESCENCE PROPERTIES

Figure 6.10 (a and b) shows the Photoluminescence emission spectra in NIR for all the different architecture under non- resonant excitation through UV(355 nm) . A sharper and more abundant emission lines with fine crystal field splitting corresponds to the transition $^4F_{3/2}$ to its low lying multiplets $^4I_{9/2}$ (panel a) and $^4I_{11/2}$ (panel b) were observed in NIR region. Since there is no direct absorption of Nd^{3+} in this region and from the results of PL excitation and emission characteristics in Chapter 5, such emission in NIR under the non resonant excitation (3.49 eV)indicates that the neodymium emissions are associated with the energy transfer from titania host matrix to Nd^{3+} ions.

It can be observed that the film architecture which gave the best PL characteristics in the 860-1000 nm region was the sample STR 1, followed by the STR 4 sample, and then STR2 and STR 3. The STR 1 sample was also the best one for the PL emission in the 1080 – 1150 nm range, however all the other films behaved in the same manner: no great differences were seen between them.
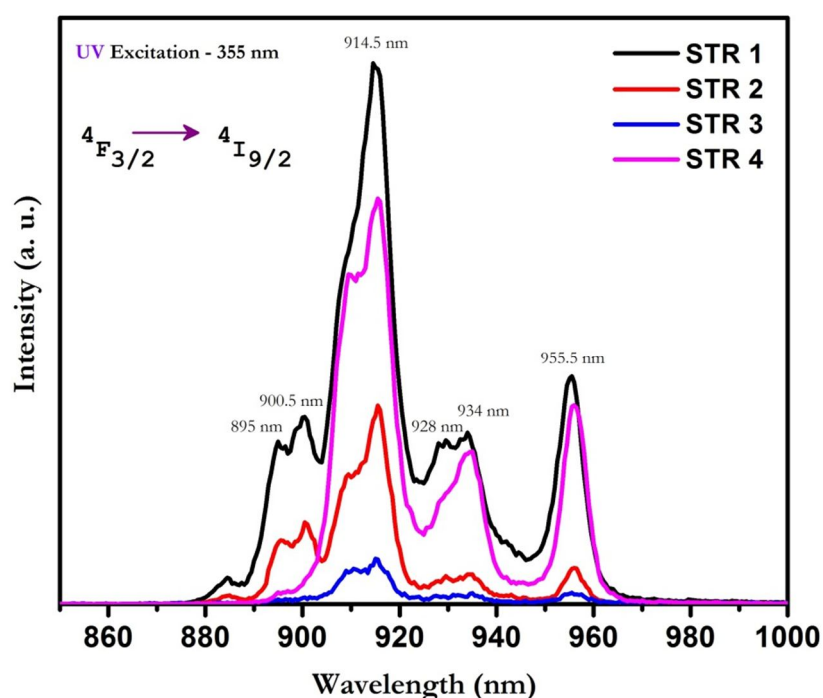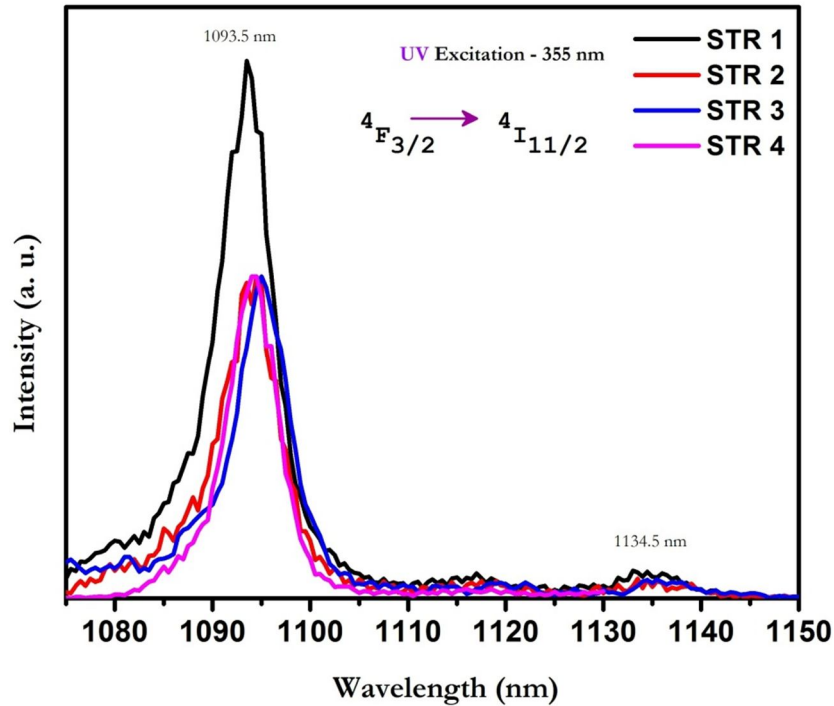
Figure 6.10: *Room temperature NIR PL emission of Nd^{3+} ions under non resonant UV excitation (355 nm)*

6.4 EVALUATION OF THE FILM CAPABILITY AS DS LAYERS ON CRYSTALLINE- SI SOLAR CELL

Materials considered for use as luminescent down shifting materials have to absorb light effectively in the spectral area, where the solar cells, on which they are used, have poor internal quantum efficiency. At the same time these materials have to emit most of the absorbed spectral powers at lower energies, where the internal quantum efficiency of the solar cell is close to its maximum.

6.4.1 DESCRIPTION OF THE C-SI SOLAR CELL

The aim of this task is to validate the interest of the optimized LDS layer for crystalline-Si solar cells on the basis of the films studied on the system RE^{3+}-TiO$_2$. A "home-made" c-Si cell was used for testing. The samples composed of the different

films deposited on quartz substrates (1mm thick) were placed externally onto the front side of the cell. The tests were conducted under a solar light simulator. A schematic representation of the cell is depicted in figure 6.11 (a and b).
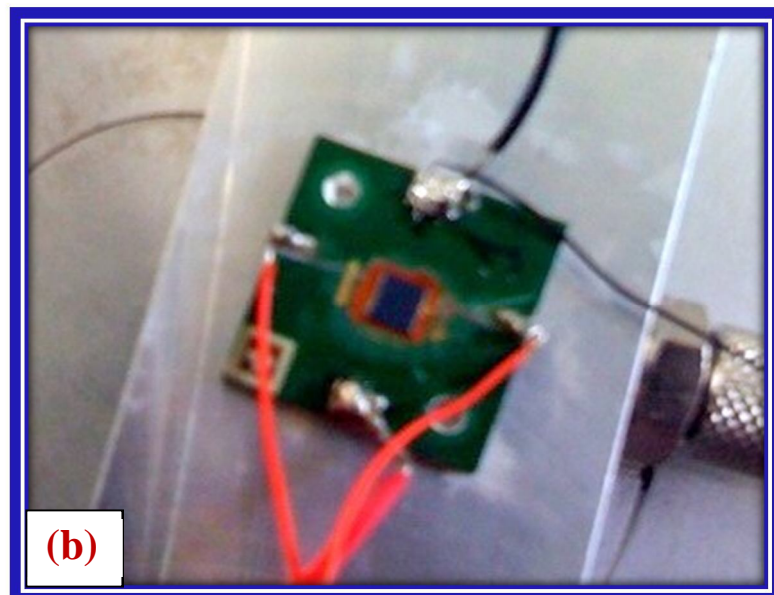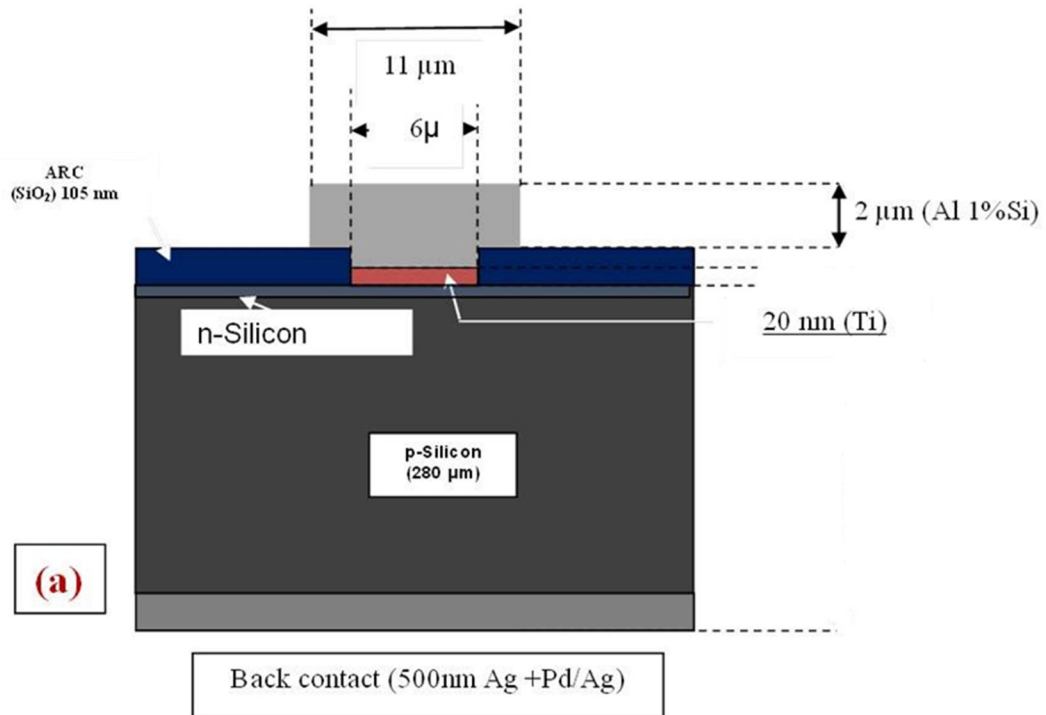
Figure 6.11: *Schematic representation of the c-Si cell (a) cross section and (b) front view*

The different characteristics of the cell are listed below:

- Substrate: Silicon FZ p-type (Boron doped). Thickness: (280 ± 5) μm.

  Resistivity: 0.4-0.7 Ohm*cm.

  Boron Concentration measured by SIMS: $(3.5\pm0.1)\ 10^{16}\ cm^{-3}$

- Size of the device: 4250 x 4250 $μm^2$

- Size of the active area: (n-doped zone): 3650 x 4000 $μm^2$

- Busbar: 4000 x 200 $μm^2$

- Front Metal (Finger e BusBar): 20nm Ti + 2 μm Al 1%Si.

- Fingers: 40 wires.

  Finger Pitch: 100 μm.

- Back metal: back non-polished. Uniform contact: 500nm Al + Pd/Ag

- ARC: SiO_2 105 nm ± 5 nm. Textured surfaces

The electrical characteristics of the cell were:

Sheet resistance: 56 ± 6 Ohm/sq

Metal resistivity: $(9.0 \pm 1.0)\ 10^{-6}$ Ohm*cm

Contact resistivity: $(1.5 \pm0.5)\ 10^{-5}$ Ohm*cm^2

Bulk lifetime: 100-200 μs

The internal and external quantum efficiencies (IQE, EQE respectively) of the cell are presented in Fig. 6.12. As can be seen the quantum efficiency is much lower in the highest frequency part of the spectrum. It's in this wavelength range where the LDS has to be active. Even if the Nd^{3+} emission is in the NIR region (around 900 nm), the spectrum is in a wavelength region were the internal quantum efficiency is not rather low (close to the maximum IQE).
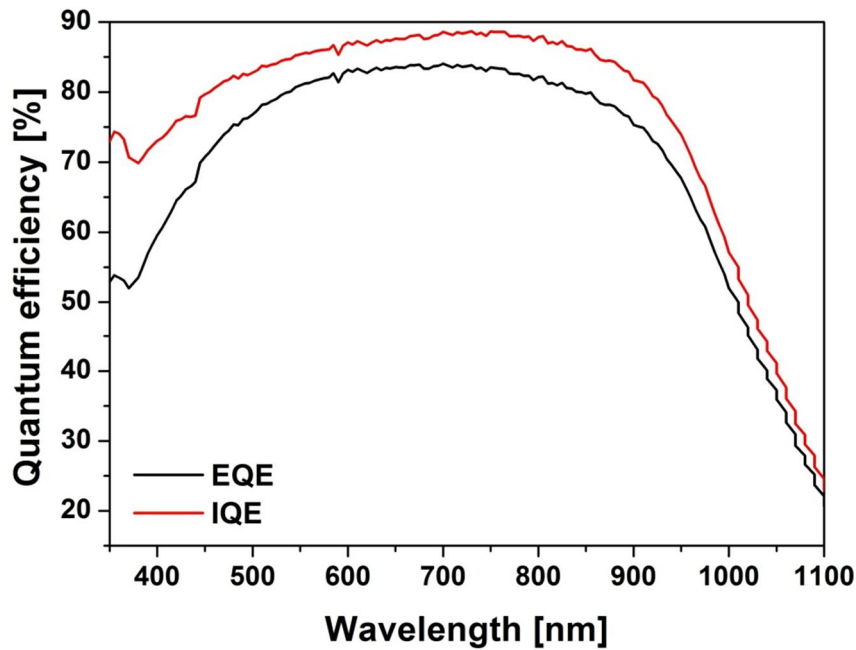
Figure 6.12: *Internal (red curve) and External (black curve) quantum efficiency of the c-Si cell.*

6.4.2 EFFICIENCY MEASUREMENTS ON C-SI SOLAR CELLS INTEGRATED WITH A DS LAYER

Efficiency measurements were performed using an ABET sun 2000 solar simulator class AAB following closely the procedure described in the international standard CEIIEC60904-1. In the following we indicate only the most important parts of the procedure. The temperature of solar cells and reference cell is actively controlled to be 24°C during the measurements. I–V curves were measured with a Semiconductor Source Measure Unit from Keithley Instruments Inc. using a 4 wire connection and the measurements are corrected for the external series resistance. All the solar cell characteristic measurements were carried out in APP laboratory, FBK. The solar cell characteristics were studied by capping the solar cell externally by the prepared TiO_2:Nd thins films deposited on quartz substrate.

6.4.3 Choice of films for active LDS layer

The series of samples made of titania thin films doped with Nd^{3+} ions deposited by RF sputtering on quartz substrates, with the different architectures described before were tested. All the samples were annealed at 600°C for 6 hours. Additionally, 2 samples were tested too: an un-doped titania and a Nd-doped titania monolithic film. The first sample, corresponding to sample #S1, was only pure TiO_2 deposited on quartz substrate. In the sample S2 (the same kind of sample described in Chapter 3, obtained by RF sputtering of TiO_2 after target cross-contamination), the Nd/Ti atomic was Nd/Ti=0.9%(corresponding to a Nd concentration [Nd]=0.3%). The solar cells capped with naked quartz substrates were also tested and served as reference for the coatings.
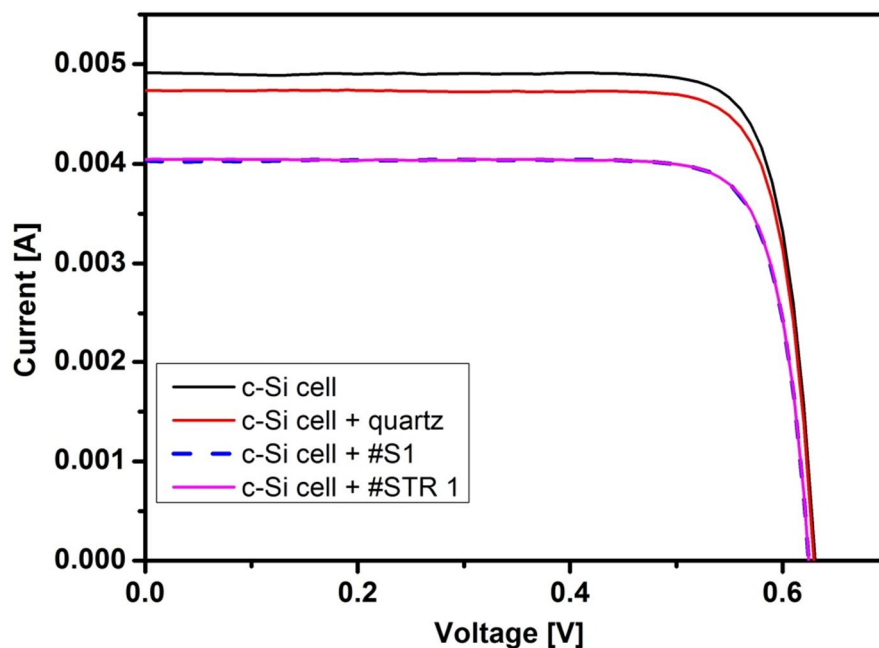
Figure 6.13: *I-V curves of the c-Si cell with and without the DS layer located on the top surface of the cell.*

The I-V curves obtained with and the related parameters are presented in Figure 6.13. Short circuit current, I_{SC}, open circuit voltage, V_{OC}, and fill factor, FF, given in Table

6.5, were extracted from the I–V curves taken under the conditions described below. After measurement of the reference cell, i.e. cell without the DS layer, a measure of the cell with a quartz substrate located on the top surface has been performed in order know the real contribution of the DS layer. Plain glass was also tested.

Samples Analyzed	Open Circuit Voltage Voc (mV)	Short Circuit Current Isc [mA]	Integrated Photon Flux [x10^{21} m^{-2} s^{-1}]	Fill Factor [%]	Efficiency [%]	Isc/Φint [mA/ 10^{21} m^{-2} s^{-1}]
Solar cell 1	630.8	4.955	2.50	83.20	18.06	1.98
Solar cell 1 + Quartz	627.9	4.711	2.32	80.77	16.59	2.03
Solar cell 1 + plain Glass	628.8	4.633	2.26	82.81	16.75	2.05
Solar cell 1 + TiO2 (#S1) Annealed	623.2	4.029	1.91	82.76	14.43	2.10
Solar cell 1 + #S2	620.8	3.756	1.63	82.58	13.37	2.30
Solar cell 1 + # STR 1	622.0	3.898	1.40	80.14	13.49	2.78
Solar cell 1 + # STR 2	622.8	3.924	1.83	82.69	14.03	2.14
Solar cell 1 + # STR 3	623.6	4.032	1.83	82.63	14.43	2.20
Solar cell 1 + # STR 4	623.6	4.059	1.85	82.85	14.56	2.19

Table 6.5: *Solar cell parameters with a TiO$_2$:Nd layer deposited on quartz on front side*

As can be seen in Table 6.5 the most influenced parameters are the short circuit current, and the Power Conversion Efficiency (PCE). In this case we can observe a decrease in the PCE of each cells, indicating that the LDS has an *"apparently"* negative effect on the cell performance.

This result can be understood by considering different issues:

(a) the reflectance of the films: no ARC was applied on the LDS

(b) the transmittance of the DS layer: in the spectral interval from 500nm to 1250 nm. Reflectance and transmittance spectra for Nd-TiO$_2$ containing 0.9at.% of Nd/Ti ratio and the analysis of the transparency spectra of the different DS layers deposited on quartz substrates are presented in Fig.6.14. In this case in the spectral interval from 500nm to 1250 nm only about 75% - 80% of the incoming light manages to reach the cell.

In order to decouple the effects of the optical properties of the layers (transmittance, reflectance) and the effects of the down-shifting process, instead of the cell efficiency variation, we considered the Isc/integrated photon flux ratio (Isc/Φint), i.e. the current obtained per incident photon which effectively reaches the cell. For this doing, the photon flux was calculated as

$$\Phi = I(\lambda).T(\lambda).\frac{\lambda}{1.24}$$

where I(λ) is the solar irradiance (given in Fig.6.14 (a)), λ the wavelength and T(λ) the sample optical transmission. The obtained photon flux spectrum obtained for sample #S2 is shown in Figure 6.15 (b). Such curve was integrated over the wavelength range of 200 – 1250 nm to determine an integrated photon flux. The Isc/Φint ratio values obtained for the selected samples are given in the last column of Table 6.5. The values can be compared to those of the reference cell and of the cell covered by plain quartz. Similar results were obtained with plain quartz and plain glass. This ratio was higher

for the Nd-doped layers than for the cell and for the sample made of un-doped TiO_2. The highest current-per-photon yield was obtained for sample #STR 1, followed by sample #S2. The yield of the other samples was not very far from the pure titania (#S1) value.

It is interesting to note that this behaviour is quite similar to the one concerning the PL emission intensity for the transition from $^4F_{3/2}$ to $^4I_{9/2}$, under excitation by UV. In fact in the range 1080-1150 nm, shown Fig. 6.10(b), the sample STR#1 PL intensity was dominating that of all the other layered films, which exhibited similar PL spectra. On the other hand, we know from the results given in Chapter 3 that the PL spectrum of the sample #S2 had good intensity and narrowness characteristics (see Fig. 3.15). This fair correlation between the capacity of frequency down-shifting from UV to NIR of the samples and the current-per-photon yield measured during the films testing on c-Si cell under simulated solar light, demonstrates the capacity of the solar spectrum modification.

The possibility of a gain in the Isc/Φint ratio, when Nd- doped TiO_2 layers were applied to a c-Si cell, is confirmed by the evolution of the Isc in function of Φint. Such a plot is shown in Figure 6.16. For a passive layer, the data point should be well fitted by a linear curve passing through the origin of the graph. This is indeed observed when the cell is capped with plain quartz, plain glass and plain sapphire, and the corresponding points (in red in the plot) align well with the reference cell. Here, no modification of the solar spectrum could be expected. In contrast, a layer activity appears quite possible when Nd-doped TiO_2 layers are applied onto the cell. In the plot we reported all the tested samples, obtained in a variety of deposition conditions and with different architectures.
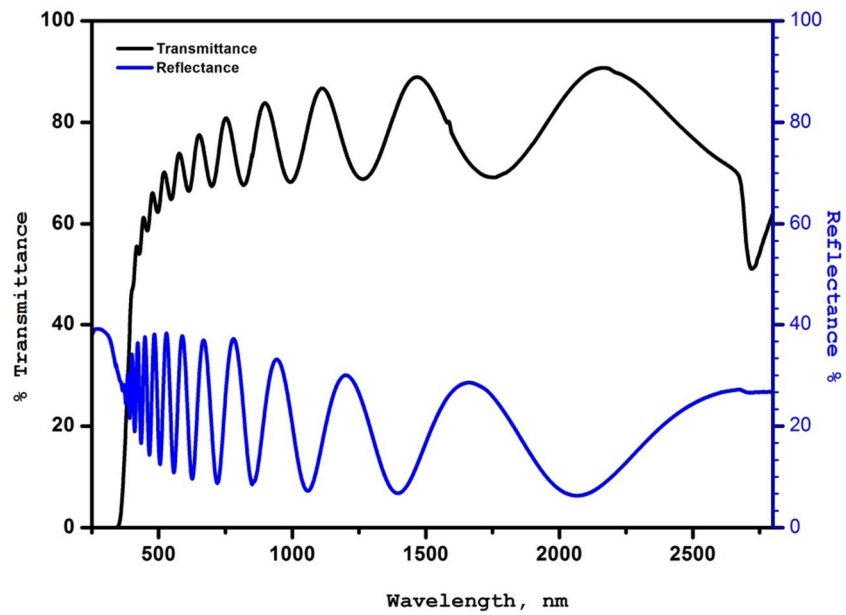
Figure 6.14: *Transmittance and Reflectance spectra of Nd-TiO$_2$ (0.9% Nd) film, deposited on quartz*

Some samples resulted more likely inactive; the relative data points remain close to the linear curve fit, such as the pure TiO$_2$ layers (in green in the plot). Many other samples significantly deviate from the linear curve, lying significantly higher. It means that for a given photon flux value, the samples yield more short circuit current than what it would be with a passive layer.
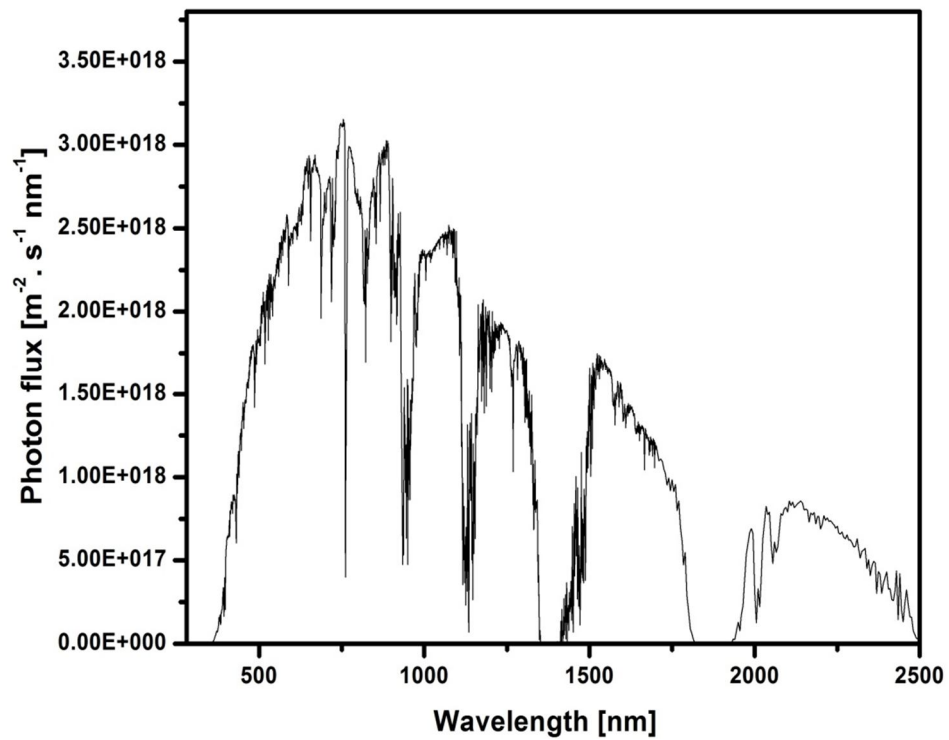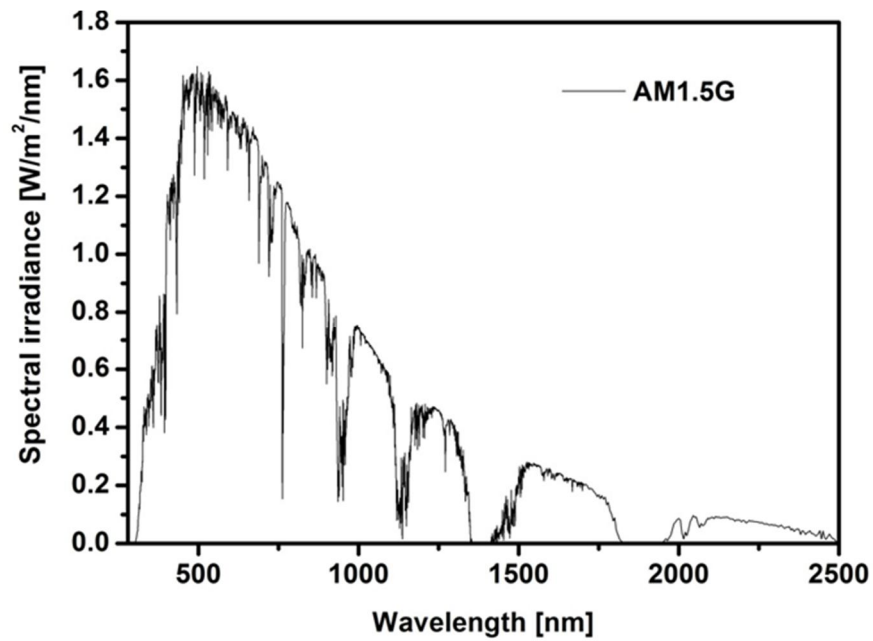
Figure 6.15: *(a) Solar irradiance (AM 1.5G) and (b) photon flux incident onto a solar cell with sample #S2 on front side*
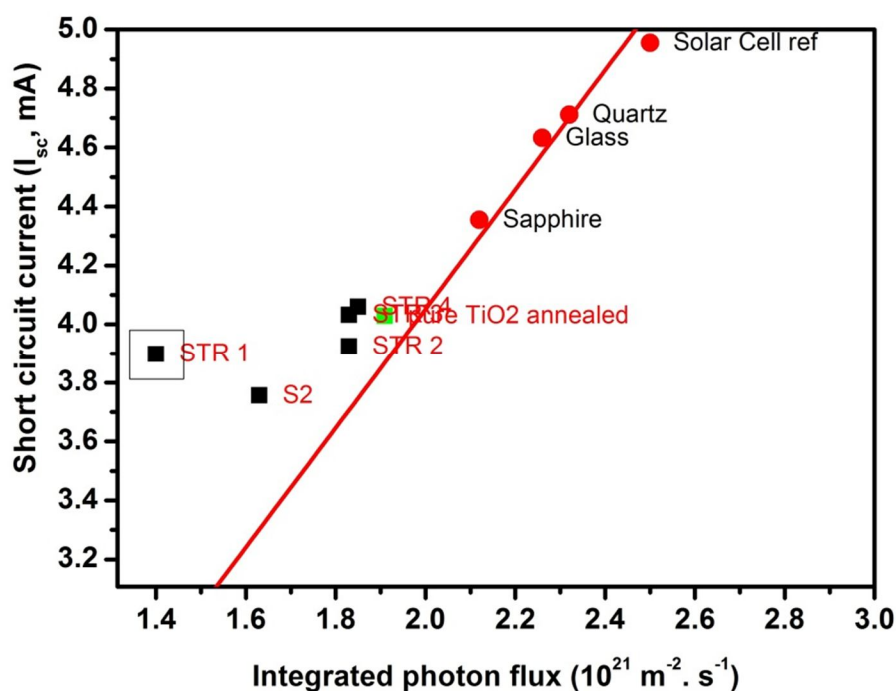
Figure 6.16: *Plot of the short circuit current in function of the integrated photon flux*

6.5 PHOTOCATALYTIC PROPERTIES OF Nd – DOPED TITANIA THIN FILMS

The effect of different Nd-dopant concentrations and its influence on the photocatalytic efficiency has been explored by measuring the photodegradation of methylene blue (MB) dye aqueous solution of 4 ml with a concentration of 10mg/L using distilled water in a cuvette. The Nd –doped titania samples deposited on quartz substrate are immersed in MB solution and irradiated with the 8W monochromatic UV source of 254 nm wavelength. The distance between the sample cuvette and the UV lamp is 5 cm. The effect of this UV radiation on MB is measured without the photo catalyst also. Then the concentration change of MB dye (de-coloration) while undergoing photocatalytic reaction in the presence of the catalyst (pure and Nd-doped

Titania films) is monitored in the visible absorbance intensity at 664.05 nm as a function of irradiation time using Ocean Optics bench type – Maya Pro 2000 spectrophotometer.

Figure 6.17 shows the absorption spectra of MB for the pure Titania and for the sample deposited with a power of 3 watts, corresponding self-bias voltage V_{Nd} = -32V (Nd/Ti at.ratio: 3.7%), under 254 nm illumination at different time intervals and the corresponding concentration of MB as a function of time during photo degradation.
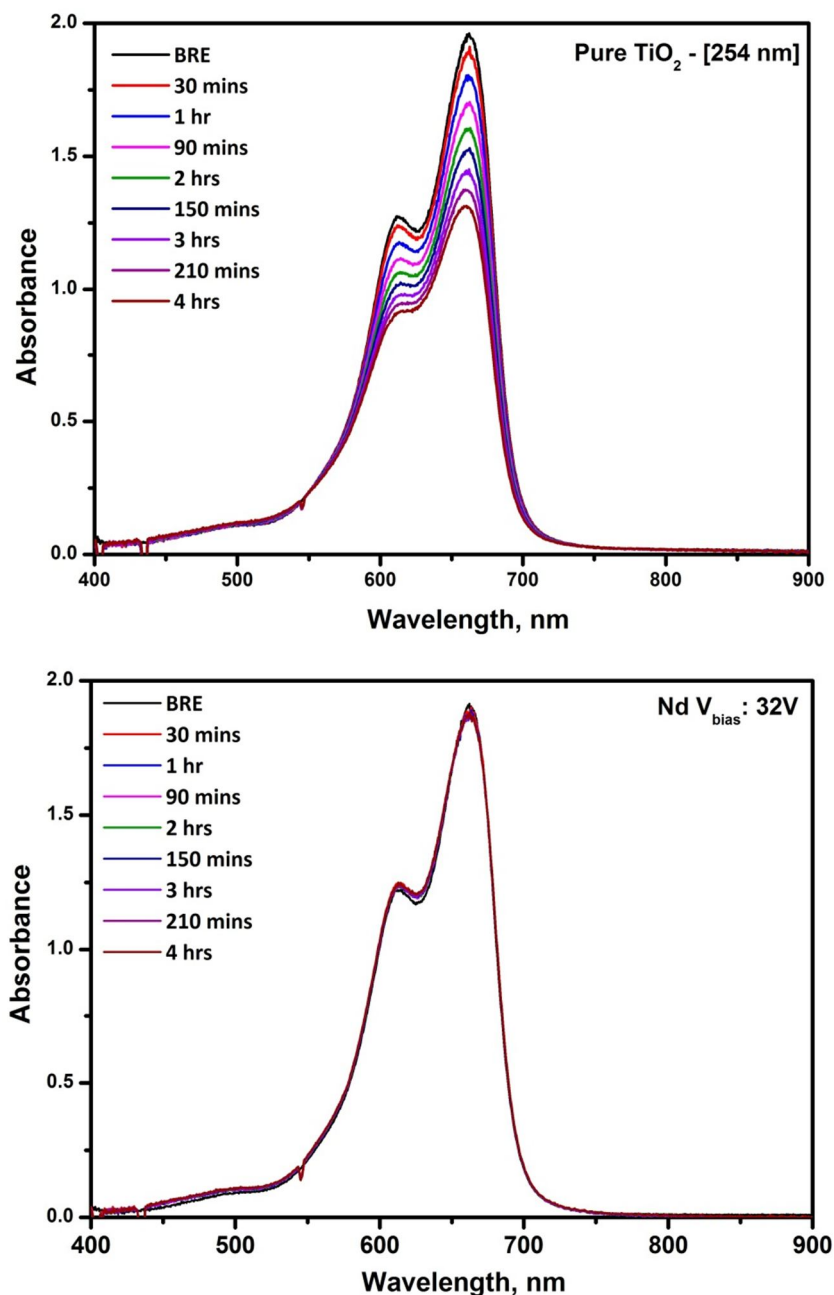
Figure 6.17: *MB absorption spectra in the wavelength range 400nm -700nm for pure and Nd –doped titania film at different time intervals under 254 nm UV irradiation*

It can be seen that the concentration of MB dye decreased gradually with the exposure time for the pure titania thin film. Without the photocatalyst, almost no MB dye could be degraded. The results suggest that the prepared titania film had the ability to degraded the MB dye under UV illumination. Additionally, with the increase of Nd loading in titania matrix (V_{bias}= 32V), there is abruptly no change in the photo degradation of MB dye. Figure 6.18 shows the photocatalytic oxidation curves of Nd –doped titania thin films for different concentrations loading in titania matrix (-V_{Nd}= 0, 21V, 32V, 52V, 57V and 63V, corresponding to a power of 0, 2,3,5, 6 and 7W).
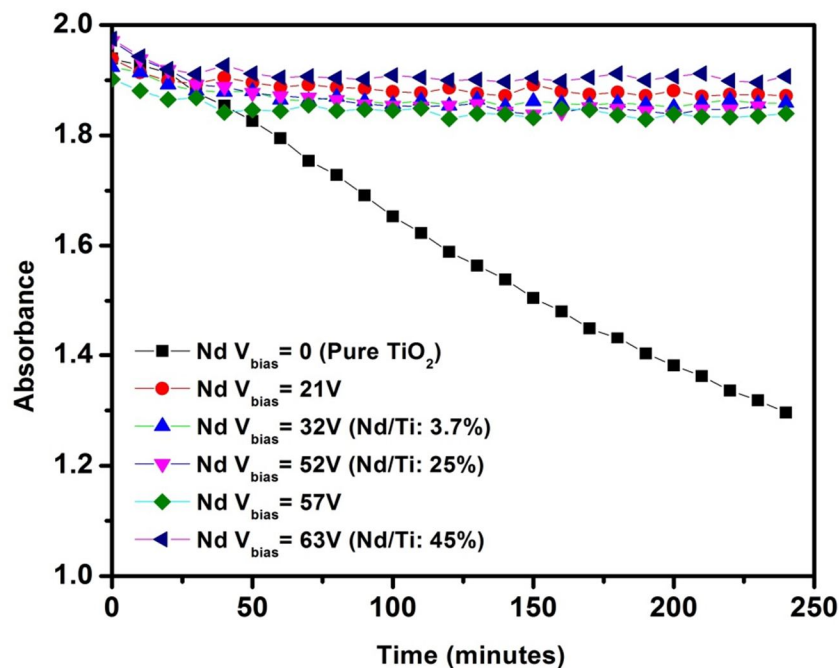
Figure 6.18: *Photocatalytic oxidation curves of Nd –doped titania thin films for different concentrations (V_{bias} on Nd target= 0, 21V, 32V, 52V, 57V and 63V).*

From the figure, it can be observed that the degradation rate for the pure titania appears more stronger than the any of the Nd – doped titania films. The presence of

neodymium in the titania has significantly altered the degradation rate of MB. After the initial period of MB degradation, the concentration of MB stopped decreasing, indicating the photocatalytic degradation has stopped almost completely. The results indicate that the presence of neodymium ions, even a trace amount, can inhibit the photocatalytic activity of TiO_2 significantly. Therefore, neodymium ion acts as an inhibitor of photocatalytic activity on loading with titania. There are many possible reasons behind this inhibition. Firstly, as we see from the view point of structural properties (from the results of Chapter 3), even a low concentration of neodymium changes abruptly the crystal structure and the crystallinity of the films. With increasing the concentration from Nd/Ti= 3.7at.% to 45%, there is a clear picture of structural deterioration in the titania host matrix (from chapter 3, Figure 3.8). This can be one of the possible reason that Nd-doped titania inhibits the photocatalytic activity. We further investigated the photo-induced change of the surface wettability of the samples, following the idea that, even if the processes underlying this property and the photo-catalycity can be different, some surface photo-response can be common to both processes.
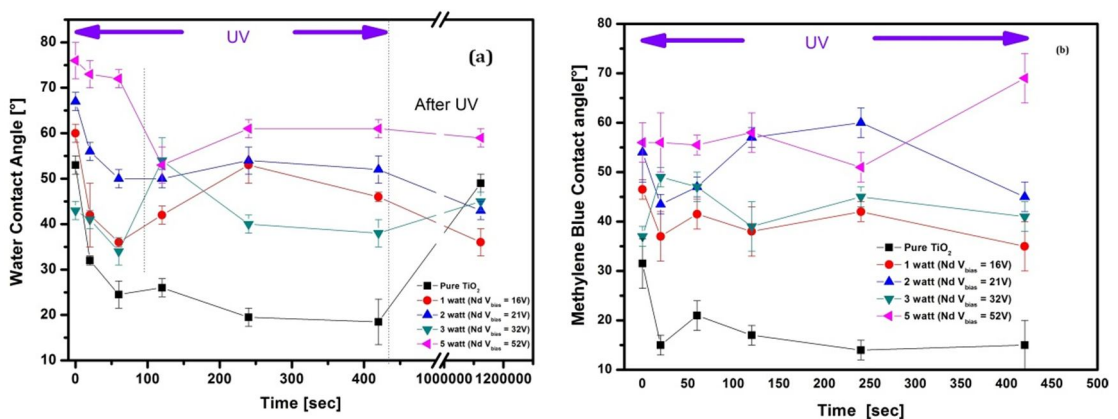
Figure 6.19: *Contact Angle Measurement for (a) water and (b) methylene blue dye under UV illumination on pure and Nd –doped titania thin films*

In order to analyse the film surface wettability, sessile contact angle measurements were measured both in water and also with Methylene blue dye before and after UV illumination. Figure 6.19 (a and b) shows the variation in the contact angle for water and Methylene blue dye under UV illumination.

In both the case, pure titania shows a strong variation in the contact angle under UV illumination which represents the typical behaviour of photo activity. Nd –doped titania films shows (a) only a slight reduction between 0 to 100 secs of UV illumination (b) no recovery of contact angle after UV illumination. This indicates that the photoactivity is completely suppressed due to the loading of Nd into the TiO_2 matrix.

From these measurements and in combination with other measurements done with polar and non-polar liquids, the total surface energy was calculated for the samples both before and after UV illumination.

The solid surface free energy (SFE) γ_s and its polar and non-polar components, indicated with γ_s^p and γ_s^d respectively, were estimated using the Owens-Wendt's equation [13],

$$(1 + \cos\theta)\,\gamma_1 = 2\sqrt{\gamma_s^d \gamma_1^d} + 2\sqrt{\gamma_s^p \gamma_1^p}$$

Testing liquids	γ_l (mJ/m^2)	γ_l^d (mJ/m^2)	γ_l^p (mJ/m^2)
Water	72.8	21.8	51
Diiodomethane	50.8	50.8	0

Table 6.6: *The surface free energies for the wetting liquids and their polar and non-polar components* [14].
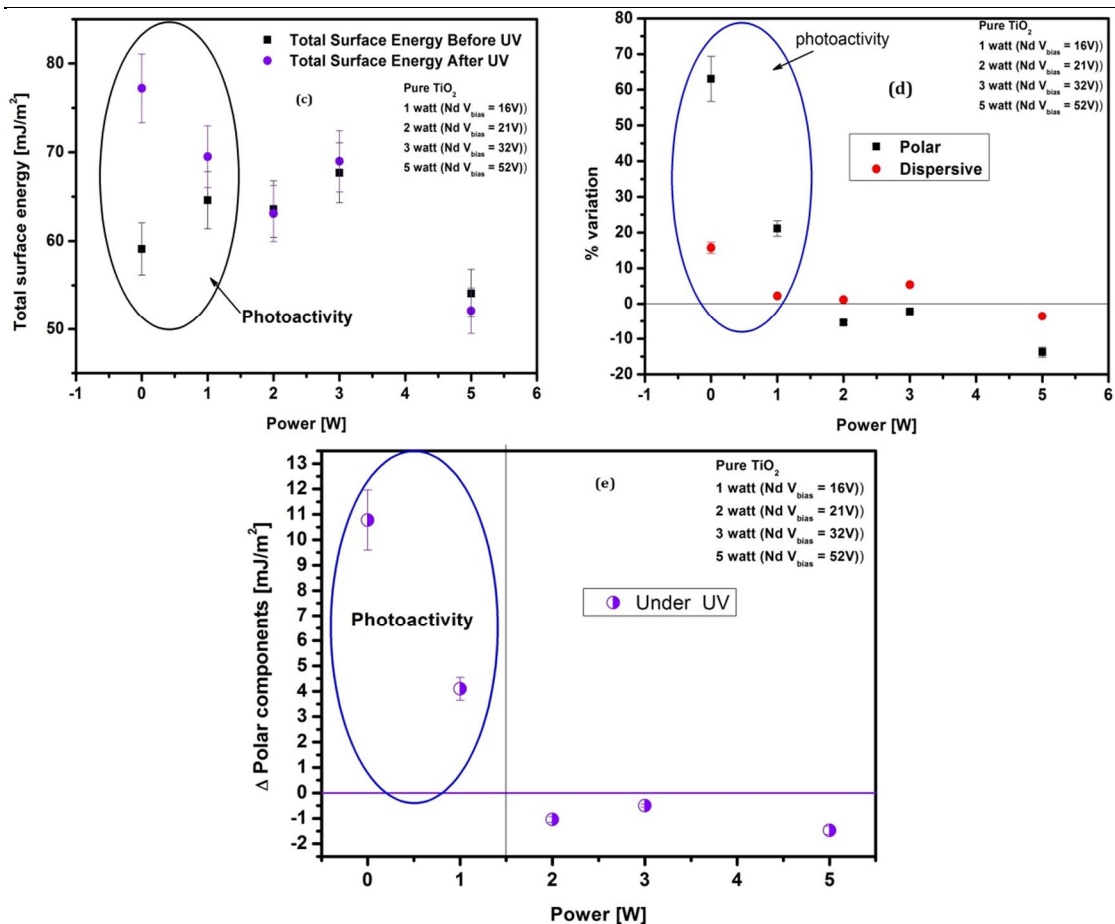
Figure 6.20: *Plots of Total surface Energy (c), % variation in the polar and dispersive components (d) and total amount of variation in the polar component (e) for Pure and Nd –doped titania thin films.*

From the figure (c), we see that the total surface energy of the films before UV illumination was between $59mJ/m^2$ and $67mJ/m^2$. After 420 seconds of UV illumination, no reasonable change in the surface energy was observed in the films doped with Nd^{3+} while in the case of pure titania after UV illumination, we observed strong increase of surface free energy. This indicates that the photoactivity tends to increase strongly the surface energy of materials. The polar and dispersive components were estimated to understand their contribution on total surface energy. By means of Owens-Wendt's method, the polar and dispersive components were estimated as shown in figure (d). The figure shows the % variation of each component

for pure and Nd –doped titania films. It appears clear that the main variation observed after UV illumination was related to surface polar component as there is no any visible change in the dispersive component. The total amount of variation of polar component is reported in figure (e). It shows that the UV illumination gives a change of 11mJ/m^2 in pure titania. The low concentration of Nd^{3+} doped films (V$_{bias}$ = 16V) are reduced and shows a change around 4mJ/m^2. The samples doped with high concentrations of Nd, didn't show any response which indicates that polar components are affected by UV illumination. Finally, it appears clear that photoactivity is mainly related to the change in polar component on surface. The change in polar component is suppressed when Nd is added in the titania matrix. The obtained results were in line with those obtained from the photo-activity tests for MB degradation under UV (no degradation in MB under UV illumination). Pure Titania shows a clear variation in the total surface energy after the UV illumination, suggesting the possibility of photoactivity, while the Nd-containing titania films, no change of the surface energy was observed.

6.6 CONCLUSIONS

In this section, the optimisation and the luminescent properties of the photon frequency downshifter layer based on rare earth ions doped titania matrix were studied. Firstly to optimise the post growth annealing temperature of the films, the different annealing temperature studies (300-800°C) shows a maximum NIR PL intensity for the film annealed at a temperature of 600°C under non-resonant excitation (through UV) which confirms the possibility of energy transfer from the titania host matrix to the Nd^{3+} ion . The film also exhibits both the anatase and rutile phase structure. From the optical point of view, there is strong reduction in the

bandgap of titania is observed. Secondly, in order to incorporate low concentration of Nd in the titania matrix, optimisation on the architecture approach have been carried out. All the films shows an intense NIR PL emission via energy transfer excited under UV (355nm). Finally these prepared films were subjected to the further testing of downshifting effect. There is no real change/increase in the efficiency as observed, but we can see the contribution of the layer through the increase in the current per photon yield. The highest current per photon yield was obtained for the film STR #1 which also shows the higher NIR photoluminescence intensity. These films were also tested for the photoactivity response in the degradation of methylene blue dye. There is no change in the degradation as observed when comparing to pure titania. This strongly shows that Nd doping inhibits the photoactivity response for the concentrations varied from Nd/Ti at.ratio: 3% to 45%, which also confirmed with the contact angle measurements under UV illumination. A clear structural deterioration and high concentration of Nd doping ($\geq$ 3%) can be one of the possible reasons that Nd-doped titania inhibits the photocatalytic activity. These results indicate that doping effect of Nd ions (shows anatase to rutile phase transformation) is dependent on not only the intrinsic physicochemical properties of doping but also the concentrations of the dopants.

REFERENCES

[1] M. Van Gysel, P. Lemberge and P. Van Espen, Implementation of a spectrum fitting procedure using a robust peak model, X-Ray Spectrom. 32 (2003) 434

[2] L. H. Christenson, Comparison between Experimental and Calculated Relative intensities for an Intrinsic Ge Detector in the energy region 11-25 keV, X-Ray Spectrometry, Vol.8, No. 4, (1979)

[3] T. Schoonjans, A. Brunetti, B. Golosio, M. Sanchez del Rio, V. A. Solé, C. Ferrero and L. Vincze, "The xraylib library for X-ray--matter interactions. Recent developments", Spectrochimica Acta B 66 (2011) 776 (doi: http://dx.doi.org/10.1016/j.sab.2011.09.011)

[4] C. N. R. Rao, Canadian Journal of Chemistry, 39 (1961) 498

[5] Laura E. Depero, Paolo Bonzi, Marcello Zocchi, Cristina Casale and Gennaro De Michele, Journal of Materials Research, 8 (1993) 2709

[6] Wang Yue, Wu Da-Jian, Yang Yue-Tao and Liu Xiao, Chinese Phys. Lett. 28 (2011) 027804

[7] Yue-Hua Xu, Chao Chen, Xue-Ling Yang, Xin Li and Bing-Feng Wang, Applied surface science, 255 (2009) 8624

[8] H. Tang, Thèse École polytechnique fédérale de Lausanne EPFL, n° 1311 (1994)

[9] Michael Grätzel and François P. Rotzinger, Chemical Physics Letters, 118 (1985) 474

[10] S. Jandl, J.-P. Rheault, M. Poirier, A. Ait-Ouali, A. M. Lejus and D. Vivien, Phys. Rev. B, 56 (1997) 11600

[11] L. Li, C.-K. Tsung, Z. Yang, G. D. Stucky, L. D. Sun, J. F. Wang and C. H. Yan, Advanced Materials, 20 (2008) 903

[12] Zeng Qing-Guang, Ding Ze-Jun, Ju Xin, Wang Yi and Sheng Ye-Qing, Chinese Phys. Lett., 24 (2007) 1368

[13] M. Zenkiewicz, "Methods for the calculation of surface free energy of solids", J. of Achievements in Materials and Manufacturing Engineering, 24 (2007) 137

[14] M. Gindl. G Sinn, W Gindl, A Reiterer S Tshegg , Colloid an Surface A: Physicochemical and Engineering Aspects 181 (2001) 279

CONCLUSION

"Now this is not the end. It is not even the beginning of the end.
But it is, perhaps, the end of the beginning"
-Sir Winston Churchill

The aim of the work presented in this thesis was a study of rare earth doping effects on the structural, chemical, optical and near infra-red photoluminescence properties of wide band gap oxide thin films. The two host matrix chosen for the study were titanium oxide and zinc oxide.

The choice of the neodymium dopant for such oxides to develop photon frequency downshifter materials necessitates first of all to understand the effects of doping on the properties of the matrix. This led us to conduct a wide characterization of the properties of the Nd-doped TiO_2 and ZnO films. The access to numerous and complementary analysis techniques was of fundamental importance for this study and allowed to establish the understanding basis of the down-shifting process occurring in these oxides.

The first step was the study of the structural, optical, chemical and photoluminescence properties of neodymium-doped titania prepared by RF co-sputtering method at room temperature. It was found that even low concentrations of neodymium (Nd/Ti=0.9%) in the titania matrix induced strong variation in the phase structure, a phase transformation from anatase to rutile is observed, accompagned by remarakable lattice distortion long the c-axis. Increase in the neodymium content to (Nd/Ti=45%) , hindered the crystallization of the titania. The optical studies showed

that addition of neodymium in the titania matrix entailed a strong reduction of the bandgap value. This variation in bandgap could be correlated with the lattice distortions: the higher the c/a lattice parameter ratio, the lower the bandgap of the doped films. PL properties have been investigated both in resonant excitation with the $^4F_{3/2}$ emitting state of Nd^{3+} and with non-resonant excitation. Intense NIR PL emission band was observed for low doping concentration of neodymium upon UV excitation, signing the occurence of the excitation energy transfer from the host titania to Nd^{3+} ions.

The same kind of investigation was done for the ZnO films about the Nd effects on the structural properties. When the concentration of neodymium is above the doping limit of the matrix , a clear deterioration of wurtzite structure was observed and also the segregation of Nd_2O_3 phase was visible. Alternately, at low concentration of Nd doping, no abrupt change were observed from either the crystallinity or optical point of view. NIR broadband PL spectra were observed, under UV excitation, for low doping concentrations showing the possibility of energy transfer from the host matrix. In contrast, at higher Nd concentrations (Nd/Zn=0.2) , NIR PL emission spectra from Nd_2O_3 phase (due to segregation of separate phase) was observed.

The third part of the study consisted of understanding the process of energy transfer from the matrix to the Nd^{3+} ions. Photoluminescence excitation measurements, jointly with optical absorbance measurements were of valuable help. Firstly, a clear evidence from PLE measurements was given to a strong characteristic excitation band in both TiO_2 and ZnO matrices cases, for an excitation energy close to their bandgap energy, confirming that the NIR emission bands arises due the electron-hole pair energy. An interesting correlation was found between the Raman measurements and the PL emission intensity of the doped titania: the lower the Raman shift of the

Eg mode of anatase, the higher the PL intensity. Emission spectra in the Visible range allowed to identify intra-gap defects states, related either to O vacancies or to self-trapped excitons, which, in combination with the XPS and XRD analyses results, led to a preferential model of the excitation energy transfer mediated by the self-trapped excitons.

Finally from an application point of view, the PL of the films were also studied by realizing different architectures in the form of bi/mulit-layers in order to reach very low concentration in the titania matrix (0.1-0.2 at.%), more easier produced by sequential sputtering than by co-sputtering. These films were characterized for their PL properties and further tested as downshifters onto a silicon-solar cell. Even though their integration to the cell remains to be optimized, they gave promising results as far as the cell efficiency is evaluated as a current-per-photon yield.

Keeping focused onto the solar applications, we also tested these films for their possible photoactivity in organic molecules degradation. The Nd-doped films behaved as degradation inhibitors (for the doping concentration of Nd/Ti at.ratio: 3.7% to 45%) of the methylene blue dye, in contrast with the un-doped films which showed a significant photoactivity.